CRANFIELD UNIVERSITY

DEMIN WU

DESIGN AND OPTIMISATION OF ELECTRIC DRIVE SYSTEM WITH HIGH PERFORMANCE AND LOW COST

SCHOOL OF WATER, ENERGY AND ENVIRONMENT
Energy And Power Engineering

PhD
Academic Year: 2012 - 2017

Supervisor: PROFESSOR PATRICK LUK
December 2017

CRANFIELD UNIVERSITY

SCHOOL OF WATER, ENERGY AND ENVIRONMENT
Energy And Power Engineering

PhD

Academic Year 2012 - 2017

DEMIN WU

DESIGN AND OPTIMISATION OF ELECTRIC DRIVE SYSTEM WITH HIGH PERFORMANCE AND LOW COST

Supervisor: PROFESSOR PATRICK CHI-KWONG LUK
December 2017

This thesis is submitted in partial fulfilment of the requirements for the degree of DOCTOR OF PHILOSOPHY

ABSTRACT

As the main component in the global trend of electrification, the electric machine will experience growing demands in many applications such as industrial equipment, domestic appliances, electric vehicles and renewable energy systems. However, nowadays the majority of electric machines are induction machines, which are robust, low-cost, but with relatively low efficiency compared to PM motors, and they face challenges to meet the stringent efficiency mandatory standards. Synchronous machines with rare-earth permanent magnets are the most promising to improve efficiency and fulfil mandatory requirements, but the price of rare-earth materials is every high and volatile. The low-price and abundant ferrite magnet offers a promising solution for non-rare-earth permanent magnet synchronous machines to replace induction machines with similar material cost but higher efficiency. The ideas of *high performance* and *low cost* are not only limited on the machine body itself, but also include the considerations of its whole life cycle, such as motor design, motor manufacture, and motor controller. In the thesis, the particle swarm optimisation algorithm is applied in the ferrite IPM machine design, and with the help of VBScript programming language, a time-efficient electric machine design method is proposed to reduce substantially the designer's designing time and hence the total cost of machine design. The design of experiment (DOE) assisted Six Sigma DMADV method is proposed for the quality control of the electric machine, and the motor quality is improved by realistic adjustment of the tolerances to minimise variations in output performance. The iron loss analysis considering the effects of press fitting stress, shrink fitting, and PWM harmonics results in accurate loss estimation and provides useful advice for implementation of vector control for high performance of the motor. To lower the controller cost, optimised speed and current sensing algorithms are developed based on low-cost Hall Effect speed feedback and single-shunt current sampling. Finally, a prototype machine is manufactured and extensive tests are undertaken to validate the proposed low cost and high performance motor technology.

Keywords:

Ferrite material, interior permanent magnet, particle swarm optimisation, quality control, Six Sigma, design of experiment, optimality design, iron loss analysis, thermal analysis, Hall Effect speed feedback, single-shunt current sensing

ACKNOWLEDGEMENTS

I would like to acknowledge everyone who has knowingly and unknowingly helped me and wished me the best in successfully accomplishing this research.

I would like to express particular thanks to my supervisor, Professor Patrick Chi-kwong Luk. His supportive encouragement and supervision over the whole study have been extremely helpful and essential.

I would like to thank Dr Weizhong Fei, Dr Bing Xia and Dr Wenyi Liang for the valuable helps and discussions during the research.

I would like to thank the Engineering and Physical Sciences Research Council (EPSRC) for their sponsorship of this research (VESI project, reference: EP/I038543/1).

I would like to give my special thanks to my parents and my wife for their unconditional support and care. I owe every step forward in my life to them.

CONTENTS

LIST OF FIGURES

LIST OF TABLES

NOMENCLATURE

All units are in SI unless otherwise stated.

Alphanumeric

a	Acceleration of motor (Chapter 6)
a, b	Half of the design regions (Chapter 4)
A_{copper}	Cross-section area of copper wire
A_{slot}	Cross section area of slot
a_{start}	Acceleration at starting point
B	Flux density
B_m	Flux density of PM
B_{s1}	Top width of slot
B_{s2}	Bottom width of slot
c_1, c_2	Scaling factors
d	Thickness of one lamination sheets
D_1–D_{12}	Mechanical dimension
D_{up}	Upper distance between primary and secondary magnets
D_{dw}	Lower distance between primary and secondary magnets
d_c	Diameter of the copper wire
f	Operating frequency
f_{11}	Fitness of the first design in the first generation
f_g	Fitness of the global best design
f_{i1}	Fitness of of the i^{th} design at the initial generation
f_{ik}	Fitness of of the i^{th} design at the k^{th} generation
$f_{measure}$	Measuring frequency
f_{pi}	Fitness of the personal best of the i^{th} design
f_{sample}	Sampling frequency
g_d	Global best particle at d^{th} dimension
H	Magnetic Field Intensity

H_s	Depth of stator slot
I	Current flowing in the copper coil
I_A, I_B, I_C	Current in three phase windings
i_d, i_q	d- and q-axis stator current in the rotor reference frame
I_{shunt}	Current in shunt resistor
K	Constant multiplier in PSO
k_c	Coefficient of eddy current loss
k_e	Coefficient of excessive loss
k_h	Coefficient of hysteresis loss
k_{rpac}	Increment factor
L_{copper}	Length of copper wire in each phase
L_d, L_q	d- and q-axis synchronous inductance components
L_{eff}	Axial effective length of the motor
L_{tooth}	Width of the tooth
n	Spinning speed of motor
N_c	Number of the conductors in a coil
$N_{counter}$	Number of observed edge signals by counter
$n_{encoder}$	Calculated speed by encoder
n_{Hall}	Calculated speed by Hall sensors
N_p	Winding pitch counted in slots
N_s	Number of all slots
N_{slit}	Number of encoder slits
p	Pole pairs of actual machine
p_c	Eddy-current loss density
P_{cpl}	Copper loss
P_{cpl_ik}	Copper loss of the i^{th} design at the k^{th} generation
P_{crl}	Core loss
p_e	Excessive loss density
p_h	Hysteresis loss density

p_{id}	Personal best of the i^{th} particle at d^{th} dimension
P_{loss}	Total losses of motor
P_{mech}	Mechanical output powder
p_v	Iron-core loss density
R	Electric resistance of copper coil
R_a	AC resistance of the winding
rand	A random number between 0 and 1
R_{dc}	DC resistance of the winding
R_s	Resistance of stator phase winding
T	Output torque
t	Operating time
T_1–T_{12}	Mechanical tolerance
T_{em}	Electromagnetic torque
T_{ik}	Output torque of the i^{th} design at the k^{th} generation
$t_{interval}$	Time interval between two edge signals
T_{MIN}	Minimum time required to perform ADC sampling
T_N	Time duration of the noise
T_S	Sampling time of ADC
u_d, u_q	d- and q-axis stator voltages in rotor reference frame
V	Velocity of motor (Chapter 6)
V	Velocity of the PSO motor design parameter (Chapter 3)
v	Velocity of the particle in PSO
V_{DC}	DC voltage
v_{id}	Velocity of the particle in the d^{th} dimension
V_{max}	Maximum velocity factor
w	Inertia weight
W_{pm}	Width of primary magnet
W_{sm}	Width of secondary magnet
W_t	Width of stator tooth

X	Parameter of motor design
x	Particle's coordinate in PSO
X_{max}	Upper limit of the varying range of motor design parameter
X_{min}	Lower limit of the varying range of motor design parameter
x_{id}	Particle's coordinate in the d^{th} dimension
α	Resistivity-temperature coefficient
δ	Skin depth
ΔT	Change of temperature
$\Delta\rho$	Change of the resistivity
θ	Angle position
$\theta_{encoder}$	Angle position obtained by encoder
θ_{ref}	Reference angle position
μ_r	Relative permeability of conductor
ρ	Resistivity of copper
ρ_0	Original resistivity
σ	Conductivity of a lamination sheet
φ_1, φ_2	Cognitive and social components of PSO
ψ_d, ψ_q	d- and q-axis stator flux linkage in rotor reference frame
ψ_f	Permanent magnet magnetic flux linkage
ω_e	Rotor electrical angular frequency

Subscripts

A, B, C	Associated variables of phase A, B and C
d, q	d- and q-axis components of associated vector in rotor synchronous reference frame
d	The dimension of a particle in PSO process
g	Global best (*gbest*) in PSO
i	The number of particle in PSO process
k	The generation/iteration of the swarm in PSO process

max	The maximum value of the range
min	The minimum value of the range
p	Personal best (*pbest*) in PSO

Abbreviations

AC	Alternating Current
ADC	Analogue to Digital Converter
AFPM	Axial Flux Permanent Magnet
AMM	Amorphous Magnetic Material
BLDC	Brushless Direct Current
CPSR	Constant Power Speed Range
DC	Direct Current
DEA	Differential Evolution Algorithms
DFSS	Design for Six Sigma
DMADV	Define Measure Analysis Design Verify
DMAIC	Define Measure Analysis Improve Control
DTC	Direct Torque Control
DOE	Design of Experiments
DT	Dead Time
EMF	Electromotive Force
EMSM	Electrically Magnetised Synchronous Machine
EV	Electric Vehicle
FEA	Finite Element Analysis
FFT	Fast Fourier Transform
FSCW	Fractional Slot Concentrated Winding
FSPM	Flux Switching Permanent Magnet
GA	Genetic Algorithm
IC	Integrated Circuit
IGBT	Insulated Gate Bipolar Transistor
IM	Induction Motor
IPM	Interior Permanent Magnet
MMF	Magneto Motive Force

MOSFET	Metal-Oxide Semiconductor Field-Effect Transistor
MTPA	Maximum Torque-per-Ampere
NdFeB	Neodymium-Iron-Boron
OFAT	One Factor At a Time
PID	Proportional Integral Derivative
PM	Permanent Magnet
PMAC	Permanent Magnet Alternating Current
PMASynRM	Permanent Magnet Assisted Synchronous Reluctance Machine
PMDC	Permanent Magnet Direct Current
PMSM	Permanent Magnet Synchronous Motor
PSO	Particle Swarm Optimisation
pu	Per Unit
PValue	Probability Value
PWM	Pulse Width Modulation
RFM	Radial Flux Machine
RMSE	Root Mean Square Error
rpm	Revolutions Per Minute
RSM	Response Surface Method
RSq	R Squared (coefficient of determination)
SCR	Silicon Controlled Rectifier
SDM	Steepest Decent Method
SMC	Soft Magnetic Composite
SmCo	Samarium-Cobalt
SPC	Statistical Process Control
SPM	Surface Permanent Magnet
SPWM	Sinusoidal Pulse Width Modulation
SVPWM	Space Vector Pulse Width Modulation
SynRM	Synchronous Reluctance Machine
TQM	Total Quality Management
VBScript	Visual Basic Scripting edition

1. INTRODUCTION

1.1 Background

Electrification brings considerable environmental benefits by shifting people's dependence on fossil fuel sources, and in many cases electrification increases energy efficiency. Most of electric industrial equipment and domestic appliances that have actuating parts require one or more electric motors, such as washing machines, fans and blowers, electric lawn mowers, air compressors, water pumps, woodworking machinery, and so on. There is a tremendous market for electric machines [1]. However, these pervasive electric machines in household and industry consume 35–40% of the electricity generated worldwide [2]. In the industrialised economies, electric motor systems account for 70% of all industrial electric energy [3]. Electric machines with higher efficiency are therefore of great interest, which not only can cut down energy bills but also reduce greenhouse gas emissions. Studies show that potentially 25–30% of energy saving could be achieved if higher efficiency motors have been used in the past decade [4]. As well known, induction machines (IMs) are the most widely used machine type in industry due to the robust structure, mature manufacturing techniques and low cost, taking up 90% of the overall industrial installation [2]. However, IMs have relatively low efficiency, due to the requirement of reactive power for excitation and high copper loss in the rotor cage bars/windings. The technologies of IMs are relatively mature and it is difficult to further improve their performance [5]. And the low efficient IMs face challenges to meet the mandatory efficiency standards that have been enacted in US and European countries [6,7].

With the development of high-energy permanent magnet (PM) materials, such as neodymium-iron-boron (NdFeB), permanent magnet synchronous machines (PMSMs) are becoming more attractive in various applications with the advantages of high power density, high efficiency and controllability. Since reactive excitation current is not required when using pre-magnetised PMs, the overall loss can be reduced and thus higher power factor and efficiency is possible. Statistical data shows that a vast amount of energy can be saved by

replacing old low efficient induction machines with high efficiency machines [8]. Compared to IMs, 3–4% improvement in efficiency could be achieved by using PM machines, and the cost difference due to the PM materials could be paid back through operating cost savings in less than 2.5 years at 50% percent duty cycle [9]. Thus, PM machines with high energy rare-earth materials have been an appealing contender for various high performance applications owing to their outstanding features of high efficiency and power density [10–14].

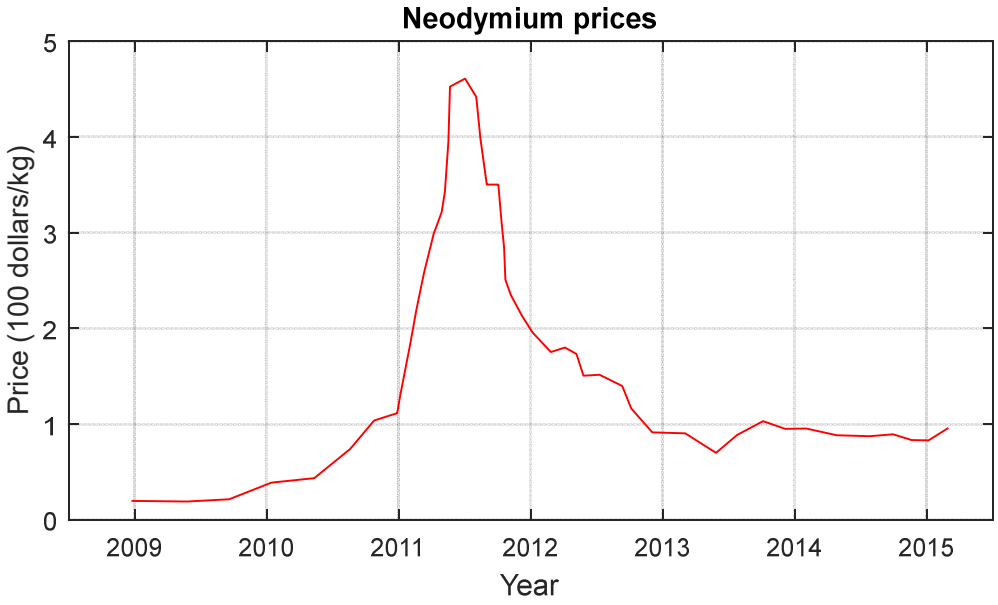

Figure 1-1 The price history of Neodymium material from 2009–2015[15]

However, the price of rare-earth material is high and its supply chain is unstable. The price history of neodymium material from 2009–2015 is shown in Figure 1-1. Because of China's rare earth output restriction on 6th October 2008, the price of neodymium grows sharply from late 2009 to its peak in early 2011, and then decreased dramatically in the next two years [15]. The rare-earth market is still volatile and highly relies on China's exportation. Therefore, there have been a surge of interests in seeking alternative solutions to rare-earth PM based electric machines. It is of strategic importance to develop alternative electric machines solutions with less or even no rare-earth PM materials for high performance with low cost [16–18].

Ferrite magnets, on the other hand, are abundant in supply and much cheaper than rare-earth. As one of the commonly used PM materials, ferrite PM is

considered as the most promising alternative for high-performance low-cost applications. The drawback of ferrite magnet is its low residual flux density, only one third of NdFeB magnet, which raises a challenge for ferrite PM machines to achieve high torque density. But with well-designed geometric configurations ferrite PM machines are able to achieve comparable power density as rare-earth PM machines [19–21].

1.2 Motivation

In the trend of global electrification, there is a huge market of electric machines for electric industrial equipment and domestic applications. With concerns over environmental impact and fossil fuel shortage, energy efficiency has been given high priority in order to reduce greenhouse gas emissions. So the electric machines with high efficiency are in demand. However, nowadays the majority of electric machines are IMs, which are robust, low-cost, but with low efficiency, and they face challenges to meet the strict efficiency mandatory standards that are introduced in US and European countries. The synchronous machines with rare-earth PMs are the most promising to improve efficiency and fulfil mandatory requirements, but the price of rare-earth materials is every high and volatile. With the advantages of low price and abundant supply, ferrite magnets are the most potential candidates for non-rare-earth PMSMs to replace the IMs with similar material cost but higher efficiency. Considering the huge number of IMs installed in industry, there is a vast prospect in developing ferrite PM machines.

In the mass production, the low-cost high-performance electric machine is of great interest. However, the idea of *low cost and high performance* is not only limited in the machine body itself, but also include the cost of its whole life cycle, the cost of design and optimisation, and the cost of manufacturing. For a synchronous machine drive, the motor controller is an indispensable part, so the cost of controller should also be taken into consideration. Therefore the best design of a low-cost high-performance ferrite PM machine drive system should consider all of above factors.

1.3 Aims and Objectives

The thesis aims to design a high-performance and low-cost electric drive system for general industrial and household applications and provide a viable alternative solution to the widely used IMs. The objectives of this thesis can be summarised as follows:

1. To identify the research gap by undertaking an extensive review on the developments and current state of electric drive systems, and critically evaluating different electric machines based on cost and performance.
2. To propose a time-efficient and cost-effective optimisation method for electric machine design, using the approach to design a low-cost and high-performance electric machine.
3. To develop an effective approach to control the quality of electric machines in mass production so that the quality of end-product improves and the overall cost of manufacturing reduces.
4. To improve the performance of the ferrite IPM machine by analysing the generated losses, thermal distribution and temperature variation.
5. To reduce the cost of motor control system by adopting single-shunt resister for current sensing and Hall Effect sensors for position and speed feedback.
6. To validate the proposed methods and ideas by comprehensive experiments on a prototype electric drive system.

1.4 Outline

The thesis is organised as follows:

Chapter 1 introduces this thesis, which includes background, motivation, aims and objectives, outline, main contributions, and publications.

Chapter 2 reviews the state of the art of electric drive systems to select the best candidate to meet the requirements of high performance and low cost. The electric drive of a two-layer spoke type ferrite IPM machine with single shunt current sensing and Hall Effect speed feedback is selected as the best choice for the study.

Chapter 3 discusses the time-efficient and cost-effective method of machine design and optimisation. Particle swarm optimisation (PSO) is introduced and applied in the design of the ferrite IPM machine, and the optimally designed machine is compared with IM to show its advantages over the latter.

Chapter 4 proposes a quality control method to improve the overall quality of electric machine in mass production. The proposed DOE assisted Six Sigma DMADV method minimises the variation of output performance and increase the consistency of machine performance in mass production.

Chapter 5 analyses the loss source and loss consumption of the studied machine and compares with that of the IM. The iron loss analysis is considered with the effect of press fitting, shrink fitting, and PWM harmonics. The thermal effect of the losses and temperature change of the machine is discussed as well.

Chapter 6 discusses the control system of the low-cost electric drive. The single-shunt current sampling and Hall Effect speed feedback are applied in the low-cost electric drive system, and the cost-effective control system is validated by experiments.

Chapter 7 discusses and analyses the experimental results of the prototype ferrite IPM machine, which include the open-circuit test, no-load test, loaded test and thermal test.

Chapter 8 summarise the outcomes of the thesis and discusses possible future work.

1.5 Main Contributions

The contribution of the research to the electric machine engineering can be summarised as follows:

1. A general electric machine design method using particle swarm optimisation (PSO) is proposed in thesis and is successfully applied in the design of two-layer spoke type ferrite IPM machine.
2. A novel quality control method, DOE assisted Six Sigma DMADV method, is proposed for electric machine in mass production, which is applied in

the studied low-cost machine by adjusting mechanical tolerances to minimise the variation of its output performance.

3. Iron loss analysis of two-layer spoke type ferrite IPM machine is carried out considering with the effect of press fitting, shrink fitting, and PWM harmonics.
4. A simple but effective method is used in motor control system to locate reference position of PM machine that has large cogging torque and cannot correctly secure its location directly.
5. A Hall Effect sensor angle position estimation method is proposed and validated in the thesis.
6. A single-shunt current sampling method considering all the voltage space regions is proposed and validated in the thesis.

1.6 Publications

1. Weizhong Fei, P.C.K. Luk, Bing Xia, D. Wu, "Design improvement of outer-rotor permanent magnet flux switching machine for direct-drive urban electric vehicle propulsion," *39th Annual Conference of Industrial Electronics Society (IECON)*, pp.7319-7324, Nov. 2013.
2. Weizhong Fei, P.C.K. Luk, D. Wu, Bing Xia, "Approximate three-dimensional finite element analysis of large permanent magnet synchronous generators with stator radial ventilating ducts," *39th Annual Conference of Industrial Electronics Society (IECON)*, pp.7313-7318, Nov. 2013.
3. Demin Wu, Weizhong Fei, P.C.-K. Luk, Bing Xia, "Design Considerations of Outer-Rotor Permanent Magnet Synchronous Machines for In-Wheel Electric Drivetrain Using Particle Swarm Optimisation," *7th IET International Conference on Power Electronics, Machines and Drives (PEMD 2014),* pp.1-6, April 2014.
4. Bing Xia, Weizhong Fei, P. C. K. Luk, Demin Wu, "Design of a Multi-Layer Interior Ferrite Permanent Magnet Synchronous Machine for Traction Applications," *7th IET International Conference on Power Electronics, Machines and Drives (PEMD 2014)*, pp.1-6, April 2014.

5. D. Wu, W. Fei, and P. C. K. Luk, “Design optimisations of outer-rotor permanent magnet synchronous machines with fractional-slot and concentrated-winding configurations in lightweight electric vehicles” 6th International Conference on Power Electronics Systems and Applications (PESA 2015), pp.1-8, Dec. 2015. (*Second Prize*)
6. D. Wu, P. C. K. Luk, and W. Fei, “Quality Control of Low-cost Electric Machine for Electric Vehicle Applications by DOE Assisted Six Sigma DMADV” 7th International Conference on Power Electronics Systems and Applications (PESA 2017), Dec. 2017.
7. D. Wu and P. C. K. Luk, “Loss Analysis of Two-Layer Spoke Type Ferrite Interior Permanent Magnet Machines Considering the Effect of Press Fitting and Shrink Fitting” IEEE Transaction Industrial Electronics, Submitted in Dec. 2017.
8. D. Wu and P. C. K. Luk, “Thermal Analysis and Temperature Distribution of Two-Layer Spoke Type Ferrite Interior Permanent Magnet Machines” IEEE Transaction Energy Conversion, Submitted in Dec. 2017.

2. LITERATURE REVIEW

The electric drive system can be generally dived in two parts: the machine and its control system, so the literature review is categorised in two sections corresponding to two parts of electric drive.

2.1 The Electrical Drive System

Nowadays, the ever-increasing development activities on electrical adjustable speed drives have been propelled by huge demands of mechanical motion automation, sustained development in power semiconductors and integrated circuits, as well as the advent of new magnetic materials. The trend from constant speed systems to adjustable speed systems mainly rests on the demands of energy efficiency, speed or position control and excellent dynamic performance [22]. The adjustable speed is widely employed in applications such as fans, pumps and compressors to improve the efficiency. Meanwhile, there are also vigorous demands on the drive to achieve speed or position control in applications such as industrial automation, elevator traction and household appliance. Excellent transient performances are quite essential in applications of electric propulsion, aerospace, aviation and wind power.

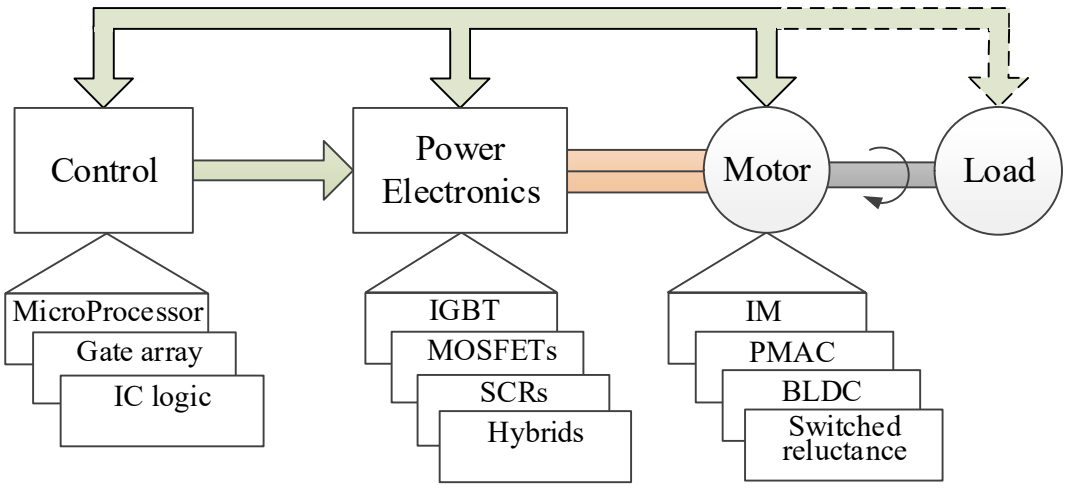

Figure 2-1 Structure of drive system [23]

Generally, modern electrical drive system includes the following four distinct elements [22,24]: (1) controller, (2) power electronic converter, (3) electric machine, and (4) load, which is illustrated in Figure 2-1. The control algorithms

are embedded in the controller collecting corresponding system status by sensors and generating modulation signals. The converter offers the electrical energy to the machine in an available form by power switch module following the reference signals from the controller. The electric machine is the prime device that transfers power from the source into rotating motion to drive the load. The load device ultimately realises the purpose of the drive system. As a result, the drive accomplishes the target torque, speed, position or power.

There are various types of electrical drives available in industry. However, their basic structures remain unchanged. The electric machines generally determine the characteristics of the drive. The basic machine type can be divided into two main categories: (1) DC commutator variable-speed drive, (2) AC variable-speed drive. Basically, two types of machine are available in the DC commutator drive system. One is DC commutator machine; the other is PMDC commutator machine. The AC drives can be further categorised into AC IM drive and PM brushless machine drive.

The DC Drives

The first direct current (DC) commutator machines were developed around 1830, and have been used as traction motors for over one hundred years. The DC machines were originally chosen because of their inherent compatibility with traction power supplies and ease of controlling.

The technologies for traditional DC motors are mature, and many researchers investigate the control algorithm to improve the performance DC motors. For the series DC motor, the armature and field winding are connected in series and the excitation is proportional to the load current. This characteristic of series motor is ideal for traction since the machine develops a high starting torque and approximately constant mechanical power output. The control system of series DC motor is very simple. In the separately-excited motor, the field excitation is obtained using a power supply independent from that of the armature circuit. Since the flux density in the airgap can be adjusted by the independent field excitation, the output torque can be control as required. The separately-excited motor is more favourable for traction because it may be controlled to produce

high torque at low speed range, and yet fully utilise its rated power at high speeds.

Prior to the development of reliable high-power solid-state switching devices, the DC motor was the dominant electric machine for all variable-speed motor drive applications. It has a wide range of applications in automotive, aerospace, material processing, manufacturing, etc. and it is often the most economical choice in the applications[25–28].

However, because of the existence of the mechanical commutator, DC machines have low reliability and require frequent maintenance. Also the brush constrains the maximum speed and power capability of DC machines, which results in low power density and power range.

Due to the development of digital drives and power electronics technologies in the last decades, as well as to the well-known advantages of AC machines, AC drive technology has become the technology of choice in many industrial applications. Though DC motors can still be found in many low power ratings applications today, the transition from DC to AC technology is happening in many applications[25].

The Induction AC Drives

The IM is widely adopted for various AC drives. IM drive with simple constant voltage/frequency scalar control method suffices most unsophisticated machinery. By adjusting the voltage magnitude in proportion to the supply frequency, adjustable speed can be achieved. The voltage drop on the stator resistance has to be compensated for low frequency operation. The voltage amplitude saturates to the level in the case of operation speed above the base value. Field oriented vector control is developed to further improve the steady-state and transient performance of the drive. Such method emulates the IM to separately excited DC machines. Both magnetic field and torque components can be controlled independently in the rotating reference frame. Moreover, DTC scheme, based on magnetic flux and torque estimation, is also widely investigated for such drive to offer better robustness [29].

However, the ohmic losses in the rotor conductors can considerably reduce the efficiency of IM drive. The power factor of IM drive also deteriorates because of the magnetizing current in the stator winding. Distributed winding arrangement is common practice in IM to achieve sinusoidal MMF. It implies that the pole-pair number is somewhat restricted in IM. That limits its direct deployment for low speed applications. As a result, mechanical transmissions such as gears are required for low-speed applications. The efficiency of the overall drive system can be compromised. In addition, the associated maintenance of the mechanical transmission can eventually jeopardise the system in some cases. All these shortages are moving it away from high performance applications.

The PM Brushless Drives

The PM brushless machine normally has the armature reaction windings accommodated in the stator slots in the same way as IM. On the other hand, the PMs in the rotor provides constant rational magnetic field. As a consequence, an average electromagnetic torque is produced by the interaction of stator and rotor magnetic fields, when the current induced MMF is precisely synchronised in the same frequency of the rotor. The PMs in the construction of such electrical machines bring the following benefits [30]:

- Energy saving as no excitation losses is required to build the magnetic field, and hence substantially increasing the drive efficiency;
- Higher torque and power per volume;
- Better dynamic performance than electrical excitation counterparts due to higher associated magnetic flux density in the air gap and lower moment of inertia;
- More simplified construction and maintenance;
- Versatile configuration and more topologies.

Compared with IMs, the PM brushless machines have become a more attractive option in variable-speed drives, due to the enhanced steady-state and dynamic performance, together with improved torque and power density. The advancements of semiconductor, microprocessor and digital techniques have made the control of such brushless machines easy to realise. The vector control

scheme is much more straightforward to implement in PMSM drives in comparison with IM drives. This is facilitated by the fact that the PM magnetic field aligns with the d-axis of the rotor reference frame. Therefore the space angle of the PM magnetic field is same as the rotor angle, which can be directly detected by the position sensor. However, the detection of magnetic field position is much more complicated in IM. Normally a magnetic flux model estimating the slip position is always required to derive the space angle, which is different from the rotor position [31]. The range of operational speed can be extended in PM brushless machines with relatively high efficiency. The PM brushless machine is also a more viable option than its induction counterpart in the applications with low-speed, high-efficiency, and easy-maintenance requirements. In particular, direct drive system can be developed based on large pole-pair structure with concentrated-winding configuration. All these merits have constantly pushed the industrial penetrations of PM brushless machine drives over the last decades.

2.2 Electric Machine with Permanent Magnets

2.2.1 Permanent Magnet AC Machine

Permanent magnets (PMs) are today widely used as a field source in electrical machines. Compared to electrical machines with field windings, permanent magnets have the advantage of no losses in excitation system, lower weight, higher torque and/or output power, lower maintenance and a simplification of the machine construction, as a result of the absence of mechanical components such as slip rings and brushes. High energy PM materials make it possible to use smaller magnetic thickness to achieve high flux density in the air gap, resulting in smaller motor diameter and mass [10,13]. Also, permanent magnet machines generally have higher efficiency than their field wound counterparts [28,32]. There are numerous types of electrical machines which use permanent magnets as magnetic field source. Lower weight (smaller size) and a simplification in the machine construction imply less material use which leads to less energy consumption in the manufacturing process. Together with high

power density and efficiency permanent magnet machines seems like the perfect choice.

Compared to induction motors in which the stator current contains magnetizing as well as torque-producing components, the use of the permanent magnets in the rotor of permanent magnet machines makes it unnecessary to supply magnetizing current through the stator to obtain constant air-gap flux, so the stator current is mainly used to produce torque. Therefore, for the same output, the PMSM will operate at a higher power factor and it will be more efficient than the IM[33]. The use of permanent magnets in construction of electrical machines brings the followings advantages [33]:

- The magnetic field is provided by the permanent magnet and there is no need for additional DC supply for magnetisation (excitation circuit). Therefore, without slip rings, and brushes the machine becomes robust and maintenance free.
- The efficiency of the PMSM in comparison with an Electrically Magnetised Synchronous Machine (EMSM) is higher since the rotor copper losses disappear as there is no rotor winding。
- Higher torque to weight ratio compared to other AC machines。
- Better dynamic performance than the electrically magnetised synchronous machines.

However, the PMSM has some disadvantages:

- At high temperature or at powerful magnetic fields inside a machine, the permanent magnets could be demagnetised (although this is rarely a problem today).
- Difficulties for transportation and security in delivery as well as high cost of permanent magnet material.

Due to the fixed PM-excited magnetic field PM motor has limited field weakening capability and relatively small constant-power region. And another problem is about the high performance rare-earth PM materials, which has a

high environmental impact and the price of which is high and very unstable the last several years.

When designing any type of permanent magnet electrical machine, the magnet type and grade are considered in an early stage of the design process. First, regarding rotor type, for permanent magnets with high energy product, e.g. NdFeB or Samarium-Cobalt (SmCo), a surface mounted rotor could be used. If lower performance permanent magnets are to be used, e.g. Ferrites or Alnico, a field concentrating pole shoe rotor may be required to achieve the acquired flux. The rotor/magnets need to produce the required flux for the machine to reach the desired torque or induced voltage. At the same time the magnet cannot be damaged (demagnetised) under periods of high load[34]. Unfortunately, these material properties are strongly related to one another and it is hard to get both at the same time.

2.2.2 The Types of PM Brushless Drives

The PM brushless motor drives can be mainly categorised into two principal types of square and sinusoidal wave machines [30,35,36]. The square wave excitation machine is essentially equivalent to PMDC commutator machine with a different reference frame. The main magnetic field is introduced by the rotating PMs. This explains the motor with square wave current are called brushless DC machines. Similar to the DC commutator machine, the currents in the stator windings reverse with alternating polarity of the magnetic field by power transistors, which are performed in synchronisation with the rotor position angle. Hence, the electromagnetic torque keeps unidirectional, and the resultant characteristics are essentially identical to DC commutator machines mathematically.

The polarity alternation of PMs in the rotor requires square-wave AC excitation in the phase winding. Therefore the phase back EMF is normally designed as trapezoidal waveform to achieve smooth torque with minimum fluctuation. The BLDC machine can be driven by open-loop configuration. However, current surge can be introduced in the start process. Consequently, closed-current-loop,

normally realised by chopper control, is employed to achieve square wave current in each phase.

Sinusoidal currents are normally employed in PM brushless machines with sinusoidal back EMF. This kind of machine is simply named as PMSM. The PMSM structure and associated controller hardware are physically the same to the BLDC drive, with the distinction of the difference in control algorithms being incorporated. Normally, the electromagnetic torque in PMSMs can be expressed in the form of the cross vector product of the fundamental stator flux linkage space vector and fundamental stator current space vector in the rotating reference frame. Consequently, the vector control can be simply implemented by tracking the d- and q-axis current references, which are determined by the speed or torque reference. The sinusoidal forms of the current from the inverter and back EMF of PMSM are essential to establish ideal stator current space vector with synchronous frequency and achieve smooth instantaneous torque.

PMSM drives possess distinctive advantages on efficiency, low-speed performance and ease in implementation of control scheme over induction counterparts. The high performance PMSM drives have been successfully applied in various applications. In particular, high power and torque density, great efficiency, excellent dynamic performances are of prime interest. By eliminating the transition torque fluctuation caused by current commutation in windings, PMSM drives can offer superior torque quality over BLDC drives.

2.2.3 The Types of PMSM

Based on flux path pattern of the machine, there are mainly three types of PMSMs[37]: (1) radial flux PMSM, (2) axial flux PMSM, and (3) linear PMSM. Each type can be applied for the specific application based on the characteristics. The radial flux structure is the dominant one, while the axial flux PMSM is particularly suitable for applications with special aspect ratio requirement. Linear PMSM is quite popular for high performance direct-drive linear motion systems. Normally, there are two types of winding arrangements for PMSMs: (1) distributed winding, and (2) concentrated winding.

The distributed winding configuration normally has the coils embracing several stator slot pitches, and is commonly implemented in the machine with slot per pole per phase larger than one. On the other hand, for concentrated winding configuration each coil covers only one stator tooth, which is widely employed in small fractional slot machines. Concentrated winding configuration can achieve short end winding and high slot fill factor, and hence results in lower resistance and better copper wire usage. PMSM with FSCW configuration can easily accommodate large number of rotor poles to achieve low-speed direct-drive applications [38,39]. Moreover, FSCW configuration can increase the inductance significantly so that good flux weakening capability can be easily achieved. However, FSCW configuration will reduce the machine saliency and hence reluctance torque. The inter-harmonic MMF components from such winding configuration can produce severe iron core losses and magnet eddy losses.

Radial Flux PMSM

The radial flux PMSM can be further classified into inner rotor and outer rotor configurations [37]. The radial flux inner rotor structure is the most common form of PMSMs. The PMs allocated in the internal rotor, as depicted in Figure 2-2(a), introduce the PM magnetic flux, which crosses the air gap into the stator in the radial direction. The fundamental MMF produced by the stator armature interacts with PM magnetic field, and pulls the rotor in synchronisation with

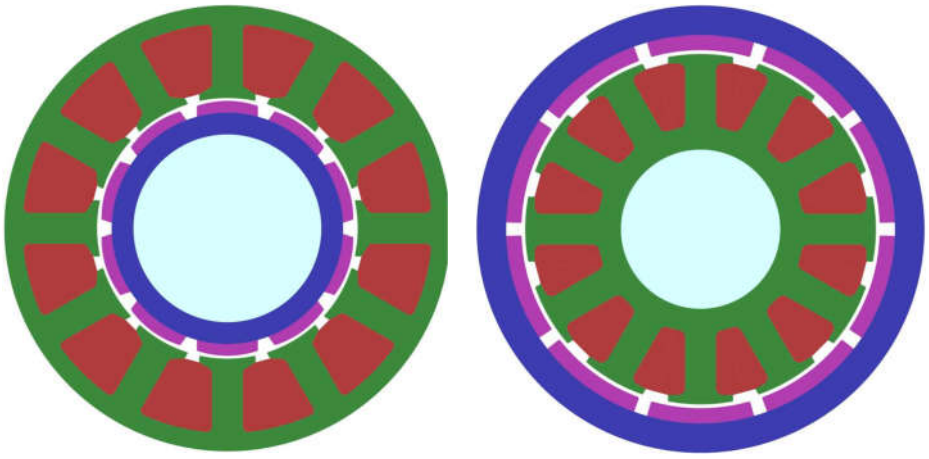

(a) inner rotor (b) outer rotor

Figure 2-2 Radial flux PMSM topologies [37]

traveling speed of stator MMF. As an alternative, the PM rotor can be placed outside the stator in a PMSM. Surface-mounted PM configuration is the most common among this type of PMSMs to achieve thin rotor yoke, as shown in Figure 2-2(b). The magnetic flux path of outer rotor PMSM is very similar to the inner rotor one. With the same machine envelope, outer rotor configuration can offer more circumferential space for PMs to generate the magnetic field so that the electromagnetic torque can be improved to some extent. The winding process can be significantly simplified as the stator openings are on the outer surface of stator core. However, the heat removal of the stator winding can be problematic since it is more difficult to implement an effective stator cooling system. The rotational inertia of the machine can be considerably increased from the inner rotor to out rotor structure. Consequently, outer-rotor PMSMs are rarely employed for servo system, which usually requires excellent dynamic response. Normally, only one side of the rotor is mechanically supported in this type of machine. Thus the short axial length of outer rotor PMSM limits the deployment. Such machines are heavily used as spindle motors for hard disc drives and ventilation fans for computer cooling. The large air-gap radius and hence high torque density make outer rotor PMSM an ideal contender for high torque direct drive applications. They commonly appear in wheel hub drive of electric vehicles, gearless traction drive of elevators. It is noteworthy that the FSCW configuration is normally preferred for outer rotor PMSM to achieve large rotor pole number. The applications of outer rotor PMSMs in wind power generation have been intensively carried out. Mature commercial products are readily available for large direct-drive wind power applications [37].

Axial Flux PMSM

Different from its radial flux counterpart, the windings and PMs are arranged along the radial direction in axial flux PMSM, as illustrated in Figure 1.2(a). The magnetic flux travels axially in the air gap to generate electromagnetic torque. Axial flux PMSM is informally named as pancake motor due to its flat appearance. Single sided configuration, as shown in Figure 2-3(a), has been employed for many applications, such as small wind power systems [40]. The

unbalanced axial force in this structure, which can reduce the bearing service life significantly, is one of most distinctive issues. The torque production capacity is low due to the relatively large air gap area. Therefore, double-sided configuration with either internal rotor or internal stator is more popular for axial flux PMSM [41]. The axial force can be effectively balanced and the torque density can also be significantly improved.

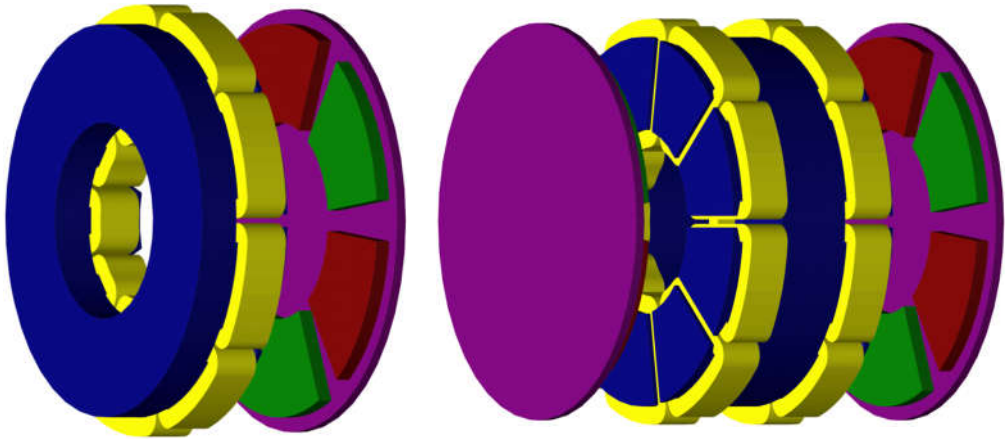

(a) single-sided (b) double-sided

Figure 2-3 Axial flux PMSM topologies [40]

Figure 2-3(b) depicts a typical double-sided axial flux PMSM with internal stator configuration. The disc type rotor results in large moment of inertia and compromises dynamic performance. However, it can improve stability against disturbance in return. Similar to outer rotor radial flux configuration, axial flux PMSM can facilitate large number of rotor poles. Hence, axial-flux PMSMs are widely used for low-speed applications such as electromechanical traction drive, elevator hoist and wind generator [42,43].

They are inherently of large aspect ratio and extremely attractive to the applications with stringent axial length constraint. It can be easily noticed that the laminated stator is rather difficult to construct and can increase the cost considerably. Soft magnetic composite material is employed instead to overcome the practical burden in stator manufacture. On the other hand, coverless stator configuration is widely implemented to eliminate the stator core. However, extensive PM material is required to offer competitive magnetic field

and the resultant small winding inductance can bring new challenges to the power inverter [40].

Linear PMSM

In high-performance linear motion applications, linear PMSM possesses inherent advantages. They can offer direct and accurate translation of speed and position without mechanical transmission. Better dynamic performance can be potentially accomplished. The mechanical speed of the translational motion synchronises with the armature-reaction magnetic field. As in axial flux PMSMs, both single-sided and double-sided configurations can be employed in linear PMSM. The structural diagrams of both types are depicted in Figure 2-4.

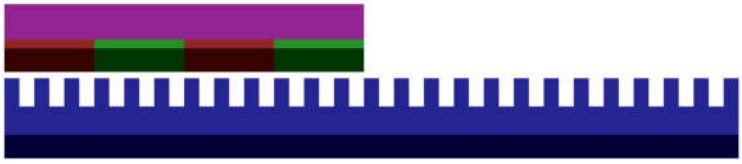

(a) single-sided

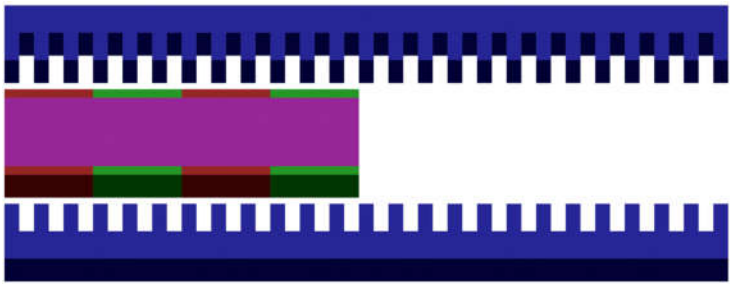

(b) double-sided

Figure 2-4 Linear PMSM topologies [44]

Based on the applications, either the PMs or windings can be placed on the mover. By eliminating the intermediate mechanical transmission, high-precision control on translational force, speed and position can be delivered in linear PMSM direct-drive systems. Therefore, linear PMSMs have been increasingly applied in various industry applications. With the assistance of contactless magnetic suspension technique, linear PMSMs can be implemented on maglev train to achieve highly efficient high-speed transport. It can deliver good safety, high reliability and low environmental impact. The applications on elevator hoisting and electromechanical actuation have also been investigated to improve the overall efficiency and minimise the package size. However, the cost

of active material can be a challenging issue in such machines for long-stoke applications. A large amount of PMs or windings are required for the stationary part [44].

2.2.4 Radial Flux PM Machine

PM rotors are the most popular structures among radial flux machines (RFMs), and on the basis of different positions of PMs in the rotor, they can be assorted into four topologies: surface-mounted, surface-inset, interior-radial, and interior-circumferential [10,13], which are shown in Figure 2-5.

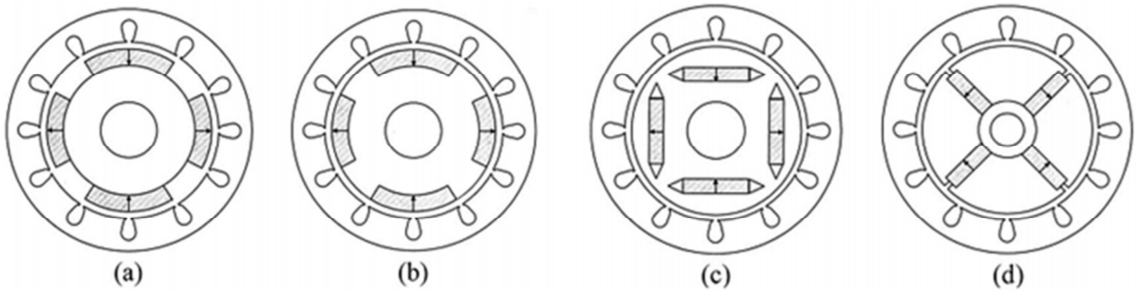

(a) Surface mounted; (b) Surface inset; (c) Interior radial; (d) Interior circumferential

Figure 2-5 The topologies of rotor PMs [10]

Surface mounted permanent magnet synchronous machines can more easily have a lower torque ripple while interior and inset mounted permanent magnet synchronous machines on the other hand generate flux concentration in the rotor that can allow thinner or weaker magnets[45]. Interior and inset mounted permanent magnet synchronous machines have unequal direct and quadrature inductance which produces a reluctance torque in addition to the magnet torque. Interior mounted permanent magnet machines more easily have robustness against magnet demagnetisation. However, the vibration and noise production in surface mounted permanent magnet synchronous machines is less than in interior permanent magnet machines [46].

For a simpler classification, rotor PM motors can be classified into two categories: surface PM (SPM) and interior PM (IPM) motors. In this classification, the topologies shown in Figure 2-5 (a) and (b) are called SPM

since PMs are on the rotor surface. And the latter two in in Figure 2-5 (c) and (d) are grouped as IPM because PMs are buries into the rotor lamination stack.

Surface-mounted PM machines have the simplest structure with the PMs simply mounted on the surface of the rotor. Because the PMs have a similar permeability with air, the magnetic air gap consists of the physical air gap length and PM thickness. Thus, the stator winding inductance is low and the armature-reaction is small for SPM motors. Additionally, stator winding inductances are almost the same between d-axis and q-axis, which means that the reluctance torque is approximate zero.

In the interest of extending the flux weakening ability and operation speed range, researchers have proposed many suitable design methods. Using concentrated, fractional-slot stator windings can improve the flux weakening of SPM motors. F. Magnussen et al. in [47] compared the performance of SPM motors with distributed and concentrated windings. It was shown that motors with concentrated windings had considerably higher inductance because of higher slot leakage. Thus motors with concentrated windings had a wider field weakening region, lower winding losses, low cogging torque and torque ripple [48,49]. Abolhassani in [48] proposed machine utilising a novel 48/45 pole/slot configuration with shorter end windings and high winding factor of 0.952, while S.C. Yang et al. in [49] proposed a 48/44 structure for high torque and low torque ripple.

Because SPM machines have relatively low armature reaction, the SPM rotors exhibit isotropic characteristics. In order to estimate rotor position and achieve sensorless control, Adriano Faggion et al. and N. Bianchi in [50,51] presented a ringed-pole SPM synchronous motor design, using an electrical winding coil wounded around the PM poles to detection the electrical coupling anisotropy between stator winding and rotor ring of rotor angular position.

PM shape and rotor configuration are the key parameters for SPM machines. Rasmussen [52,53] proposed an method to improve magnetic density distribution in the air-gap using a non-uniform magnetisation waveform of PM taking the amplitude and angle the PM magnetisation into consideration to

obtain a sinusoidal back-EMF. However, the manufacture of this non-uniform PM is difficult and impractical for massive industrial production.

A surface inset PM rotor is similar to a commonly used SPM rotor. The difference between surface inset and SPM machine is that there is iron tooth between adjacent PMs, as shown in Figure 2-5 (b). The existence of iron teeth in the rotor produces rotor anisotropy. Since the PMs are inset into the rotor surface, surface inset magnet machines have several advantages compared to SPM machines, such as higher rotor mechanical robustness, lower PM eddy current losses, higher q-axis inductance than d-axis, and wider flux weakening region [54–56]. However, compared to interior PM machines, saliency ratio of surface inset PM is quite low, and thus, the contribution of the reluctance torque is limited and often not exploited [55]. SPMs are very difficult to meet the high requirements of wide speed range applications, because of limited flux-weakening capability and susceptible irreversible demagnetisation risks.

IPM machines have the advantages of wide constant power speed range and are thought to be perfect for a number of applications where the overall efficiency under different operating condition is more important to save energy [57–61]. Large saliency differential ratio of rotor exists which produces a reluctance torque. When added to the PM alignment torque, increases the torque from the machine. Thus the power density of the machine can be improved. A wide speed range can also be achieved through field weakening due to the large d-axis inductance Ld. By burying PMs into the rotor lamination stacks a number of advantages can be created. The rotor is mechanically robust giving protection to the PMs. Also lamination stack gives partial protection from demagnetisation from the stator winding currents. Eddy currents on PMs can be reduced.

However, there is a disadvantage with IPM rotor arrangements and that is the magnetic flux which is short circuited in the rotor bridges between the PMs, and results in a reduction of the air-gap flux per pole and a subsequent reduction of the PM alignment torque.

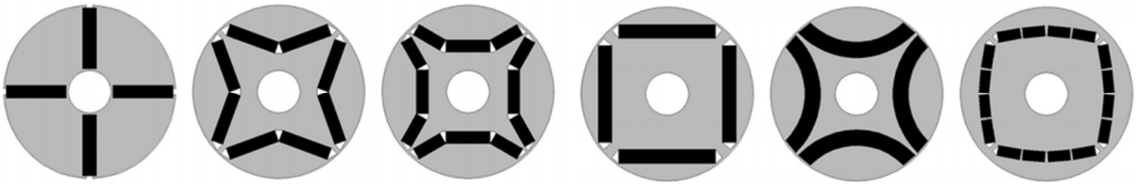

Figure 2-6 Different rotor configurations for IPMs [62]

For conventional laminated rotors, many rotor configurations with different PM shapes and positions are investigated. S. Wu et al. in [62] compared different IPM rotor configurations, as shown in Figure 2-6. Based on the requirements of an indirect-drive medium-scale hybrid electric bus, motor designs with V-type or U-type IPM structure combined with non-overlapping winding, show better performances with high torque and power density, while circumferential IPM rotor has better flux-weakening capability with overlapping winding, though the torque density is a little lower.

IPM synchronous machines are commonly used for electrical drives in automobiles with hybrid or full electrical drives, and they often have a very large speed range from 0 to 15,000 rpm. Arranging the permanent magnets (PM) in a V-magnet shape is a good solution for this kind of application as it produces a high reluctance torque next to the PM torque [63]. This leads to an advantage in efficiency as the field weakening current needed above rated speed is also torque-producing. Additionally, it decreases the dependency of the design on temperature variations according to the temperature dependency of the PM flux. Since the used rare-earth Magnets have a great effect on the machine costs it is advantageous to reduce the needed magnet volume per torque. This is a motivation to produce a high share of torque through the reluctance effect.[63]

Along with the high power-to-volume ratio and energy efficiency of the IPM motor, a wide constant power speed range is very suitable for EV application. W. L. Soon et al. in [64] designed of an axially-laminated IPM motor, and achieved excellent field-weakening performance, but the manufacture and assembly of the rotor is difficult.

2.3 Electric Machines with Ferrite PMs

With the development of power electronics, magnetic materials and electric machine design technologies, PMSMs are becoming one of the most promising solutions for various applications, with the remarkable features of high torque density, excellent controllability and good efficiency. During the past decade, most of the high performance PMSMs has been using high-energy rare-earth magnets to deliver high power density and efficiency. However, the soaring price and uncertainty in the supply chain of the rare-earth materials have been a major concern for developers and researchers, which would definitely hinder further developments. After the difficult struggle in 2011 when the price of rare-earth material hiked over 20 times, PM machine manufacturers started the search of alternative solutions to substitute rare-earth for the PM machines.

2.3.1 Ferrite Magnets and Its Application in Electric Machines

Ferrite magnets, also known as ceramic magnets, are made from oxides of iron, so they do not corrode when immersed in water (even saltwater) or exposed to moisture. They are even resistant against solvents, weak acids, lubricants, salts and glasses. This is just one of the characteristics that make ferrite magnets really popular for many applications. Because they are corrosion-resistant they can usually be used without any additional coating and will last a long time, generally exceeding the lifecycle of the application they are used in [65,66]. Like all magnets, temperature affects their behaviour, but unlike rare-earth magnets, when ferrite magnets get hotter their resistance to demagnetisation increase because their intrinsic coercivity improves. This unique characteristic makes them extremely popular for applications that require high operating temperatures such as electric motors and generators. The maximum working temperature can be up to about 180 °C [65]. Like neodymium magnets they are very hard and brittle. Because of this, most ferrite magnets are supplied in basic shapes such as square or rectangular or rectangular tiles, cylinders and rings. Machining after the production process is costly and required diamond coated machining tools [65,66].

As one important type of PM materials in the market, ferrite magnet is drawing people's attentions for the design of high performance PM motors. In fact, ferrite PMs were first commercialised in the 1960s, and are still the most widely used magnets today on the basis of the consumption mass. However, the residual flux density and energy product of ferrite PMs are the much lower compared with its rare-earth counterpart, as illustrated in Figure 2-7. The typical remanence of ferrite magnets is in the vicinity of 0.4T, which is only one third that of NdFeB. Thus, the machine characteristics would be greatly reduced simply by replacing rare-earth with ferrite PM or even increasing the amount of ferrite PM in the original design based on conventional PM machine configurations. Nevertheless, with merits of abundant raw material resources, low price, stability to corrosion and temperature, and very high electrical resistivity, ferrite magnets are considered as a most potential candidate for low-cost high-performance PM machines [67–69]. To fulfil the design requirements of high efficiency, large power density and wide speed range, suitable design needs to be investigated to maximise the torque capability of ferrite PM machines.

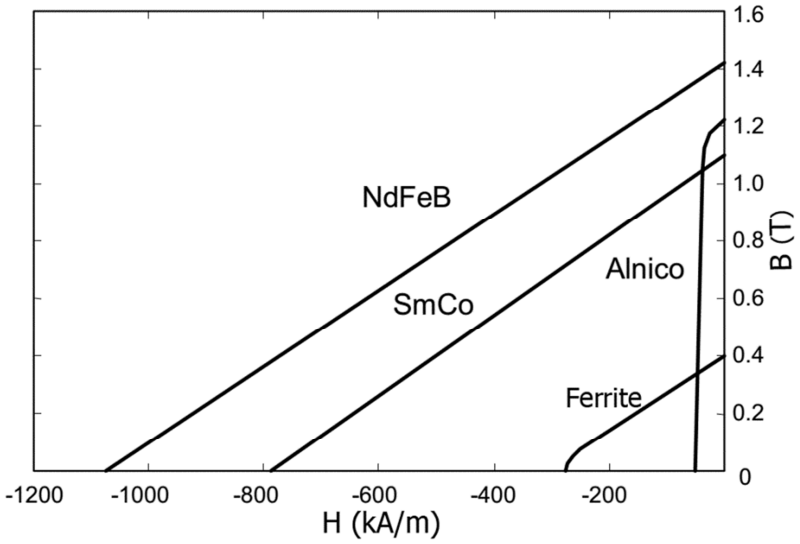

Figure 2-7 Comparison of B-H curves among different PM materials [67]

There are normally two types of electromagnetic torques induced in PMSMs: the PM torque arising from the interactions between the PM field and the armature windings, and the reluctance torque produced by the winding

inductance variation with the rotor position due to the rotor saliency. It is obvious that ferrite PM machines would suffer lower PM torque component as a result of much lower PM strength. To compensate the lower PM torque, special attention should be paid to the machine configurations with higher reluctance torque component.

Ferrite PM materials have long been used in the design of PM machines very soon after their commercialisation [9,70–74], and various machine configurations with different PM materials were investigated and compared in [16,75–77]. Based on the existing literature, ferrite machine solutions can be divided into three categories:

- Conventional PM machines, which are of similar structure as the rare-earth machine with larger amount of ferrite PM;
- PM assisted synchronous reluctance machines (PMASynRMs), whose structures originate from synchronous reluctance machines (SynRMs) with PMs in the flux barriers;
- Spoke-type PM machines, using flux focusing techniques to achieve similar airgap flux density and torque density as rare-earth machines;

2.3.2 Conventional PM Machines with Ferrite Materials

Conventional structure PM machines adopted similar configurations as rare-earth ones by using ferrite instead of rare earth PM. Due to the low residual flux density of ferrite, usually larger amount of PM was used to increase the flux density. Even so, the power density ferrite machines are still very low comparing to its rare-earth counterparts. As a result, ferrite machines with conventional structures were mostly used in low-cost and low-power applications such as electric assisted bicycles [78], pumps [23] and fans [79]. According the location of PM poles, they could be further divided into surface-mounted PM (SPM) and Interior PM (IPM) machines.

S. Pal in [80] study the different performances of SPM machines with exactly the same machine geometry but different PM materials of ferrite, SmCo and NdFeB respectively. The ferrite machine can only achieve 36% torque of SmCo

and 31% that of NdFeB, because of the low residual flux density of ferrite. P. Sekerak in [81] optimised ferrite SPM design and obtained a final design with slightly larger size but only 60% torque of rare-earth one. To increase the airgap flux density for SPM ferrite machines, one method is to increase the size of the machine to accommodate larger amount of PMs. D.G. A.M. Mihai et al. in [82] and S. Laurit et al. in [83] also considered rare-earth PMs as the best solutions for wind power generator, in terms of overall weight , size and most importantly cost, as the extra cost would be paid on the larger housing and foundation structure for ferrite machines. But for small power machines, lower energy PMs can be competitive with machines adopting rare earth PMs, if the machine designs were optimised specially for each PM material [84,85]. Nevertheless, the drawback of much larger volume restricted the usage of ferrite PM generators.

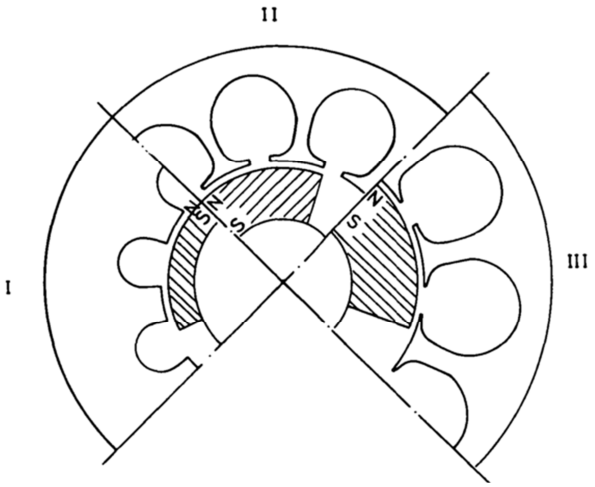

Figure 2-8 Design consideration with more PM material [73]

In spite of larger amount of ferrite being using in SPM machine, the airgap flux density still couldn't achieve that of rare-earth ones [82]. Thus, the stator yoke thickness can be reduced and larger diameters were necessary in order to place more armature conductors to increase electric load and power output [73], as shown in Figure 2-8. In this case, the copper loss would be increased and over 10% lower efficiency was observed under the same current density. K. Kim et al. in [86] compared rare-earth and ferrite SPM machines with the same size, and the ferrite model had over 5 times higher copper loss due to larger amount

of copper used. In [87], copper loss of ferrite generator was almost 3 times as that of NdFeB with the same outer diameter, and thus ferrite machine suffered 7% lower efficiency. And with 30% larger diameter, the efficiency of ferrite motor was still 1% lower compared to NdFeB motor in [88]. R. Gupta et al. in [79] proposed a ferrite SPM machine with radial- and Halbach-magnetised magnets to increase the flux density and improve the efficiency, but extra cost was brought in due to the Halbach-magnetisation.

D. Woo et al. and H. Kim et al. in [89,90] proposed another way to increase the flux density in armature flux linkage by applying the structure of longer rotor than stator, which is called rotor overhang configuration. With this structure, the leakage flux loss would be offset at the end of the lamination cores, and thus the performance of the machine can be improved. With 3 mm overhang, up to 6.8% of increase in load torque can be achieved at the expense of more PM material and larger mass. Moreover, the overhang structure required 3D analysis for accurate predictions in the design period, which would increase the calculation time.

To conclude, due to the low residual flux density of ferrite materials and the large magnetic airgap length, SPM machines are not able to achieve the required torque density and efficiency. Despite that the airgap flux density can be improved by IPM structures, it is unlikely for conventional IPMs fulfil the requirements of high torque density and efficiency simply by increasing the amount of PM as the available space inside the rotor to accommodate PMs is limited.

2.3.3 PM-Assisted Synchronous Reluctance Machines

PMASynRMs are derived directly from SynRMs, as illustrated in Figure 2-9. By adding proper amount of PM materials into the flux barriers of the SynRM rotor lamination, the torque density, power factor and efficiency of the PMASynRM can be improved, and this makes it a potential solution for ferrite IPM design [91–93]. E. Armando in [94] pointed out that with even a small amount of PM, not only the torque output but also the constant power speed range could be improved greatly compared with SynRM design for washing machines. And with

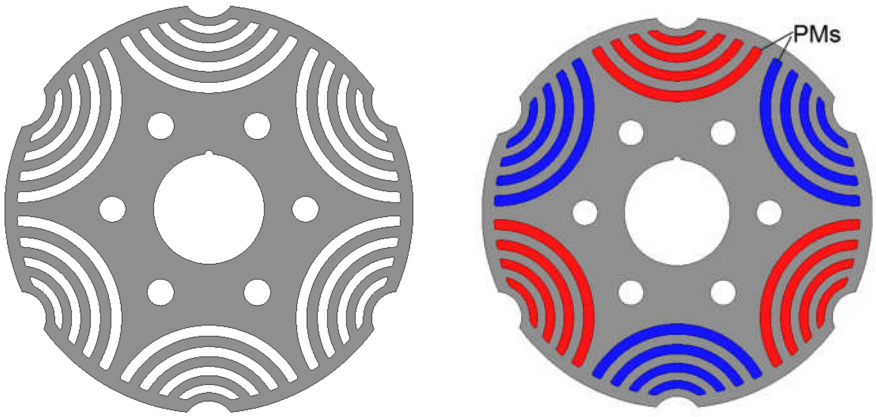

(a) SynRM (b) PMASynRM

Figure 2-9 Configurations of SynRM and PMASynRM rotor [95]

more ferrite PM added to the original SynRM lamination, higher power factor as well as efficiency could be achieved [96,97]. However it is not always the case that more PM results in higher torque. The main component of the torque for PMASynRMs is reluctance torque, and the rotor with too much PM would affect the thickness of barrier ribs and thus the saliency. D. Prieto et al. in [98] investigated the influence of the thickness of inserted PM poles, and suggested more PM material could improve power factor, but also may cause significate decrease in torque output. M. Barcaro and N. Bianchi in [95] optimised the length and thickness of PMs and indicated with similar rotor structure, reduced PM thickness can still attain similar torque capability, but slightly lower power factor.

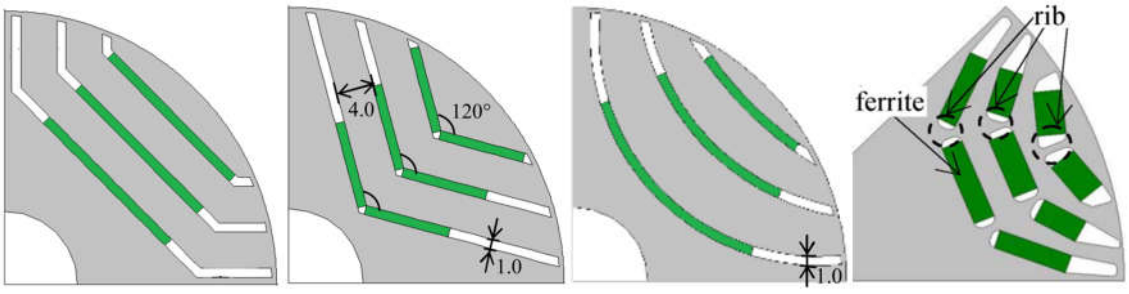

(a) Flat; (b) V-shaped; (c) Circular arc; (d) Segmented;

Figure 2-10 Rotor with different shapes flux barriers and PMs [99]

The shape of the PMs and flux barriers also showed great importance to the PMASynRM design. S. Musuroi et al. in [99] presented a two-layer V-shape

ferrite PMASynRM since it has simple flux barriers and rectangular PM poles. K. Hayakawa et al. investigated the influence of flat, V-shaped and circular arc flux barriers, as shown in Figure 2-10. And results revealed that circular arc structure could substantially improve the maximum torque and power output with three flux barriers [100]. It should be noted that ferrite PM was brittle especially when large thin arc shape was used. Y. Matsumoto et al. in [101] proposed a barrier structure that the third flux barrier divided into three parts by 0.5mm ribs, so as to reduce the mechanical stress on the PMs. But the ribs provided extra path for the PM flux and the torque output was reduced. When taken massive production in consideration, long arc shape PMs were more expensive to produce and difficult to assemble. Thus, rectangular segmented PMs were proposed in place of arc shaped magnets for easy manufacturing and assembly [102,103]. Though there was about 4% decrease in the torque output, both the amount of ferrite and manufacturing cost was reduced.

PMASynRMs with three flux barriers were the most common configurations for the rotor design, with a compromise between complexity and saliency. However designs with higher number of flux barrier were also adopted in some research works. M. Paradkar et al. in [104] presented a design with 4 flux barriers, and Y. Jeong et al. in [105] proposed a design with 5 flux barriers to gain a higher saliency. But the structures became too complicated. With the thickness of the PMs reduced, designs with more flux barriers made the PMs more fragile against mechanic stress and armature demagnetizing field. Researchers also found the thickness of saturation bridges, pitch and angle of flux barriers could affect the machine performance. Since the saturation bridges provide flux path for PM flux leakage and d-axis flux, both PM torque and reluctance torque could be reduced. H. Cai et al. proposed a design with all the bridges removed and yielded 8% increase of overall torque [106]. However, the lamination rib layers would be completely detached from one another, and the assembly of the rotor was not discussed, which would seriously affect robustness of the rotor especially during high speed operation.

To conclude, PMASynRM machines are descendent from SynRM and mainly rely on the reluctance torque component. Due to the inherent limitations of reluctance machines, PMASynRMs have inferior performances in terms of torque ripple, power factor and efficiency. Higher number of flux barriers is able to increase the rotor saliency and thus the power density, but it also complicates the rotor structure.

2.3.4 Spoke-Type IPM Machines

The spoke-type configuration, also known as flux-squeezing configuration, has long PMs magnetised in the circumferential directions as shown in Figure 2-11. This structure concentrates the fluxes from the PMs to lamination poles achieve approximately the same air-gap flux density as the rare-earth machine. Thus the spoke-type structure is also considered as one of the most potential solutions for high performance ferrite PM machines.

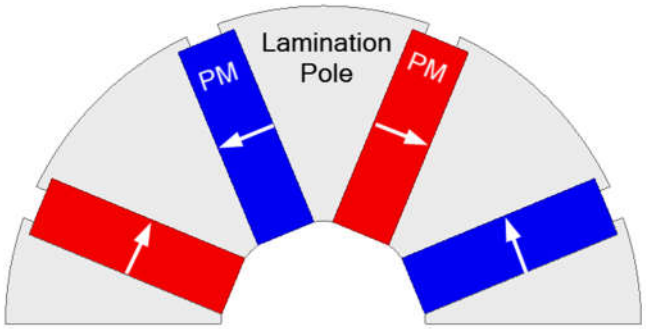

Figure 2-11 Rotor configuration of a typical spoke-type machine [107]

A. Isfanuti et al. in [108] compared surface NdFeB and spoke-type ferrite machines within the power range of 100–2000 W, and results showed that same torque can be achieved with low cost, but higher mass and torque ripple. Eriksson and Bernhoff in [109] evaluated the spoke-type wind generators of the same power range with ferrite and NdFeB PMs, and revealed that ferrite generators would be 50% heavier but with only 30% of PM cost. E. Spooner et al. proposed a modular design of ferrite spoke-type wind generators for easy assembly and low manufacturing costs [110]. For vertical wind turbines, low-cost ferrite rotor was preferred since there was little influence on the foundation structures. On the other hand, for horizontal turbines, NdFeB rotor would be

better for the design with reduced hub weight and requirements for other parts of structure. D.G. Dorrell in [111] presented a spoke-type design benchmarked with Prius rare-earth IPM, and the amount of ferrite PM was almost maximised in the rotor while only 2/3 torque was obtained even though larger machine diameter was adopted. Design, optimisation and assembly of ferrite spoke type machines were presented in [107,112], and promising results were achieved for prototype machines. Although the torque density was much lower than rare-earth machines, it was still considered to be viable alternative solution in the sense of cost. To increase the torque density, F. Demmelmayr et al. in [113] proposed an outer-rotor spoke-type design. In order to achieve the same performance with rare-earth design, larger amount (5.7 times) of PM was used and thus outer diameter was enlarged by 26%. To compensate the low residual flux of ferrite and reduce the consumption of rare-earth, hybrid PM arrangements with both ferrite and rare-earth PMs were presented in [112]. Though the amount was reduced, rare-earth PM was still necessary for the design. Another issue should be paid special attention to was the cross-demagnetisation between strong rare-earth and weak ferrite PMs.

To achieve similar airgap flux density as rare-earth machines, various designs are proposed to use more PM to enhance the PM excited field. K. Kim et al. in [114] proposed a ferrite spoke-type design with large axial overhang and the air-gap flux density was increased by 33%. I.C. Chabu et al. obtained a 55% increase in the airgap flux density applying 68% longer rotor stacking than the stator [115]. W. Kakihara et al. in [116] also applied 6 mm rotor overhang and 6 mm PM overhang, the torque output was improved and PM demagnetisation rate was reduced. Large rotor overhang would certainly increase the amount of PM and rotor lamination, but the overhang PMs were not actually fully utilised since considerable part of the flux didn’t go through the airgap directly but became flux leakage and wasted.

Compared with PMASynRM, spoke-type suffers higher risks of irreversible demagnetisation [76], and the investigation of irreversible demagnetisation is critical for the robustness of ferrite machines. Demagnetisation occurred in

many of the papers reviewed above [69,117–119], but no solution was presented. Wider and thicker PM poles were used to enhance PM MMF [112], but this would affected the whole electromagnetic design of the machine, especially for those harnessing reluctance torque. B. Lee et al. in [120] proposed flux barriers in between the adjacent spoke type poles to reduce the demagnetizing armature field, but PM flux would also be reduced. It was indicated in [121] that divided main pole structure had lower risk of demagnetisation than conventional one. Since the part of PMs near the airgap was facing strong armature field, the PM edges closer to the stator suffered higher risk of local demagnetisation. Thus, chamfered PM edges were applied in [122], and deeper burying of PMs were presented in [111,116,123]. Although PM flux field was weakened, local demagnetisation on the PM edges could be greatly reduced. After all, demagnetisation was discussed during the design for certain cases, but no systematic research was published for ferrite PM machines yet.

Since the optimisation of the design is a very complicated work considering the flux distribution, torque generation, efficiency and so on, various multi-objective optimisation algorithms were used to accomplish optimal design. K. Hwang et al. applied steepest decent method (SDM) to minimise the cogging torque and response surface method (RSM) to reduce harmonics in airgap flux distribution and cogging torque in [124] and [125] respectively. P. Zhang et al. in [126] used a combined design of experiments (DOE) and differential evolution algorithms (DEA) to optimise three key objective of loss, cost and torque ripple. Although good results were achieved, the optimisations still required finite element analysis (FEA) to evaluate each design. Also, no clear relation between the performance and sizing parameters were derived, and provided weak guidance on the design.

For more useful theoretical guidance during the preliminary design period, analytical methods were required for fast calculation. Approximate open-circuit flux density was obtained in [115,127,128] for conventional spoke type configurations. PM flux distribution equations were derived for spoke type with

auxiliary ring poles [129,130], wing-type [131], and wing-shaped [132]. However, the overall torque profiles, especially the reluctance torque component, could not be express only by PM flux field, and thus the analytical were not complete. PM flux together with dq-axis inductance were derived for spoke type configuration in [133,134], showing the influence of different design parameters on the performances. But only the fundamental flux was considered, which could bring in relatively larger error.

To conclude, spoke-type ferrite PM machines have the potential of achieving high torque density, power factor and efficiency with flux focusing structures. But the reluctance torque is relatively low and further improvement needs to be explored. What's more, the rotor structures of spoke-type motors needs to be design very carefully due to the higher risks of irreversible demagnetisations.

2.4 Control System of PMSM

2.4.1 Control Strategies of PMSM Drives

Based on the d- and q-axis inductances and PM flux linkage, the electromagnetic torque in PMSM can be expressed in the form of the d- and q-axis current vector components. A wide variety of control strategies based on the different d- and q-axis current combinations can be implemented in PMSM drive in order to achieve specific objectives [31,135]. The non-saliency characteristics of surface-mounted PMSM make the corresponding electromagnetic torque proportional to the q-axis current component. Consequently, the id = 0 vector control strategy is widely implemented in such machine drive to achieve simple yet effective operation.

Although it can also be employed in surface-inset and interior PMSMs, MTPA control strategy is preferred to harness the potential reluctance torque and hence maximise the electromagnetic torque for unit stator current. Normally, the real-time numerical derivations of d and q-axis currents in MTPA control strategy are too complex and computationally intensive to realise. With minimal compromise, the reference current distribution can be efficiently derived from separate look-up tables instead. Such tables can be generated off-line based on

numerical FEA or experimental results. The unity power factor control strategy is another option which can fully utilise the volt-ampere rating of the inverter by keeping the power factor as unity. Off-line look-up tables are also commonly involved in such strategy. As the upper limit of phase voltage is determined by the available DC link voltage, the maximum operational speeds under specific load conditions are restricted under normal vector control strategies due to the constant PM flux linkage.

Flux weakening control strategy, which injects demagnetisation current in d-axis, can be employed to extend the corresponding speed range with constant power operation. It is noteworthy that the maximum demagnetizing current should be restricted to avoid the irreversible demagnetisation of PMs, particularly in ferrite PMSMs. By selecting optimal inverter switching modes, fast torque response can be effectively achieved based on the direct control of both overall flux linkage and electromagnetic torque in DTC strategy. The hysteresis band-band control algorithm is normally incorporated to carry out the switching selection so that high torque ripple can be potentially induced. The synergy of the SVPWM technique and DTC strategy can significantly improve the torque ripple characteristics associated with the switching process.

Besides, there are other control strategies in PMSM drives such as maximum efficiency per ampere control. However they are only good candidates for particular applications rather than as a norm. Hence, only the most common control strategies, the id = 0 vector control, MTPA and flux weakening control, are employed in this study.

2.4.2 Control Algorithms of PMSM Drives

The speed-current double-closed-loop control system is generally a universal solution for PMSM drives to achieve high performance. For some cases with position control requirement, another closed-loop position controller should be implemented outside the double-closed loop to form a triple-closed-loop system [136]. The classic PI control algorithm is commonly employed for these closed-loop controllers. Various modern control algorithms such as sliding mode control [137], neural control and fuzzy logic control [138] are developed in

PMSM drives, which may improve the dynamic response, stability or robustness. The common PI control algorithms suffice the corresponding current and speed controllers in this study.

Voltage source inverter (VSI) with PWM techniques are extensively used to power the PMSMs to achieve high performance. SPWM and SVPWM techniques are the two most popular practices in PMSM drives [139–141]. By comparing the phase sinusoidal reference modulation wave with the triangular carrier wave, the switching sequence of all power modules can be obtained for the SPWM technique. The resultant simple and straight implementation makes it very popular for industrial inverters. On the other hand, SVPWM technique is becoming the new formidable candidate for high-performance PMSM drive due to its advantageous features such as high utilization of DC link voltage and inherent vector control capability[140].

2.4.3 Current sensing

The current feedback signal is necessary for current close loop control in an electric drive system, and the accuracy of the current sensing will affect the control quality. There are generally four types of current sensing devices [142]: 1) current shunts, 2) current transformers, 3) DC current transductor, 4) Hall effect sensors.

The most common current sensing device is probably the shunt, which actually is a high precision resistor. When a current is passing through the shunt resister, a voltage drop can be read across the resister. Applying Ohm's law $I = E/R$, where *I* is the unknown current, *E* is the voltage drop across shunt, and *R* is the shunt resistance, the current can be measured by the shunt resister. There are some advantages about the shunt current measuring. It is a simple and robust device with lost cost, and it is not affected by neighbouring conductors. It is able to measure both AC and DC currents with high accuracy, and there is no requirement of orientation when it is mounted in the electric circuit [142,143]. However, since the shunt resistor is connected in series in measured circuit, it is not isolated from measured conductor and consumes some electric power. To install the shunt resistor the measured circuit has to be broken, and two terminal

connections are made for the voltage drop measuring. And the user should also be aware that the accuracy of shunt current sensing can be affected by conductive dirt, and it is working in closed ambient [142].

Current transformer is a convenient device to measure AC current. When the unknown current passes through the primary conductor, generally a proportional voltage signal can be measured through the terminals of the inductive coupling secondary winding. It has fixed and clamp-on types of current transformer, and extensively used in power utility industry [142,144]. The current transformer is portable and easy to take a reading during the operating. It is isolated to the measured conductor, thus it is safer and suitable to measure larger current. But current transformer is unable to measure DC current, and it is susceptible to adjacent conductors. The accuracy may be varied for different frequency and is affected by non-sinusoidal waveforms [144,145].

DC current transductor is a saturable reactor device. It is consisted of two cores, an AC excitation supply, an output rectifier and a DC meter[142]. The DC transductor is isolated from the measured electric circuit and able to work in harsh environment. It has a wide current range up to 10,000 amperes. However, an external AC supply and an output rectifier are required for the DC transductor, which make it with high price. It can only measure DC current, but it is unable to indicate the polarity[146,147].

Hall Effect sensor is designed on the basis of the Hall Effect that was discovered by physicist Edward H. Hall in 1879 [142]. According to Ampere's law, a magnetic field is generated around a current-carrying conductor and is sensed by a Hall plate. A circuit voltage that is proportional to the unknown current is generated across the plate, and the value and direction of the current can be calculated by the obtained voltage. The non-contact operation makes the measurement convenient and provides high voltage isolation. The Hall Effect sensor is able to measure both AC and DC current with wide measuring range and frequency bandwidths [148,149]. But this sensor is susceptible to external magnetic fields and some configurations are affected by physical damage [150].

For the electric drive system in the thesis, shunt resister is adopted to sense current thanks to its compact size and low cost, without compromise with accuracy. The clamp-on current transformer is often used in the control debugging process, because it is convenient to measure current occasionally without damage to control board.

2.4.4 Speed and position feedback

There are generally four types of speed sensor used in electric drive system, which are resolver sensor, absolute encoder sensor, incremental encoder sensor, and Hall Effect sensor, which are depicted in Figure 2-12. The resolver sensor is a rotary electrical transformer. The primary winding is mounted on the rotor and provides reference voltage. When the rotor is driven by an external machine, two sinusoidal waveforms with 90° displacement are induced in the secondary windings that are installed in the stator. Through the two voltage

(Courtesy: Dynapar company)

(a) Resolver sensor

(Courtesy: Allen-Bradley Company)

(b) Absolute encoder sensor

(Courtesy: YUMO Company)

(c) Incremental encoder sensor

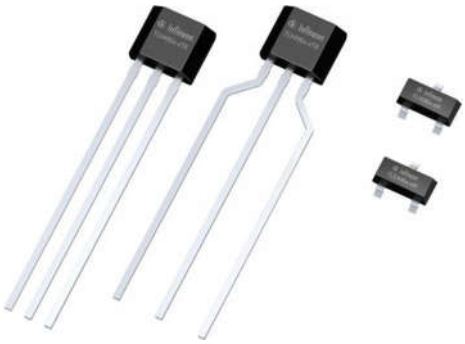

(Courtesy: Infineon Company)

(b) Hall Effect sensor

Figure 2-12 Resolver speed sensor appearance and structure

signals, the absolute angle position can be calculated and it is not susceptible to aging and temperature change [151,152]. The encoder sensor has three essential parts: light emission diodes, a rotating plate, and photodetectors [153]. The rotating plate has alternating opaque and transparent slits to block or pass the light through to the photodetector. For the absolute encoder, there are multiple layers of slits in the rotating plate, so that a multi-bit word is obtained from the photodetectors, which indicates a specific position of the round plate. The position information is maintained even when the system is power off [154]. However, the incremental encoder only has one circle round of slits in the rotating plate and two photodetectors that have 90° phase difference. And the position information is provided by counting the slits between the current position and a defined reference position, and index pulse is often used as the reference position [154,155]. The Hall Effect sensor is a small device to detect the presence of magnetic field [156]. It works like an electronic switch. When the Hall Effect sensor experiences alternating magnetic field, a square voltage waveform is obtained from the terminal. Generally, three Hall Effect sensors are used in an electric machine and mounted inside the machine with electrical 120° between each other [157].

The above four position and speed sensors are compared in Table 2-1. As there are various models in each type of sensors, the data shown in the table only present the general performance and cost.

Table 2-1 Comparison of different sensors

	General resolution (deg.)	Position	Cost*
Resolver	0.33 (two-pole resolver)	absolute position	140
Absolute Encoder	0.0879 (12 bit)	absolute position	90
Incremental Encoder	0.022 (4096 slots)	relative position	50
Hall Effect sensor	20 (six-pole motor)	absolute position	1

*This is relative cost only used for comparison, and the prices referred to RS Components Ltd. at 1st Dec. 2017. The Hall Effect sensor is about £1.50 that may be varied in different retail companies and/or countries.

Resolvers and absolute encoders are able to provide absolute position, retaining correct position even if power fails without homing at start-up. The

resolvers offer high reliability and robustness, and it is an ideal choice for high temperature, high shock and vibration, and harsh environments, such as EV applications, but the price of which is relative high. Incremental encoders and Hall Effect sensors provide speed, direction and relative position feedback by generating a stream of binary pulses proportional to the rotation of a motor or driven shaft. Incremental encoder is commonly used in electric drive control system, due to its high resolution and relative cheap price. It is obvious that Hall Effect sensors are the most economical device. Although only six states are provided in an electrical revolution, with proper algorithms, the approach of using Hall Effect sensors can offer comparable position and speed estimations.

For the design of low-cost drive system in the thesis, Hall Effect sensor is best candidate to provide position and speed feedback owing to its compact size and low cost. Incremental encoder is recommended to adopt in the debugging process of the control system, as it is more accurate and easier to control.

2.5 Summary

The demand for high efficient electric machine is ever increasing as both energy consumption and CO2 emission can be greatly reduced. The widely installed IMs are not able to fulfil the efficiency requirements, and PMSMs with low-cost ferrite magnets are considered to be the most attractive solution. In this chapter, extensive review on the current development of electric drives were made searching for low-cost high-performance candidates, and the focus was concentrated on torque density and efficiency. According the existing literature, ferrite spoke type machines are the most promising candidates to replace currently widely used low efficient IMs. Spoke type machines adapt the flux-squeeze structure for flux concentration to compensate the low residual flux density of ferrite material, and exhibit higher torque density, power factor and efficiency. With well-designed geometric configurations ferrite PM machines are able to achieve comparable power density as rare-earth PM machines. And among the existing configurations the two-layer spoke type ferrite IPM configuration appears to show great potentials in maximising the torque density of ferrite PM machine by combining flux-focusing techniques and high saliency

multilayer structure. In order to increase the competitive capability of the ferrite IPM electric drive system, the cost of motor controller can be reduced by adopting low-cost Hall Effect sensors for estimating velocity and position and single-shunt resistor for the current sampling. Therefore, the candidate low-cost high-performance electric drive system is consisted of a two-layer spoke type ferrite IPM motor, Hall-effect speed sensors, and single-shunt current sensor.

Even though the ferrite IPM machine has been studied by many researchers, there are still some aspects that are not researched thoroughly. The whole life cycle of the machine should be considered to further improve its performance and reduce its overall cost. The optimisation process of the machine design might be further improved by advanced intelligence based algorithm, such as PSO. And some automatic optimisation tool will be welcome for electric machine designers to simplify design process and save operating time. The machine quality could be further improved with consideration of manufacturing process. And the estimation of iron losses could be more accurate when the effects of press fitting, shrink fitting, and PWM harmonics are considered. In addition, when the proposed ferrite IPM motor is controlled by the low-cost controller with Hall Effect sensors and single current shunt, some new problems may appear, which require more research to solve. Therefore, these concerns lead to the study of the thesis.

3. FERRITE INTERIOR PERMANENT MAGNET MACHINE DESIGNED BY PARTICLE SWARM OPTIMISATION METHOD

3.1 The Studied Ferrite IPM Machine and Design Aspects

According to the literature, the ferrite IPM machine with two-layer spoke type configuration is the best candidate to replace the current widely used IM due to its higher power density and efficiency. And the ferrite IPM machine also shows great potentials in maximising the torque density by combining flux-focusing techniques and high saliency multilayer structure. Once the materials of the machine are fixed, the performance of the machine is mainly determined by its geometrical structure. Considering the large number of design parameters in the configuration, it is of great importance to have an effective and time-efficient method to design and optimise the machine.

This chapter proposes a machine design method based on PSO algorithm to solve the multi-parameter machine design issue. This method not only provides optimal geometric structure of the machine, but also substantially saves designers' operating time.

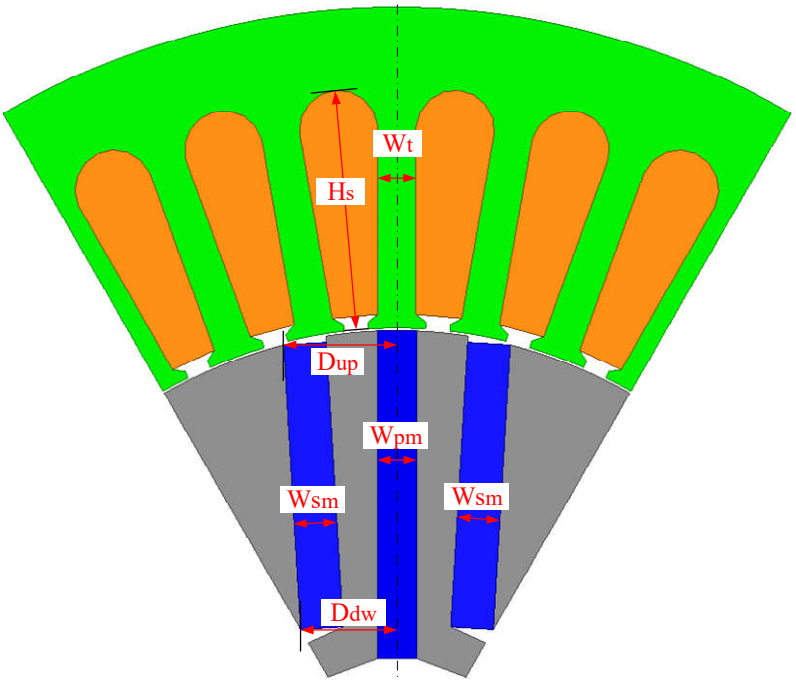

Figure 3-1 Investigated parameters of the studied electric machine

Some of the basic structural parameters of the designed IPM machine have been directly determined by its application constraints and rules of thumb, such as the diameters of stator and rotor, machine axial length, the numbers of poles and slots, which are listed in Table 3-1. And some other geometrical parameters that affect the machine performance significantly are not determined yet, such as the depth of slot, the width of stator tooth, the width of magnet and its position in the rotor. These parameters need further optimisation, which are summarised in Table 3-2 and illustrated in Figure 3-1.

Table 3-1 Determined parameters

Parameters	Value
Outer diameter of stator (mm)	160
Inner diameter of stator (mm)	95
Outer diameter of rotor (mm)	94.5
Inner diameter of rotor (mm)	28
Slot openness (mm)	2.5
Axial length of machine (mm)	94
Number of poles	6
Number of slots	36

Table 3-2 Investigated parameters

Parameters	Symbol
Width of stator tooth	W_t
Depth of stator slot	H_s
Width of primary magnet	W_{pm}
Width of secondary magnet	W_{sm}
Upper distance between sec. mag. and central line	D_{up}
Lower distance between sec. mag. and central line	D_{dw}

As shown in Figure 3-1, the PM flux goes the stator teeth to the stator yoke, and the width of stator tooth W_t affects the flux density in the teeth. The flux density will increase when W_t is widened. If W_t is too thin, the teeth will be saturated and PM flux cannot be fully utilised. The volume of copper winding is restricted by the depth of stator slot H_s and the width of stator tooth W_t. When H_s is deepened and W_t is narrowed, the area of slot cross-section is enlarged and more copper wires can be accommodated. But if too much of the stator area is occupied by slots, the stator core may be likely to be magnetically saturated and the mechanical structure becomes weak. The shapes of primary and secondary magnets are mainly determined by their width parameters W_{pm} and W_{sm} and also affected by position parameters D_{up} and D_{dw}. In the ideal electric machine model, the shape of the magnet is only limited by the rotor boundaries, such as the outer and inner diameters of the rotor. And the shape and location of the magnets are controlled by parameters W_{pm}, W_{sm}, D_{up} and D_{dw} together, which are coupled with each other. When the position parameters D_{up} and D_{dw} are

varied, the shape of the secondary magnet is changed as well. The performance of the machine is affected by both of rotor and stator, thus all the six parameters should be taken into consideration when the machine is evaluated.

Therefore, the design of the machine becomes an issue of finding the best values of these parameters within their varying ranges. And the most common method is “trial and error”, investigating any possible combinations of these parameters and selecting the one with best performance. Following the idea of trial and error, here are six parameters to be investigated, and if six trial points are evaluated for each parameter, there will be 6^6=46656 trials to find the best design. If each trial takes five minutes to obtain FEA results, there will be 46656*5/60/24=162 days to finish all the trials, which is too long for most design requirements. In addition, the resultant design might not be the best one, as the trial resolution is too low for some parameters. For example, the varying range of the parameter *Hs* is from 6 mm to 32 mm, if the range is evenly divided into five subsections, there will be (32-6)/5=5.2 mm difference between two tested points, which is far too larger to obtain an optimal design. If the resolutions are increased to get more accurate results, the computation time will be extended exponentially. Hence, a more efficient and convenient approach to optimise the machine is desirable.

3.2 Particle Swarm Optimisation Method

3.2.1 Introduction of Particle Swarm Optimisation

The complexity of the electric machine structure makes the optimal design a difficult and challenging task. The nonlinearities in materials and the complex relationships between many of the geometrical parameters truly make optimal machine design a multi-objective optimisation. All of these render most classic optimisation algorithms ineffective because the optimisation problem needs to be formulated as a nonlinear, non-gradient, constrained minimisation problem, which requires a computational intelligence based method. Thus particle swarm optimisation (PSO) method is introduced to the design of the proposed ferrite IPM machine.

PSO is an evolutionary computation technique developed by Eberhart and Kennedy [158,159] in 1995, which was inspired by the social behaviour of bird flocking and fish schooling, where the optimal search is attained by a combination of self and swarm knowledge[160–162]. PSO has been shown to be effective in optimising difficult multidimensional discontinuous problems in a variety of fields [163,164]. PSO has the following advantages. 1) PSO is easier to implement and there are fewer parameters to adjust; 2) every PSO particle remembers its own previous best value and the neighbourhood best, so it has a more effective memory capability; 3) PSO is more efficient in maintaining the diversity of the swarm (more similar to the ideal social interaction in a community), since all the particles use the information related to the most successful particle in order to improve themselves [163].

As PSO is able to solve complex system optimisation problems, it has been applied to PM machine design optimisation [165–169]. PSO is applied in [170] to optimise a synchronous reluctance motor for traction applications, in [171,172] for IMs, in [173] for a SMPM motor with a segmented pole, in [174] for an outer-rotor SMPM for direct drive application ,in [175] for a linear machine, in [176] for a transverse flux permanent motor, and so on. Auto-tuning multi-grouped PSO is proposed in [177] for optimising multimodal functions and applied in [178] to optimise an IPM generator. These researches show that PSO is a superior tool for multidimensional parametric machine design in terms of simplicity, computational efficiency and effectiveness [171,174,176,179].

Due to its good characteristics and successful application on electric machine design, PSO method is suitable to the design of two-layer spoke type ferrite IPM machine with complicated structure and considerable amount of design parameters. Therefore, the design of the machine will be carried out by the PSO technique. The concepts, formulations, and developments of PSO will be first introduced in this section, and its application on machine will be discussed in details in the next section.

3.2.2 The Process of PSO Implementation

The terminologies used to discuss PSO are summarised in Table 3-3, which refer to [161,164,180]. The analogy that a swarm of bees are trying to find the places with most flowers is used in the section to help readers understand these POS terminologies.

Table 3-3 The key terminologies used in PSO

Particle/Agent	One single individual in the swarm
Position	An agent's N-dimensional coordinates which represents a solution to the problem
Fitness	A single number representing the goodness of a given solution (represented by a location in solution space)
pbest	The location in parameter space of the best fitness returned for a specific agent
gbest	The location in parameter space of the best fitness returned for the entire swarm
Vmax	The maximum allowed velocity in a given direction

Particle/Agent: Each individual in the swarm (bees in the analogy above) is referred to as a particle or agent. All the particles in the swarm act individually under the same governing principle: accelerate toward the best personal and best overall location while constantly checking the value of its current location.

Position: In the analogy above position referred to a bee's place in the field. This is represented by coordinates on the x-y plane. In general, however, this idea can be extended into any N-dimensional space according the problem at hand. This N-dimensional space is the solution space for the problem being optimised, where any set of coordinates represents a solution to the problem. In the analogy above the solution is a physical location on the x-y plane, but this could just as easily represent amplitude and phase of element excitation in a phased array. In general these can be any values needed to be optimised. Reducing the optimisation problem to a set of values that could represent a position in solution space is an essential step in utilising the PSO.

Fitness: As in all evolutionary computation techniques there must be some function or method to evaluate the goodness of a position. The fitness function

must take the position in the solution space and return a single number representing the value of that position. In the analogy above the fitness function would simply be the density of flowers: the higher the density, the better the location. In general this could be antenna gain, weight, peak cross-polarization, or some kind of weighted sum of all these factors. The fitness function provides the interface between the physical problem and the optimisation algorithm.

Pbest: In the analogy above each bee remembers the location where it personally encountered the most flowers. This location with the highest fitness value personally dis- covered by a bee is known as the personal best or *pbest*. Each bee has its own *pbest* determined by the path that it has flown. At each point along its path the bee compares the fitness value of its current location to that of *pbest*. If the current location has a higher fitness value, *pbest* is replaced with its current location.

Gbest: Each bee also had some way of knowing the highest concentration of flowers discovered by the entire swarm. This location of highest fitness encountered is known as the global best or *gbest*. For the entire swarm there is one *gbest* to which each bee is attracted. At each point along their path every bee compares the fitness of their current location to that of *gbest*. If any bee is at a location of higher fitness, *gbest* is replaced by that bee's current position.

Vmax: Particles' velocities on each dimension are clamped to a maximum velocity *Vmax*. If the sum of accelerations would cause the velocity on that dimension to exceed *Vmax*, which is a parameter specified by the user, then the velocity on that dimension is limited to *Vmax*.

After understanding the basic concept of the PSO, the next step is to implement the algorithm to optimisation work. The basic process of implementing PSO is summarised in the flow chart of Figure 3-2.

- Define the solution space: The first step to implement the PSO is to select the parameters that need to be optimised and give them a reasonable range in which to search for the optimal solution.

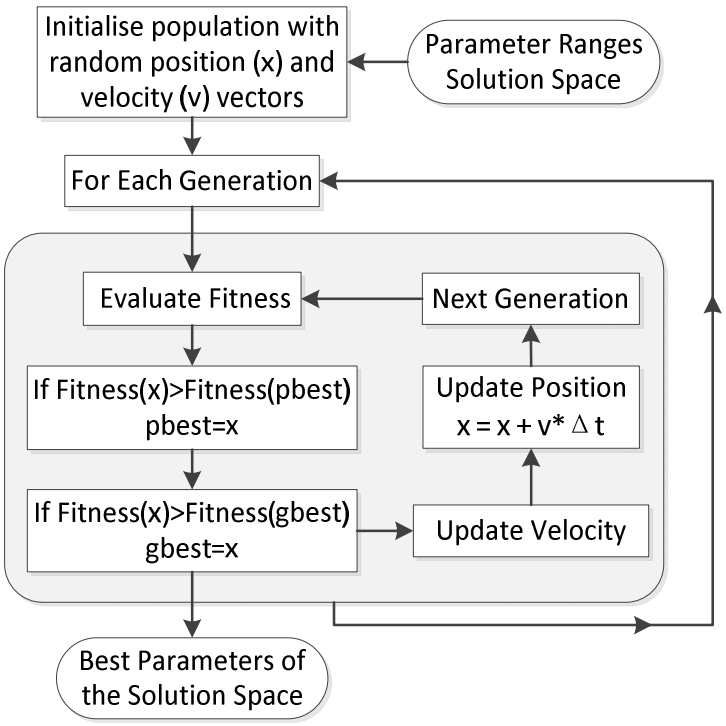

Figure 3-2 The flow chart of PSO algorithm

- Define a fitness function: It is also called objective function which builds the link between the optimisation algorithm and the physical world to evaluate the goodness of a position. The fitness function must take the position in the solution space and return a single number exhibiting the value of the position.
- Initialise random swarm location and velocities: To start searching the optimal position in the solution space, each particle begins at its own random location with a random velocity that is random both in magnitude and direction.
- Systematically “fly” the particles through the solution space: Each particle must then be moved through the solution space as if it were a bee in a swarm. The algorithm acts on each particle one by one, moving it by a small amount and cycling through the entire swarm. An example of two-dimension parameter space is shown in Figure 3-3. Each individual particle is exerted by three velocities, which is demonstrated by the particle 1 and 2 in the figure. One of the velocities is caused by its own motion inertia, retaining its velocity from last move, which is indicated in green line. The other two velocities are caused by the attraction from the global best solution *gbest*

and its own personal best solution *pbest,* which are indicated in red and blue lines. The resultant velocity is the vector sum of the above three velocities. The following steps are performed on each particle individually:

- Evaluate particle fitness: Compare to global best *gbest* and personal best *pbest*. If the fitness value is greater than the value of the respective *pbest* for that particle, or that of the *gbest*, then the appropriate locations are replaced by the current location.

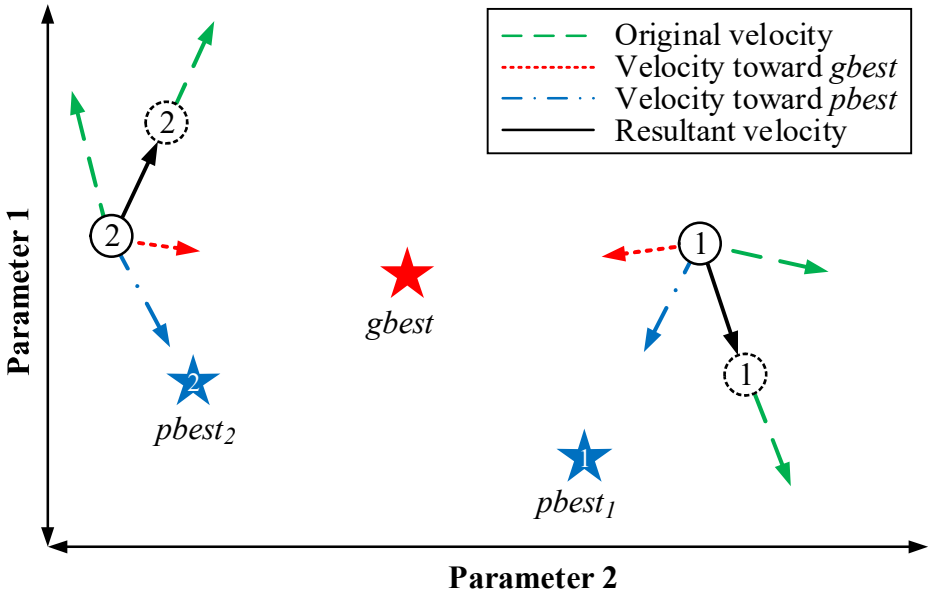

Figure 3-3 Illustration of the movements of PSO particles

- Update the particle's velocity: The manipulation of a particle's velocity is the core element of the entire optimisation. The velocity is changed according to the relative values of the *pbest* (p_{id}) and *gbest* (g_d), using the following expression:

$$v_{id(k+1)} = v_{idk} + c_1 \cdot rand \cdot (p_{id} - x_{idk}) + c_2 \cdot rand \cdot (g_d - x_{idk}) \quad \textbf{(3-1)}$$

Where v_{idk} is the velocity of the particle in the *d*th dimension and x_{idk} is the particle's coordinate in the *d*th dimension; c_1 and c_2 are scaling factors that determine the relative "pull" of personal best particle p_{id} and global best particle g_d. And $rand$ is a random number between 0 and 1.

- Advance the particle: The velocity is applied for a given time-step *Δt*, usually chosen to be 1, and the position is updated to

$$x_{id(k+1)} = x_{idk} + \Delta t \cdot v_{id(k+1)} \quad \textbf{(3-2)}$$

The particle is then moved to the location calculated by the above equation.

- Repeat: After the process is carried out for each particle in the swarm, the process is repeated. In this way the particles move for discrete time intervals until the termination criteria are met.

Often in engineering applications it is desirable to limit the search to what is physically possible. Experience has shown that constriction factors, and inertial weights do not always confine the particles within the solution space. To address this problem, the authors in [160] have imposed three different boundary conditions.

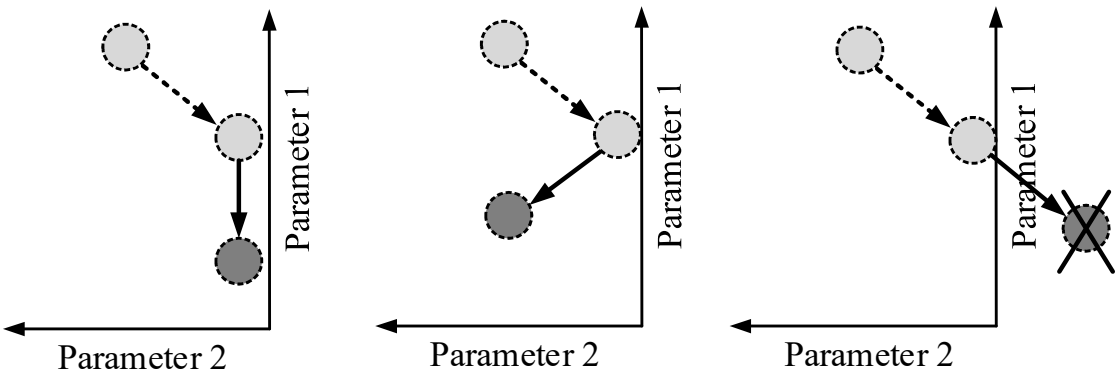

(a) absorbing walls (b) reflecting walls (c) invisible walls.

Figure 3-4 PSO boundary conditions

- Absorbing Walls: When a particle hits the boundary of the solution space in one of the dimensions, the velocity in that dimension is zeroed, and the particle will eventually be pulled back toward the allowed solution space. In this sense the boundary “walls” absorb the energy of particles trying to escape the solution space.
- Reflecting Walls: When a particle hits the boundary in one of the dimensions, the sign of the velocity in that dimension is changed and the particle is reflected back toward the solution space.
- Invisible Walls: The particles are allowed to fly without any physical restriction. However, particles that roam out- side the allowed solution

space are not evaluated for fitness. For nearly all engineering applications, the computationally expensive portion of the algorithm is the fitness evaluation. The motivation behind this technique is to save computation time by only evaluating what is in the allowed solution space, while not interfering with the natural motion of the swarm

The authors in [160] tested the above three conditions by using PSO algorithm optimising a series of benchmark functions. The results show that the “invisible walls” technique is slightly better than other two techniques.

3.2.3 Developments and Variants of PSO

- **The original version of PSO**

The procedure introduced in section 3.2.2 is the original version of PSO. In the PSO algorithm, it is known that the maximum velocity *Vmax* is an important parameter. It determines the resolution, or fineness, with which regions between the present position and the target (best so far) position are searched. If *Vmax* is too high, particles might fly past good solutions. If *Vmax* is too small, on the other hand, particles may not explore sufficiently beyond locally good regions. In fact, they could become trapped in local optima, unable to move far enough to reach a better position in the problem space. *Vmax* is the only parameter that is routinely adjusted, and it is often set at about 10-20% [164] of the dynamic range of the variable on each dimension.

The acceleration constants c_1 and c_2 in equation (3-1) represent the weighting of the stochastic acceleration terms that pull each particle toward *pbest* and *gbest* positions. Thus, adjustment of these constants changes the amount of "tension" in the system. Low values allow particles to roam far from target regions before being tugged back, while high values result in abrupt movement toward, or past, target regions. Early experience with particle swarm optimisation (trial and error, mostly) led us to set the acceleration constants c_1 and c_2 each equal to 2.0 [164] for almost all applications.

Population size is another parameter that needs careful selection. Large population, while providing the most thorough exploration of the solution space, come at the cost of more fitness evaluations and computation time. For the PSO, it has been found that relatively small population sizes can sufficiently explore a solution space while avoiding excessive fitness evaluations. The population size selected was problem-dependent, and the size of 20-50 were probably most common[164]. Parametric studies have found that a population size of about 30 is optimal for many problems [181], and even smaller population sizes of around ten to 20 particles have been effective for engineering problems [160].

- **Inclusion of Inertia Weight**

The maximum velocity *Vmax* serves as a constraint to control the global exploration ability of a particle swarm. As stated earlier, a larger *Vmax* facilitates global exploration, while a smaller *Vmax* encourages local exploitation. The concept of an inertia weight was developed to better control exploration and exploitation. The motivation was to be able to eliminate the need for *Vmax*. The inclusion of an inertia weight in the particle swarm optimisation algorithm was first reported in the literature in 1998 [182,183].

$$v_{id(k+1)} = w \cdot v_{idk} + c_1 \cdot rand \cdot (p_{id} - x_{idk}) + c_2 \cdot rand \cdot (g_d - x_{idk}) \quad \textbf{(3-3)}$$

Equations (3-3) and (3-2) describe the velocity and position updating equations with an inertia weight included. It can be seen that these equations are identical to equations (3-1) and (3-2) with the addition of the inertia weight w as a multiplying factor of v_{id} in equation (3-3).

The use of the inertia weight w has provided improved performance in a number of applications. As originally developed, w is often decreased linearly from about 0.9 to 0.4 during a run [164,182]. Suitable selection of the inertia weight provides a balance between global and local exploration and exploitation, and results in less iteration on average to find a sufficiently optimal solution.

After some experience with the inertia weight, it is found that although the maximum velocity factor *Vmax* couldn't always be eliminated, the particle swarm algorithm works well if *Vmax* is set to the value of the dynamic range of each variable [164] (on each dimension). Thus, it is no longer necessary to think about how to set *Vmax* each time when the particle swarm algorithm is used.

- **Introduction of Constriction Factor**

Because particle swarm optimisation originated from efforts to model social systems, a thorough mathematical foundation for the methodology was not developed at the same time as the algorithm. Within the last few years, a few attempts have been made to begin to build this foundation. Recent work done by Clerc [184,185] indicates that use of a constriction factor may be necessary to insure convergence of the particle swarm algorithm. A detailed discussion of the constriction factor is beyond the scope of this paper, but a simplified method of incorporating it appears in equation (3-4), where K is a function of c_1 and c_2 as reflected in equation (3-5).

$$v_{id(k+1)} = K \cdot [v_{idk} + \varphi_1 \cdot rand \cdot (p_{id} - x_{idk}) + \varphi_2 \cdot rand \cdot (g_d - x_{idk})] \quad \textbf{(3-4)}$$

$$K = \frac{2}{\left|2-\varphi-\sqrt{\varphi^2-4\varphi}\right|}, \text{ where } \varphi = \varphi_1 + \varphi_2,\ \varphi > 4 \quad \textbf{(3-5)}$$

Clerc and Kennedy assert that the sum of the values of the cognitive and social components of the PSO (φ_1 and φ_2) should be larger than 4.0 [184] Typically, when Clerc's constriction method is used, φ is set to 4.1, thus $\varphi_1 = \varphi_2 = 2.05$ and the constant multiplier K is 0.729 [160]. So the two deviation terms $(p_{id} - x_{id})$ and $(g_d - x_{id})$ are multiplied by 0.729*2.05= 1.49445, and then they times a random number between 0 and 1. Considering the constriction factor, the scaling factors c_1 and c_2 in equation (3-3) has evolved, i.e. $c_1 = K\varphi_1 = 0.729 \times 2.05 = 1.49445,\ c_2 = K\varphi_2 = 0.729 \times 2.05 = 1.49445.$

However, in an earlier work, Kennedy also looked at models where the two components φ_1 and φ_2 had varying values, specifically, $\varphi_2 = 0$ for the cognition-only model, $\varphi_1 = 0$ for the social-only model, and setting the two components equal $\varphi_1 = \varphi_2$ for the full model [186]. In that work, he found a

performance advantage to the social-only model. To see the effect of changing the relationship between the cognitive and social components, Carlisle and Dozier varied the cognitive component φ_1 from 0.0 to 4.1, and computed the matching social component φ_2, where $\varphi_2 = 4.1 - \varphi_1$[181]. The results showed that the usual settings ($\varphi_1 = \varphi_2 = 2.05$) did not result in the best performance for the swarm on any of the benchmark functions, and the swarm performed better as the social component diminished. This implies that the social component tends to lead to more local minima trapping. A reasonable compromise for the cognitive and social component values appear to be 2.8 and 1.3 respectively, viz., $\varphi_1 = 2.8$, $\varphi_2 = 1.3$ [160]. Clerc's constriction factor was another attempt to eliminate the need for, but most authors agree that it is still best to set in each dimension to the dynamic range of that dimension [164,181].

The suggested parameter values for the two different velocity equations are summarised in Table 3-4. As the suggested parameters for equation (3-3) is derived from Clerc and Kenney's ideas, this set of parameters are named as *Clerc-Kenney* parameters. Similarly, the suggested parameters for equation (3-4) are termed as *Clerc-Carlisle* parameters.

Table 3-4 Suggested parameter values for the two velocity equations

Name	Suggested Parameters			Reference
Clerc-Kenney	$w = 0.9 \sim 0.4$ (linearly decreased)	$c_1 = 1.494$	$c_2 = 1.494$	Equation (3-3)
Clerc-Carlisle	$K = 0.729$	$\varphi_1 = 2.8$	$\varphi_2 = 1.3$	Equation (3-4)

In conclusion, the operating procedures of these variants of PSO method are similar, but due to different selections of inertial weights, scaling factors, *Vmax* values, and boundary conditions, the final optimal results will have some difference. And effects of these different PSO setup parameters on electric machine design will be evaluated in the following sections.

3.3 Electric Machine Optimisation by PSO

According to the process that is introduced in 3.2.2, the PSO method is applied on the design of two-layer spoke type ferrite IPM machine. The details of the application are described clearly step by step in the following sections.

3.3.1 Solution Space and Objective Function of the Studied Machine

It is known from the discussion of Figure 3-2 that the first step to implement the PSO is to select the parameters that need to be optimised and give them a reasonable range in which to search for the optimal solution. For the studied IPM machine, there are six design parameters that are illustrated in Figure 3-1.

Table 3-5 The investigated parameters and varying range

Parameters	Symbol	Upper limit x_{max} (mm)	Lower limit x_{min} (mm)
Width of stator tooth	W_t	6	1
Depth of stator slot	H_s	32	6
Width of primary magnet	W_{pm}	10	1
Width of secondary magnet	W_{sm}	10	1
Upper distance between secondary magnet and central line	D_{up}	21	2
Lower distance between secondary magnet and central line	D_{dw}	20.5	8

And their varying ranges are constrained by their corresponding upper limit x_{max} and lower limit x_{min}, which are listed in Table 3-5. The upper and lower limits are determined by mechanical constraints and machining conditions [187]. Thus the solution space of the studied ferrite machine is defined as:

$$\begin{cases} 1 < W_t < 6 \\ 6 < H_s < 32 \\ 1 < W_{pm} < 10 \\ 1 < W_{sm} < 10 \\ 2 < D_{up} < 21 \\ 8 < D_{dw} < 20.5 \end{cases} \quad \textbf{(3-6)}$$

The fitness function builds the link between the optimisation algorithm and the physical world to evaluate the goodness of a position. For the studied IPM machine, the fitness function of the optimisation is to achieve maximum torque

output at the same heat radiation condition. As most of the heat is generated from copper loss when the machine is operating at rated speed, the fitness function can be defined as:

$$f_{ik} = f(x_{ik}) = \frac{T_{ik}}{P_{cpl\_ik}} \quad \textbf{(3-7)}$$

where, x_{ik} presents the parameters of the i^{th} machine design (particle) at the k^{th} generation, and the f_{ik} is the corresponding fitness result of the machine design. T_{ik} and P_{cpl_ik} are output torque and copper loss of that design. The x_{ik} has six dimensions, which are W_t, H_s, W_{pm}, W_{sm}, D_{up}, D_{dw}. Due to the complexity of electric machine, FEA model is used to evaluate its performance. The design parameter x_{ik} is input into the FEA model, and T_{ik} and P_{cpl_ik} can be directly obtained from FEA results. The objective is to achieve the maximum value of the fitness function, i.e. to achieve the maximum output torque when the copper loss is constant. As copper loss is the major loss of the studied motor, maximising output torque with the same copper loss also means to achieve maximum motor efficiency, which is of high importance for a low-cost electric machine.

Referring to the flowchart in Figure 3-2, and the motor optimisation process will start from random initial values, and then iterate until the termination criteria are met.

3.3.2 Initialisation and Iteration of PSO Process

Parametric studies have found that a population size of about 30 is optimal for electric machine problems [160,182]. Thus the population size is set as 30 in the study, i.e. 30 particles in each generation. The initial values of the PSO process are obtained according to the dynamic range of each parameter that is defined by the upper limit x_{max} and lower limit x_{min}. The particles' positions, velocities and *pbest* and *gbest* are initialised by the following equations that are referred to the analysis of PSO in [160,188]. The initial value is randomly selected from the dynamic range of each design parameter, and it is obtained by Equation (3-8).

$$x_{id1} = x_{dmin} + (x_{dmax} - x_{dmin}) \cdot rand \quad \textbf{(3-8)}$$

In this equation, x_{id1} stands for one of the initial parameters used in the ferrite IPM machine design. The subscript *i* indicates the number of particles in the swarm, where *i*=1, 2, 3 … 30 since there are 30 motor models in each generation. The subscript *d* indicates the dimension of each particle, i.e. the design parameters of each motor model. Since there are six parameters used in the motor design, *d*=1, 2, 3 … 6, which are W_t, H_s, W_{pm}, W_{sm}, D_{up}, D_{dw} to be specific. The subscript *1* indicates the initial/first generation of design parameters. $(x_{imax} - x_{imin})$ is the dynamic range of each parameter, and $rand$ is a random number between (0, 1). Due to the use of the random number *rand*, the parametric values of 30 particles are casually selected in their dynamic ranges.

According to the discussion in Section 3.2, when the maximum velocity *Vmax* is set as 15% of the dynamic range of the variable, a more effective exploration can be achieved [164]. Thus the initial velocities can be obtained by the equations (3-9).

$$v_{id1} = 0.15(x_{dmax} - x_{dmin}) \cdot (1 - 2 \cdot rand) \quad \textbf{(3-9)}$$

In this equation, V_{id1} stands for the initial velocity of its corresponding parameter x_{id1}, and the subscripts *i, d, 1* have the same definition as that in Equation (3-8). And $0.15(x_{imax} - x_{imin})$ means the 15% of the dynamic range of each parameter; $(1 - 2 \cdot rand)$ is a random number between (-1, 1). Owing to the random number, the generated initial velocity can be positive or negative, which indicate the direction of the velocity can be either positive or negative. According to Equations (3-1)–(3-4), these initial velocities will be used to generate next generation of velocities and parameters.

The PSO process is started when the initial set of parameters are input into the FEA machine model. All the motor designs (particles) of the first generation are evaluated by one by one in the FEA model. The output torque T_{ik} and copper

loss P_{cpl_ik} of each design are obtained from simulation results. Then the fitness of the design is calculated by Equation (3-7).

For the initial/first generation of PSO design, as there is no prior generation to compare, the fitness of *pbest* is same as the fitness of the initial design, and *pbest* parameters are same as the initial set of parameters.

$$f_{pi} = f_{i1} \tag{3-10}$$

$$p_{id} = x_{id1} \tag{3-11}$$

where, f_{pi} and p_{id} represent the *pbest* fitness and parameter of the i^{th} motor design, and the subscript *1* means the first generation.

From the second generation, the newly obtained fitness f_{ik} compares with existing *pbest* fitness f_{pi}. If f_{ik} is larger than f_{pi},

$$f_{pi} = f_{ik} \tag{3-12}$$

$$p_{id} = x_{idk} \tag{3-13}$$

the *pbest* parameter p_{id} is updated with the better parameter x_{idk}. Otherwise, f_{pi}.and p_{id} will not be changed.

The *gbest* fitness f_g is the largest fitness among all the available designs, and *gbest* parameter g_d is best set of parameter corresponding to f_g. The initial f_g is the fitness of the first design.

$$f_g = f_{11} \tag{3-14}$$

where, f_{11} means fitness of the first machine design in the first generation. From the second design, the newly obtained fitness f_{ik} compares with existing *gbest* fitness f_g. If f_{ik} is larger than f_g,

$$f_g = f_{ik} \tag{3-15}$$

$$g_d = x_{idk} \tag{3-16}$$

the *gbest* parameter g_d is updated with the better parameter x_{idk}. Otherwise, f_g.and g_d will not be changed.

Once all the machine designs of the current generation have been evaluated, the next generation of designs will be generated on base of the results of the current generation, as it is illustrated in Figure 3-2. The new velocities can be generated by *Clerc-Kenney* method Equation (3-3) or *Clerc-Carlisle* method Equation (3-4). In this study, both of the two methods are applied and their differences are discussed in Section 3.4.1. Once the new velocities are obtained, the new generation of designs are obtained by Equation (3-2) , where the Δt is set to one in this case, and $\mathrm{i} = 1,2,\ldots,30$.

Sometimes the newly generated parameter x_{idk} may run out of its solution space, i.e. the new parameter may be larger than its upper limit x_{max}, or smaller than its lower limit x_{min}. The boundary conditions deal with this issue. In the absorbing walls boundary condition, the boundary value will be used instead of the run-out parameter. If the new parameter x_{idk} is larger than its upper limit x_{max}, $x_{idk} = x_{max}$; if the new parameter x_{idk} is smaller than its lower limit x_{min}, $x_{idk} = x_{min}$. While in the invisible walls boundary conditions, the newly generated parameter that runs out of its solution space will be ignored. The procedure of velocity generation and parameter generation will be repeated until valid parameter is obtained. Because there are two *rand* terms used in the velocity equation (3-3) or (3-4), the generated parameters will be different for each time, and a satisfied parameter will be obtained after several tries. Both of the two boundary conditions are applied in the research and their differences are discussed in Section 3.4.1.

The maximum velocity *Vmax* has effect on the velocity generation and it can be set to the value of the whole dynamic range for each variable, or 15% of the dynamic range. Both of the two *Vmax* setting are applied in the research and their differences are discussed in Section 3.4.1. And the new generation of

machine designs will be evaluated by FEA model one by one until all of them is finished. This process will be repeated until all the required generation of designs are evaluated.

3.3.3 Machine Optimisation Automation Programmed in VBScript

VBScript standing for Visual Basic Scripting edition is a general-purpose, lightweight programming language developed by Microsoft [189–191]. Typically, scripting languages are described as "glue" languages, binding things together. The “things” are the objects exposed by the environment for which the script is being written and objects that are exposed by external applications, environments, or components [189]. The FEA software used for machine design is programmed by VBScript. The simulation results exported from FEA are stored in Excel that can be controlled by VBScript. Hence the FEA simulation and Excel data storage can be interacted with each other by VBScript.

In order to improve computation efficiency and save data processing time, the whole process of machine optimisation by PSO method is programmed in VBScript language, which is illustrated thoroughly in Figure 3-5. The FEA simulation, Excel data storage, and PSO algorithm are integrated into an automatic electric machine design tool by VBScript language. As shown in Figure 3-5, the purple block represents FEA simulation that simulates each motor model with its specific set geometrical parameters. As copper loss of every model is given constant, input current is calculated based on cross-section area of winding (slot area) that is different for every new set of geometrical parameters. The green parallelogram block in Figure 3-5 means Excel table that stores all the data extracted from FEA simulation and calculated by PSO algorithm. One of the benefits of redundantly using Excel tables to save data is that once the automation programme collapses during the middle of PSO optimisation process, any finished data will not be lost and it is easy to recover and continue the remnant process. The white blocks in Figure 3-5 represents VBScript programmes that help to implement PSO method on electric machine design.

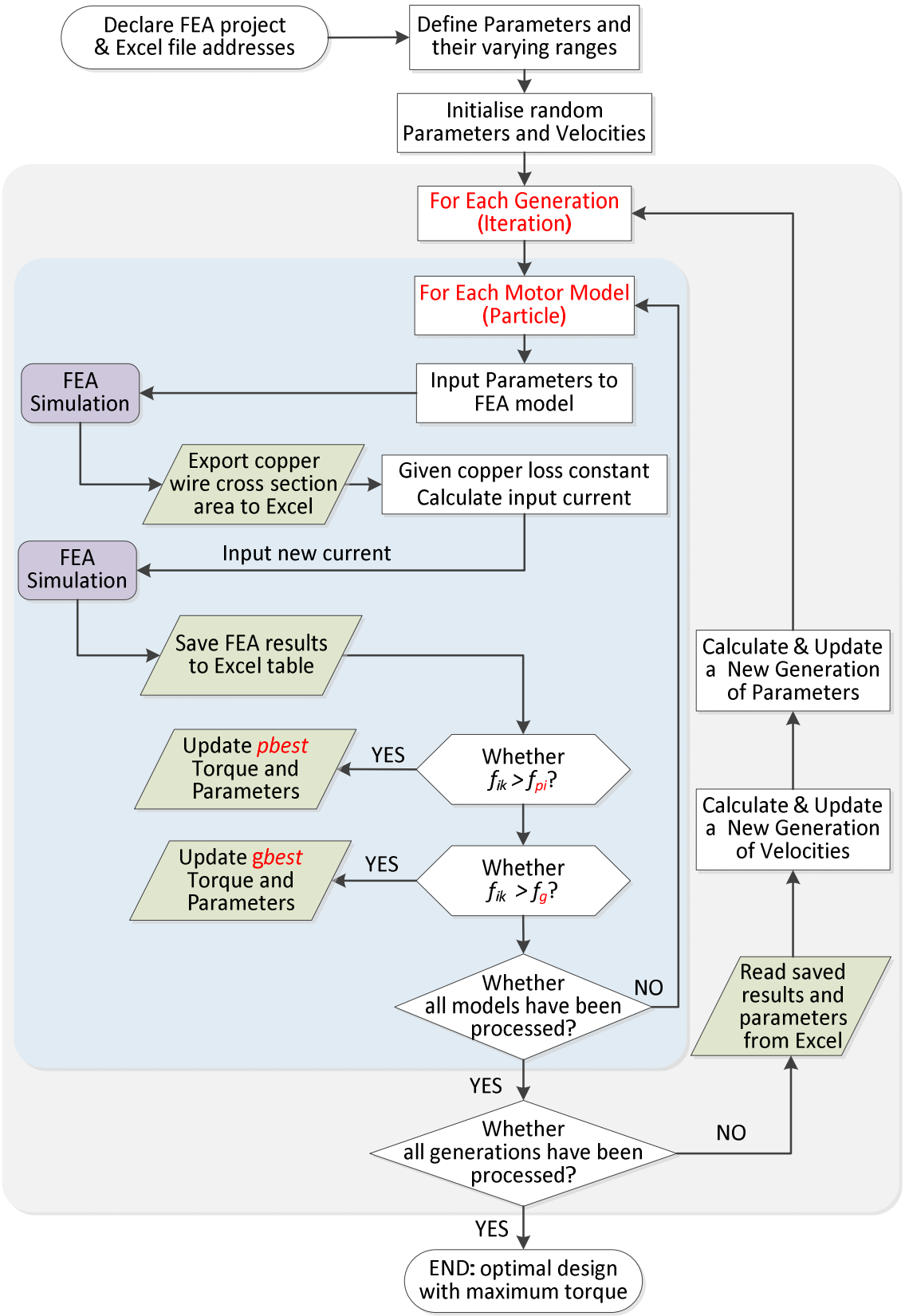

Figure 3-5 Flowchart of machine optimisation automation using PSO algorithm programmed in VBScript

With the automatic electric machine design tool that is programmed in VBScript using PSO algorithm, the design of studied ferrite IPM motor becomes much easier. When solution space, objective function, and iterative parameters are well set in the computer programme, the optimisation of electric machine design will be carried out automatically. After several days, which depend on computer performance, the optimal design will be achieved automatically without any more interference during the process. The design programme is attached in Appendix A. The machine optimisation method using PSO algorithm programmed in VBScript are also applicable for other types of electric machines.

With the convenient design programme, the PSO methods with different setup parameters are evaluated, such as different inertial weights, scaling factors, *Vmax*, and boundary conditions. The evaluation results and discussion are in following section.

3.4 Results and Discussion

3.4.1 Discussion on Different Combinations of PSO Parameters

In order to understand the effects of the parameters in PSO algorithm on electric machine design, such as inertial weights, scaling factors, *Vmax* values, and boundary conditions, five different combinations of these parameters are implemented and analysed. The combinations of different parameters are listed in Table 3-6.

Table 3-6 Different combinations of PSO parameters

Cases	Inertial Weight	Scaling Factor	Scaling Factor	Vmax	Boundary Conditions
Case 1	$w = 0.9{\sim}0.4$ (linearly decreased)	$c_1 = 1.494$	$c_2 = 1.494$	100% Dynamic Range	Invisible Walls
Case 2	$w = K = 0.729$	$c_1 = K\varphi_1 = 2.0412$	$c_2 = K\varphi_2 = 0.9477$	100% Dynamic Range	Invisible Walls
Case 3	$w = 0.9{\sim}0.4$ (linearly decreased)	$c_1 = 1.494$	$c_2 = 1.494$	15% Dynamic Range	Invisible Walls
Case 4	$w = K = 0.729$	$c_1 = K\varphi_1 = 2.0412$	$c_2 = K\varphi_2 = 0.9477$	15% Dynamic Range	Invisible Walls
Case 5	$w = 0.9{\sim}0.4$ (linearly decreased)	$c_1 = 1.494$	$c_2 = 1.494$	100% Dynamic Range	Absorbing Walls

Firstly, different PSO boundary conditions are discussed. Comparing *Case1* and *Case 5*, only the boundary condition is different in the two cases, and their optimisation process of PSO are displayed in Figure 3-6. In this figure, *gbest* line shows the global best fitness result (the output torque) in each iteration, and average line shows the average value of all the personal best fitness. From the data it is seen that the results of PSO optimisation using invisible walls boundary condition are better than that using absorbing walls boundary condition. Both of *gbest* and average output torque are higher using invisible walls boundary condition than using absorbing walls boundary condition. At the first half of process, there is no much difference in the performance of the two boundary conditions, while at the second half invisible walls boundary condition exhibit its advantage. A possible reason for it may be that the inertial weight that is linearly decreased becomes smaller in the second half of the progress, so the velocity of the particle is reduced as well. Under invisible walls boundary condition, the particles that *roam* out of the allowed solution space are not evaluated for fitness, so the particles have more chances to exploit the maxima.

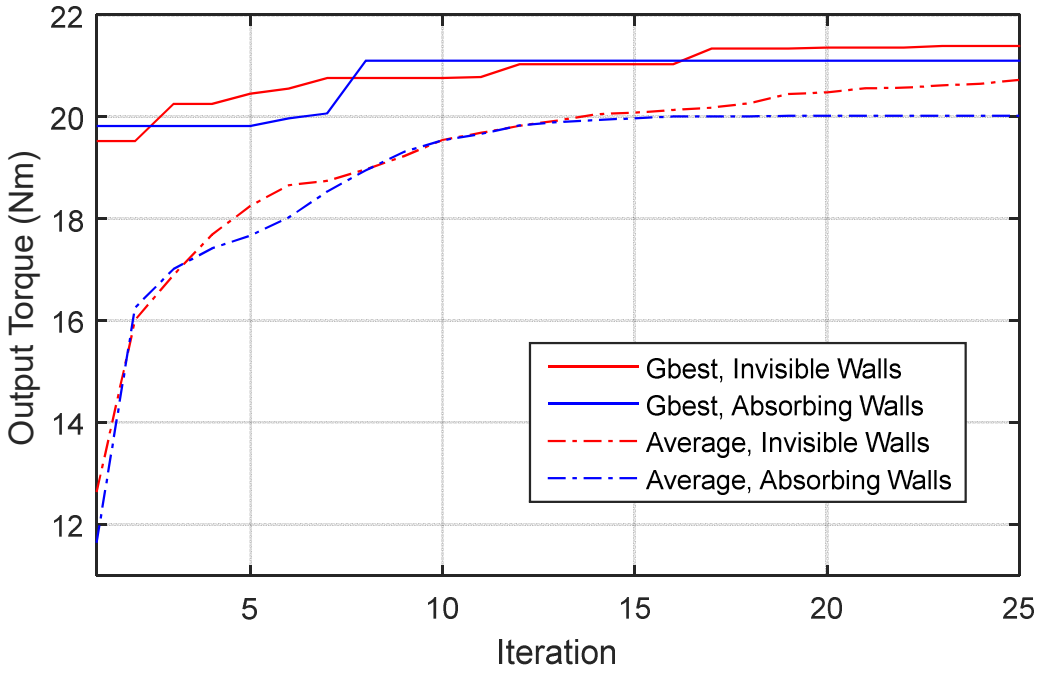

Figure 3-6 Boundary condition comparison between invisible walls and absorbing walls

Secondly, the PSO settings with different maximum velocity *Vmax* are compared. *Vmax* is an important parameter and it determines the resolution, or fineness, with which regions between the present position and the target (best so far) position are searched. If *Vmax* is too high, particles might fly past good

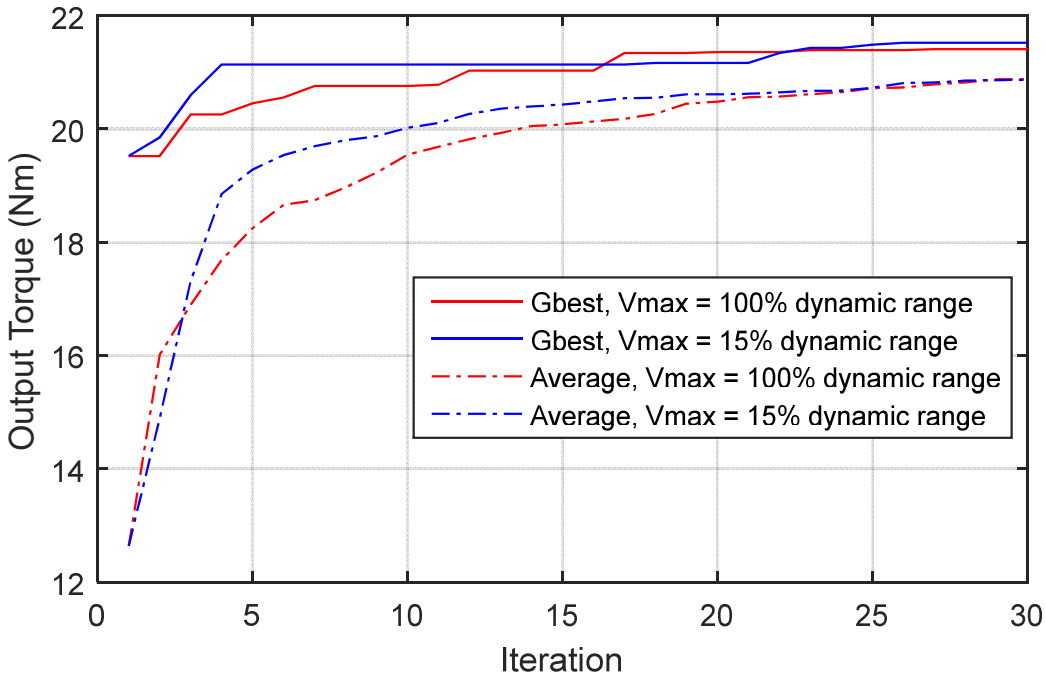

(a) Using Clerc-Kenney parameters

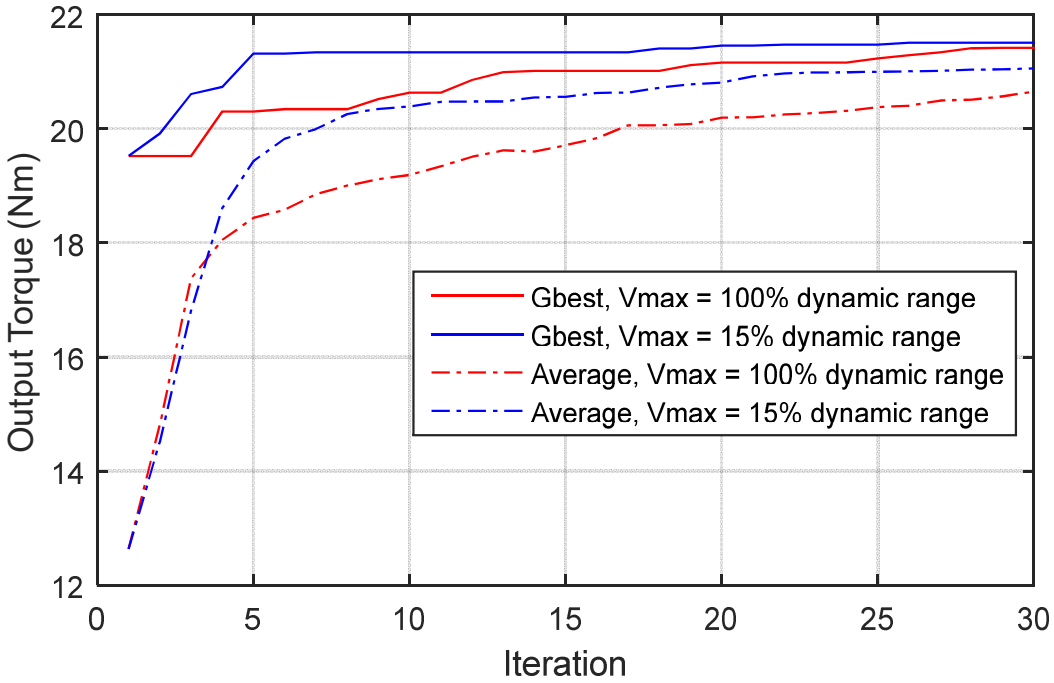

(b) Using Clerc-Carlisle parameters

Figure 3-7 Comparison of different Vmax values

solutions. If *Vmax* is too small, on the other hand, particles may not explore sufficiently beyond locally good regions. Eberhart and Shi [164] found that without inertial weight *Vmax* was best set around 10–20% of the dynamic range of each dimension; while with introduction of inertial weight it is better to set

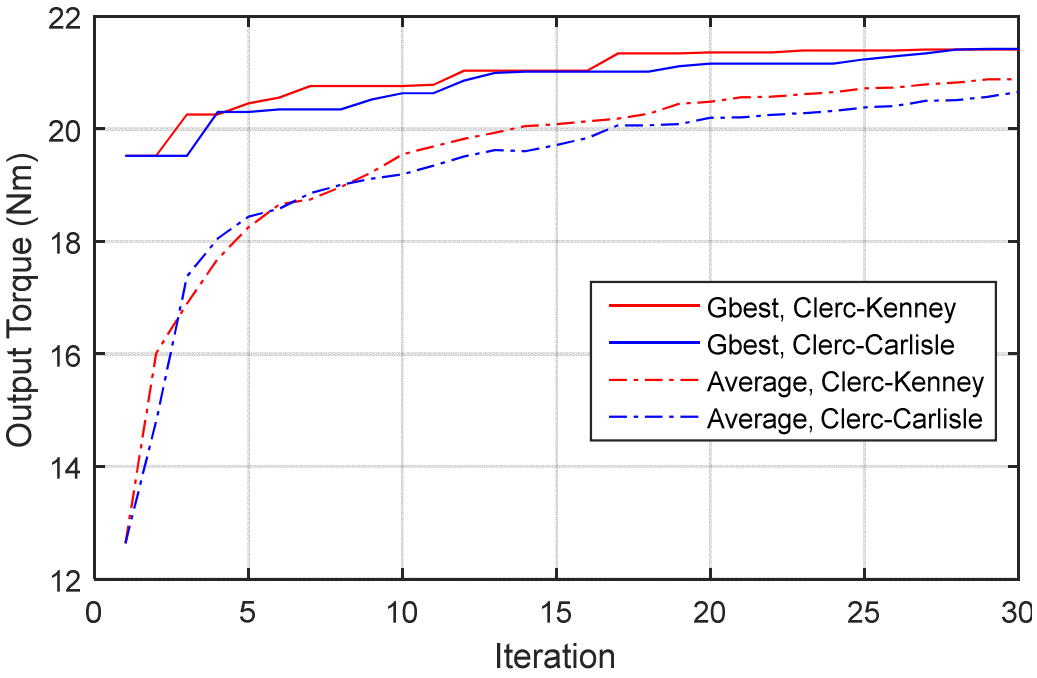

(a) When Vmax = dynamic range

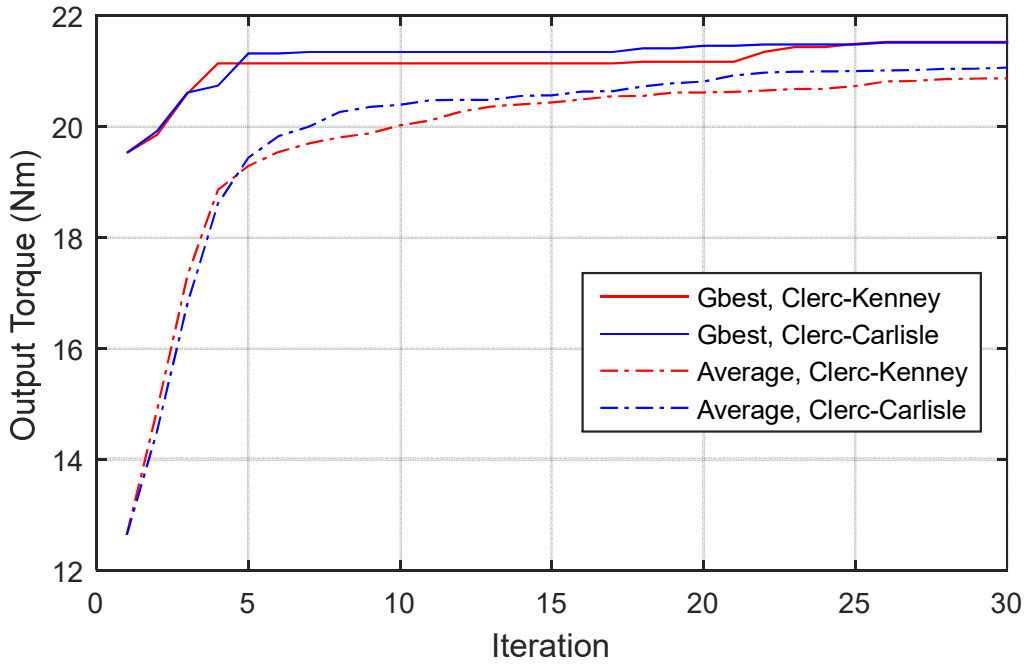

(b) When *Vmax* = 15% dynamic range

Figure 3-8 Comparison between Clerc-Kenny and Clerc-Carlisle parameters

Vmax equal to the dynamic range of that dimension, which performed better than negating the need of *Vmax*. However, from the FEA results shown in Figure 3-7 (a) (*Case 1* vs *Case 3*) and (b) (*Case 2* vs *Case 4*), it is found that even with inclusion of inertial weight, the PSO still perform better if *Vmax* is set to 10–20% of the dynamic range (fractional range) than the full dynamic range (full range). Using Clerc-Kenny parameters, there is not much difference of the average output torque by the two different *Vmax* setting, but the *gbest* value of fractional range *Vmax* outstrips that of full range. In the use of Clerc-Carlisle parameters, it is obvious to note that the PSO with fractional range *Vmax* performs much better than that with full range *Vmax*, exhibiting in both *gbest* and average output torque. Therefore, it is recommended to set *Vmax* to 10–20% of the dynamic range, so that the particles are able to explore the solution space sufficiently without flying past good solutions.

Finally, the PSO processes with different velocity equations are discussed. From the discussion in Section 3.2.3, two sets of PSO parameters are suggested for two different velocity equations, which are named *Clerc-Kenney* parameters and *Clerc-Carlisle* parameters respectively. Both of them are tested in the PSO for electric machine design application, and results are illustrated in Figure 3-8 (a) (*Case 1* vs *Case 2*) and (b) (*Case 3* vs *Case 4*). After 30 iterations, the PSO using *Clerc-Kenney* parameters and the one using *Clerc-Carlisle* parameters reach the same (or almost same) *gbest* fitness, no matter what the *Vmax* value is. But if the average fitness of all particles is taken to comparison, it is found that the PSO using Clerc-Kenney parameters performs better when *Vmax* is equal to the full dynamic range, and the PSO using Clerc-Carlisle exhibits better performance when *Vmax* is equal to 15% dynamic range. So it is concluded that both of two sets of parameters are suitable for the PSO of electric machine design, and there is no much difference between their ultimate designs.

3.4.2 The performance of the best optimised design

The best optimised design is collected from the machine design of Case 3, because its final design has the largest fitness result among the five study

cases. The geometrical parameters of the final design from PSO process are listed in Table 3-7, and it is illustrated in Figure 3-12 (a). The evolvement history of the six design parameters is clearly illustrated in Figure 3-9. The figure shows that in the first five iterations of the PSO process, the particles are moving fast, because the change of each dimension in a step is large at the beginning. While, after boldly exploring the solution space, the particles slow down their advancing speed and start to exploit around the optima. In the 10 iterations, the particles gradually approach to the optimal design and stabilise around it. The whole PSO design process takes 30 iterations to achieve the final optimal machine design. With the optimal set of geometrical parameters, the performance and other related information of the optimal machine design are collected from FEA simulation and summarised in Figure 3-8. The machine is able to output 21.52 Nm torque, but its cogging torque and torque ripple are

Table 3-7 Geometrical parameters of the best design

Parameters	Symbol	Value (mm)
Width of stator tooth	W_t	3.88
Depth of stator slot	H_s	24.40
Width of primary magnet	W_{pm}	3.98
Width of secondary magnet	W_{sm}	4.33
Upper distance between secondary magnet and central line	D_{up}	10.90
Lower distance between secondary magnet and central line	D_{dw}	9.79

Table 3-8 The performance of the best optimised machine

Performance Index	Value
Maximum Torque (Nm)	21.52
P-P Cogging Torque (Nm)	4.57
P-P Torque Ripple (Nm)	34.86
Copper Loss (W)	126.75
Core Loss (W)	68.29
Efficiency (%)	94.55
Copper Volume (cm^3)	328.50
Magnet Volume (cm^3)	216.46
Lamination Volume (cm^3)	1100.70

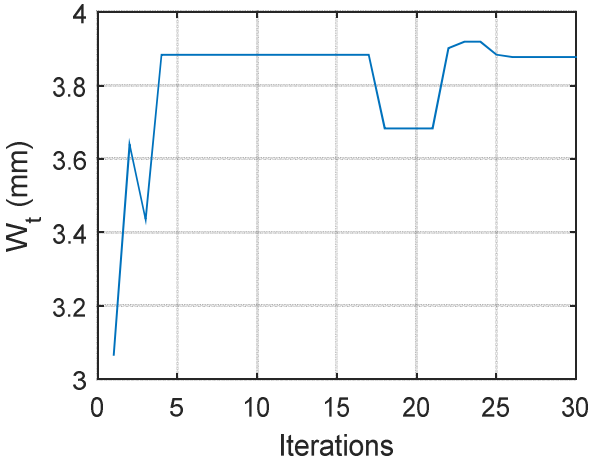

(a) Width of stator tooth, W_t

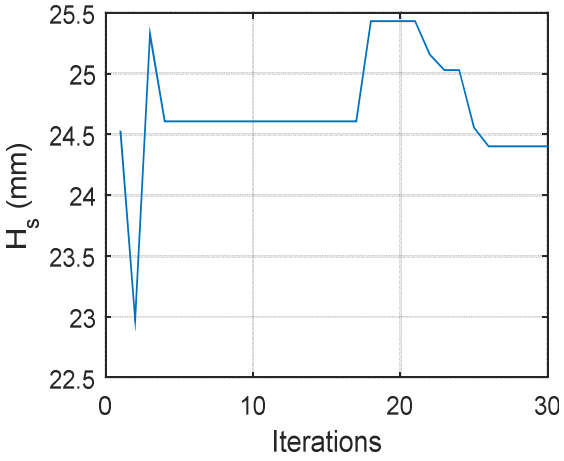

(b) Depth of stator slot, H_s

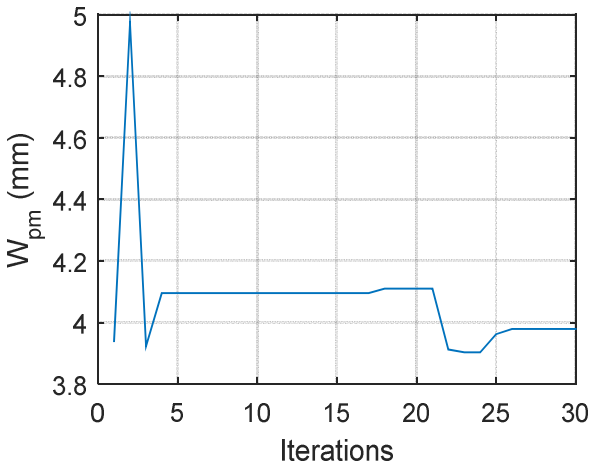

(c) Width of primary magnet, W_{pm}

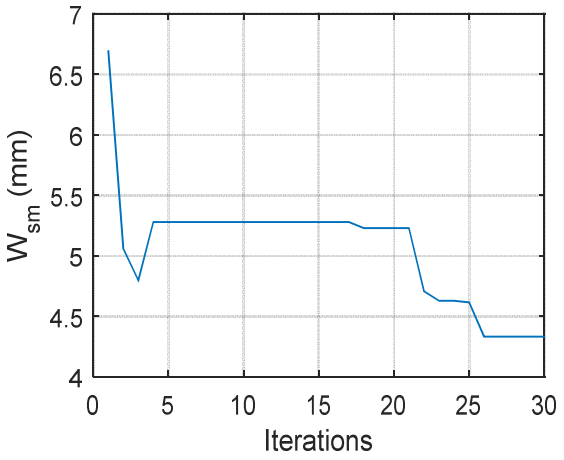

(d) Width of secondary magnet, W_{sm}

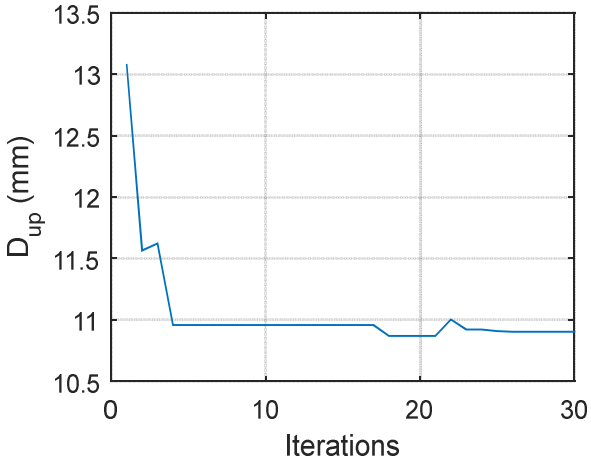

(e) Upper distance between secondary magnet and central line, D_{up}

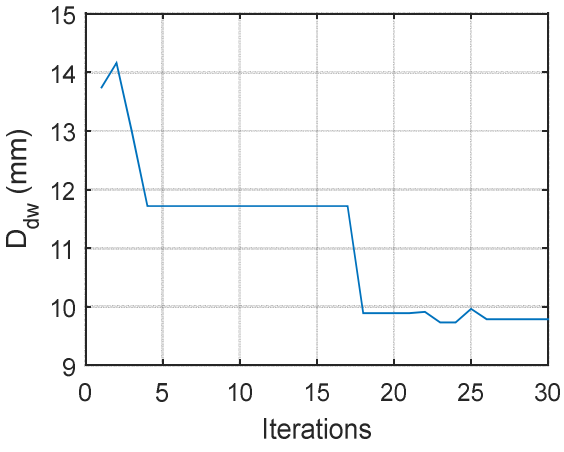

(f) Lower distance between secondary magnet and central line, D_{dw}

Figure 3-9 The evolvement of the optimised parameters in PSO

relatively large. The overall losses are 195.04 W, which include the copper loss and core loss. So the electromagnetic efficiency can be calculated from the output torque and losses results, which is 94.55%. The volumes of different materials are also collected from the FEA model.

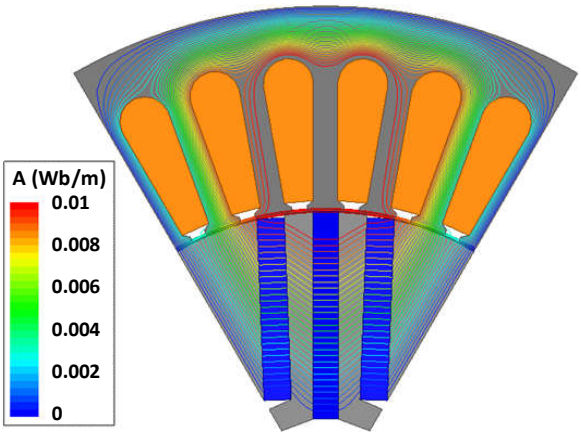

Figure 3-10 The best optimised model with flux lines at no-load

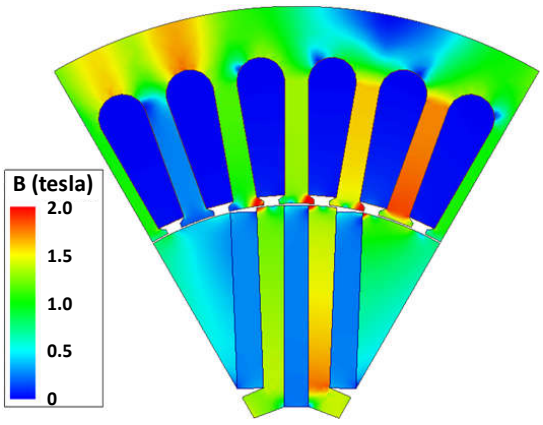

Figure 3-11 The best optimised model with flux density at rated-load

Figure 3-10 shows the best optimised model with flux lines at no-load condition, from which it is seen that the primary magnets and the secondary magnets are nearly parallel, and the width of the them are quite similar. For the manufacturing convenience, all the magnets are set in the same width and parallel located in the rotor core. Simplifying the manufacturing process will reduce the fabrication cost of studied motor.

Figure 3-11 shows the flux distribution of the best designed model, it is seen that there is only few regions saturated in the rotor core and stator tooth tips, most of the lamination sheets are well used to improve power density of the machine.

3.4.3 Final Design Considering Manufacturing Constraints

The design of the ferrite IPM machine optimised by PSO method in the last section, as shown in Figure 3-12(a), is in ideal conditions to achieve the best performance within the outer diameters limitations without considerations of mechanical robustness, assembling process and manufacture ability. Therefore, the final prototype of the machine will be slightly different and a few

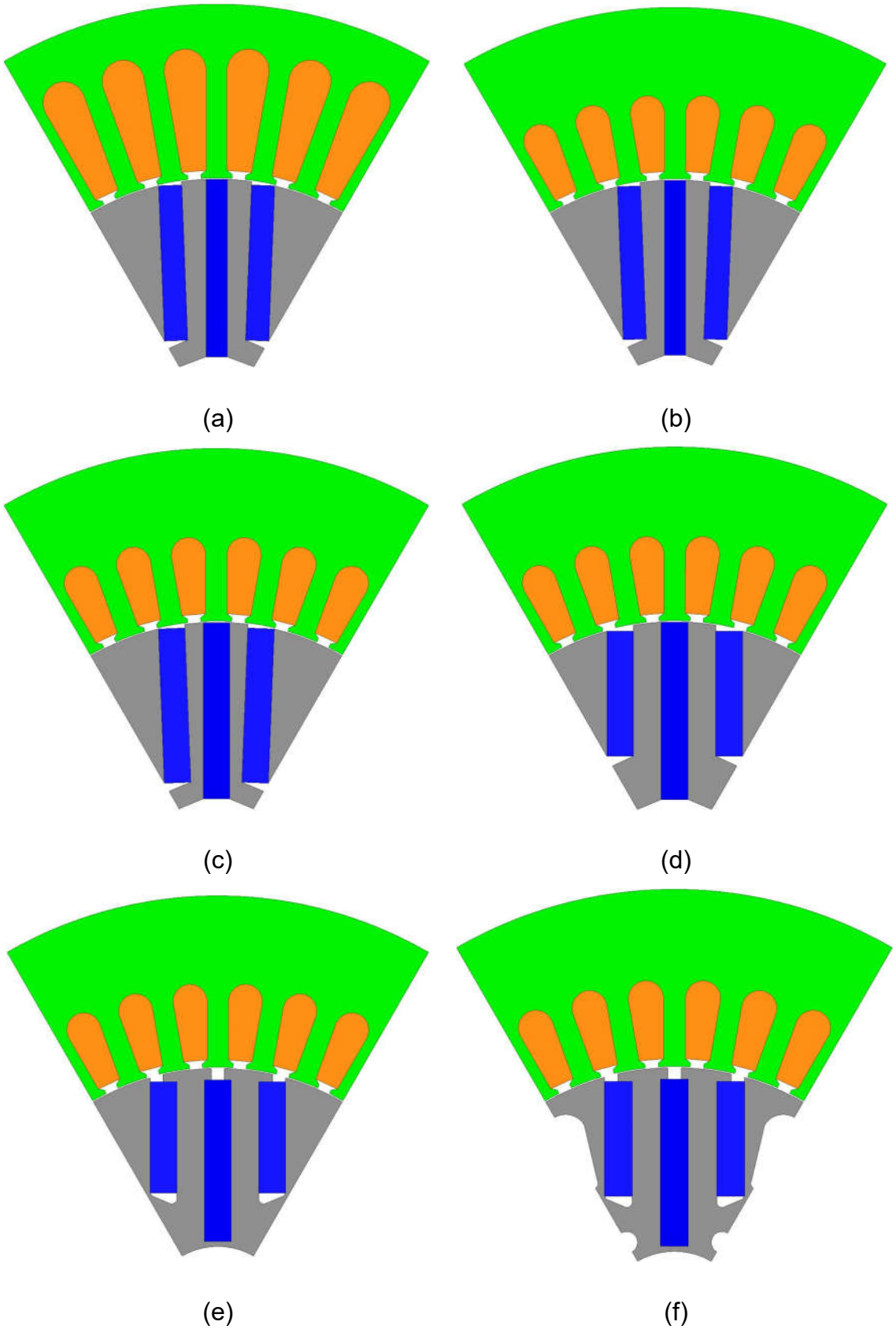

Figure 3-12 The design evolution of the ferrite IPM machine

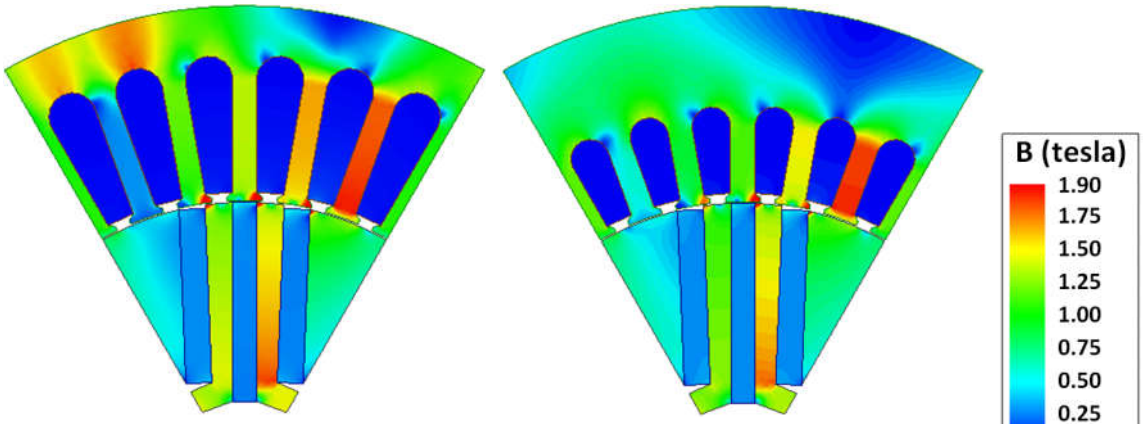

(a) Long slot depth (b) Short slot depth

Figure 3-13 Flux density comparison of stator iron core

compromises have to be made based on the original electromagnetic design to make it easier for fabricating and assembling, and strong enough to withstand vibrations and shocks from the machine itself and outside operating environment.

- **The iron core of stator**

The optimisation of the machine was based on that the heat radiation condition is constant, i.e. the copper loss is unchanged, and so that the input current was increased when the cross-section area of the copper winding was enlarged as the copper resistance is inversely proportional to the cross-section area of the copper. Since the objective function of the machine optimisation is the maximum value of output torque, the optimal design that generates max torque has relative large input current through the copper windings. As a result, the cross-section of the copper is relatively large. As seen in Figure 3-13(a), some of the outer area of stator core is saturated, and, more importantly, the outer circumference area of stator core is not thick enough to withstand serious impact from harsh working environment. Since the outer diameter is given, the stator slot area is reduced to give more space for stator yoke thickness, and Figure 3-12(b) is the modified motor model. Figure 3-13 (b) also shows that the modified model with much less flux saturated area.

- **The size of magnets**

The widths of the ferrite PM bars in the optimal design are different, seen Figure 3-12 (a), which are 3.98 mm and 4.33 mm respectively. Because ferrite material is hard and brittle, thicker magnets are able to withstand larger impact from working environment. And thick magnets can effectively prevent the demagnetisation of the PMs. In addition, in order to reduce the cost of magnet fabrication, the widths of the magnets are better to be same. Considering all reasons above, the widths of all the magnets are set to be 5mm, the modified motor model is shown in Figure 3-12 (c),

- **The position of magnets**

The IPM machine has wide speed range, and the maximum speed is about 6000 rpm that is four times of base speed. Considering the mechanical strength of the rotor, the barriers between magnets should be thick enough to withhold strong acting fore on the magnets when the machine are running in high speed or output larger torque. As the angle between the central primary magnet and its adjacent secondary magnet is not significant, for manufacturing convenience, the magnet bars are determined to be laid parallel between each other. The magnets are adjusted to new positions as shown in seen Figure 3-12 (d).

- **Connection ribs**

It is noticed that the iron core of the rotor in the ideal optimal design is divided in several parts, not connected together, seen in Figure 3-12(a). Some ribs and semi-ribs are added to the rotor core to make it a complete integrity and hold the magnets in the right place from being threw apart by the strong centrifugal forces when it is rotating in high speed. The new design is illustrated in Figure 3-12 (e), where the PM bars are truncated to satisfy the mechanical restricts.

- **Assembly and weight reduction**

In order to reduce the overall mass of the machine and enhance agility of the rotor, some holes are punched in the rotor lamination. As shown in Rotor flux distribution comparison under rated load Figure 3-14 (a), the flux density of the rotor area between the secondary PMs is quite low, even under rated load most of the area is still less than 0.5 T. That means the permeability in these areas is

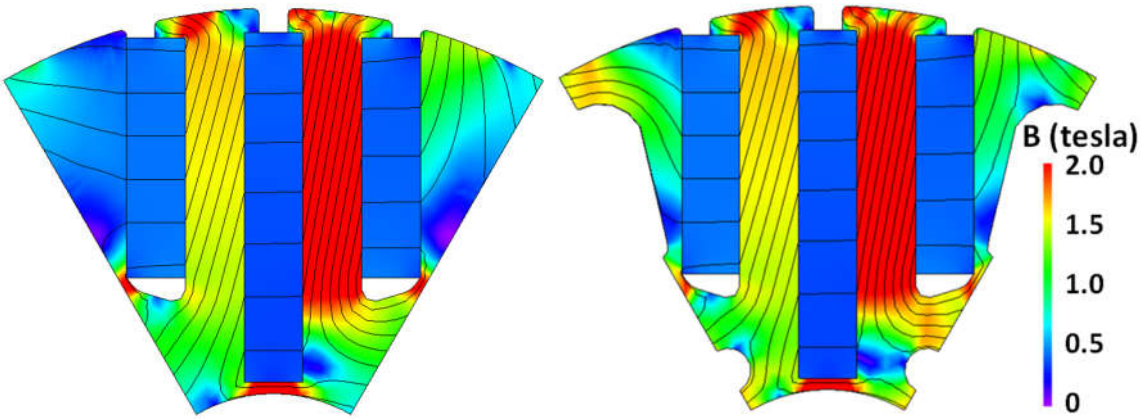

(a) Rotor without cut-outs (b) Rotor with cut-outs

Figure 3-14 Rotor flux distribution comparison under rated load

relatively high, and even with a considerable part removed, as shown in Figure 3-14 (b), no noticeable influence will be imposed on the overall flux distribution. The result shows that no saturation is caused by the cut-outs, and the FEA simulation confirms that torque output is not affected at all. In addition, the laminations of the rotor core are fastened by the bolts that go through the holes. Thus the final design of motor prototype is shown in Figure 3-12(f). Its detailed drawings are attached in Appendix B.1.

Table 3-9 The performance of the final design

Performance Index	Value
Maximum Torque (Nm)	14.09
P-P Cogging Torque (Nm)	1.63
P-P Torque Ripple (Nm)	8.28
Copper Loss (W)	126.75
Core Loss (W)	36.88
Efficiency (%)	93.12
Copper Volume (cm^3)	178.54
Magnet Volume (cm^3)	208.83
Lamination Volume (cm^3)	1276.20

The performance of the final machine design is list in Table 3-9. With the same copper loss, the input current gets smaller when the cross-section area of copper winding decreases and winding resistance increases. So the maximum torque is smaller than that of ideal design in Figure 3-8.

3.5 Comparison with Induction Machine

3.5.1 The Induction Machine Used for Comparison

For the performance evaluation of the proposed machine design, a benchmark is necessary to reveal its advantages. IMs, especially the cage ones, are the most widely machine type in industry due to its low cost and rigid rotor structure. Since one objective of the project is to replace the low efficiency IMs in the vast industrial and domestic market, it is preferable to benchmark a commercial IM with the same housing and stator dimensions.

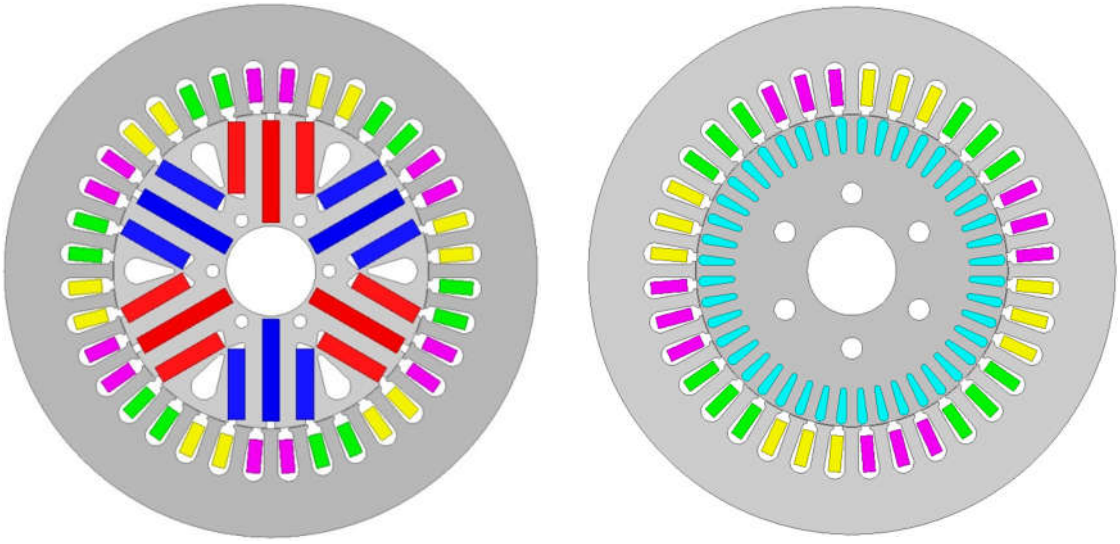

(a) Two-spoke type ferrite IPM (b) IM

Figure 3-15 The 2D model comparison of the ferrite IPM and IM

The cross sections of the proposed two-layer ferrite IPM and a commercial IM models are demonstrated in Figure 3-15. The size and geometry of the stator lamination are exactly identical for the two machines, and the inner and outer diameters of the rotor are also of the same size. Both machines are facilitated by short-pitched single-layer distributed windings. The IPM has 36 slots in the stator and 6 poles in the rotor with two slots per pole per phase, while the IM has 36 slots in the stator and 44 slots in the rotor with 4-pole armature windings. The detailed dimensional specifications are listed in Table 3-10. The number of poles is not the same for the two machines, so the windings distributions are different from each other. The ferrite IPM is equipped with single-layer chain windings, and the IM is facilitated by single-layer cross windings. The material

Table 3-10 Dimensional specifications of the ferrite IPM and IM

Parameters	IPM	IM	Unit
Stator Outer Diameter	160	160	mm
Stator Inner Diameter	95	95	mm
Rotor Outer Diameter	94.5	94.5	mm
Rotor Inner Diameter	27	27	mm
Airgap Length	0.25	0.25	mm
Stacking Length	90	90	mm
Number of Stator Slots	36	36	
Number of Poles	6	4	
Number of Rotor Slots	-	44	
Number of Conductors per Slot	108	100	
Material of Rotor PM/Cage	Ferrite	Aluminium	
Material of Lamination	50W470	50W470	

of lamination are same for the two machines, but the IPM machine has ferrite PMs inserted in the rotor and the IM has aluminium bars die-cast in the rotor. Not to lose generality in the comparison, the maximum electrical loads of the stators are kept the same. Both of the two machines are evaluated by FEA models. Torque capability, power factor and other relevant information can be collected from the FEA simulation. More detailed comparisons are followed.

3.5.2 Performance Comparison with Induction Machine

3.5.2.1 Torque Capability

The torque profiles against armature current are illustrated in Figure 3-16 for both the IPM and IM with MTPA control scheme. The ferrite IPM exhibits much better torque capability than its IM counterpart. Since the excitation field of the IM is generated by armature current, the current is 0.36 pu under no-load condition. For the IPM, the excitation field is mostly produced by the PMs under light and medium loadings, which improves the utilisation of the armature current for torque production purpose. Thus, the no-load current of the IPM is very low, ideally only to overcome the no-load losses. With the increase of armature current, the increment in torque against current is close for the two machines. As the current grow higher, though the PM excited field abates owing

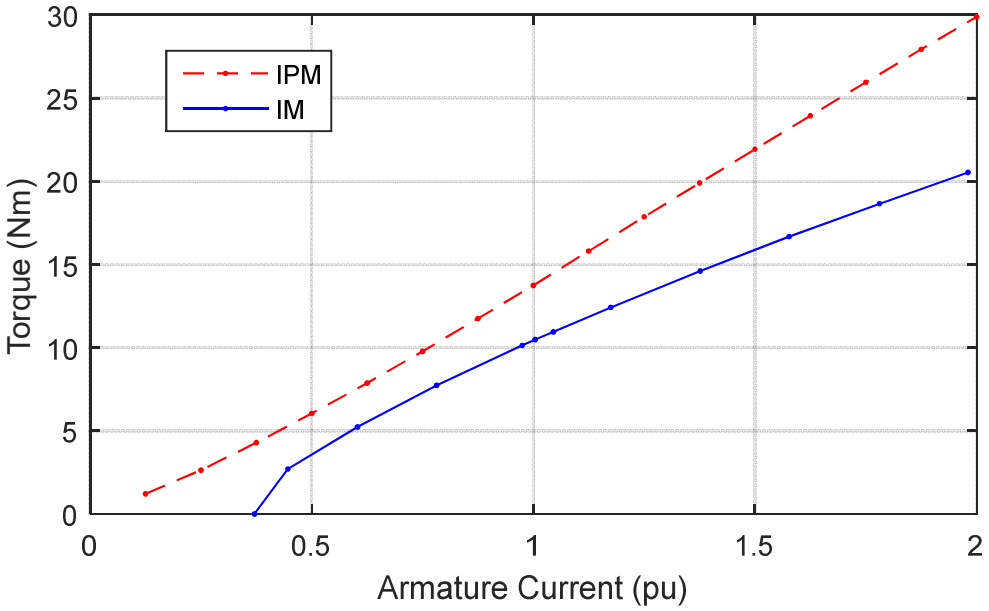

Figure 3-16 Comparison of average torque between IPM and IM

to the saturation, the reluctance torque increases and dominates under heavy and over load conditions, which would help to further increase the torque ability of the IPM. On the other hand, the current in the squirrel cage increases dramatically with the load for the IM due to larger rotor slip, which consumes part of the input power and places a negative influence on the torque increment under overload conditions. Thus, the ferrite IPM has a much better torque profile. At rated current, the torque output of the IPM is 1.27 times that of the IM, which means 27% higher torque and power density is achieved with the same electric loading. And the IPM exhibits even more remarkable advantages over the IM under overload conditions.

3.5.2.2 Torque-Speed and Torque-Power Curve

Figure 3-17 (a) depicts the torque-speed characteristics of the IPM and IM at rated current under MTPA control strategy. Since the torque capability of the ferrite PM has been improved greatly, much higher torque can be delivered within the rated base speed range comparing to the IM. But under flux weakening operation, the torque output of the IPM reduces faster with speed. Hence, the torque difference between the two machines becomes smaller and the torque delivered by the IM eventually exceeds that of ferrite PM when the speed is over 4500 rpm. What's more, the IM has a wider operational speed

range of over 6000 rpm, while the induced voltage of the ferrite PM exceeds that of power supply at the speed of 5400 rpm. For the performance evaluation of the proposed machine design, a benchmark is necessary to reveal its advantages.

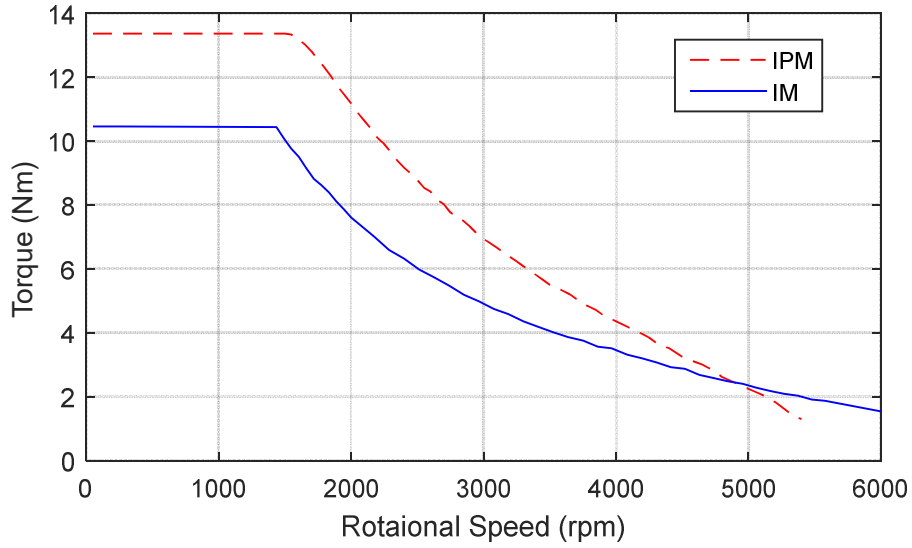

(a) Torque-speed curves

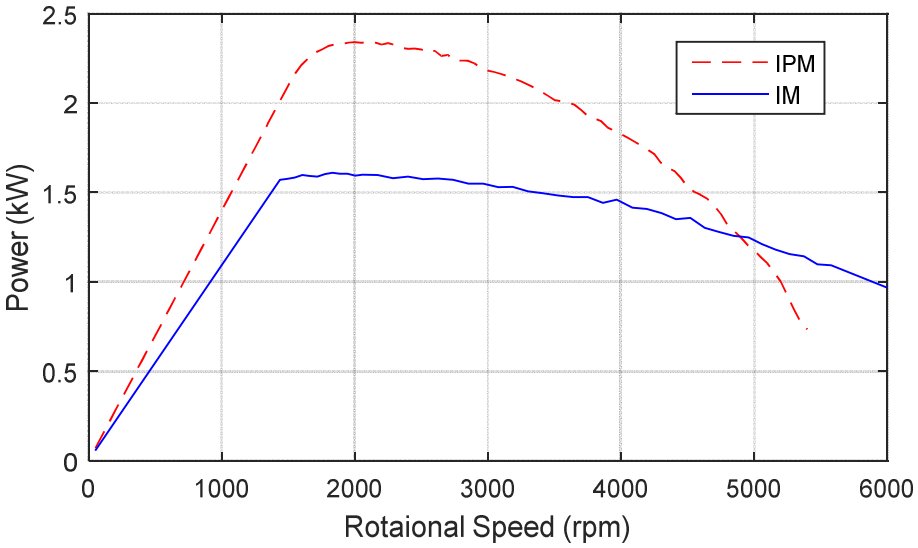

(b) Power-speed curves

Figure 3-17 Torque-speed and power-speed characteristics of the IPM and IM

The power-speed curves of the ferrite PM and IM are illustrated in Figure 3-17 (b). With rated current, the ferrite PM machine is able to deliver 2.1 kW at rated speed and 2.3 kW at 2000 rpm. Then the output power reduces with speed, and drops below 2.1 kW when the speed exceeds 3100 rpm. The IM achieves 1.5

kW at rated speed and 1.6 kW at 1600 rpm, and its constant power speed range (CPSR) of the IM reaches 3500 rpm. Due to the better flux weakening performance, the power of the IM drops much slower than the IPM. The IM delivers 1.1 kW power at 5400 rpm and nearly 1 kW at the speed of 6000 rpm. Because the excitation field of IMs is generated by armature current, it can be directly adjusted by controlling the reactive current. Thus better flux weakening performances and wider operational speed range can be achieved for the IM. For PM machines, the exciting field is mainly provided by PMs, which is not adjustable since the PMs are pre-magnetised. To operate over the rated base speed, flux weakening control strategy is applied to generate armature reactive field opposing the PM magnetisation for weakened excitation. The flux weakening performance depends on the ratio of the product of current amplitude I_m and d-axis inductance L_d over PM flux linkage Ψ_f. According to d-axis magnetizing inductance derivation, L_d is greatly influenced by the width of PMs and reduces with PM width. Besides, wider PMs will enhance PM flux field and thus Ψ_f. Hence, the flux weakening performance deteriorates dramatically with the increase of PM width. However, the design of spoke-type machines requires certain PM width for sufficient PM excitation and rotor saliency to achieved high torque density, which inevitably leads to relatively small L_d and inferior flux weakening ability.

3.5.2.3 Power Factor

Power factor is an important index for electric machines especially in inverter-fed variable speed systems. High power factor can reduce the power rating of the inverter and thus reduces the cost for power electronics since lower apparent power and current can be achieved.

The IPM achieves relatively high power factor from low to medium speed range owing to PM excitation, as illustrated in Figure 3-18. Its power factor decreases slightly with the increase of torque load when below rated speed, because higher current generates higher armature reactive field which increases the leading phase angle of the armature voltage vector. When the speed is over the rated, larger advanced current angle is required for flux weakening, and the

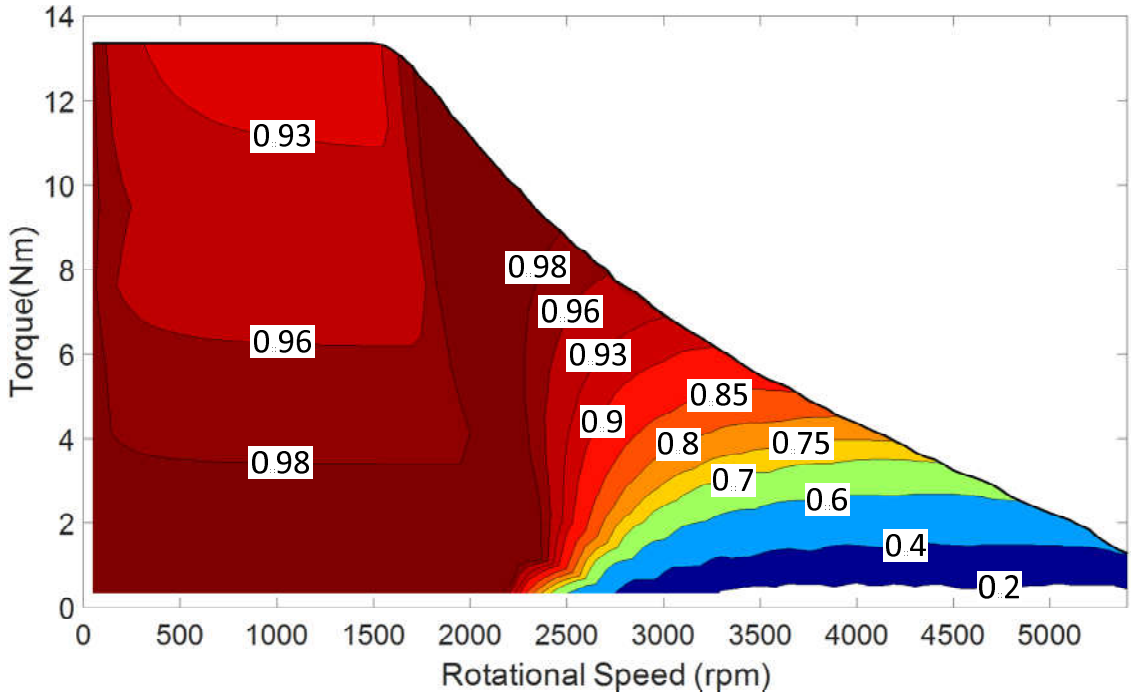

Figure 3-18 Power factor map of the IPM

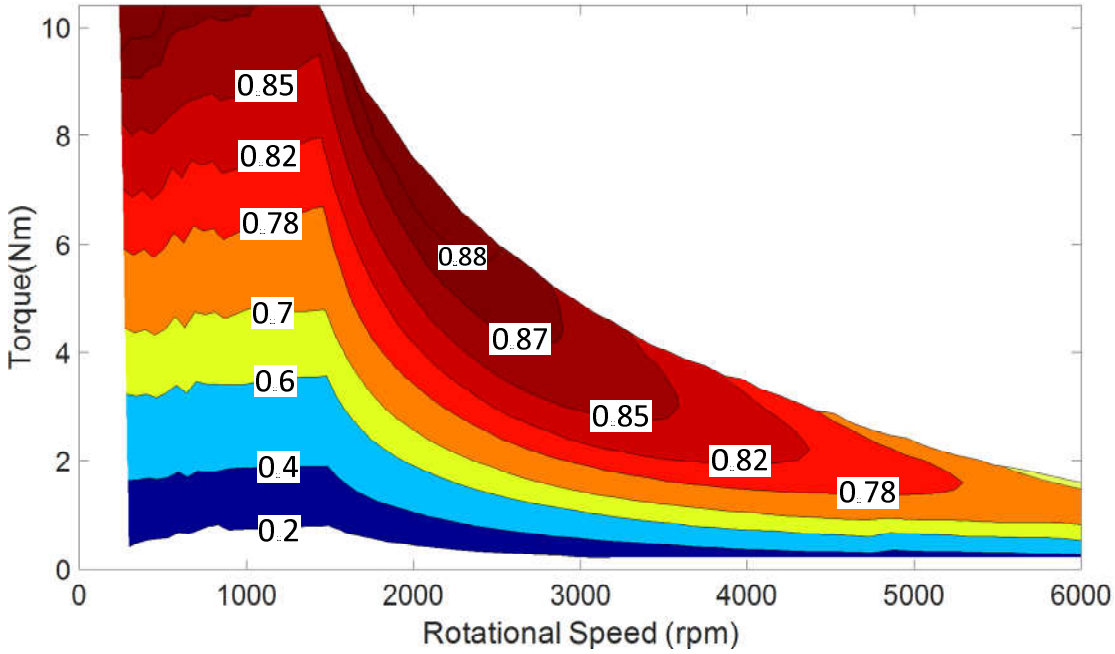

Figure 3-19 Power factor map of the IM

power factor increases as the phase angle difference between winding voltage and current reduces. When entering the high speed sub-region, even larger current angle is necessary. This makes power factor change from lagging to leading, and decreases dramatically with speed.

The power factor map of the IM is depicted in Figure 3-19. Due to the inherent disadvantage of the IM, it has a much lower power factor when below rated speed. The power factor is extremely low under no-load or light load because of its indispensable magnetizing current, even though the active power is very low. With the increase of loading, the active power rises and so does the power factor. The IM only shows its advantage over the IPM during high speed range, when the excitation current is reduced.

3.5.3 Material Cost Comparison with Induction Machine

The financial cost and overall weight of the motor is also very important from the market perspective. The main materials of electric machines include silicon steel lamination, copper wires, ferrite PMs, and aluminium. The volumes and densities of these materials can be collected from the FEA models of the two machines. Then the masses of these used materials are calculated, and they are listed in Table 3-11. The total weight of the two motors is approximately the same, since the same stator lamination, shaft, rotor dimension, and housing assembly are used. The IM has slightly heavier rotor lamination as the IPM motor uses large amount of ferrite material in the rotor. And because the mass density of ferrite is lower than silicon steel, the overall weight of the IPM is marginally smaller.

Table 3-11 Material costs of the ferrite IPM and IM

	IPM	IM	Unit
PM/Aluminium Mass	1.0	0.5	kg
Copper Mass	2.1	2.1	kg
Lamination Mass	10.0	10.7	kg
Total Mass	13.1	13.2	kg
PM/Aluminium Cost	8.0	2.0	£
Copper Cost	14.7	14.7	£
Lamination Cost	20.0	21.4	£
Total Cost	42.7	37.1	£
Output Power	2.8	2.0	hp
Cost per Horsepower	15.1	18.5	£/hp

The material cost estimation is based on the UK market price in [192]. And the costs of each material used in the IPM and IM machines are calculated and listed in Table 3-11. The costs of motor cores and stator windings are almost the same due to the similar material usage. The difference is reflected in the rotor. The IM rotor contains only die-casted aluminium bars besides lamination core, making IM rotor one of the cheapest structures in electric machines. Although highly expensive rare-earth PM materials are excluded for the IPM, the considerable amount ferrite used still costs more than the IM rotor. Therefore, the overall cost of the PM motor is 15% higher. However, the ferrite IPM machine can obviously deliver much higher torque density. If the power output is taken into consideration, the cost per horsepower of the IPM is about 18% lower than the IM, which makes the two-layer ferrite IPM much more attractive for various applications.

3.6 Summary

This chapter proposed an efficient and accurate method to design a low-cost electric machine. The studied two-layer spoke type ferrite IPM machine having six geometrical parameters to be determined, as the parameters are coupled with each other, it is very difficult to design it by the most common “trial and error” method. The PSO method is good at multi-parameter optimisation, which can be used for electric machine design. Firstly, the terminologies, implementation process, and different variants of PSO are introduced in the chapter. Then according to the characteristics of the study case, the PSO method is applied on the IPM motor design. In order to improve computation efficiency and save data processing time, the whole process of machine optimisation by PSO method is programmed in VBScript language. The optimal design will obtained automatically without any more interference during the process. With the convenient design approach, the PSO methods with different setup parameters are evaluated, such as different inertial weights, scaling factors, *Vmax*, and boundary conditions. With considerations of manufacturing constraints, the final design is adjusted on basis of the optimal motor model optimised by PSO. The structure, cost, and performance of the final design

machine are compared with IM that is used as benchmark to evaluate the proposed machine design. The ferrite IPM has better torque capability and larger output torque, power, and power factor in most of the speed range.

The ferrite PM machines, offering the advantages of PM machines but with cheap magnet materials, are able to fill the requirements of low cost and high efficiency. By using PM excitation and salient rotor structure, higher efficiency, torque density and power factor can be achieved for the proposed ferrite IPM motor. Furthermore, due to the increasing mandatory efficiency standards to be implemented, the proposed ferrite machine will become more and more competitive in near future, and has a huge potential market in both industrial and domestic applications.

4. QUALITY CONTROL OF THE PROPOSED MACHINE

Quality control of electric machine in manufacturing process is of importance to maintain its performance and reduce its overall cost. So this chapter discusses how to control the quality of the studied ferrite IPM machine in mass production.

4.1 Introduction of Quality Control and Six Sigma Method

4.1.1 Quality Control Approaches

There are a multitude of pieces that have to be put together to create a safe and efficient machine, and there are many steps set in place to transform assorted parts into an assembled entity in a production line. This process does not always go according to plan, but failure can be prevented through effective quality control in manufacturing. The goal of implementing manufacturing quality control is to conform to industry, company and consumer expectations, and produce products that are of sound quality while minimising costs and maximising efficiency.

When customers receive high-quality defect-free products, manufacturers will benefit from using quality control in manufacturing:

- Increase customer loyalty
- Gain repeat business
- Gain new customers from referrals
- Maintain or improve the position in the market
- Improve safety
- Reduce liability risks
- Contribute to overall positive branding of your product

Manufacturers with quality control procedures in place are far less likely to face product recalls or place customers at risk from poorly made products. The cost associated with these recalls can be steep. Considering all benefits mentioned above, it is necessary to apply quality control procedures on the studied ferrite IPM machine to maintain its performance and reduce overall cost.

Quality control via the use of statistical methods is a very large area of study, and it is central to success in modern industry with its emphasis on reducing costs while improving quality. In recent times, the Japanese have been extremely successful at applying statistical methods to industrial quality control, and they have gained a significant advantage over many of their competitors. Because of the global nature of modern industrial competition, quality control, or more precisely, statistical quality control has become an area of central importance to engineers[193,194].

Quality control is important for motor manufacturing and there are several popular approaches, such as Statistical Process Control (SPC), Total Quality Management (TQM), Lean manufacturing, and Six Sigma.

- SPC is a method of quality control which employs statistical methods to monitor and control a process. The advantage of SPC is that it emphasizes early detection and prevention of problems, rather than the correction of problems after they have occurred [195,196]. But the implementation of SPC is a costly endeavour, and it takes time to rigorously in a manufacturing setting as it requires more observations [196].
- TQM consists of organisation-wide efforts to install and make permanent a climate in which an organisation continuously improves its ability to deliver high-quality products and services to customers [193,197]. But TQM ignores the artificiality and thus arbitrariness of the difference between structure and process. And the complexity of management cannot be reduced to standardized (mathematical) procedures [198].
- Lean manufacturing is a systematic method for waste minimisation within a manufacturing system without sacrificing productivity[199]. It is good at waste management, making obvious what adds value and reducing everything else that is not adding value. But this approach needs adequate management to avoid failed implementation of lean methodologies, and it often looks good to the manager but fail to improve the situation [200].
- Six Sigma seeks to improve the product quality by identifying and removing the causes of defects and minimizing variability in manufacturing process. It

considers the entire process behind the product rather than just the final outcome. It is proactive rather than reactive [201]. However, because Six Sigma is applied to all aspects of the production and planning process, it may create rigidity and bureaucracy that can create delays and stifle creativity [202].

For the study of the thesis, Six Sigma approach is more suitable for the quality control of electric machines, and the details of Six Sigma are introduced in the following section 4.1.2.

4.1.2 Six Sigma Method

Six Sigma (6σ) is a disciplined, statistical-based approach to eliminate defects in a product, process or service, including a set of techniques and tools for process improvement. It was introduced by engineers Bill Smith & Mikel J Harry while working at Motorola in 1986. Jack Welch made it central to his business strategy at General Electric in 1995 [203]. And now hundreds of companies around the world have adopted Six Sigma as a way of quality control. The term Six Sigma (capitalised because it was written that way when registered as a Motorola trademark on December 28, 1993) originated from terminology associated with statistical modelling of manufacturing processes.

Sigma represents the population standard deviation, which is a measure of the variation in a data set collected about the process. If a defect is defined by specification limits separating the good from bad outcomes of a process, then a six sigma process has a process mean (average) that is six standard deviations from the nearest specification limit [204]. This provides enough buffers between the process natural variation and specification limits, as shown in Figure 4-1. For example, if a product must have a thickness between 10.32 and 10.38 centimetres to meet customer requirements, then the process mean should be around 10.35, with a standard deviation less than 0.005 (10.38 would be 6 standard deviations away from 10.35).

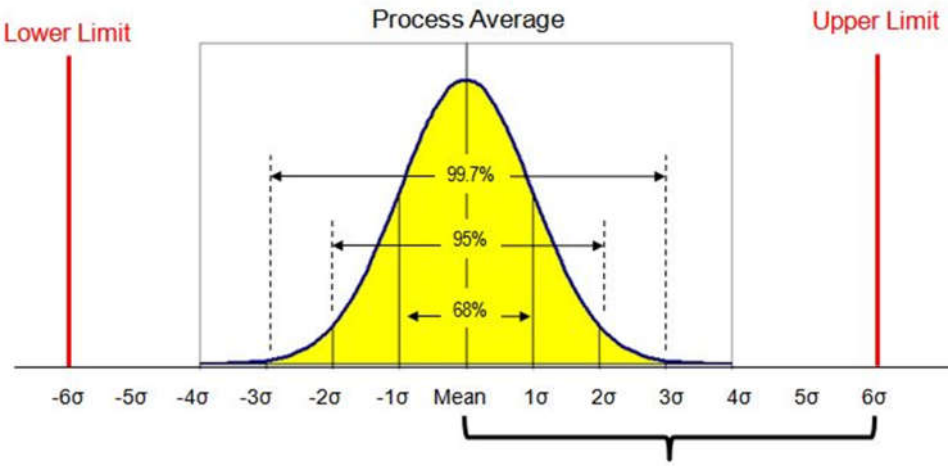

Figure 4-1 Six sigma deviations in normal distribution

Six Sigma, a systematic approach for eliminating errors, uses statistical methods to improve quality by minimising variability in business processes, from manufacturing to engineering and purchasing. Six Sigma accomplishes its goal by using two Six Sigma Methods: DMAIC and DMADV [201]:

The Six Sigma DMAIC approach is typically used to improve an existing process. DMAIC is an acronym that stands for:

- Define the problem and desired outcome
- Measure the ability of the process
- Analyse the data and identify the root cause of variations (defects)
- Improve or modify the process so that fewer variations (defects) are produced
- Control the process. Prevent and correct variations before they result in defects

When designing a new process, the Six Sigma DMADV is used. It is also known as DFSS (Design for Six Sigma). The DMADV acronym stands for:

- Define design standards that align with the product or process goals
- Measure and identify characteristics of the product or process that are critical to quality
- Analyse the data, and identify possible sources of defects
- Design changes that will eliminate the source of defects or errors

- Verify that the design will meet the requirements

The electric machine manufacturing is a complicated process from various assorted raw materials to a well-functioned machine. At the motor design stage, the Six Sigma DMADV approach is more suitable for us to identify the problem and improve the quality of the motor.

4.2 Motor Quality Control by Six Sigma DMADV Method

4.2.1 The Studied Machine for Quality Control

In mass production of electric machines, the consistency of machine performance is an essential criterion to evaluate its quality. Thus minimising the variation of machine performance is of great importance to improve its quality. For example, the variance of output torque and efficiency of electric machine should be limited in an acceptable range. However, there are many factors affecting the ultimate performance of the machine in the manufacturing process, such as material consistency, machining accuracy, and assembling accuracy.

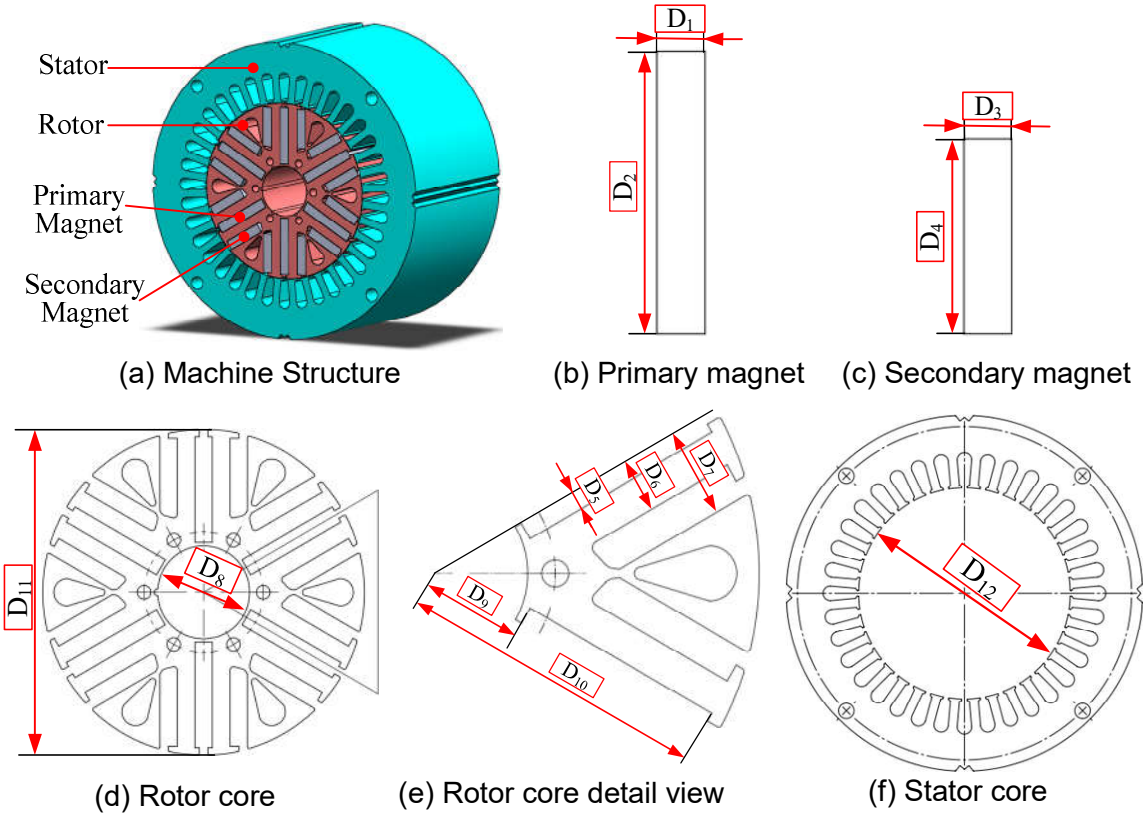

(a) Machine Structure (b) Primary magnet (c) Secondary magnet

(d) Rotor core (e) Rotor core detail view (f) Stator core

Figure 4-2 Essential dimensions of the studied machine

Table 4-1 Dimensions and tolerances of the machine

Dimension		Tolerance	
Symbol	Value (mm)	Symbol	Allowable Range (mm)
D_1	$5.10^{0}_{-T_1}$	T_1	0.01~0.20
D_2	$30.60^{0}_{-T_2}$	T_2	0.02~0.40
D_3	$5.10^{0}_{-T_3}$	T_3	0.01~0.20
D_4	$21.00^{0}_{-T_4}$	T_4	0.02~0.40
D_5	$2.55^{+T_5}_{0}$	T_5	0.02~0.10
D_6	$7.75^{0}_{-T_6}$	T_6	0.025~0.10
D_7	$12.85^{+T_7}_{0}$	T_7	0.03~0.10
D_8	$27.00^{+T_8}_{0}$	T_8	0.035~0.04
D_9	$14.50^{0}_{-T_9}$	T_9	0.03~0.20
D_{10}	$45.10^{+T_{10}}_{0}$	T_{10}	0.04~0.20
D_{11}	$94.50^{0}_{-T_{11}}$	T_{11}	0.055~0.20
D_{12}	$95.00^{+T_{12}}_{0}$	T_{12}	0.055~0.20

In this study, only the machining accuracy is taken into consideration, as it is controllable in design stage and suitable for academic research. And the other factors are assumed ideal and constant. Once the materials and topology of the motor is given, the performance of the motor was generally determined by its physical geometry. In order to minimise the variability of the motor performance, it is essential to control the geometrical tolerance of each dimension. Of course, the smaller the tolerance is, the more consistent performance the motor implements. But the requirement of high accuracy will increase the manufacturing cost [123,205,206]. Therefore, it is better to firstly sequence all the studied tolerances by their significance to motor performance, and then adjust the most significant tolerances. So that will reduce the variation of motor performance without much rise of manufacturing cost.

As shown in Figure 4-2 (a), the two-layer spoke type ferrite IPM motor is designed in the last chapter. It has 36 slots in the stator and three pole-pairs in the rotor. One central primary magnet and two adjacent secondary magnets constitute one rotor pole. Twelve dimensions are selected as the essential dimensions to the motor performance, and they are numbered from D_1 to D_{12} *and* illustrated in Figure 4-2 (b)-(f). D_5–D_{12} are dimensions of stator and rotor

lamination cores that are made by steel sheets. In mass production the steel sheets are cut by stamping press and the machining cost is relatively low, thus the tolerances of these dimensions are preferable to be adjusted first. Since the machining accuracy of the steel sheet fabrication is mainly determined by the accuracy of its stamping mould, the increased cost of manufacturing high-accuracy mould should be considered as well. D_1–D_4 are the dimensions of ferrite magnets that are cast in shape and then ground to final dimension. Their tolerances can be very fine but this will increase the manufacturing cost, so they are the last option to be reduced. Table 4-1 shows all the definition of the twelve dimensions and their corresponding tolerances that are numbered T_1–T_{12}. The allowable ranges of the tolerances are determined by manufacturing process and dimension size [187]. If the tolerance is lower than the allowed minimum value, the machining cost will be substantially increased, thus the tolerance is not suggested to be smaller than the minimum value. These numbered tolerances T_1–T_{12} will be used in the following quality control of the electric machine.

4.2.2 Implement of Six Sigma DMADV by Conventional Method

In order to systematically analyse the issue of geometric tolerances and quality variation, the methodology of Six Sigma DMADV is applied as following.

1. Define design standards that align with the product or process goals

In mass production of electric machines, the consistency of machine performance is a criterion to evaluate their quality. The quality of end products is improved by minimising the variation of machine performance. According to the rule of thumb, the design standards are defined as that the variation of the motor's output torque and efficiency cannot be more than 2% [207,208]. So the objective is to limit the variance of output torque and efficiency of the designed motor to 2% or less.

2. Measure and identify characteristics of the product or process that are critical to quality

The real quality of motors and drives in mass production highly depends on the available machinery technology and those unavoidable variations or uncertainties in the manufacturing process, assembly process and operation environment. In the design stage, only the machining accuracy is considered and other factors are assumed ideal and constant. As the performance of the motor was generally determined by its physical geometry, the variation of torque and efficiency comes from the variation of geometrical dimensions, and the tolerances are the critical factors to motor quality.

3. Analyse the data, and identify possible sources of defects

Controlling the tolerance of each dimension is the key to control motor quality. Smaller tolerance will increase the consistency of motor performance, but the manufacturing cost will increase as well. Therefore, selecting and minimising the significant tolerances will reduce the variation of motor performance without much rise of manufacturing cost. For example, the tolerances of rotor outer diameter and stator inner diameter will change the size of air gap and then affect the magnetic reluctance. The tolerances of magnet dimensions will change the size of ferrite magnets and then affect the magnetic field intensity.

4. Design changes that will eliminate the source of defects or errors

The motor quality is improved by minimising the geometric tolerances in the manufacturing stage. Small tolerance reduces variation but it will largely increase the manufacturing cost. Therefore, the necessary tolerances are firstly sequenced by their significances to motor performance, and then the adjustments of the tolerances are started from the most significant one. So the optimal tolerance combination can be achieved with relatively low cost.

5. Verify that the design will meet the requirements

The optimal tolerances of the designed motor will be verified by FEA software. The verification of quality variability demands a large amount of motor samples. The most feasible way is to verify the design by computer simulation. When the motor is in mass production, further verification by actual motor samples is necessary. Tolerance Evaluation by One Factor at a Time Method

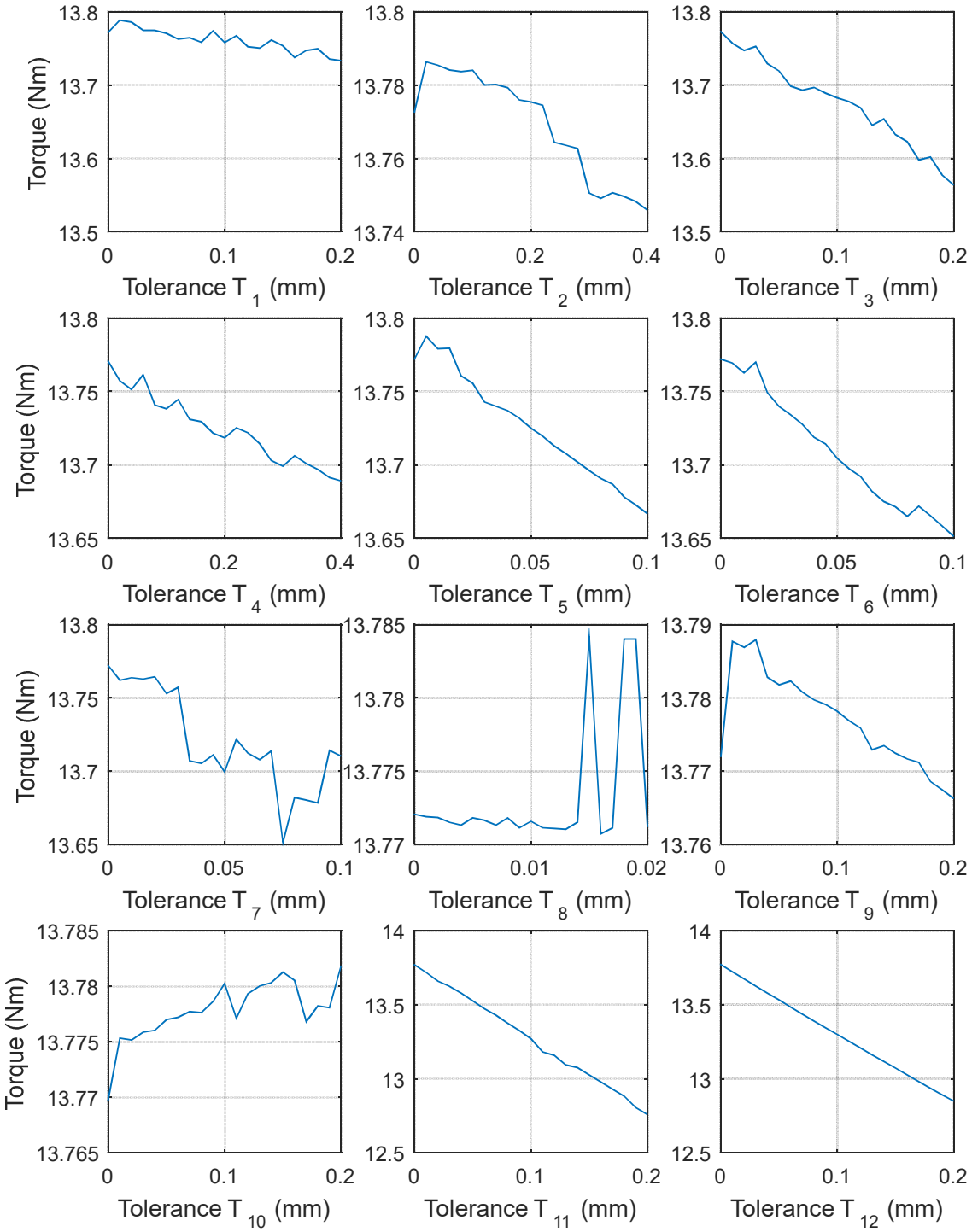

Figure 4-3 Relationship between output torque and each tolerance when other tolerances are unchanged

In the studied machine, there are 12 tolerances, and how to evaluate them and select significant ones is a critical issue. The most common method is “trial and error” or “one factor at a time (OFAT)” method, only evaluating one factor at each time and keeping others unchanged. Figure 4-3 shows the relationship

between output torque and each tolerance, which is obtained by OFAT method. From the twelve subplots it is seen that the significance of each tolerance to output torque is different, and T_{11}, T_{12} are the most significant tolerances inversely proportional with output torque. T_1—T_6 have same trend as T_{11}, T_{12} but their significance is much lower. T_8–T_{10} almost have no influence on the output torque. T_7 has effect on torque but the trend is not unidirectional. The significance of the twelve tolerances to output torque is roughly sequenced as $T_{11}>T_{12}>T_3>T_7>T_6>T_5>T_4>T_1>T_2>T_9>T_{10}>T_8$. So the maximum output torque can be obtained by reducing all the inverse proportional tolerances to the lowest (e.g. T_1, T_3, T_4, T_5, T_6, T_{11}, T_{12}) and increasing all the proportional tolerances to the highest (e.g. T_{10}), and similarly the minimum torque can be obtained as well. According to [208], the variation of motor performance can be calculated by Equation (4-1).

$$\text{Variation} = \frac{Max - \frac{Max + Min}{2}}{\frac{Max + Min}{2}} \cdot 100\% \quad \textbf{(4-1)}$$

Where, the *Max* and *Min* are the maximum and minimum values of the performance index. Thus the variation of the output torque is estimated by Equation (4-1). However, as an integration of a machine, the tolerances are coupled and depended with each other, and some of them have combination effects on the output torque or efficiency. The above OFAT method is adept at uncoupled system, but for the coupled dependent system like electric machine it may not exhibit correct features of the studied object. So a method considering all the parameters including their individual and interactive influences simultaneously is desired.

In addition, if all the possible torque responses to the tolerance factors are in need to explore, only taking three values (max, median, min) in each tolerance range, there will be 3^12= 531441 trials to complete the whole evaluation. If each trial takes one minute to finish its FEA simulation, the whole exploration will cost more than a year to complete. Therefore a more efficient method is necessary to realise quality control of electric machine.

4.3 DOE Assisted Six Sigma DMADV Quality Control Method

4.3.1 Introduction of DOE and Optimality Designs

Design of experiment (DOE) is a practical and ubiquitous approach for exploring multifactor opportunity spaces. In the experimental research, the determination of sampling groups plays a very important part, which affects the accuracy of prediction and the total cost of experiments. The statistical DOE is an efficient procedure for planning experiments so that the data obtained can be analysed to yield valid and objective conclusions. Due to its advantage of efficient and effective information gathering, DOE is adopted in many applications [209–211]. DOE begins with determining the objectives of an experiment and selecting the process factors for the study. An Experimental Design is the laying out of a detailed experimental plan in advance of doing the experiment. Well-chosen experimental designs maximise the amount of "information" that can be obtained for a given amount of experimental effort [209,212]. In addition, all of this is carried out under the constraint of a minimal expenditure of engineering runs, time, and money.

There are four general engineering problem areas in which DOE applies: Comparative, Screening, Modelling, and Optimising[213]. And obtaining good results from a DOE involves these seven steps [214]:

- Set objectives
- Select process variables
- Select an experimental design
- Execute the design
- Check that the data are consistent with the experimental assumptions
- Analyse and interpret the results
- Use/present the results (may lead to further runs or DOE's).

The quality control of motor manufacture is implemented by DOE approach according to the above steps. It is worthwhile to note that planning to do a sequence of small experiments is often better than relying on one big experiment to give you all the answers. An iterative approach is useful and

economical, because it is logical to move through stages of experimentation, each stage providing insight into how the next experiment should be run. Therefore, the process of obtaining optimal combination of geometrical tolerance is divided by several small steps, which is more time-effective and convenient.

The most commonly used designs in industry are the classical designs (full factorial designs, fractional factorial designs, Latin square designs, Box-Behnken designs, Taguchi designs, etc.). They are so extensively used because they are optimal in their own right and have served superbly well in providing efficient insight into the underlying structure of industrial processes. Classical designs have assured degrees of precision, orthogonality, and other optimal properties that are important for the exploratory nature of most experiments [209,210,215]. But in some cases, the tabulated classical designs do not cover a particular practical situation, such as the number of factors and/or the number of levels of some factors intended for use may not be included in tabulations of classical designs. When classical designs are not applicable, optimality designs are a useful option. Optimality designs are generated from a computer algorithm, so they are also referred to as computer-aided designs. Optimality designs are a class of experimental designs that are generated based on a particular optimality criterion. Optimal designs may be optimal in many different ways, and what may be an optimal design according to one criterion may be suboptimal for other criteria[194,216]. D-optimal and I-optimal are the two of the most popular methods in optimality design. D-optimal design minimises the variance-covariance matrix of the factor effect estimates and it is a natural choice to identify which factors are significant [214]. I-optimal minimises the average prediction variance across the entire design region and more precise predictions will be obtained in large portions of the experimental region, so it is a good method to find optimum settings of a process [214].

4.3.2 DOE Assisted Six Sigma DMADV Method

As there are 12 factors in the studied case, the classical DOE designs are not suitable, so optimality design is adopted in the electric machine quality control

process. D-optimality is used to evaluate the significance of each geometrical tolerance to motor performance, so that the tolerances are sequenced by the resultant significances. And then the adjustment of tolerances is started from the most significant one. The motor performance of each combination of tolerances is estimated by I-optimality method that gives more precise predictions. The optimality designs can be implemented by statistical software, such as JMP, Minitab, and SPSS. The DOE assisted Six Sigma DMADV method is clearly illustrated in the flowchart of Figure 4-4.

The five steps of Six Sigma DMADV are highlighted in *italic* font, and specific operations in each step are included in parentheses. The general procedure of DOE assisted Six Sigma DMADV is basically the same as described in 4.2.1.

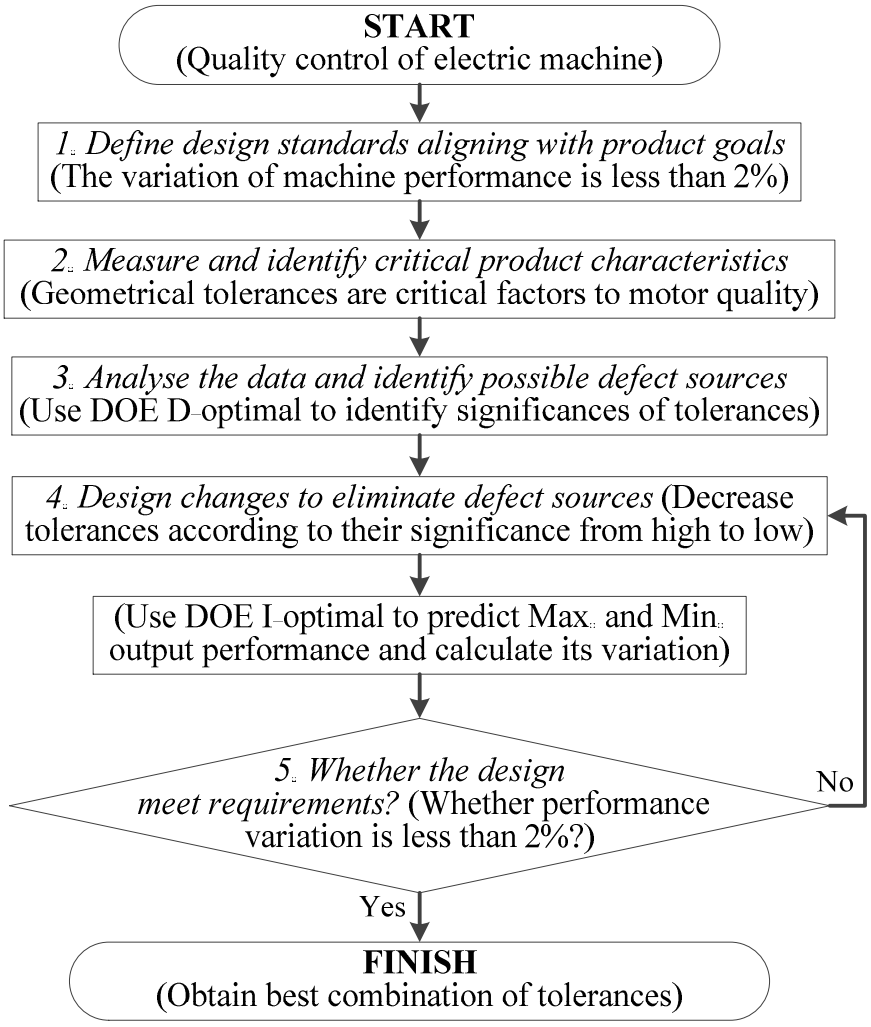

Figure 4-4 Flowchart of DOE assisted Six Sigma DMADV method

In this study, DOE D-optimal is used to identify significance of each tolerance at the 3rd step, and then DOE I-optimal is applied to predict *Max* and *Mini* output performance at the 5th step. Output torque and efficiency are important criteria of motor performance, so they are used as responses in DOE. According to the Six Sigma quality requirement, the aim of the quality control is set to limit the variability of output torque and efficiency less than 2%.

Table 4-2 The initial geometrical tolerances

	T_1	T_2	T_3	T_4	T_5	T_6	T_7	T_8	T_9	T_{10}	T_{11}	T_{12}
Tolerance (mm)	0.2	0.4	0.2	0.4	0.1	0.1	0.1	0.04	0.2	0.2	0.2	0.2

The essential dimensions that are included in the quality process are illustrated in Figure 4-2, and their tolerance varying limits are shown in Table 4-1. The initial set of tolerances is listed in Table 4-2, which are the maximum values in the varying ranges for each parameter. More details of implementing the method on the quality control of electric machine are discussed in the following sections.

4.3.3 Significance of Each Tolerance by DOE D-optimality

Because D-optimality is good at identifying the significances of the factors, the initial set of the 12 tolerances are evaluated by D-optimality to reveal their significances to output torque and efficiency. The DOE table is generated by using D-optimality criterion. 97 trials with different combinations of tolerances are carried out and the detailed result is attached in Appendix C.1. For each motor trial, the corresponding tolerances are input into the FEA, and then the motor model has a new set of dimensions. After the simulation of the trial motor, torque and efficiency can be obtained from the results. All of the 97 trials are implemented one by one, and resultant torque and efficiency are saved in the table of Appendix C.1. At last, the torque and efficiency responses of all the trials are processed by DOE method and the significances of the 12 tolerances are obtained. The torque responses are shown in Figure 4-5 and Figure 4-6, while the efficiency responses are demonstrated in Figure 4-7 and Figure 4-8.

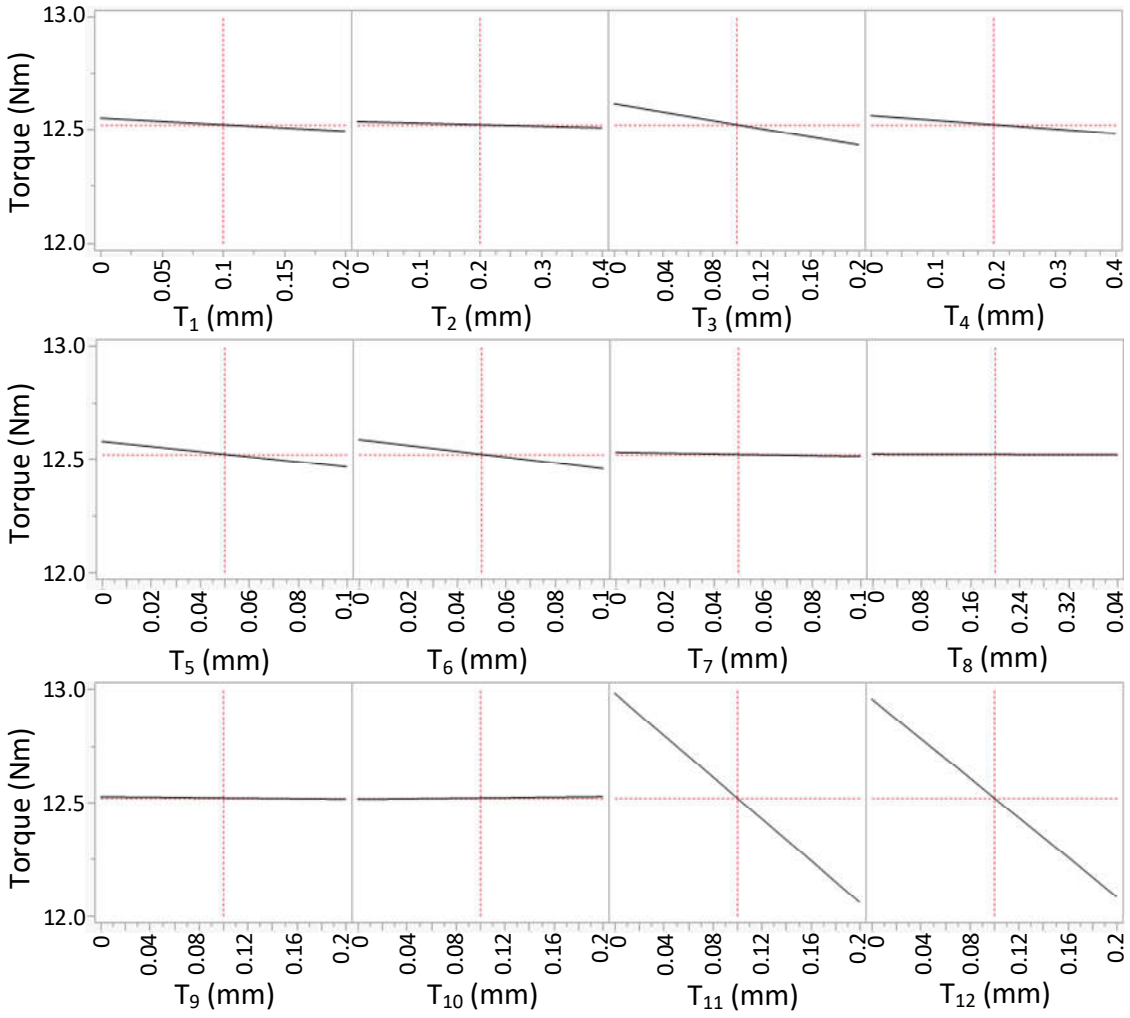

Figure 4-5 Significances of factors to output torque

Source(mm)	LogWorth	PValue
T_{11} (0, 0.2)	105.762	0.00000
T_{12} (0, 0.2)	103.770	0.00000
T_3 (0, 0.2)	48.430	0.00000
T_6 (0, 0.1)	37.325	0.00000
T_5 (0, 0.1)	33.710	0.00000
T_4 (0, 0.4)	23.658	0.00000
T_1 (0, 0.2)	15.180	0.00000
T_2 (0, 0.4)	5.460	0.00000
T_7 (0, 0.1)	3.074	0.00084
T_{10} (0, 0.2)	1.749	0.01784
T_9 (0, 0.2)	1.623	0.02383
T_8 (0, 0.04)	1.112	0.07722

Figure 4-6 PValue and LogWorth of factors to output torque

PValue or probability value is the probability for a given statistical model when the null hypothesis is true, which helps to determine the significance of the results in a statistical hypothesis test [194]. A small *PValue* (typically ≤ 0.05) indicates strong evidence against the null hypothesis, so the null hypothesis is rejected; and a large *PValue* (> 0.05) indicates weak evidence against the null hypothesis, so the null hypothesis is failed to be rejected. When *PValues* are too small to be visualised graphically, the *PValues* are transformed into *LogWorth* [217], which is defined as:

$$LogWorth = -log_{10}^{(PValue)}$$

Thus a smaller *PValue* or a larger *LogWorth* mean the factor is more significant. With the help of *LogWorth* and *p-values*, the significances of the 12 tolerances to torque and efficiency are clearly sequenced in Figure 4-6 and Figure 4-8.

For significances of the tolerances to output torque, shown in Figure 4-6, the tolerances T_{11}, T_{12} are with the highest significance. T_1–T_6 are less significant, and T_7–T_{10} have very less effect on the output torque. The effect of each tolerance to the output torque is also visualised in Figure 4-5. The one with large slope has large influence on output torque. T_{11} and T_{12} are the tolerances of rotor outer diameter and stator inner diameter, and they determine the final the dimension of air gap that directly affect the magnetic resistance and flux density. Thus T_{11} and T_{12} are the most significant tolerances. The dimensions of the magnets directly affect the PM magnetic field, and among the four magnet-related dimensions D_1–D_4 the length of the secondary magnet D_3 has the largest contribution to magnetic field of the motor. Therefore, in the tolerances of magnet-related dimensions T_1–T_4, T_3 has largest influence to output torque. The tolerances T_4–T_6 restrain the air gaps between magnets and stator core, and then the magnetic reluctance is changed as well. Since the dimensions D_5 and D_6 are shorter than D_7, for the same tolerance limit 0.1mm, T_5 and T_6 exhibit higher significance to output torque. As the radial dimensions D_8–D_{10} have fewer effects on output torque, the tolerances T_8–T_{10} have the least significance. Hence the significances of all tolerances are sequenced as $T_{11}>T_{12}>T_3>T_6>T_5>T_4>T_1>T_2>T_7>T_{10}>T_9>T_8$. In contrast with the results

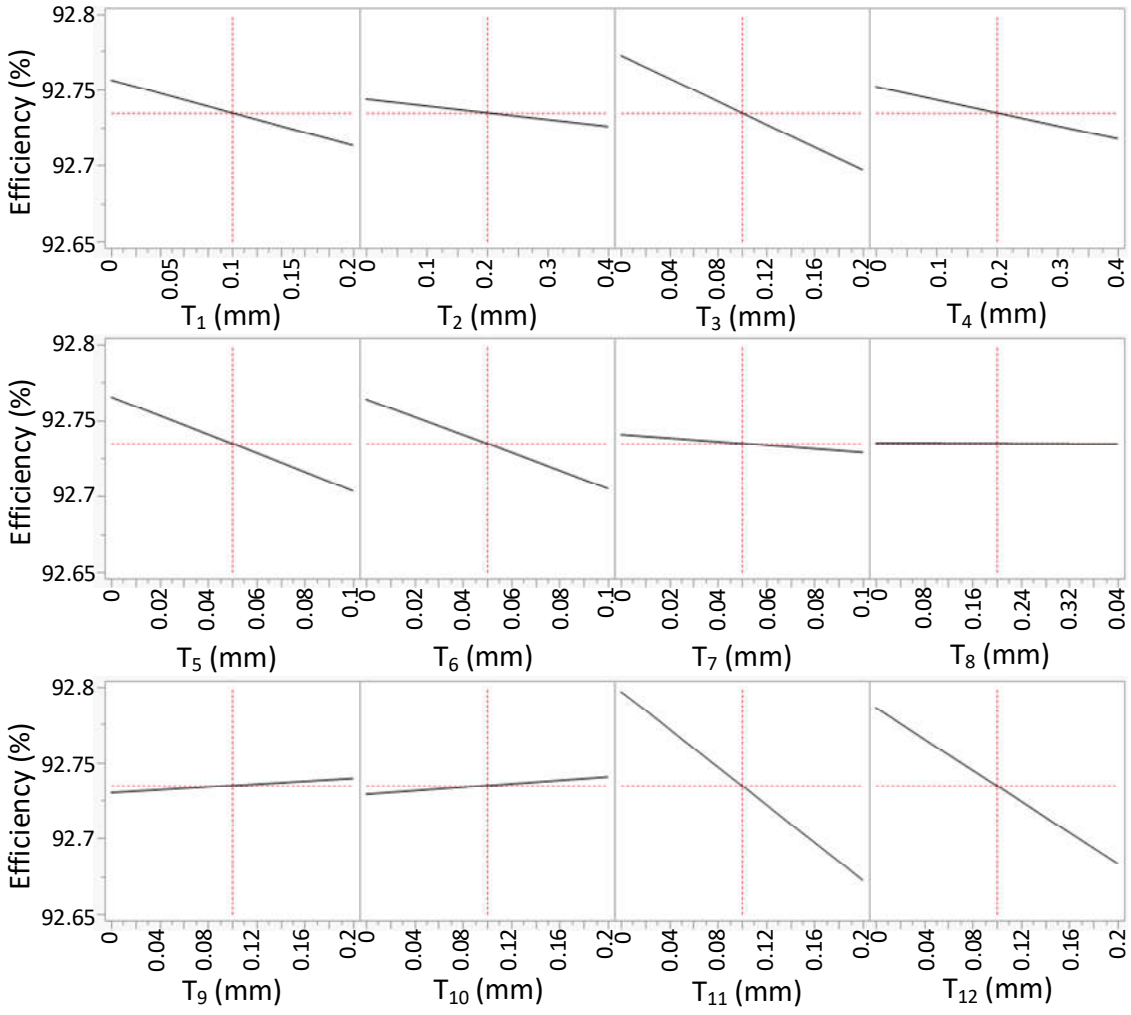

Figure 4-7 Significances of factors to efficiency

Source(mm)	LogWorth	PValue
T_{11} (0, 0.2)	367.524	0.00000
T_{12} (0, 0.2)	308.803	0.00000
T_3 (0, 0.2)	225.421	0.00000
T_5 (0, 0.1)	177.730	0.00000
T_6 (0, 0.1)	164.557	0.00000
T_1 (0, 0.4)	109.536	0.00000
T_4 (0, 0.2)	79.630	0.00000
T_2 (0, 0.4)	28.033	0.00000
T_7 (0, 0.1)	12.953	0.00000
T_{10} (0, 0.2)	11.207	0.00000
T_9 (0, 0.2)	8.099	0.00000
T_8 (0, 0.04)	0.199	0.63265

Figure 4-8 PValue and LogWorth of factors to efficiency

obtained by OFAT method Figure 4-3, both of two methods draw similar conclusion, but the process by D-optimality design uses much fewer evaluation trials and consumes much less computation time. What's more, more accurate and clearer results are exhibited by D-optimality design. In order to minimise the variation of the output torque, the tolerances T_{11} and T_{12} are preferred to be reduced firstly, and if it is still not satisfied, T_1, T_3, T_4, T_5 and T_6 will be adjusted accordingly.

Figure 4-8 show the significances of the 12 tolerances to efficiency, and they are also demonstrated in Figure 4-7, the steeper of the slope, the more significant is the tolerance. Similarly to the torque significance, T_{11} and T_{12} are the most significant tolerances to efficiency. T_1–T_6 are less significant, T_7–T_{10} are not significant to the efficiency of the motor. According to the relationship between output torque and efficiency, which is illustrated in equation (5-24), if the losses are constant, larger torque will lead higher efficiency. The 12 tolerances have similar significances to the output torque and efficiency, so the adjustments of the tolerance will have similar effects to the torque and efficiency.

However, there are still some differences between the effects to torque and efficiency. For the magnet-related tolerances T_1–T_4, apart from T_3, the tolerance of the length of primary magnet T_1 also have large influence on output torque. As the dimension D_1 is longer D_3, for the same tolerance varying range, T_1 has smaller slope than T_3. From the Figure 4-7, it is seen that the radial tolerances T_9 and T_{10} are inversely proportional to motor efficiency. Tolerance T_9 is the lower limit of dimension D_9, and the enlarged T_9 may increase the magnetic saturation of the stator bridges that are near rotor shaft. Tolerance T_{10} the upper limit of dimension D_{10}, and the increased T_{10} may deteriorate the saturation of the stator core edge region. The induced magnetic saturation will decrease the efficiency of the designed IPM motor. In sum, the significances are sequenced as $T_{11}>T_{12}>T_3>T_5>T_6>T_1>T_4>T_2>T_7>T_{10}>T_9>T_8$. To minimise the variation of motor efficiency, the tolerances T_{11} and T_{12} are preferred to be reduced firstly, and followed by T_1–T_6.

4.3.4 .Predication of Motor Performance by DOE I-optimality

DOE I-optimality is used to estimate the performance of the ferrite IPM motor design with different tolerance combinations, due to its merits of good prediction across the entire design region. The adjustments of tolerances are iteratively processed in several steps, each step providing insight into how the next experiment should be run. The DOE I-optimality starts from the initial set of tolerances shown in Table 4-2. The DOE table is generated by I-optimality criterion, and it includes 97 motor trials with different combinations of the 12 tolerances, which is attached in Appendix C.2. Actually the generated 97 trials are selected by DOE I-optimal algorithm from an overall candidate set of possible treatment combinations. The candidate set consists of all the possible treatment combinations that one wishes to consider in an experiment. If three values of each tolerance factor are taken to evaluate the model, which are the lower edge value, middle value and upper edge value, the full candidate factorial designs will be 3^12=531441 runs. However, with the DOE I-optimality method, only 97 evaluation trials are carried out to exhibit the characteristics of the designed machine, and the number of implemented trials is only a tiny fraction of such large candidate library. Huge amount of time and effort can be saved with the assistance of DOE algorithm. After finishing the 97 trials, the torque responses from FEA simulations are evaluated by the DOE processing method.

The evaluation trials and their torque responses are visualised in Figure 4-9. As only two factors can be displayed in a 2D graph, the 12 tolerance factors T_1–T_{12} are shown in six subfigures in Figure 4-9. In each subfigure, the selected evaluation trials (black dots) are scattered in the design region, and the green curved surface represents the torque response. As each tolerance factor has three possible values, there are nine possible combinations of two factors, which are shown in each subfigure of Figure 4-9. The selected 97 trials are only small fraction of total candidate combinations. Comparing the number of the black dots in the six subfigures, it is seen that the tolerance factors with high significances are likely to have more relevant evaluation trials, e.g. subfigure (a), (b), (c) and (f) have more black dots than subfigure (d) and (e). In this way, the

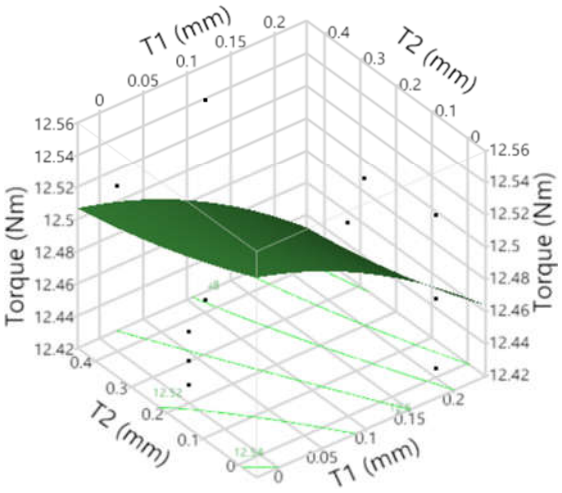

(a) Torque response to T_1, T_2

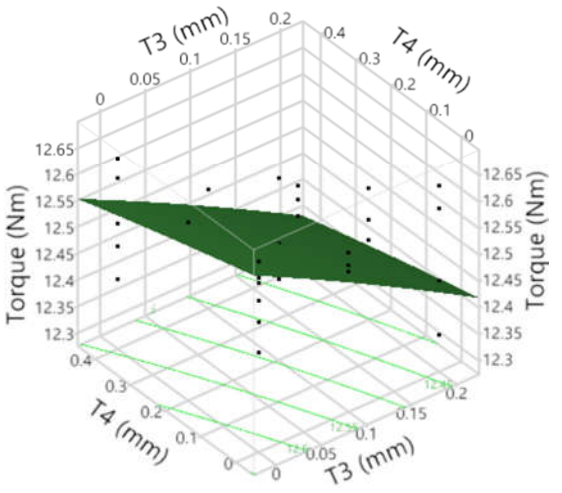

(b) Torque response to T_3, T_4

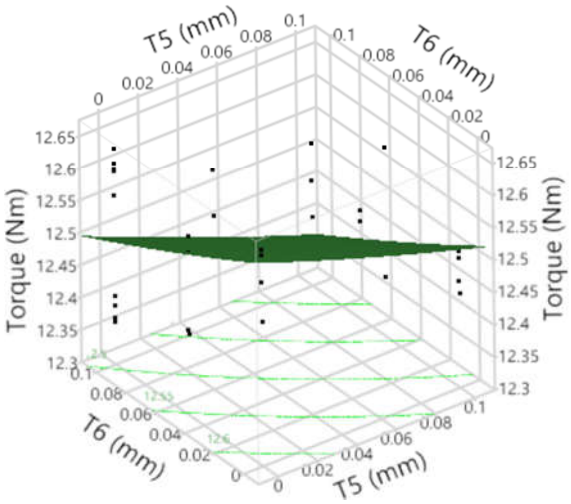

(c) Torque response to T_5, T_6

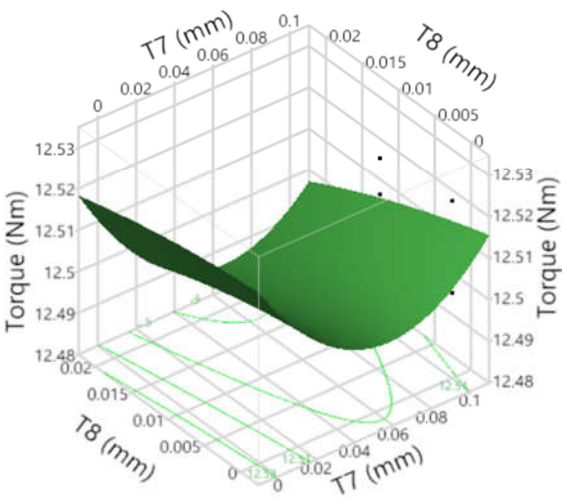

(d) Torque response to T_7, T_8

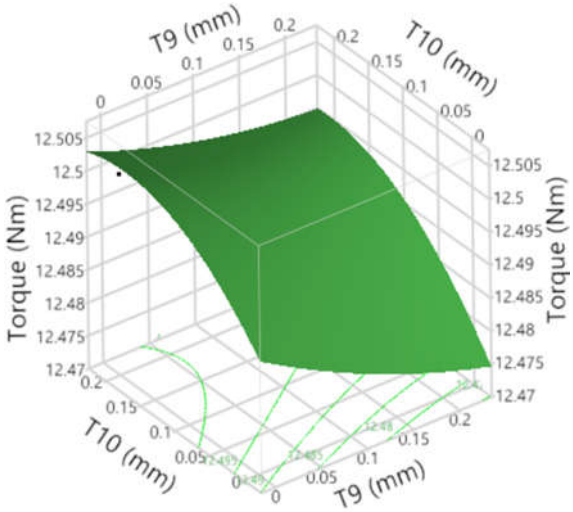

(e) Torque response to T_9, T_{10}

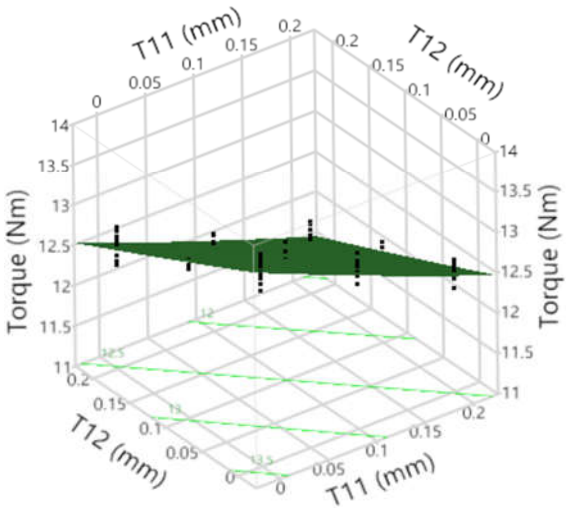

(f) Torque response to T_{11}, T_{12}

Figure 4-9 The distribution of evaluated points and their torque response surface

majority of the essential features can be exhibited by the limited few trials. In addition, since tolerances T_{11}, T_{12} are more significant than T_1–T_6, the resultant torques look concentrated in the space of subfigure (f) but look loose in the design region of subfigure (a) (b) (c). The relationship between tolerance factors and response torque can be observed by the shapes of the response surface projection. The tolerances T_1–T_6, T_{11} and T_{12} are almost linear to the output torque, so the projected lines of response surface are almost paralleled with each other. But the projected lines of response surface in subfigure (d) and (e) are curved, as some of the tolerances of T_7–T_{10} are not linear to output torque.

Optimality designs are model-dependent, the I-optimality design used in the tolerance analysis is based on RSM model, which is a quadratic model. Here is a simple example of two factors to clarify the RSM model. The two factors are X_1 and X_2, and their corresponding design regions are (0, 2a) and (0, 2b). The prediction expression is written as:

$$\mathrm{Y} = C_0 + C_1\left(\frac{X_1 - a}{a}\right) + C_2\left(\frac{X_2 - b}{b}\right) + C_{11}\left(\frac{X_1 - a}{a}\right)\left(\frac{X_1 - a}{a}\right) + C_{12}\left(\frac{X_1 - a}{a}\right)\left(\frac{X_2 - b}{b}\right) + C_{22}\left(\frac{X_2 - b}{b}\right)\left(\frac{X_2 - b}{b}\right)$$

Where, C_0, C_1, C_2, C_{11}, C_{12}, and C_{22} are coefficients of the model expression, which can be summarised in the following table. C_0 is the value of response Y when all the factors are equal to the median value of their respective design range.

Table 4-3 Coefficient table of two-factor RSM model

	X_1 (0, 2a)	X_2 (0, 2b)	Y
X_1 (0, 2a)	C_{11}	C_{12}	C_1
X_2 (0, 2b)		C_{22}	C_2

The prediction expression of the 12-factor RSM model in the thesis is a 91-terms quadratic polynomial, the coefficients of which are attached in Appendix C.3. The accuracy of the prediction model is of our keen concern. The actual torque and predicted torque are both illustrated in Figure 4-10.

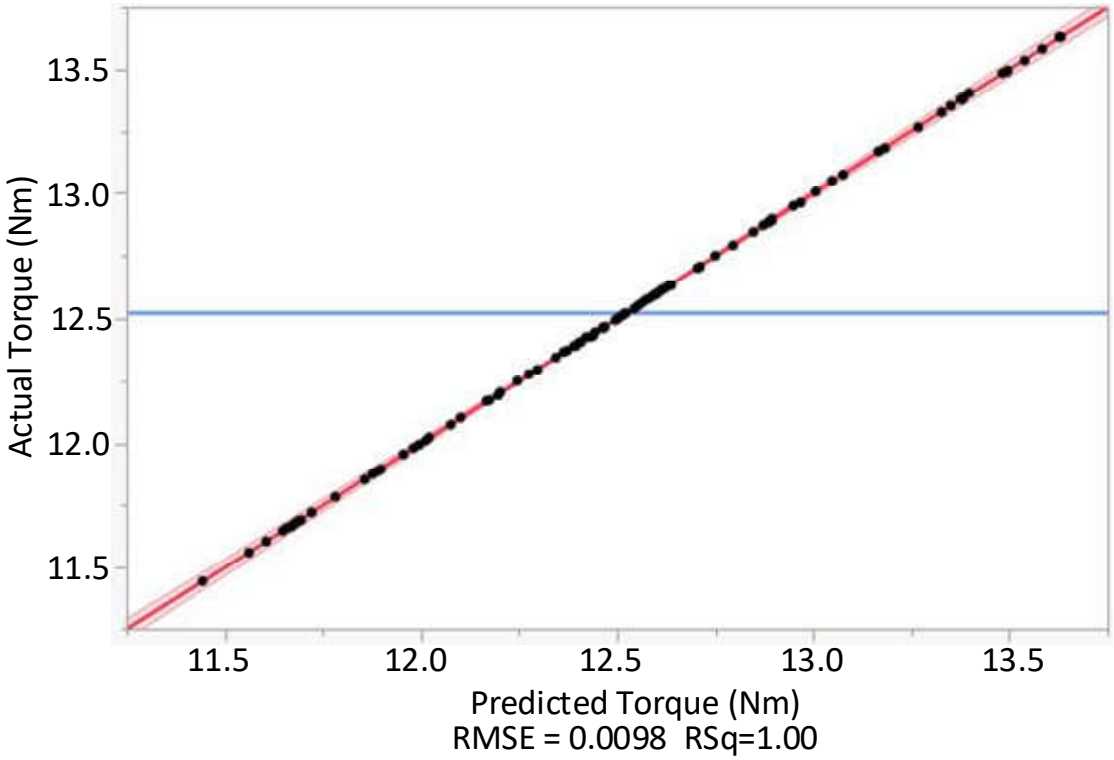

Figure 4-10 Actual and predicted torque plot

It is seen that all the actual torque points (black dots) are around the predicted torque region (red area), and the predicted region is narrow, which means the predicted expression conforms to actual design runs with high confidence. *RMSE*, root-mean-square error, is a frequently used measure of the differences between values predicted by a model and the values actually observed [217]. The *RMSE* represents the sample standard deviation of the differences between predicted values and observed values. *RMSE* is a measure of accuracy, and the smaller the value is, the better is the accuracy of the model. And *RSq*, the coefficient of determination in statistics, is the proportion of the variance in the dependent variable that is predictable from the independent variable. It provides a measure of how well actual observed responses are replicated by the model, based on the proportion of total variation of outcomes explained by the model [218,219]. *RSq* is a value between 0 and 1, and the larger the value is, the better the prediction will be.

Figure 4-10 also shows the *RMSE* and *RSq* value of the model (prediction expression), which are 0.0098 and 1 respectively. The small RMSE and large

RSq indicate that the prediction model is good enough for performance estimation. The torque residual is illustrated in Figure 4-11, which further confirms the low error level and high accuracy of the prediction model. All the torque residuals are less than 0.008 Nm, which is negligible when comparing with actual mean torque 12.5 Nm.

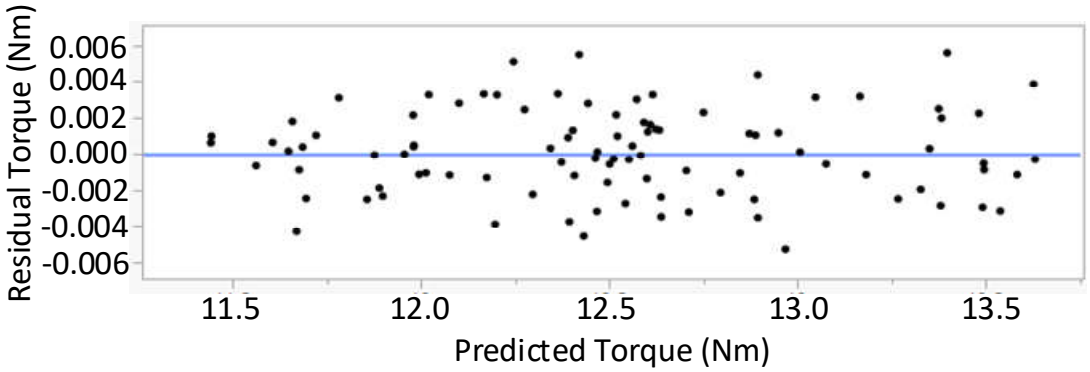

Figure 4-11 Torque residual by predicted model

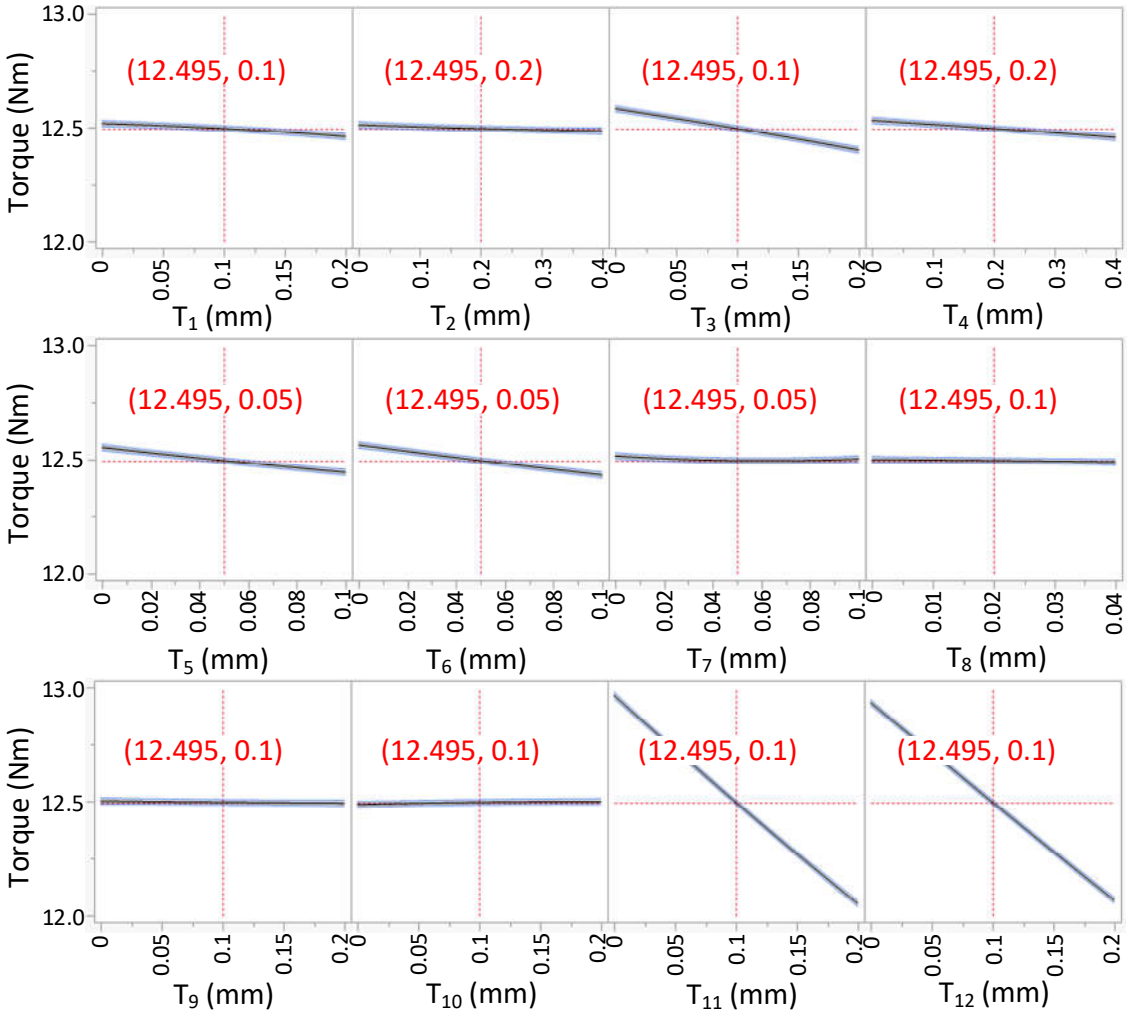

Figure 4-12 Torque prediction profiler of initial tolerances at median point

Figure 4-12 shows the predicted torque of initial set of tolerances at median point, and Figure 4-13 and Figure 4-14 depict the maximum and minimum predicted torque of initial tolerances respectively. In each subfigure, the black line is the predicted torque response to that corresponding tolerance, and the grey area around black line and enclosed by blue edges is the confidence interval, which is a type of interval estimation computed from the observed data [216]. The confidence level is the proportion of possible confidence intervals that contain the true value of their corresponding parameter, acting as good estimates of the unknown population parameter. In these prediction profilers, the torque response and its confidence intervals at the cross point are displayed at left-hand side of the rows of subfigures, which is the instant predicted response of the current combination of tolerance factors.

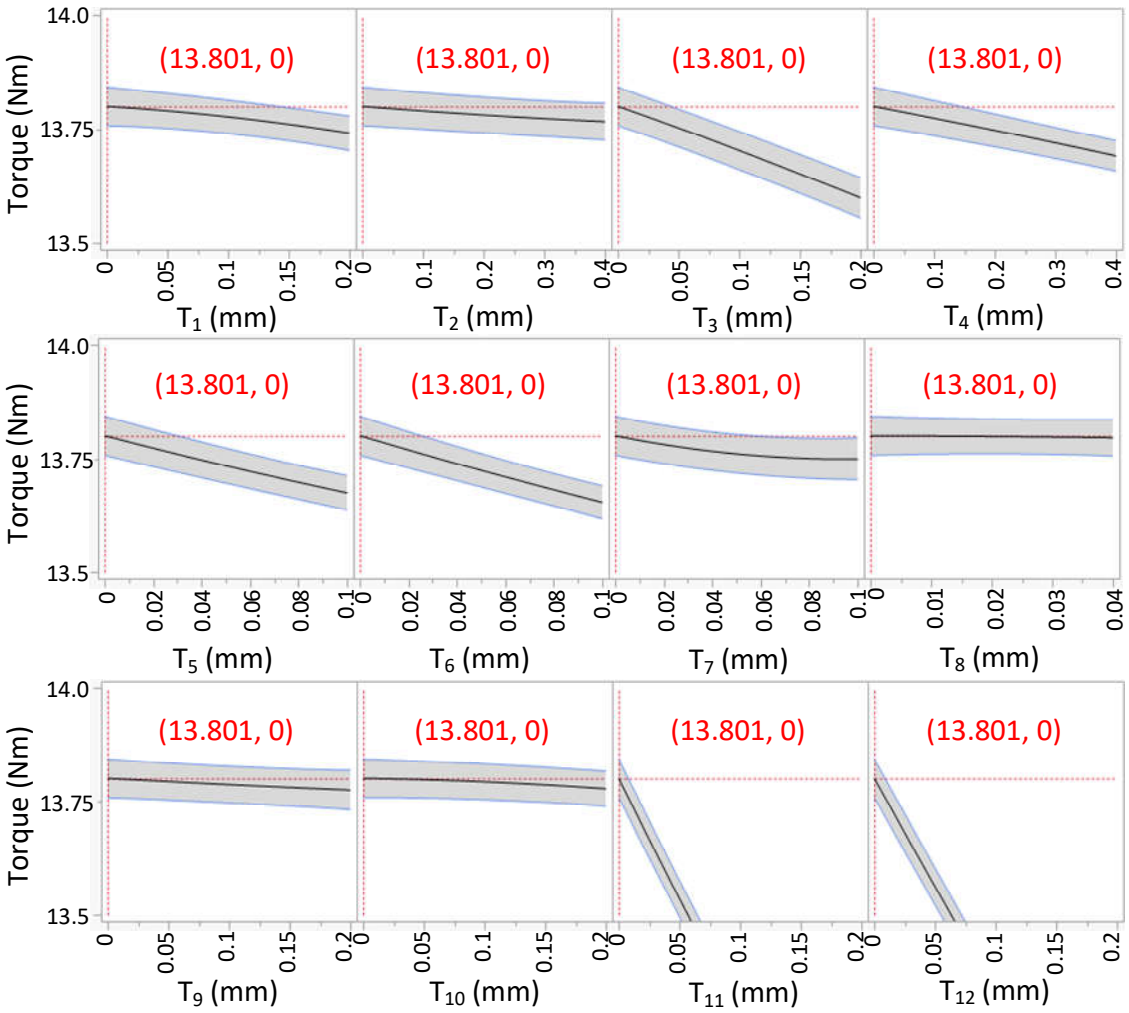

Figure 4-13 Torque prediction profiler of initial tolerances at maximum response point

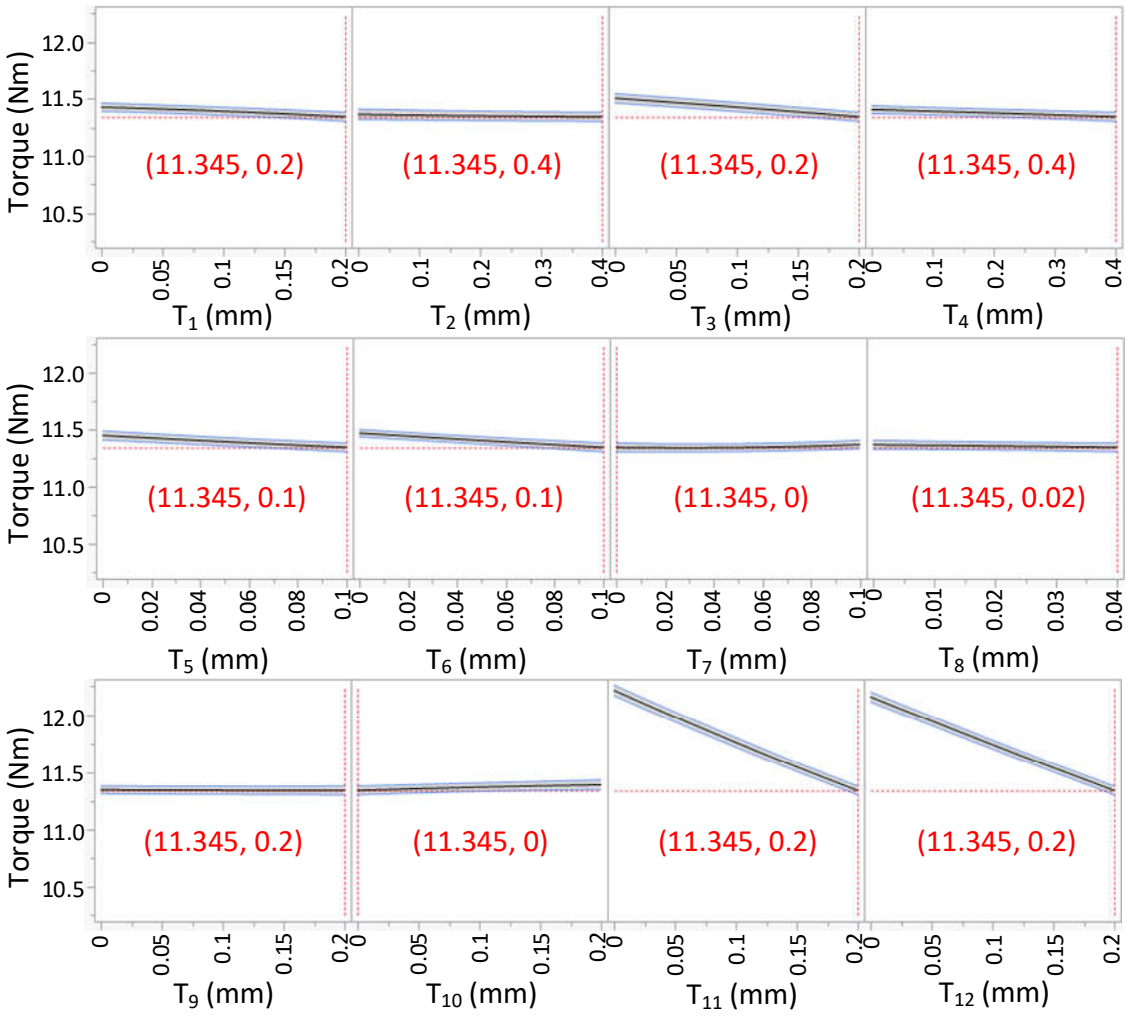

Figure 4-14 Torque prediction profiler of initial tolerances at minimum response point

The relationships between response torques and their tolerance factors are shown in these prediction profilers. At the median point of the initial set of tolerances, the predicted torque is 12.49529 Nm (shown in Figure 4-12). After adjusting the values of the 12 tolerance factors, the maximum and minimum predicted torque are found in the profiler, which are 13.8011 Nm and 11.34499 Nm (shown in Figure 4-13 and Figure 4-14 respectively). The output torque variation of the designed motor with initial set of tolerances can be calculated according to Equation (4-1). The variation is 9.7674% around average torque output, and it is much larger than the objective variation requirement 2%. So the initial set of tolerances is too large to make the output torque consistent. The tolerances need to be further adjusted to meet the requirement.

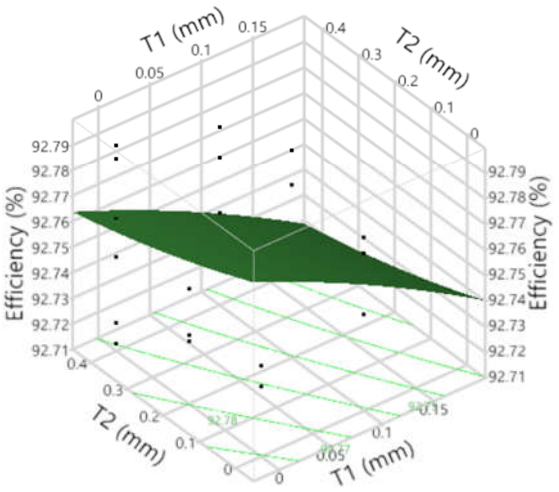

(a) Efficiency response to T1, T2

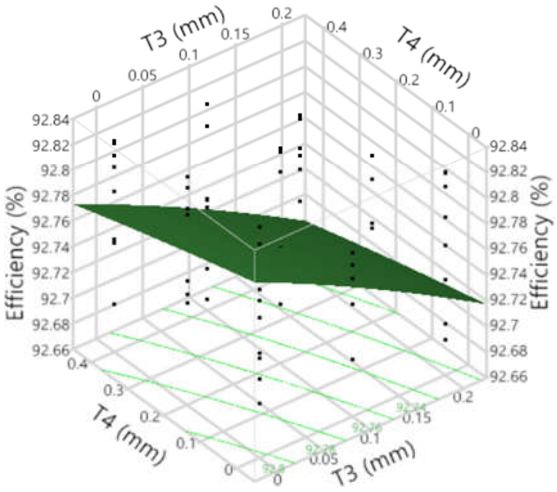

(b) Efficiency response to T3, T4

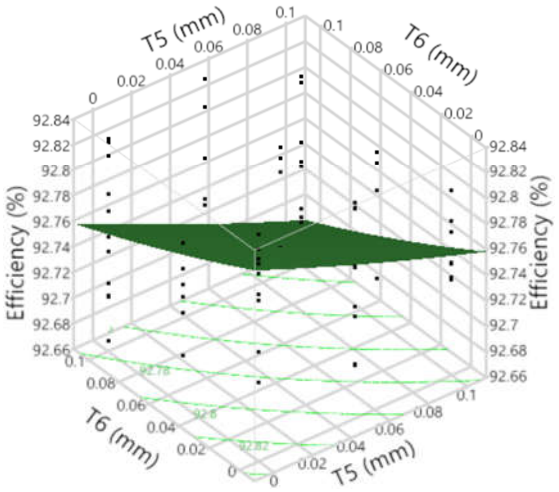

(c) Efficiency response to T5, T6

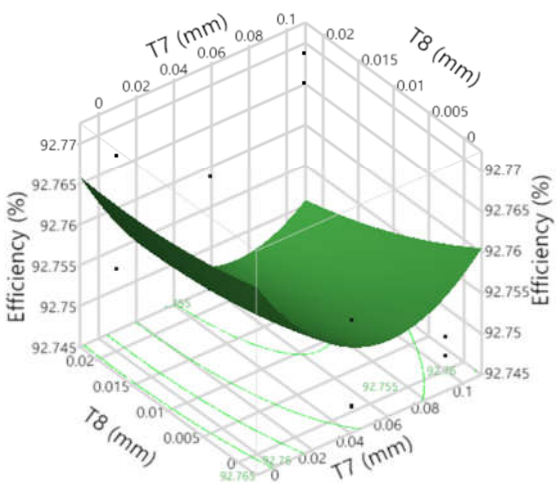

(d) Efficiency response to T7, T8

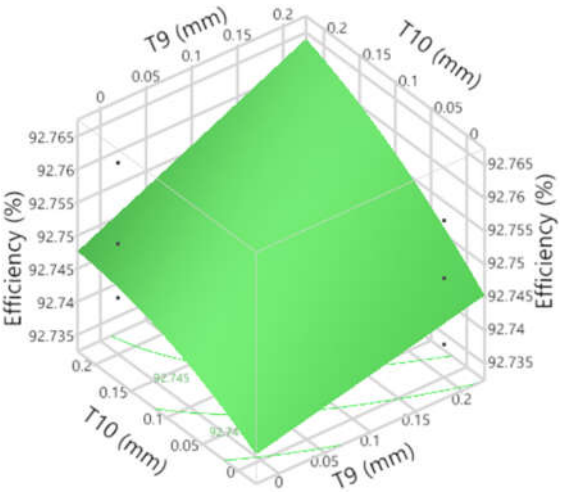

(e) Efficiency response to T9, T10

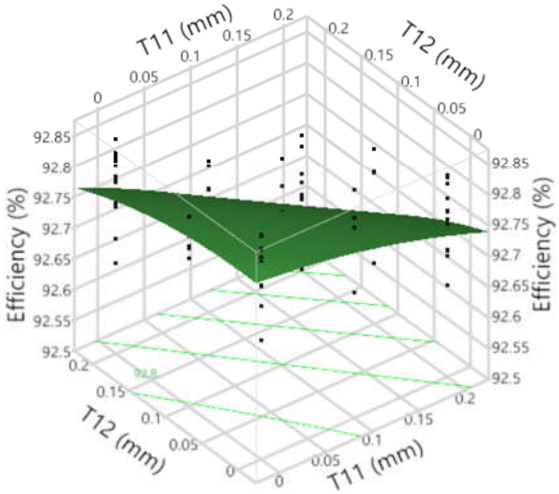

(f) Efficiency response to T11, T12

Figure 4-15 Distribution of evaluated points and their efficiency response surface

Following the same procedure, the efficiency response of the initial set of tolerances is analysed as well. The DOE table is the same as the one used for torque responses, and efficiency responses are calculated based on the FEA results, which are attached in Appendix C.2. The evaluation trials and their efficiency responses are visualised in Figure 4-15. In contrast with Figure 4-9, the efficiency has similar response surfaces to that of the output torque, indicating that the efficiency has strong connections with output torque and have alike reaction to tolerance factors. Comparing the number of the black dots in the six subfigures, it is seen that the tolerance factors with high significances are likely to have more relevant evaluation trials, e.g. subfigure (a), (b), (c) and (f) have more black dots than subfigure (d) and (e). In this way, the majority of the essential features can be exhibited by the limited few trials. The relationship between tolerance factors and response efficiency can be observed by the shapes of the response surface projection. The tolerances T_1–T_6, T_{11} and T_{12} are almost linear to the efficiency, so the projected lines of response surface are almost paralleled with each other. But the projected lines of response surface in subfigure (d) and (e) are curved, as some of the tolerances of T_7–T_{10} are not linear to the efficiency.

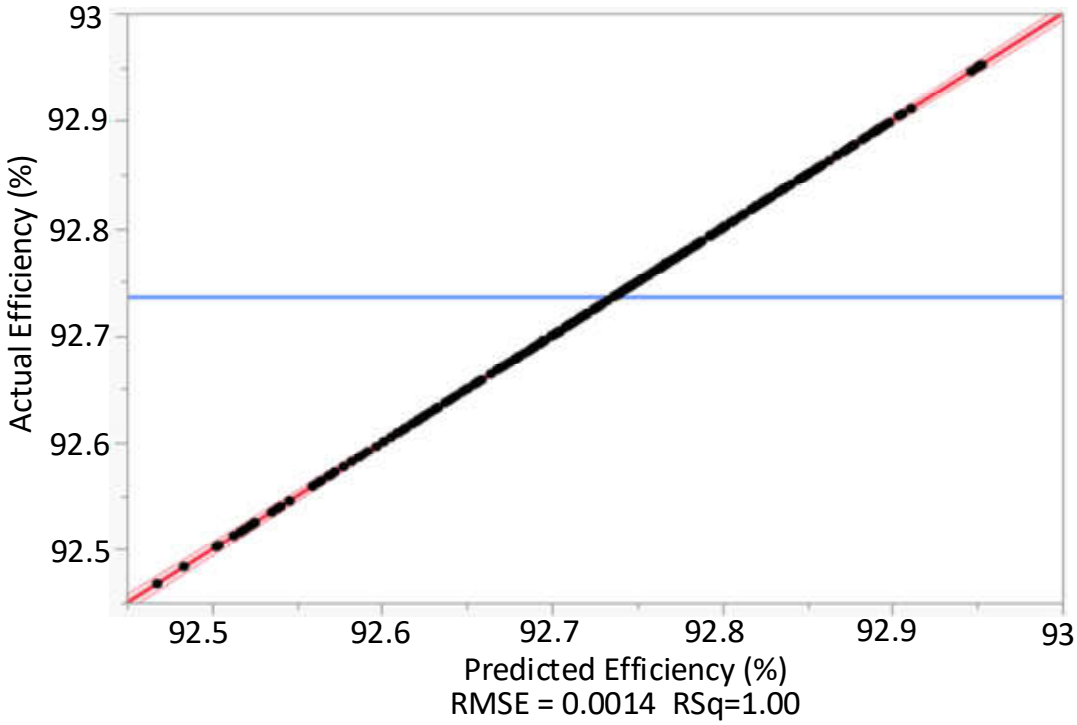

Figure 4-16 Actual and predicted efficiency plot

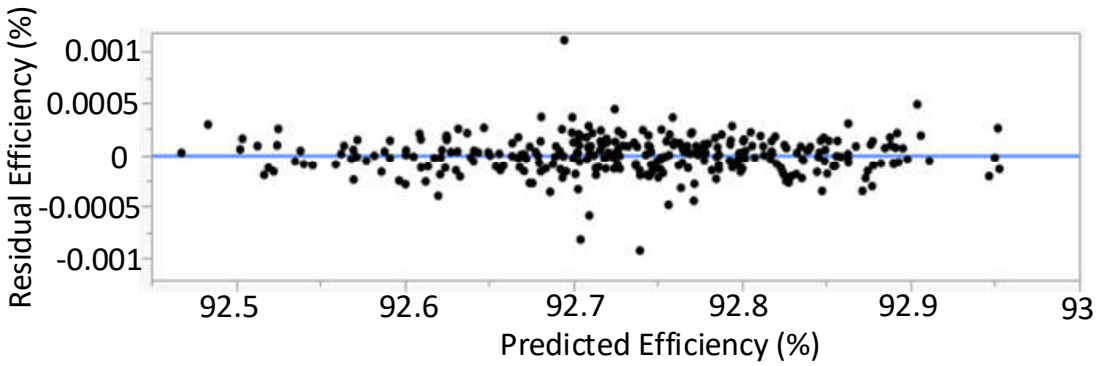

Figure 4-17 Efficiency residual by predicted model

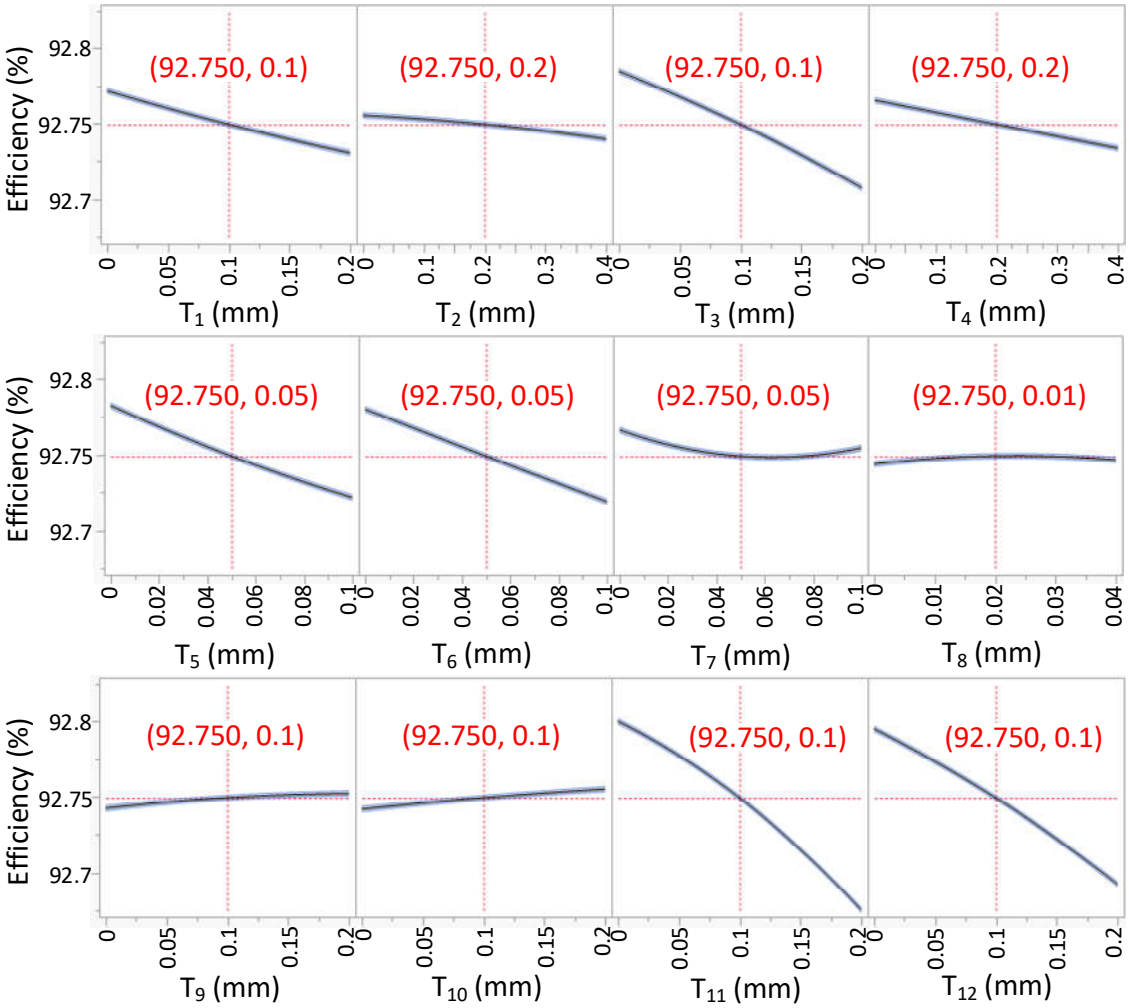

Figure 4-18 Efficiency prediction profiler of initial efficiency at median point

I-optimality design of efficiency is also model dependant. The coefficients of the quadratic efficiency prediction expression are attached in Appendix C.4. The accuracy of the estimation model (prediction expression) is revealed in Figure

4-16. All the actual efficiency points (black dots) are within the predicted efficiency region (red area with blue edge line). Small *RMSE* and large *RSq* indicate that the prediction model is good enough for performance estimation with less error. The conclusion is further confirmed by the efficiency residuals illustrated in Figure 4-17 where all the efficiency residuals are less than 0.003%. The relationships between efficiency responses and their tolerance factors are shown in Figure 4-18. The black line in each subfigure is the predicted efficiency response to its respective factor, and the grey area around black line and enclosed by blue edges is the confidence interval [216]. And the shape of the response line is different for different factors. The slope of efficiency response line relates to the significance to each tolerance factor, e.g. the most significant tolerances T_{11} and T_{12} exhibit steep slope in Figure 4-18 subfigure (f).

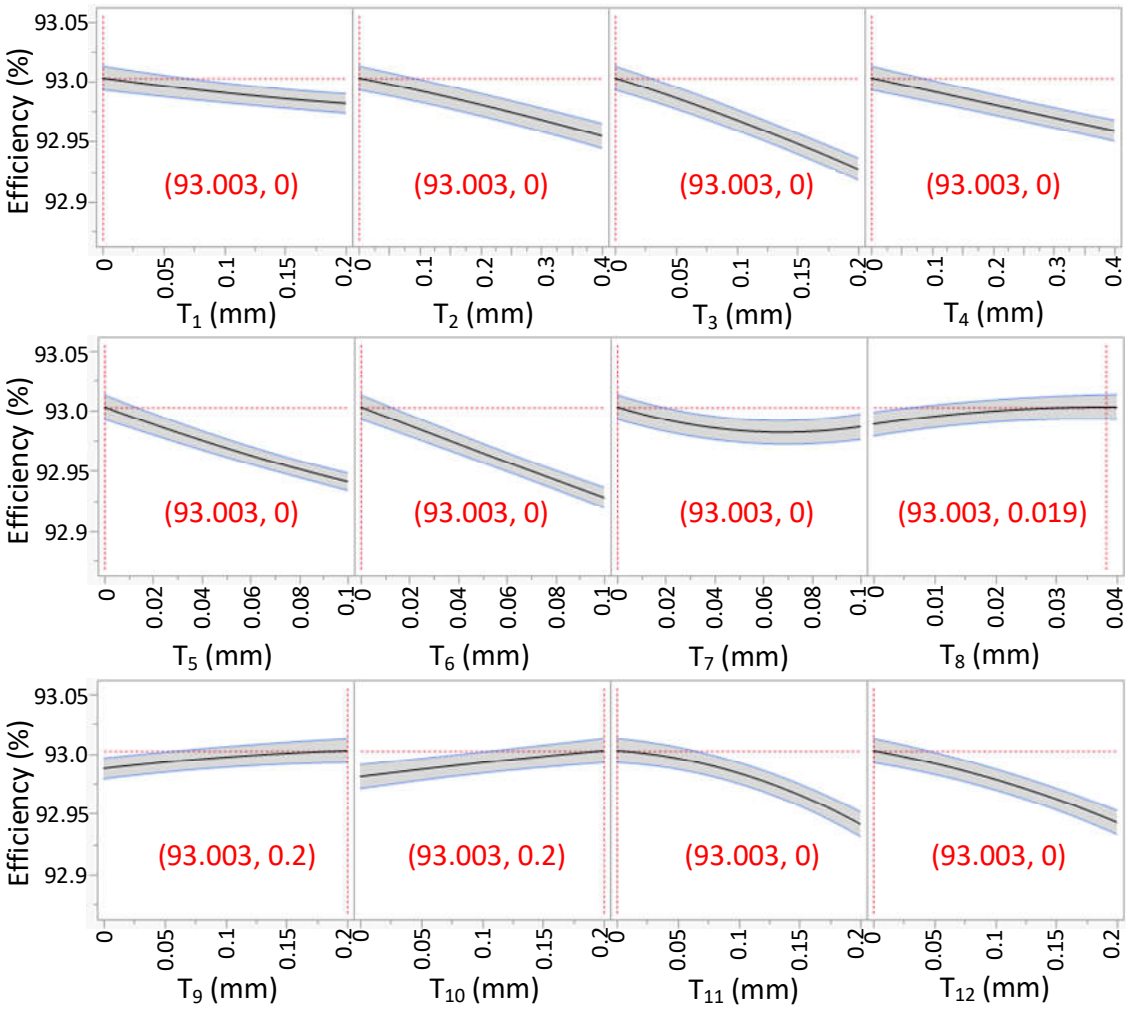

Figure 4-19 Efficiency prediction profiler of initial tolerances at maximum response point

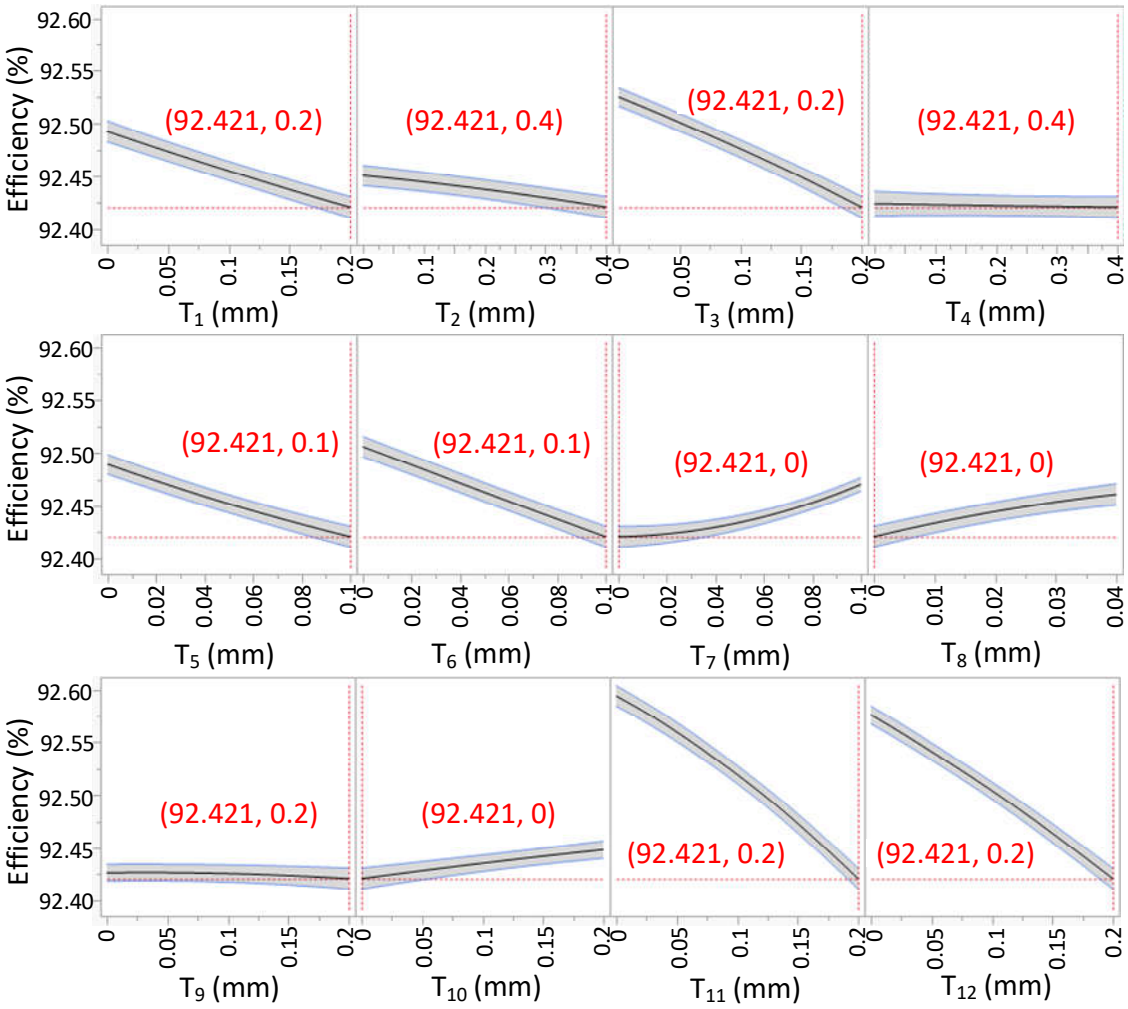

Figure 4-20 Efficiency prediction profiler of initial tolerances at minimum response point

With the initial set of tolerances, the maximum and minimum predicted efficiency responses are estimated to be 93.00314% and 92.42098%, as shown in Figure 4-19 and Figure 4-20 respectively. According to equation (4-1), the efficiency variation of the designed motor with initial tolerances is only 0.314%, which is much less than the objective variation requirement 2%. So there is no need to further adjust the tolerances for efficiency. The motor's output torque and efficiency are both affected by the change of their dimensions within tolerance gaps, but the variation of the efficiency is much smaller. As the efficiency is strongly related to the output torque, when the variation of output torque is reduced, the variation of efficiency will be reduced as well. Thus, the efficiency will always meet the variability requirement, less than 2% variation, and there is no need to worry about efficiency when the variability of output

torque is being minimised. As a result, in the future tolerance adjustments, only the output torque response is considered.

4.3.5 Tolerance Adjustments to Meet Requirement

According to the flowchart in Figure 4-4, as long as the requirement is not achieved, the tolerance factors need further iterative adjustments. Because torque response is more sensitive to the significant tolerance factors, the priority of tolerance adjustment is dependent on their significance. So T_{11} and T_{12} with high significance are preferred to be reduced first.

Table 4-4 Tolerance adjustments and their corresponding torque variation

Step	T_1 (mm)	T_2 (mm)	T_3 (mm)	T_4 (mm)	T_5 (mm)	T_6 (mm)	T_7 (mm)	T_8 (mm)	T_9 (mm)	T_{10} (mm)	T_{11} (mm)	T_{12} (mm)	Torque Variation (%)
0	0.2	0.4	0.2	0.4	0.1	0.1	0.1	0.04	0.2	0.2	0.2	0.2	9.7674
1	0.2	0.4	0.2	0.4	0.1	0.1	0.1	0.04	0.2	0.2	0.1	0.1	5.5263
2	0.2	0.4	0.2	0.4	0.1	0.1	0.1	0.04	0.2	0.2	0.08	0.08	5.0725
3	0.2	0.4	0.2	0.4	0.05	0.05	0.05	0.04	0.2	0.2	0.08	0.08	4.5712
4	0.2	0.4	0.2	0.4	0.05	0.05	0.05	0.04	0.1	0.1	0.08	0.08	4.4352
5	0.2	0.4	0.2	0.4	0.03	0.03	0.04	0.04	0.1	0.1	0.08	0.08	4.2526
6	0.2	0.4	0.2	0.4	0.02	0.025	0.03	0.035	0.03	0.04	0.055	0.055	2.9615
7	0.1	0.2	0.1	0.2	0.02	0.025	0.03	0.035	0.03	0.04	0.055	0.055	2.4361
8	0.05	0.1	0.05	0.1	0.02	0.025	0.03	0.035	0.03	0.04	0.055	0.055	2.1040
9	0.02	0.04	0.02	0.04	0.02	0.025	0.03	0.035	0.03	0.04	0.055	0.055	1.9865

As shown in Table 4-4, both of T_{11} and T_{12} are decreased to 0.1 mm at *Step-1*, then further decreased to 0.08 mm at *Step-2*. Accordingly, torque variation drops from 9.7674% to 5.0725%. It is noteworthy that minimising mechanical tolerances will increase machining cost and the best scheme of tolerances is the one with small variation of performance and low manufacturing cost. With this objective, the tolerances of lamination sheets are preferably to be reduced first, as they are cut by stamping press and machining cost is relatively low. When they reach the minimal allowable tolerances shown in Table 1, the tolerances of ferrite magnets will be diminished later as they are ground to fine dimension that takes time and increase machining cost. Following the above strategy, the tolerances are iteratively adjusted until the requirement is achieved. Table 4-4 shows the whole process of tolerance adjustments and their

corresponding torque variation. In order to easily notice the difference between steps, the adjusted tolerances are highlighted in yellow comparing with the last step. Tolerances T_5-T_{10} are diminished from *Step-3*, and at *Step-6* all the tolerances of steel laminations (T_5–T_{12}) reach the minimal allowable tolerances and the torque variation decreases to 2.9615%. From *Step-7* the tolerances of ferrite magnet start to decrease, and the requirement is finally met at *Step-9*, the torque variation of which is 1.9865%, less than design standard 2%.

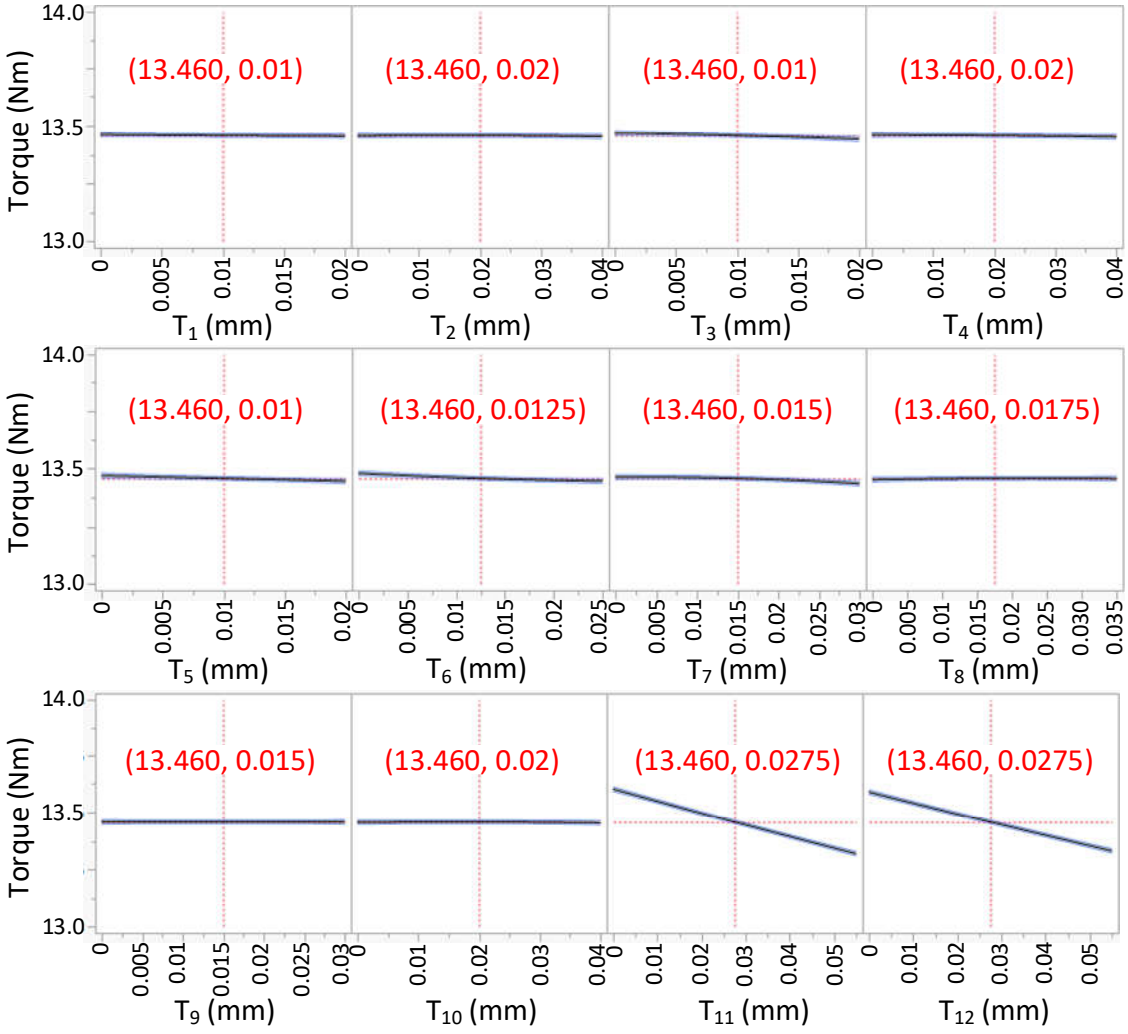

Figure 4-21 Torque prediction profiler of final tolerances

The torque prediction profiler of the final tolerances is shown in Figure 4-21. Comparing the torque response curves of initial and final tolerances in Figure 4-12 and Figure 4-21, with the same torque variation difference (1 Nm difference) at vertical axis, the response line slope of final tolerances is much smaller than that of initial tolerances. This means the influence of the final set of

tolerances on the output torque is getting smaller and the variation of output torque is diminished. Therefore, after the process of tolerance adjustments, the output performance of the designed ferrite IPM motor is more consistent and the overall quality is improved as well.

4.3.6 Validation of the Quality Control Method

In this study, a prototype of ferrite IPM motor is manufactured with the optimal set of mechanical tolerances that are determined by DOE assisted Six Sigma DMADV quality control method in the last section. The experimental results of torque capacity and corresponding efficiency are shown and compared with FEA simulation results in Figure 4-22 and Figure 4-23. The FEA results of the prototype motor are regarded as expected output, and measured output is the actual results from experiment test.

The prototype motor is tested up to 3500 rpm. At the nominal speed 1500 rpm, the expected torque is 13.51 Nm and measured torque is 13.33 Nm, so the calculated torque variation is 1.33%, less than the requirement 2%. At the same test point, the expected efficiency is 93.71% and measured efficiency is 92.71%, so the calculated efficiency variation is 1.07%, less than the requirement 2%. Therefore the quality of the prototype machine meets the design standards. However, from the torque comparison in Figure 4-22, it is seen that when the speed is too low or too high the torque variation might be larger than quality

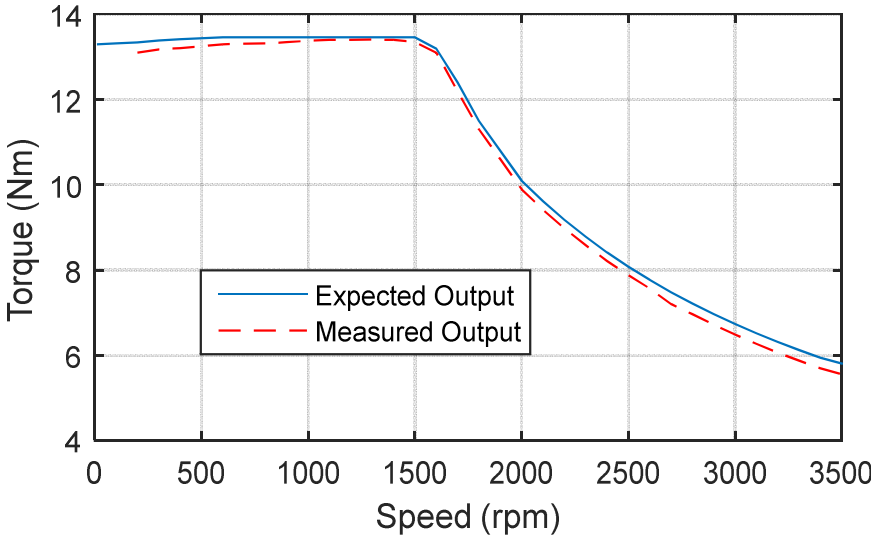

Figure 4-22 Output torque comparison of prototype machine

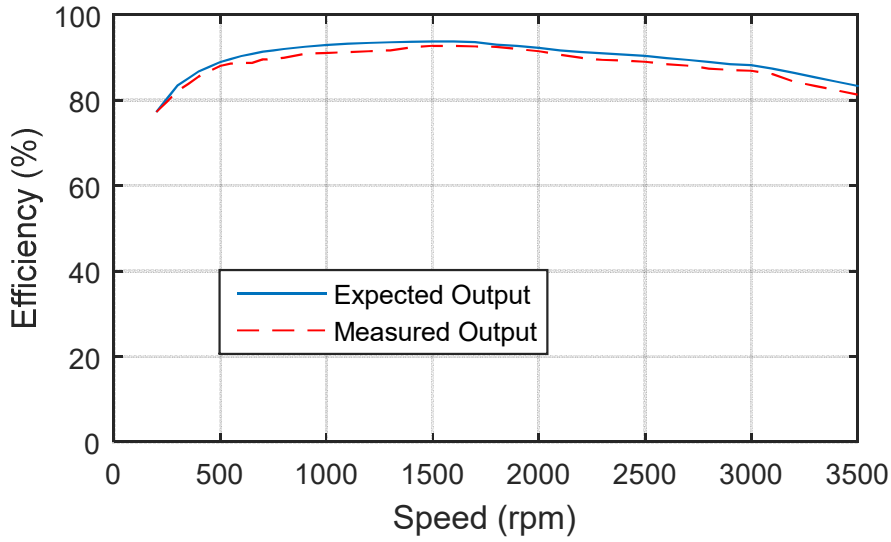

Figure 4-23 Efficiency comparison of prototype machine

requirement. That's because during the tolerance adjustment process only is considered the output torque at nominal speed and load. Since most of time the motor is working around nominal speed and load, the relative large torque variation at low and high speed will not affect the overall performance of the motor much. Due to limitation of research budget, only one motor is made for validation, but the effect of the proposed quality control approach is better to be validated by a large number of electric machine samples, which can be further tested in mass production factories.

4.4 Summary

Quality control is important for electric machine production. Less defected and rejected products will reduce the manufactory's overall cost. Customers also benefit from consistent and reliable products that have longer working lifespan and require less maintenance. With the quality control of the studied ferrite IPM machine, the low-cost feature is exhibited without compromise on its performance. The merits of quality control become more prominent when the motors are under mass production. The motor quality can be improved by minimising the variability of its performance. Because the performance of a motor is mainly determined by its geometric design, the accuracy of which is determined by the tolerances, adjusting the tolerances in reasonable ranges will control motor quality.

The methodology of Six-Sigma DMADV is introduced into the motor quality control. Because large number of tolerances are in need to be considered at the same time as they are coupled with each other, “trial and error” or “one factor at a time (OFAT)” are not applicable in the study. On the other hand, DOE optimality design is suitable for the study case, with credible prediction, substantially reduces trial samples, and computation time. The significances of the tolerances are identified by D-optimality, and the torque and efficiency responses of the designed motor are predicted by I-optimality. After several rounds of adjustments, the optimal combination of tolerances is achieved and the variation of performance is reduced to acceptable range. At last, the proposed DOE assisted Six Sigma DMADV method is validated by a prototype of ferrite IPM machine.

In this research work, The DOE assisted Six Sigma DMADV method is successfully implemented to the two-layer spoke type ferrite IPM motor as an example, and the developed method can also be used for the quality control of various types of electric machines.

5. LOSS ANALYSIS OF FERRITE IPM MACHINE

PM machines have better performance than IM in terms of torque density and efficiency. And the high-efficiency motor will reduce the overall operating cost of the electric drive system. In chapter, the losses and efficiency of the designed ferrite IPM motor will be comprehensively analysed.

5.1 Loss Composition and General Analysis

5.1.1 Energy Conversion and Loss Composition

There are various approaches to understand the force or torque developed in an energy conversion device. Figure 5-1 illustrates the energy conversion process based on the principle of conservation of energy, which states that energy can neither be created nor destroyed; can only be changed from one form to another. The electromechanical converster system has three essential parts: (1) an electric system, (2) a mechanical system, and (3) a coupling field[220].

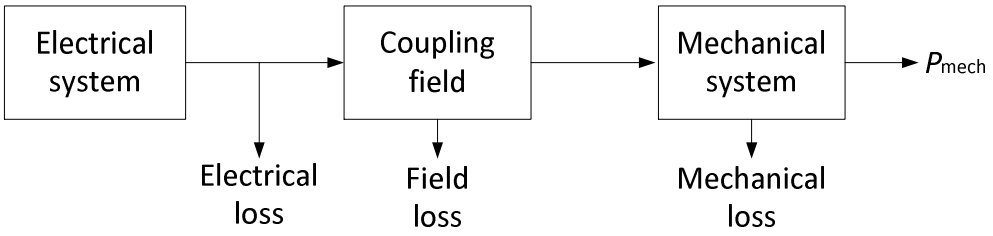

Figure 5-1 Electromechanical conversion system

The energy transfer equation is expressed as follows:

$$\textit{Electical energy input from source} = \textit{Mechanical energy output} + \textit{Increase in stored energy in coupling field} + \textit{Energy losses} \quad \textbf{(5-1)}$$

The electrical power cannot fully be converted into mechanical power, and the wasted power is the losses dissipated as heat. The electrical energy loss is the copper loss due to current flowing in the winding of the energy converter, which is also known as heating loss or ohmic loss in the resistance of the winding. The field losses include the core loss in the stator and rotor lamination cores, and eddy current loss in the PMs. The field losses are caused by the changing magnetic field in ferromagnetic materials. The mechanical loss is the friction

and windage loss due to the motion of the moving components. All these losses are eventually converted into heat, which not only leads to temperature rise of the motor, but also influences its performance and lifetime in a certain extent.

Since the ferrite magnets used in our designed motor are nonconductive, there are no losses in the PMs. The relationship of power and losses in a ferrite IPM motor is illustrated in Figure 5-2.

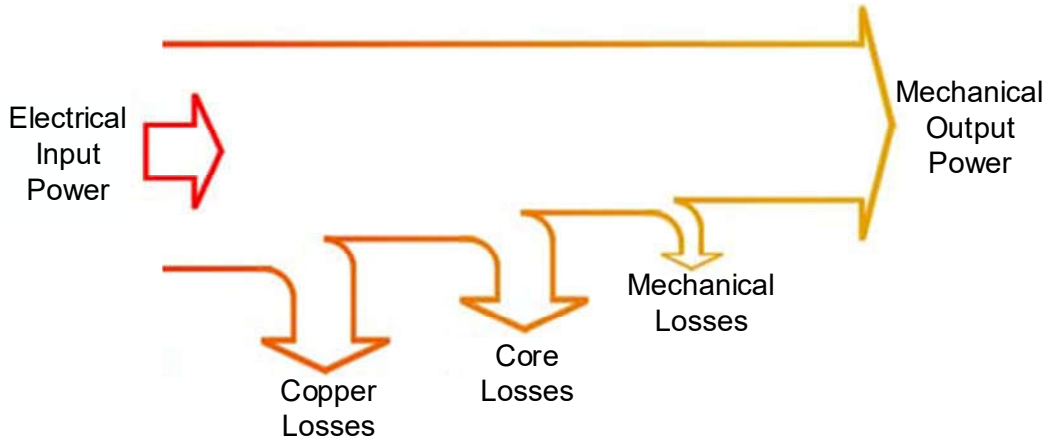

Figure 5-2 Power and loss flow diagram of the ferrite motor

The majority of losses come from copper losses and core losses, but the mechanical losses cannot be neglected. The mechanical loss due to the bearing friction and wind drag is dependent upon rotational speed but independent on the load. It is difficult to estimate it directly by calculation, because core loss is also dependent on rotational speed and coupled with mechanical loss. According to the rule of thumb, the mechanical loss is normally approximated as 2% of the rated motor power

The two dominant losses, the copper loss in the windings and the iron loss in stator and rotor core, are principally investigated in this study.

5.1.2 Theoretical Analysis of Copper Loss

Copper loss, often called ohmic loss, is always associated with conduction current distribution in conductors which are not perfect. Thus the resistivity of conductors is responsible for the ohmic power loss when current flows in such

conductors. There is always a heating effect due to the ohmic loss, often called Joule heating. The copper loss is expressed as:

$$P_{cpl} = 3I^2R \tag{5-2}$$

Where *I* is the current flowing in the copper coils and *R* is the electric resistance of the copper coils. The copper loss usually takes up a large part of the total loss. According to Ohm's law, the DC resistance of a conductor is dependent on its resistivity, length and cross-section area, and thus can be estimated. The electric resistance is calculated by

$$\mathrm{R} = \rho \cdot \frac{L_{copper}}{A_{copper}} \tag{5-3}$$

Where ρ is the resistivity of copper, L_{copper} is the length of the copper wire in each phase, and A_{copper} is the cross-section area of the copper wire. The resistivity of copper at 20°C (293 K) is 1.68×10^{-8} Ω·m, namely original resistivity. However, most of the time the motor is operating at 80°C a higher temperature because of the heat generated by the losses. After being started the motor is warming up and stays at a specified temperature when the heat generation and dissipation reach their balance. According to the relationship between resistivity and temperature, the variation of the resistivity can be expressed by

$$\Delta\rho = \alpha \cdot \Delta\mathrm{T} \cdot \rho_0 \tag{5-4}$$

Where, $\Delta\rho$ is the change of the resistivity, α is the resistivity-temperature coefficient, ΔT is the change of temperature, and ρ_0 is the original resistivity. With regard to copper, the resistivity-temperature coefficient α = 0.0039 K^{-1}, and the temperature difference ΔT = 60°C. Then the change of the resistivity can be calculated, which is 0.39312×10^{-8} Ω·m. So the resistivity of copper at 80°C is 2.07312×10^{-8} Ω·m.

All the coils of one phase are serial connected and the length of the copper wire can be estimated by the below equation [38]:

$$L_{copper} = \left(2L_{eff} + \left(L_{tooth} + \frac{B_{s1} + B_{s2}}{2}\right) \cdot N_p\right) \cdot N_c \cdot N_s/3 \quad \textbf{(5-5)}$$

Where, B_{s1} and B_{s2} are the top and bottom width of the slot. L_{eff} is the axial length of the motor, L_{tooth} is the width of the tooth, N_p is the winding pitch numbered in slots, N_c is number of the conductors in a coil and N_s is number of all slots, as mentioned before. And the cross-section area of the copper wire is

$$A_{copper} = \mathrm{e} \cdot \frac{A_{slot}}{N_c} \quad \textbf{(5-6)}$$

Where e is winding space factor, which is 0.5 in this case; and A_{slot} is the cross section area of the slot, which can be obtained from the simulation model.

In sum, the copper loss can be computed by

$$P_{cpl} = I^2 \cdot \rho \cdot \frac{\left(2L_{eff} + \left(L_{tooth} + \frac{B_{s1} + B_{s2}}{2}\right) \cdot N_p\right) \cdot {N_c}^2 \cdot N_s}{3\mathrm{e} \cdot A_{slot}} \quad \textbf{(5-7)}$$

When the motor is manufactured, the resistance of the winding can be easy to measure by multi-meters, so that the copper loss can be calculated directly by equation (5-2).

In the alternating current (AC) system, some more issues that are necessary to be considered are skin effect and proximity effect, which make the resistance of a conductor increases with the AC frequency. Skin effect is the tendency of AC current becoming distributed so that the current density decreases greatly with the depth inside a conductor. In other words, the current tends to flow at the skin of the conductor and the skin depth is usually used to describe the severity level of skin effect [221]:

$$\delta = \sqrt{\frac{\rho}{\pi f \mu_0 \mu_r}} \quad \textbf{(5-8)}$$

where δ is the skin depth, f is the operating frequency, ρ and μ_r are the resistivity and relative permeability of the conductor. In this case, copper wires with diameter of 0.6mm are used, and the skin depth at rated speed is 8.23 mm

that is much larger than the diameter of the copper conductor. So the skin effect can be neglected in our study case.

In multi-stranded coil systems, the current density distribution in one conductor becomes non-uniform because of the alternating magnetic field associated to the AC current in adjacent conductors. This phenomenon is termed the proximity effect. According to [222], the increment factor caused by proximity effect can be represented by

$$k_{rpac} = \frac{R_a - R_{dc}}{R_{dc}} = \frac{\zeta}{2}\frac{\sinh\zeta + \sin\zeta}{\cosh\zeta - \cos\zeta} - 1 \quad \textbf{(5-9)}$$

$$\zeta = \frac{d_c\sqrt{\pi}}{2\delta} \quad \textbf{(5-10)}$$

where R_a and R_{dc} are AC and DC resistances of the winding respectively, ζ is an intermediate parameter, d_c is the diameter of the copper wire in the stator slots, and δ is the skin depth calculated by Equation (5-8). According to the parameters of the proposed motor design, the increment factor k_{rpac} is calculated by the above equations (5-9) and (5-10). k_{rpac} is less than 10^{-7}, so the proximity effect can also be ignored for the copper loss estimation.

From the discussion above, both of the skin effect and proximity effect can be ignored in our study, and thus the estimation of copper losses considers only considering the ohmic losses of DC resistance.

5.1.3 Theoretical Analysis of Core Loss

Another commonly found loss in motors is iron loss that comes from the magnetic flux undergoing time variations and intersects with the core. It increases drastically at high rotation speeds and high magnetic flux densities. The increase of core loss can lead to rise in temperature and a reduction in efficiency. Consequently, it is of great importance to predict iron loss at the motor design stage.

Iron loss incorporates hysteresis loss and eddy current loss. Hysteresis loss is produced by magnetic hysteresis effect. As shown in Figure 5-3(a), there is a

net energy flowing from current source to coil-core assembly during a cycle of hysteresis loop. The loss of power is called hysteresis loss, which goes to heat the core. Eddy current loss is produced by eddy current that is generated when the ferromagnetic core undergoes time variations of magnetic flux. The cross section of a core is illustrated in Figure 5-3(b), through which the magnetic flux is rapidly changing. Assuming a path in this cross section, voltage is induced in the path because of the time variation of flux enclosed by the path, and eddy current flows around the path accordingly. Because core material has resistance, an ohmic loss is caused by the eddy current and appears as heat in the core, which is called eddy current loss.

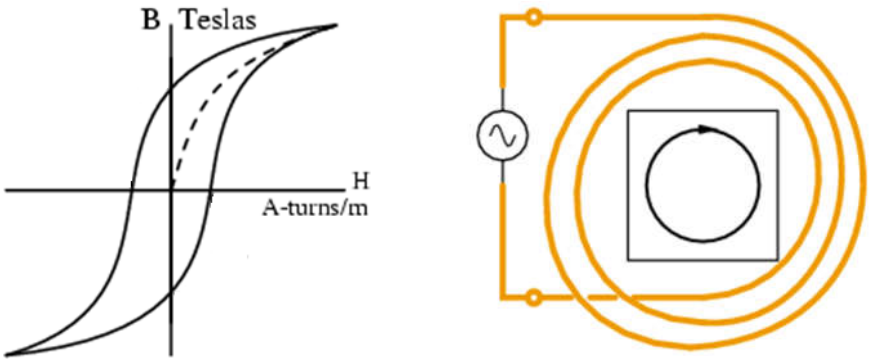

(a) Hysteresis loss (b) Eddy current loss

Figure 5-3 Mechanism of hysteresis loss and eddy current loss

Both of these losses increase when the magnetic flux density increases or the time variation frequency rises. The principles of the computation algorithm are summarised as follows.

The iron-core loss is expressed as:

$$p_v = p_h + p_c + p_e = K_1 B_m^2 + K_2 B_m^{1.5} \quad \textbf{(5-11)}$$

Where the eddy-current loss is

$$p_c = k_c (f B_m)^2 \quad \textbf{(5-12)}$$

The hysteresis loss is

$$p_h = k_h f B_m^2 \quad \textbf{(5-13)}$$

And the excessive loss is

$$p_e = k_e(fB_m)^{1.5} \quad \textbf{(5-14)}$$

Therefore

$$K_1 = k_h f + k_c f^2 \quad \textbf{(5-15)}$$

$$K_2 = k_e f^{1.5} \quad \textbf{(5-16)}$$

The classical eddy-current loss coefficient is calculated directly as

$$k_c = \pi^2 \sigma \frac{d^2}{\delta} \quad \textbf{(5-17)}$$

Where σ is the conductivity and d is the thickness of one lamination sheets. Minimise the quadratic form to obtain K_1 and K_2.

$$\mathrm{err}(K_1, K_2) = \sum_i [p_{vi} - (K_1 B_{mi}^2 + K_2 B_{mi}^{1.5})]^2 = min \quad \textbf{(5-18)}$$

where P_{vi}, B_{mi} – the i-th point of the data on the loss characteristics curve. The other two loss coefficients are obtained as

$$k_h = \frac{K_1 - k_c f_0^2}{f_0} \quad \textbf{(5-19)}$$

$$k_e = \frac{K_2}{f_0^{1.5}} \quad \textbf{(5-20)}$$

where f_0 is the testing frequency for B-H Cure.

Unfortunately, it is extremely difficult to obtain iron losses accurately in studies that use the magnetic circuit method or rules of thumb. In order to obtain them accurately, one needs to find the distribution and time variations of the magnetic flux density in each part of the motor after accounting for a fine geometry and the material's nonlinear magnetic properties. Using the finite element method (FEM) is essential in order to carry out this kind of detailed analysis. In order to simulate the physical phenomena in an analysis, firstly FEA models are created and simulated under various loading conditions. Then the time variations in the magnetic flux density produced in each part of the motor are obtained. With the

results of the amplitude and frequency of the magnetic flux density variations for each element in the model, the iron loss distribution and iron losses can be calculated according to equations (5-11)–(5-20) by referring to the material's iron loss characteristics.

5.2 Iron Loss Analysis Considering Special Conditions

Iron loss makes up a particularly large proportion of total loss in the high rotation region, and reducing iron loss and increasing motor efficiency is a critical issue for motor design. Apart from the general analysis in last section, iron loss is also affected by other factors, such as stator assembly (press fitting or shrink fitting), carrier harmonics by PWM vector control. In this section, these special conditions are considered and thoroughly discussed in the iron loss analysis of the designed ferrite IPM machine.

5.2.1 Iron Loss Analysis Considering Press Fitting Effect

The construction process of motors includes a mounting process. A common and inexpensive way of mounting the stator in the housing is the heat to press approach, also known as shrink fitting. The housing is fitted over the stator to retain it in position and to prevent it moving from the designed position as well as protecting the lamination [223]. There are other methods to mount the stator

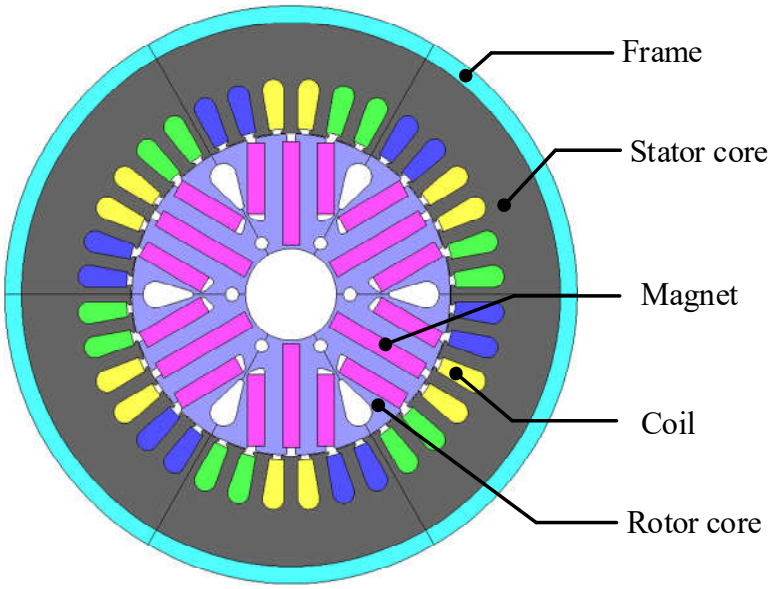

Figure 5-4 The geometry of the analysed motor

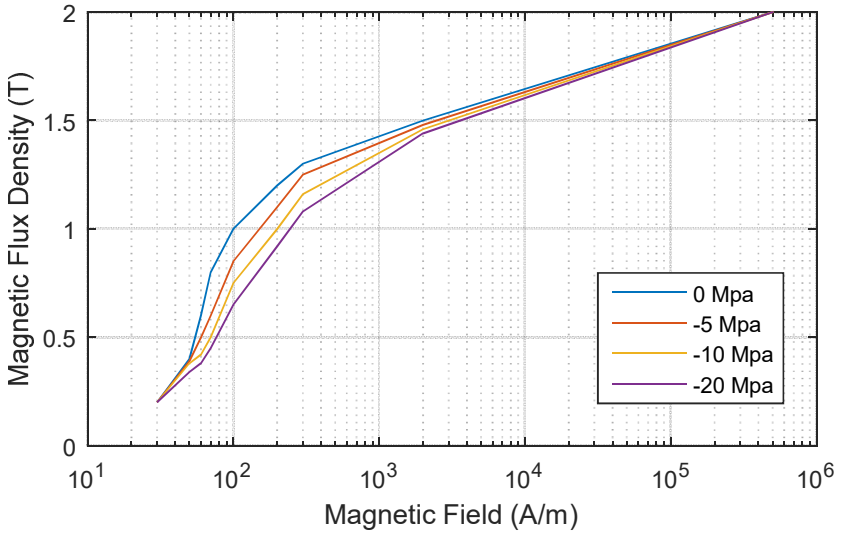

Figure 5-5 Stress dependent B-H curve

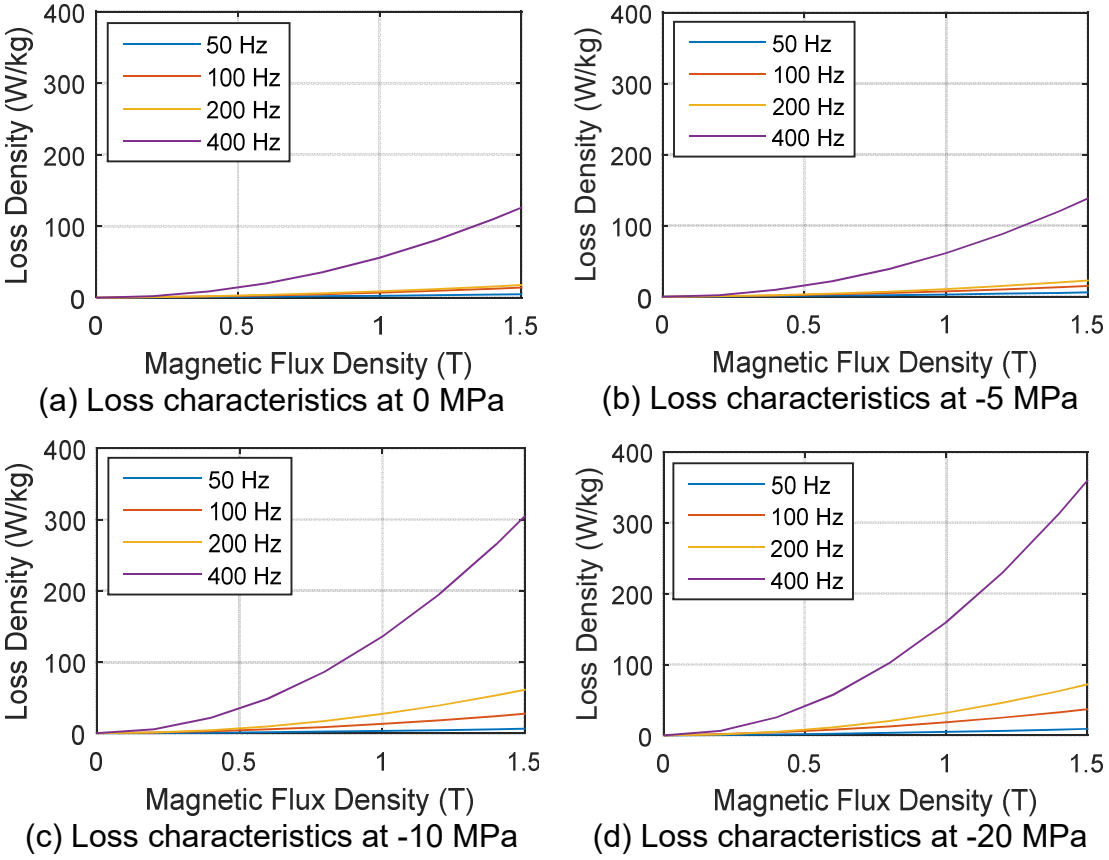

(a) Loss characteristics at 0 MPa (b) Loss characteristics at -5 MPa

(c) Loss characteristics at -10 MPa (d) Loss characteristics at -20 MPa

Figure 5-6Loss characteristics of the stator core at different press

in the housing frame, such as press fitting. The press fitting or shrink fitting applies a high stress on the stator and the stress may alter the magnetic property of the stator core and increase the iron loss. Thus it is important to take this stress into account when evaluating iron loss. The iron loss considering the

effect of press fitting or shrink fitting are analysed in the current subsection and next subsection respectively. Since the rotor is separated from the stator, the increased stress on the stator does not affect the rotor directly and can be considered irrelevant to the rotor loss. Therefore, only the stator core is discussed in the two subsections.

A press fitting is a fastening between two parts which is achieved by friction after the parts are pushed together, rather than by any other means of fastening [224]. For metal parts in particular, the friction that holds the parts together is often greatly increased by compression of one part against the other, which relies on the tensile and compressive strength of the materials the parts are made from. The press fitting process is generally done by specific hydraulic press machine and the amount of the press is determined by how much the inference is between stator core and housing frame. The geometry of the analysed motor and the names of each component are shown in Figure 5-4. The stator core is assembled into the housing frame by interference fit. The characteristics of the stator core are varied by the press upon it. The magnetic flux density of the steel sheet decreases when the press is increased from 0 MPa to -20MPa, which is shown in Figure 5-5. The weakened flux density will deteriorate the generation of output torque and affect the iron loss. It is known that the loss density of the steel sheet increases drastically with rotation speeds and magnetic flux densities. From Figure 5-6 it is seen that the loss density also grows when the press is increased. The inherent characteristics of stator core material determine that the iron loss is affected by the press upon it.

The stress caused by press fitting has its own distribution, so in order to evaluate the iron loss with good accuracy, it is necessary to correctly obtain the distribution of the stress generated during press fitting. When different interferences are applied, the corresponding principal stress distributions are obtained by FEA simulation and shown in Figure 5-7. The principal stresses are the components of the stress tensor when the basis is changed in such a way that the shear stress components become zero. Normally the stress effect is presented by the principal stress.

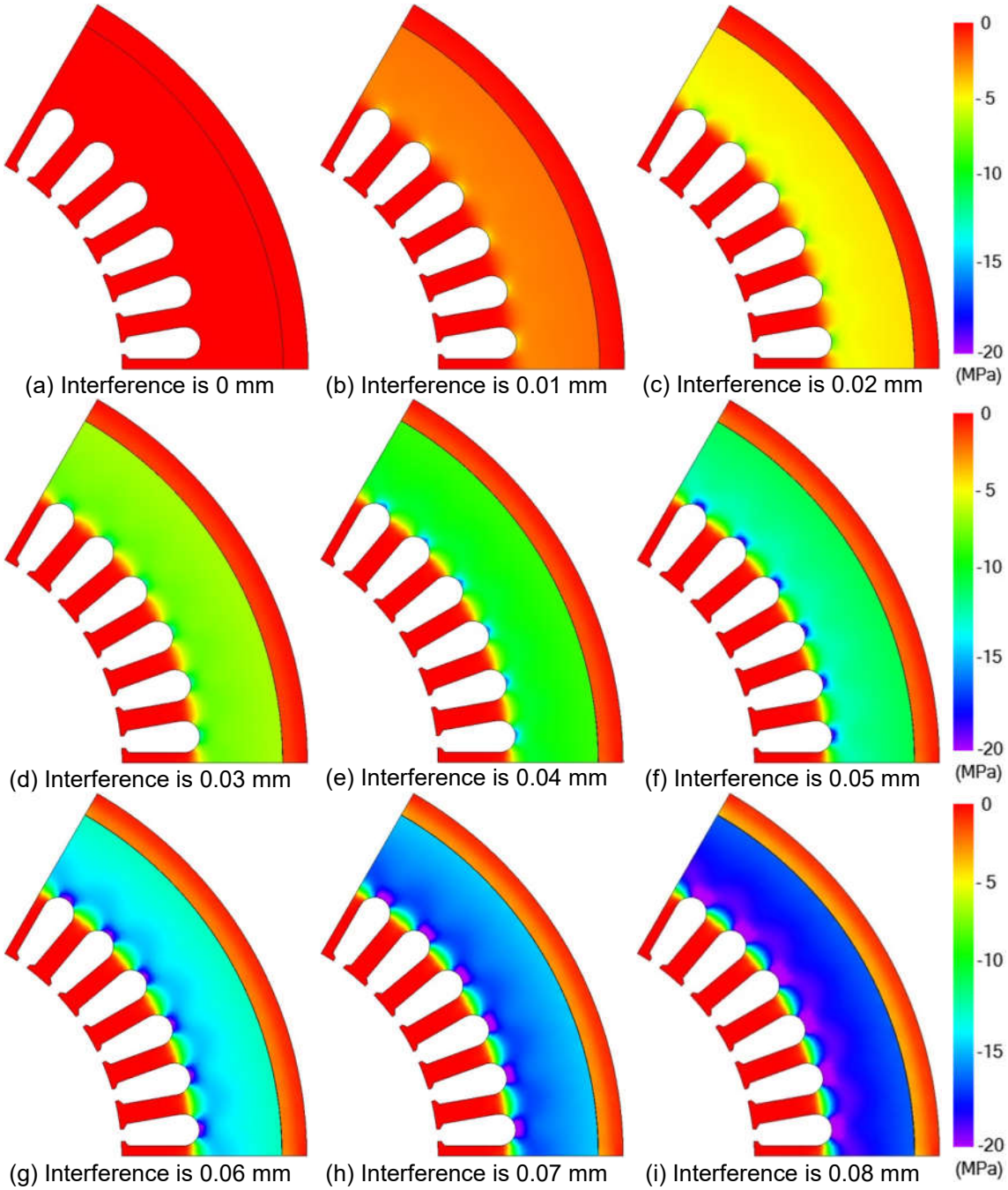

Figure 5-7 Principal stress distribution when motor is press fitted

Comparing the nine subfigures in Figure 5-7, when the interference is enlarged from 0 to 0.08 mm, the principal stress in the stator yoke is increased significantly. But the stator teeth are not affected by the pressure from the frame as they are loose and have space between each other. The largest stress change happens around the slot inner edge, which changes from 0 MPa to about 20 MPa. Because there is no supporting force from the slot side, the

pressure from the yoke side accumulates around the corner. The press in the stator yoke distributes nearly evenly, and it is increased from 0 to about 18.4 MPa. Thus the press grows about 2.3 MPa for every 0.01 mm interference increment. When the interference is 0.08 mm, the principal stress is about 18.4 MPa in the motor yoke area. The tooth root area is the stress transition region from low pressure to high pressure.

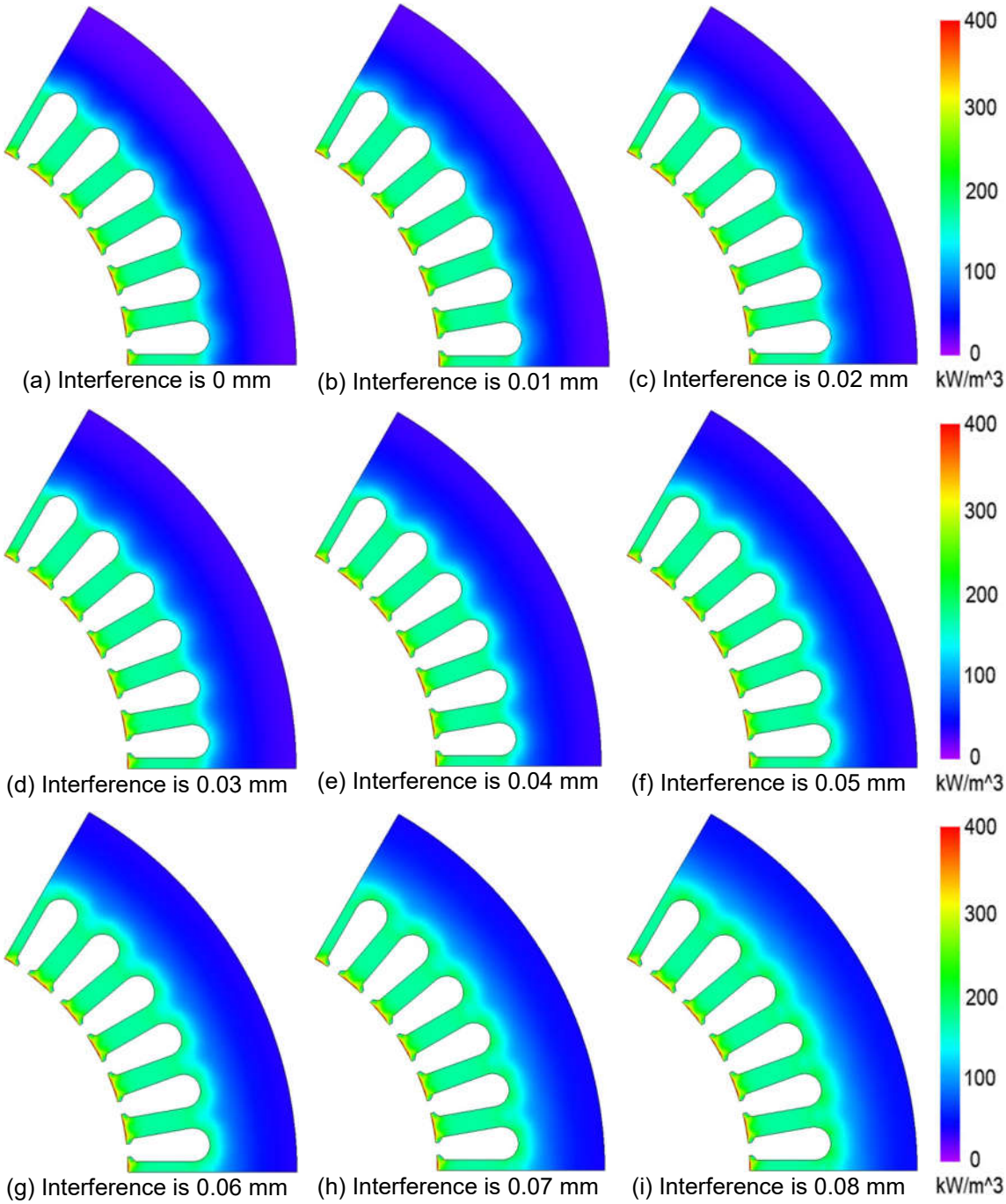

Figure 5-8 Iron loss density distribution with interference at no load condition

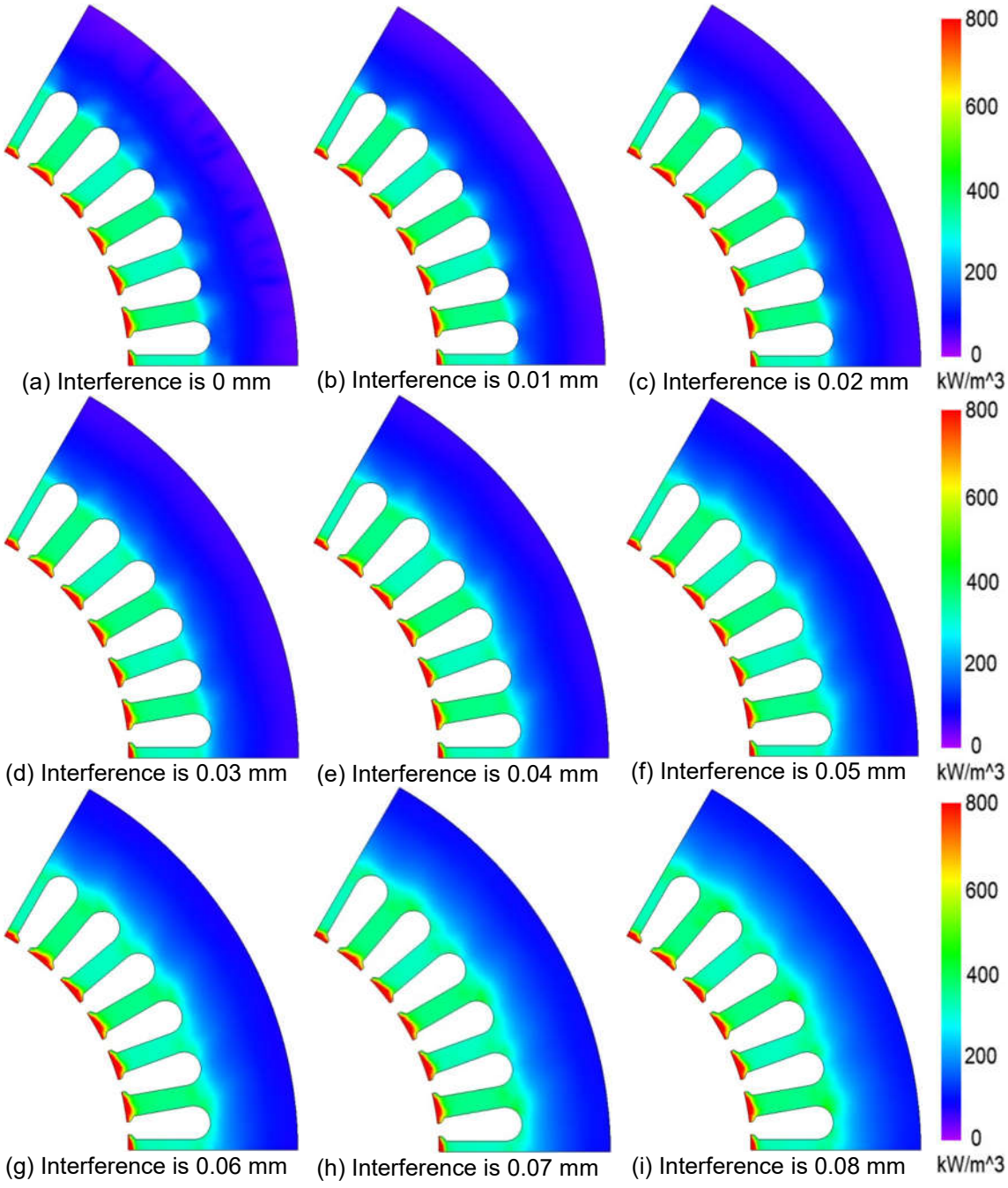

Figure 5-9 Iron loss density distribution with interference at loaded condition

Due to stress influence, the iron loss density of stator core increases with the enlarged interferences. The iron loss density distributions at no load and rated load conditions are shown in Figure 5-8 and Figure 5-9 respectively.

At no load condition, as shown in Figure 5-8, the highest density of iron loss appears at the tips of stator teeth, about 400 kW/m^3, and it is followed by iron loss density of stator teeth, about 200 kW/m^3. The high iron loss density is

mainly caused by the high flux density at the teeth. Comparing the nine subfigures from (a) to (i) in Figure 5-8, there is no obvious changing of the iron loss density around the stator teeth as they do not undergo any stress from the press fitted frame. But the iron loss density of the other part of the stator core increases with the inference dimension as the undergone stress grows as well. Especially around the tooth root areas, the iron loss has noticeable increment from about 100 W/m^3 to 200 kW/m^3. The iron loss density of stator yoke rises as well. Since the flux density of stator yoke is relatively low, the increase of iron loss density is not quite obvious around the yoke area. The trend of the stator iron loss, as illustrated in Figure 5-10, is monotonic but not linear with the change of interference. The nonlinear feature is determined by the nonlinear characteristics of the stator core materials. When interference is enlarged from 0 to 0.08 mm, the iron loss of the stator is increased by 42.5% at no load condition.

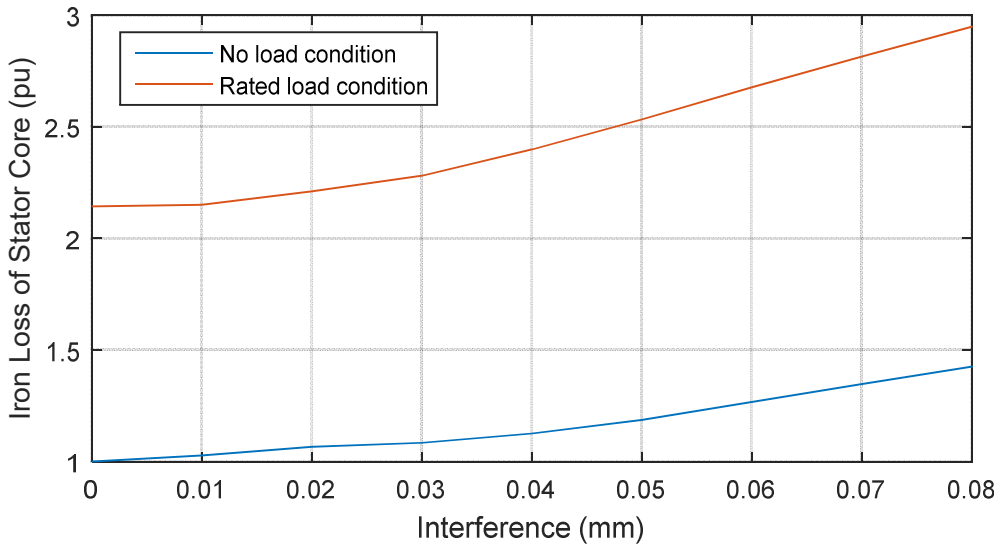

Figure 5-10 Iron losses of stator core increase with interference

When the motor operates at rated load, the flux density of the stator is strengthened by the winding current, and iron loss is increased as well. From Figure 5-9 it is found that the highest iron loss density, more than 800 kW/m^3, happens around the stator teeth tips where the flux density is high and varies frequently. The stator teeth have high iron loss density about 400 kW/m^3, but no obvious difference when the interference is increased just like the no load

condition. The iron loss density at the yoke part of the stator core has noticeable increment especially at the teeth root area. The increment of stator iron loss is shown in Figure 5-10. It has similar tend like that at no load condition, monotonically and nonlinearly, but its value is about 2.3 times that at no load condition. When interference is enlarged from 0 to 0.08 mm, the iron loss of the stator is increased by 37.6% at rated load condition.

From the above analysis it is seen that the significant effects of press fitting on core losses. It is extremely necessary to include the press fitting effect when the iron loss of the stator needs accurate estimation. In addition, on the premise that the assembling fastness is meet, it is better to reduce the interference as much as possible so that to reduce the extra iron loss caused by press fitting effects. For example, if the interference is only 0.01 mm in the case, the iron loss increment of the stator is only about 2.8% at no load condition and 0.34% at rated load condition. And the marginal increase won't affect the overall efficiency much.

5.2.2 Iron Loss Analysis Considering Shrink Fitting Effect

Shrink fitting is quite commonly used for stator lamination core and housing frame assembly. When the housing frame is heated, its diameter expands. After assembled to stator core, the frame cools down and squeezes on the stator. The friction generated by the compression holds the parts together firmly, and the amount of stress arising in shrink fitting depends on how large is the temperature difference of the housing frame. Iron loss is generated when there are magnetic-field variations in steel lamination, and the amount of iron loss depends on the steel sheet's iron loss properties. When shrink fitting is used to strengthen the joint between frames and stator cores with laminated structure, the iron loss properties of steel sheet become worse due to the compressive stress generated during shrink fitting and iron loss is increased as well. So it is important to evaluate iron loss accounting for the effects of the stress from shrink fitting.

In order to evaluate the iron loss with good accuracy, it is necessary to correctly obtain the stress distribution of steel sheet first. Hence, a structure model is built

with the consideration of temperature difference between the stator core and housing frame, and the stress distribution is obtained by FEA calculations. Figure 5-11 shows the principal stress distributions with different temperature differences. The teeth of the stator do not undergo any stress as they are loose and have space between each other. Thus the compressive stress at the teeth is the lowest, almost zero. The back yoke of the stator have a large amount of stress when the housing frame is shrinking fitted to the stator core. The stress is

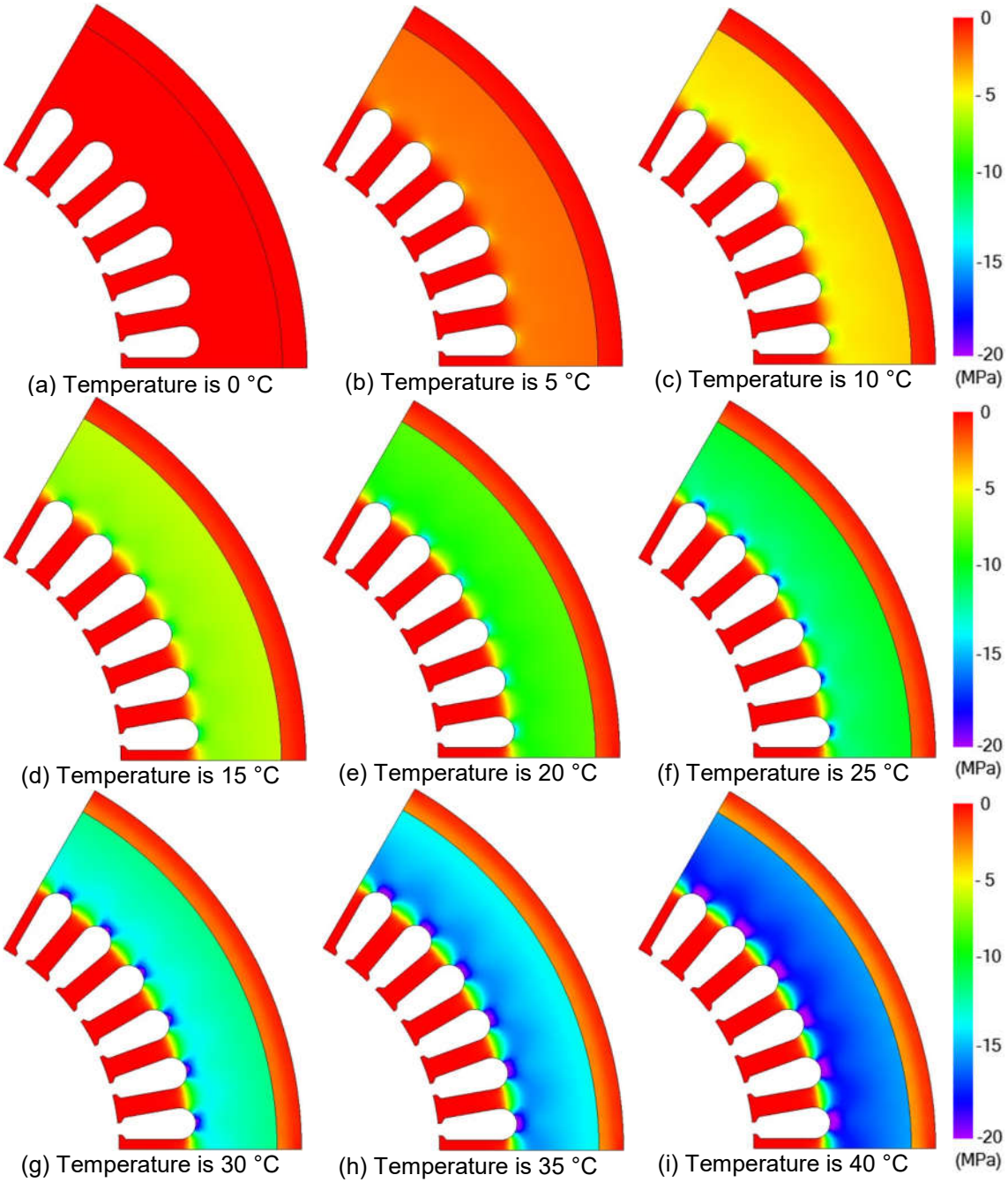

Figure 5-11 Principal stress distribution when motor is shrink fitted

distributed nearly evenly and increased substantially with the temperature differences, from about 2.5 MPa at 5°C temperature difference to about 18 MPa at 40°C temperature difference. The compressive stress caused by the frame shrinking in the radial direction is larger at the slots. This is because the stress is dampened towards the tips of the teeth, while it cannot be dampened at the slots and so concentrates there. When the temperature difference is about 40°C, the stresses at the concentrated areas are more than 20MPa.

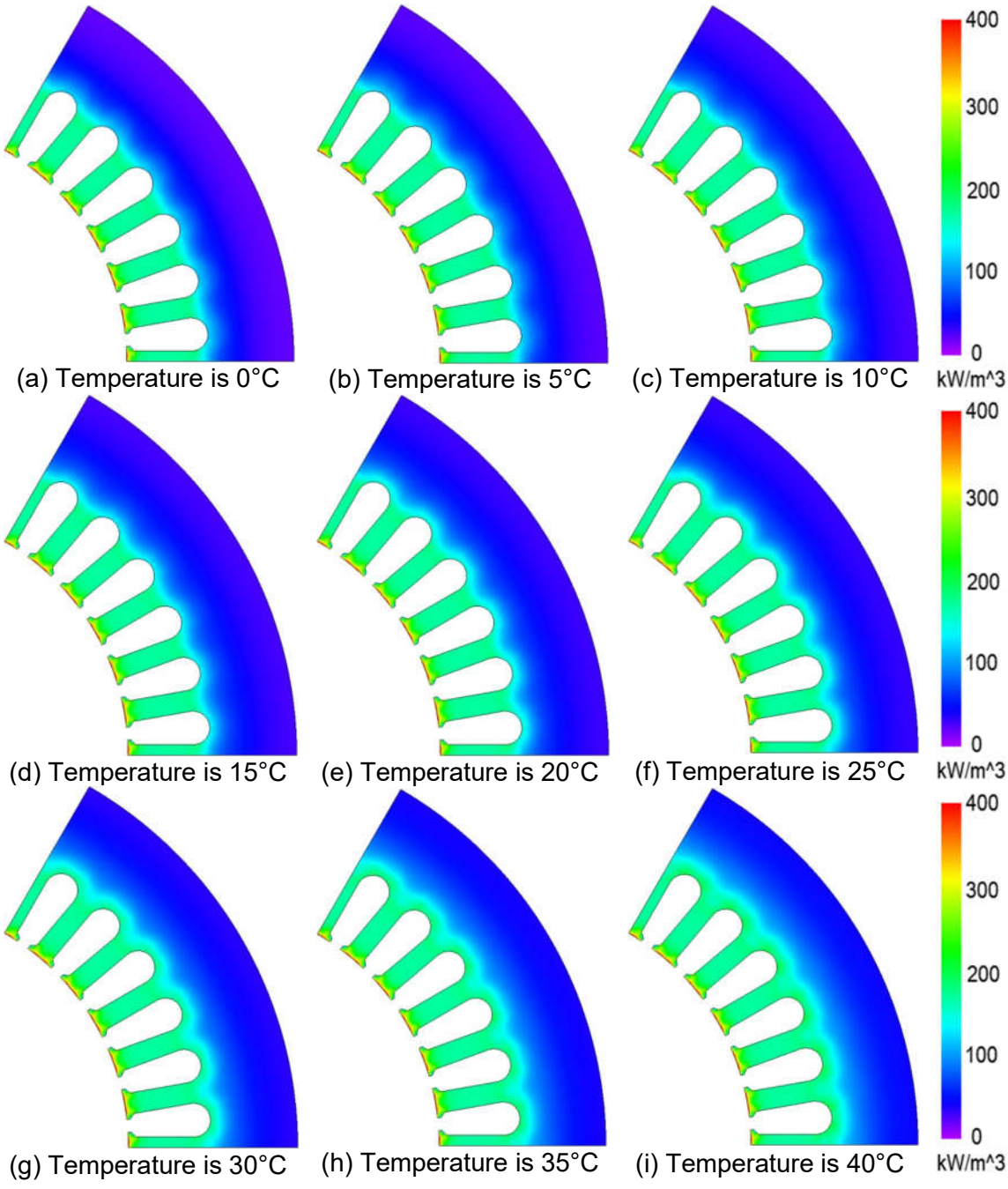

Figure 5-12 Iron loss density distribution with temperature at no load condition

The high stress on the stator deteriorates the magnetic properties and increases the iron loss of the stator core. Figure 5-12 shows the iron loss density distribution at no load condition. The stator tooth endures high iron loss due to its high flux density, and its average iron loss density is about 200 MPa. The highest density of iron loss locates around the tooth tips, about 400 MPa. Since there is no change of compressive stress in the stator tooth, the iron loss

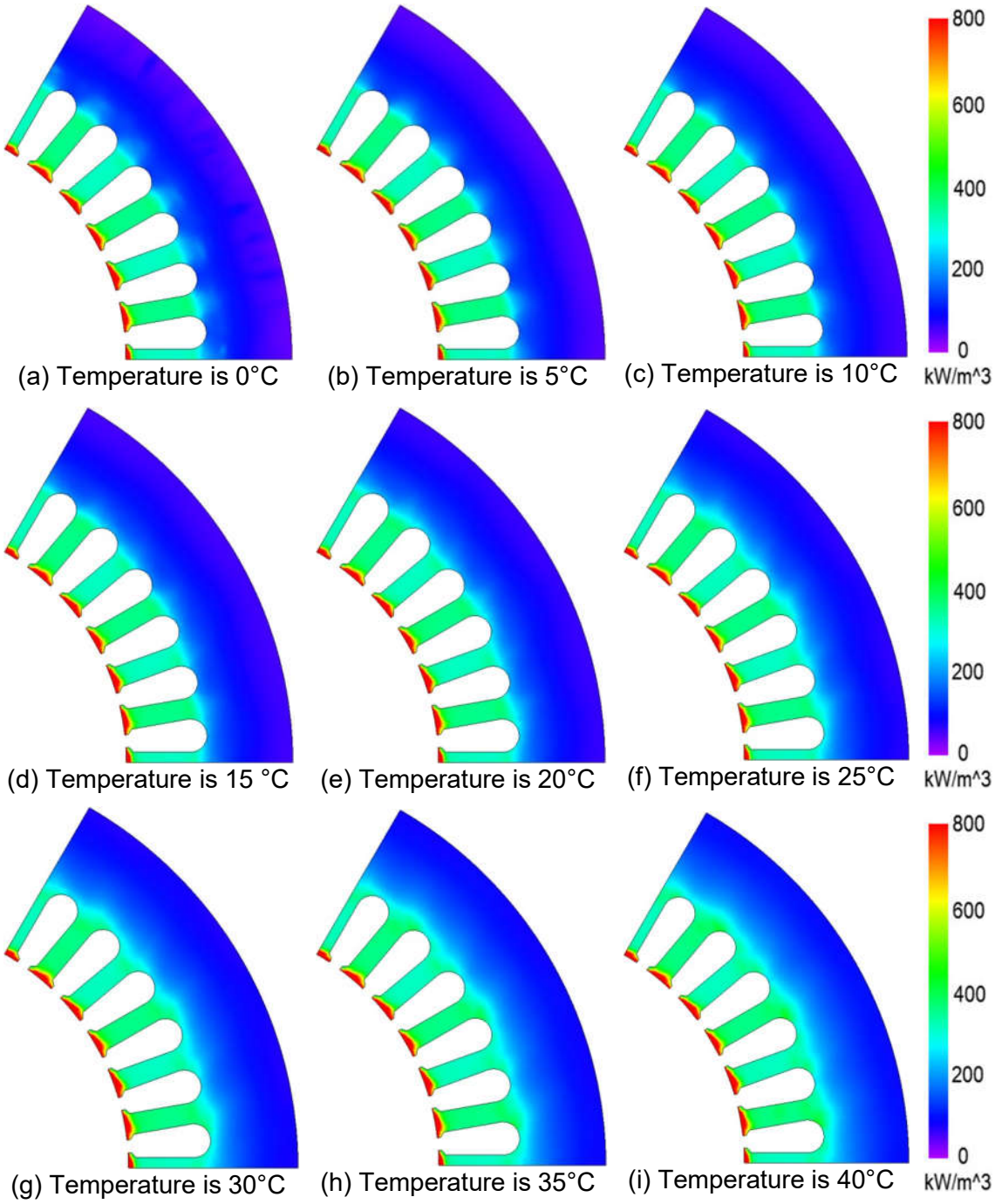

Figure 5-13 Iron loss density distribution with temperature at loaded condition

density of stator tooth does not vary with temperature differences. Because of the stress generated by shrink fitting, the iron loss density at the stator yoke increases with the temperature differences. Since the flux density of stator yoke is relatively low, the increase of iron loss density is not quite obvious. The iron loss has noticeable increment at the slot end region where compressive stress accumulates, and it is increased from around 100 kW/m^3 with 5°C temperature difference to 200 kW/m^3 with 40°C difference. The trend of stator iron loss growing with temperature differences at no load condition is illustrated in Figure 5-14. The iron loss of stator core grows monotonically but nonlinearly due to its nonlinear features of core material.

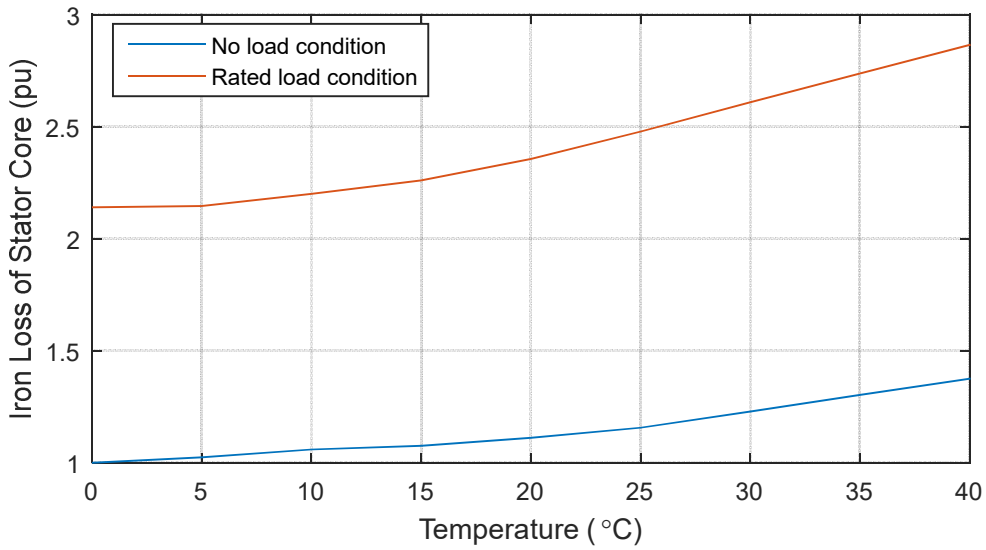

Figure 5-14 Iron losses of stator core increase with interference

More iron loss is induced when the temperature difference become larger, which causes more stress on stator core. When the temperature difference is increased to 40°C, the stator core has 37.6% more iron loss owing to the stress generated by shrink fitting. The iron loss density distribution of the shrink fitted stator core at rated load condition is shown in Figure 5-13. The winding current strengthens the flux density in the stator, and more iron loss is induced as well. The highest iron loss density of the stator core appears at the tooth tips, more than 800 Mpa, and it is followed by the iron loss density of stator teeth with average value about 400 MPa. As there is no stress arisen on the teeth, the iron loss density does not change with temperature difference. However, when the

temperature difference increases from 0 to 40°C, the iron loss density around the root of the teeth endures large variations, from about 200 MPa rising to 400 MPa. The iron loss density of motor yoke is slightly increased when the temperature difference is enlarged, and the average value is about 100 MPa. The changing progress of the stator iron loss at rated load condition is also shown in Figure 5-14. Like that at no load condition, the iron loss of stator core grows monotonically but nonlinearly with the temperature differences. But the iron loss at rated load is about 2.3 times larger than that at no load condition. With 40°C temperature difference, the stator core generates 33.8% more iron loss due to the stress by shrink fitting.

From the above analysis it is seen that the iron loss of stator core is affected by the stress that is aroused by the shrink fitting between the stator core and housing frame. It is extremely necessary to include the shrink fitting effect when the iron loss of the stator requires accurate estimation. In addition, it is better to reduce the temperature difference as much as possible so that to reduce the extra iron loss caused by shrink fitting effects

5.2.3 Comparison between Press Fitting and Shrink Fitting

Comparing the graphics Figure 5-7–Figure 5-10 with Figure 5-11–Figure 5-14, it is found that lots of similarities between the effects of press fitting and shrink fitting. Both of them have similar compressive stress distribution, similar iron loss density distribution, and iron loss increasing trend. That’s because the mechanisms of gaining extra iron loss for both press fitting and shrink fitting are same. The magnetic flux density and loss characteristics of the iron core are affected by the press upon it, which are depicted in Figure 5-5 and Figure 5-6.

When the stator core is assembled into housing frame by press fitting or shrink fitting, a large amount of stress will be generated in the core, especially in the yoke region. This stress worsen the magnetic properties and iron loss properties of the stator core, thus a larger amount of iron loss is produced in the stator. The only difference between the two interference fittings is the cause of joint pressure. The compressive stress of press fitting is formed by mechanical interference between stator core outer dimension and housing frame inner

dimension; and the compressive stress of shrink fitting comes from the squeezing force of housing frame when it cools down from the heated and expanded state.

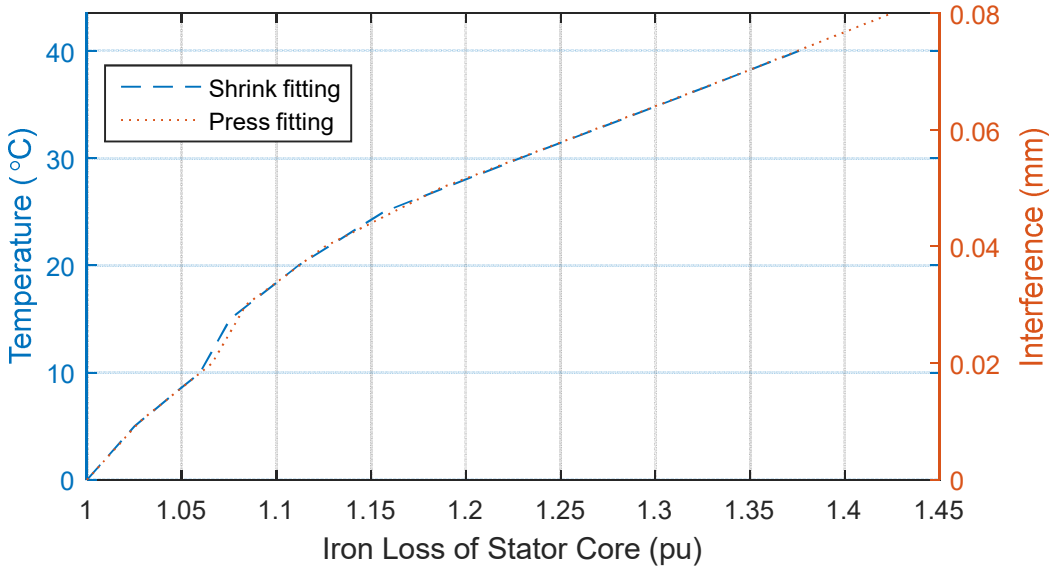

Figure 5-15 Comparison between press and shrink fitting at no load condition

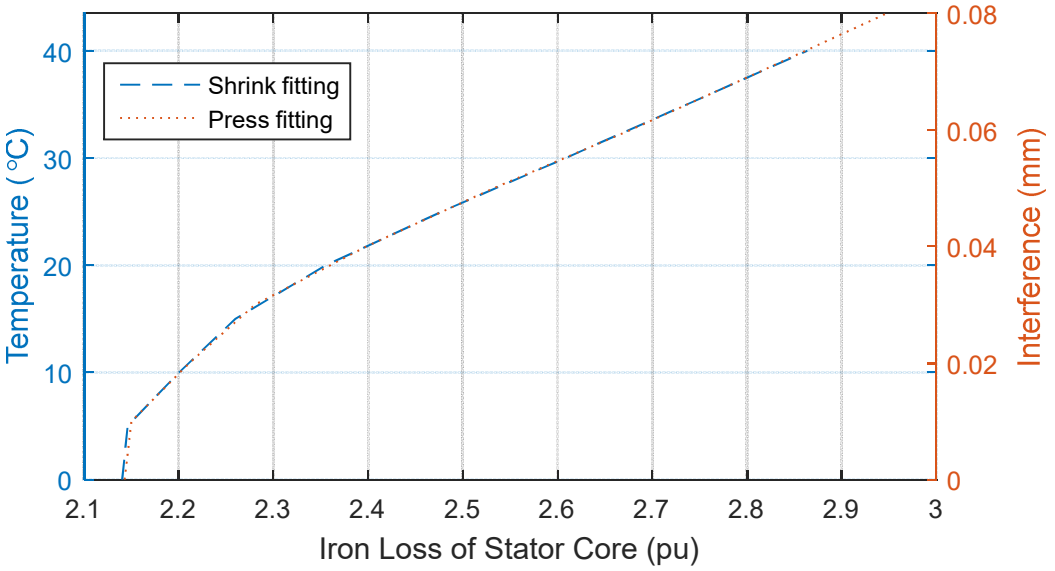

Figure 5-16 Comparison between press and shrink fitting at rated load condition

The effects of press-fitting and shrink-fitting to stator iron losses are compared in Figure 5-15 and Figure 5-16 at no load and rated load condition. As shown in Figure 5-15, at no load condition, when the iron loss of stator core affected by shrink fitting rises from 1 pu to 1.38 pu, the temperature difference is increased from 0 to 40°C; and when the iron loss of stator core affected by press fitting

rises from 1pu to 1.42 pu, the mechanical interference is increased from 0 to 0.08 mm. But if the Y axis of the graph is adjusted, making 43.5°C temperature corresponding to 0.08 mm interference, it is seen that the stator core iron losses affected by press fitting and shrink fitting have good agreement. Similarly to the rated load condition shown in Figure 5-16, when the iron loss of stator core that is affected by shrink fitting rises from 2.14 pu to 2.86 pu, the temperature difference is increased from 0 to 40°C; and when the iron loss of stator core that is affected by press fitting rises from 2.14 pu to 2.95 pu, the mechanical interference is increased from 0 to 0.08 mm. Adjusting the Y axis of the graph to make 43.5°C temperature corresponding to 0.08 mm interference, it is found that the stator core iron losses affected by press fitting and shrink fitting have great agreement.

From the comparison it is seen that the press fitting and shrink fitting have similar influence on the iron loss of stator core. Which one is more suitable to the specific machine will be determined by the facilities of manufacturing company and the cost of operating. The designed ferrite IPM motor in the thesis is carried out by shrink fitting that does not require costly pressing equipment.

5.2.4 1Iron Loss Analysis Considering PWM Effect

Vector controls using a PWM (Pulse Width Modulation) control are commonly included in the drive circuits of high efficiency IPM motors. A PWM control makes it possible to adjust the phase or amplitude of a current according to load and rotation speed, so they can achieve high efficiency in a wide operation range. The control frequency of a PWM is called a carrier frequency. To form the current waveform supplied by the PWM control, the carrier harmonic current is superimposed on the basic wave current. This carrier harmonic current applies a high-frequency magnetic field to each part of the motor. As a result, extra iron loss is generated in the IPM motor's core. The total amount of these losses is not a dominant factor, but they can be a hindrance when trying to raise efficiency. The effects of a carrier harmonic against an IPM motor's iron loss can be evaluated by inputting the actually measured current waveforms into a magnetic field analysis.

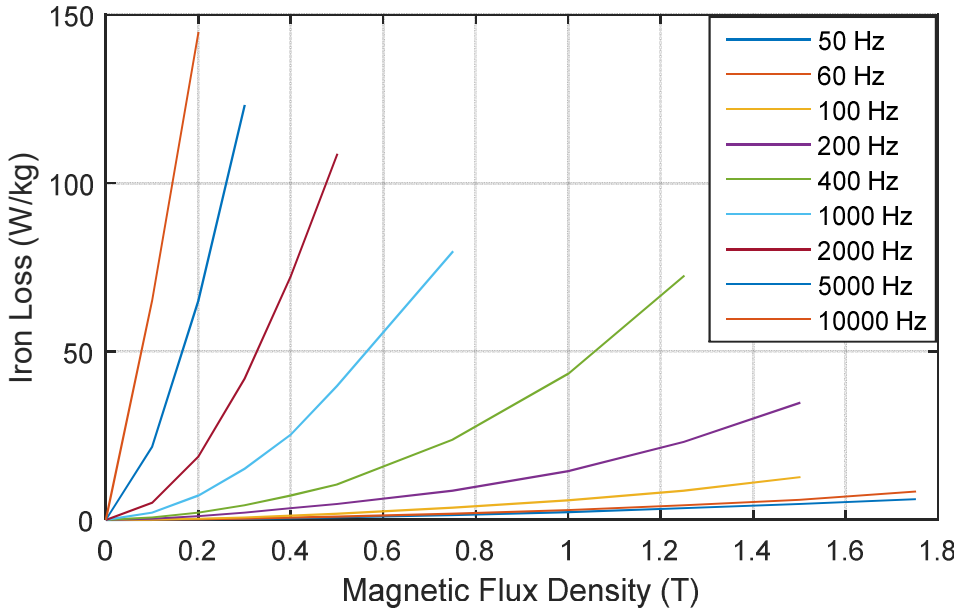

Figure 5-17 Iron loss characteristics of stator and rotor cores

Magnetic flux that varies with time is produced in each part of a motor when a current that contains a PWM carrier harmonic is input. The main components of iron loss are eddy current loss, which is caused by eddy currents produced from time variations in the magnetic flux, and hysteresis loss, which is produced from magnetic hysteresis. Both of these increase when the changes in the magnetic flux density get larger and when the time variation frequency (rotation speed, frequency) rises, as they are indicated in equations (5-12) and (5-13). The iron loss characteristics of stator and rotor cores are illustrated in Figure 5-17. The iron loss density is increased with magnetic flux density and variation frequency. When the frequency is very high, even if the magnetic flux density is relatively low, lots of losses can be generated in the motor cores. That's why the high-frequency harmonic components of the current generated by PWM inverter are able to aggrandise iron losses.

The control frequency of the PWM inverter that used to drive the ferrite IPM motor is 8 kHz. When the motor is operating at rated speed and load, the three-phase current is measured and depicted in Figure 5-18. Since the motor has three pole-pairs, the fundamental frequency of the current waveform is 75 Hz and the period is 0.013333 s at rated speed 1500 rpm. The amplitude of the fundamental current component is 8.8 A, which is same as the amplitude of

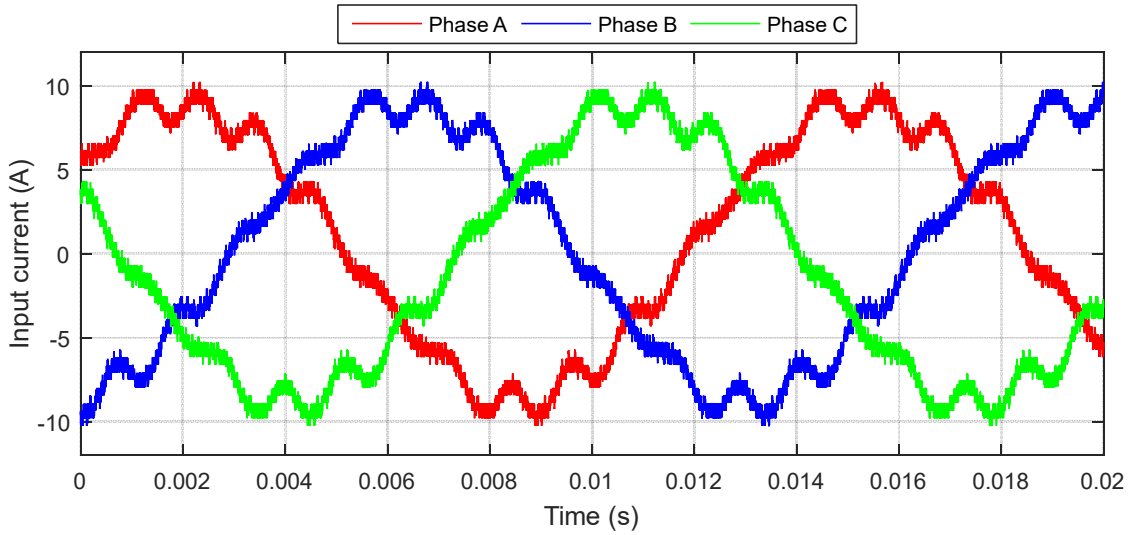

Figure 5-18 Actual current waveforms generated by PWM inverter

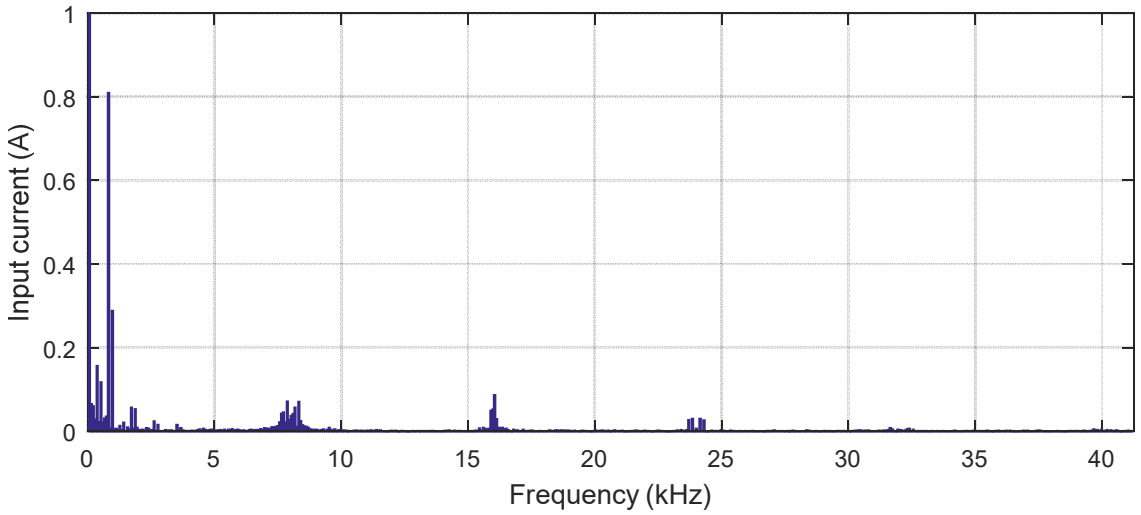

Figure 5-19 Spectrum of actual current waveforms generated by PWM inverter

conventional sinusoidal current. Apart from the fundamental component the measured current has a lot of harmonic components that are displayed in Figure 5-19, which make the actual current waveform bump not in an ideal sinusoidal shape. Aside from the major harmonics in relatively low frequency, it is worth noting that the PWM inverter generated current has many high-frequency harmonic components mainly concentrating around 8 kHz, 16 kHz, 24 kHz, 32 kHz and 40 kHz. These high-frequency components are caused by PWM carrier waves, the frequency of which is 8 kHz. Thus, the motor input current from PWM inverter drive will induce more iron loss than that from conventional sinusoidal current drive. A comparison of the iron losses,

hysteresis losses, and eddy current losses when the IPM motor is driven by a PWM inverter and a sinusoidal current are shown in Table 5-1.

Table 5-1 Ratio of iron losses caused by different current drives

	Rotor Core		Stator Core	
	Sinusoidal current drive	PWM inverter drive	Sinusoidal current drive	PWM inverter drive
Iron loss	9.49 W	13.55 W	38.28 W	46.54 W
Hysteresis loss	1.66 W	2.12 W	14.79 W	15.53 W
Eddy current loss	7.83 W	11.43 W	23.49 W	31.01 W

The iron losses in both the rotor core and the stator core increase, when the IPM motor is run by a PWM inverter. The eddy current losses increase the most severely, increasing 46% in the rotor core, and 32% in the stator core. The hysteresis losses are aggravated as well, rising 28% in the rotor core, and 5% in the stator core. Totally, the iron losses of the whole motor are increased from 48 W in sinusoidal current drive to 60 W in PWM inverter drive by 26%, with eddy current losses increased by 36% and hysteresis losses increased by 7%. The different losses of the IPM motor driven by a PWM inverter and a sinusoidal current drive are clearly illustrated in Figure 5-20 and Figure 5-21 by frequency spectra, which help to make comparisons.

Since the studied ferrite IPM motor has 6 magnetic poles in the rotor and 36 slots in the stator, the fundamental frequencies are 75 Hz in the stator core and 450 Hz in the rotor core when it is run at rated speed 1500 rpm. Therefore, the significant components of eddy current loss and hysteresis loss in the rotor core are the multiples of the fundamental frequency 450 Hz, such as 900 Hz, 1800 Hz, and 2700 Hz, as shown in Figure 5-20. When the motor is driven by PWM inverter, more eddy current losses are generated in the rotor core, than it is driven by sinusoidal current. That is because the eddy current loss in PWM inverter drive has a larger 2^{nd} order component (900 Hz) and lots of high-frequency components around 8000 Hz that are caused by PWM carrier waves. The difference of hysteresis loss in the rotor is primarily from the 2^{nd} order component at 900 Hz. The PWM driven motor has 34% more hysteresis loss.

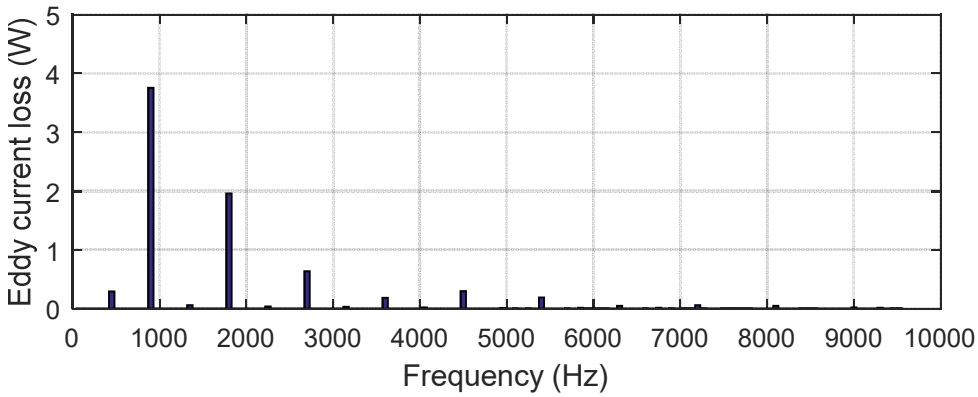

(a) Eddy current loss in sinusoidal current drive

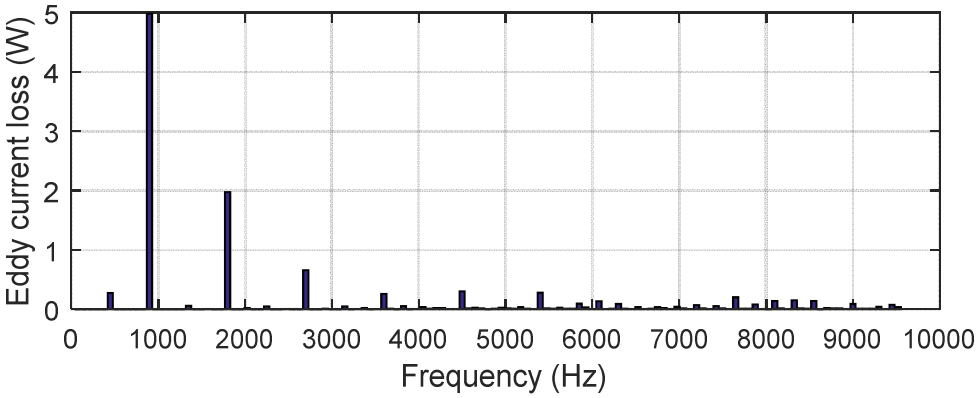

(b) Eddy current loss in PWM inverter drive

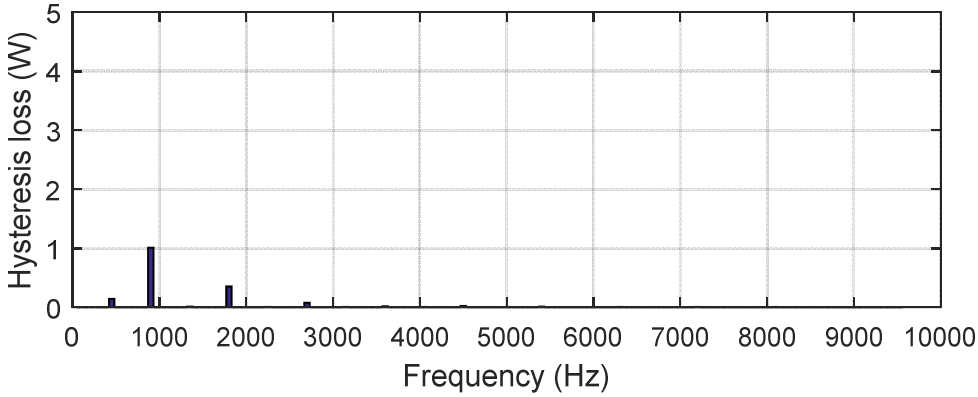

(c) Hysteresis loss in sinusoidal current drive

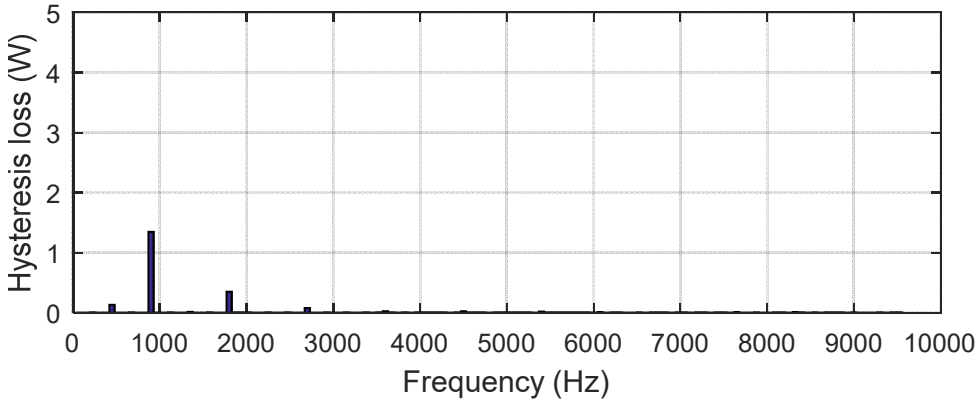

(d) Hysteresis loss in PWM inverter drive

Figure 5-20 Iron loss frequency components in the rotor core

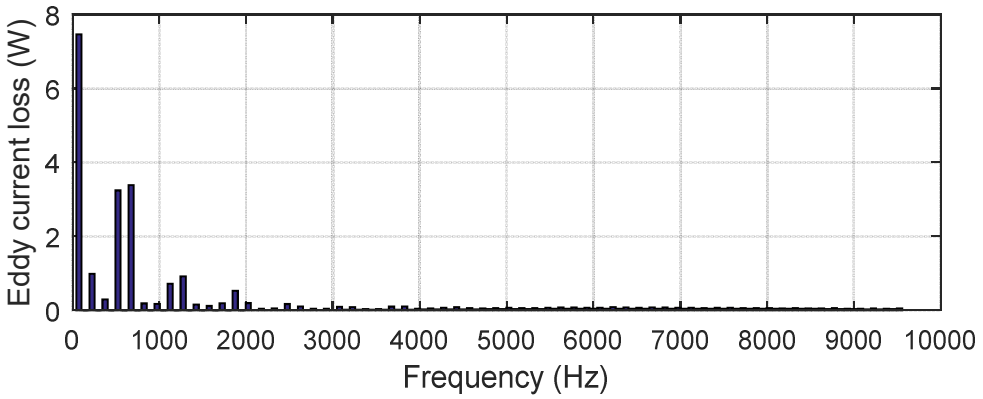

(a) Eddy current loss in sinusoidal current drive

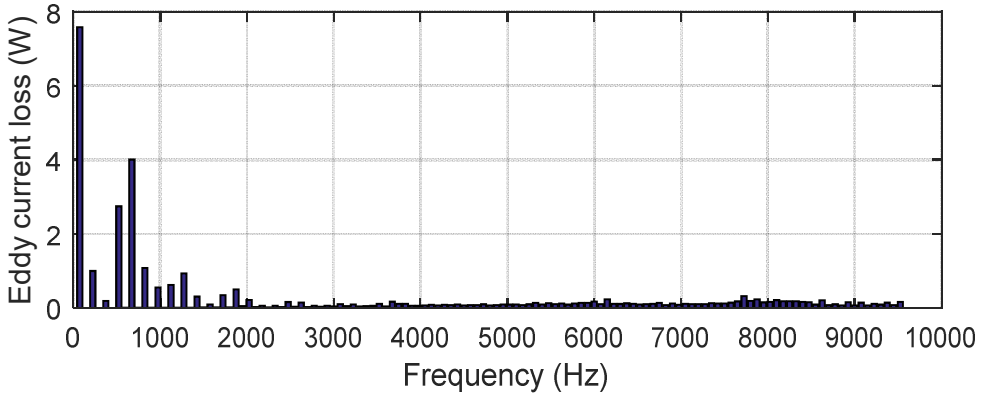

(b) Eddy current loss in PWM inverter drive

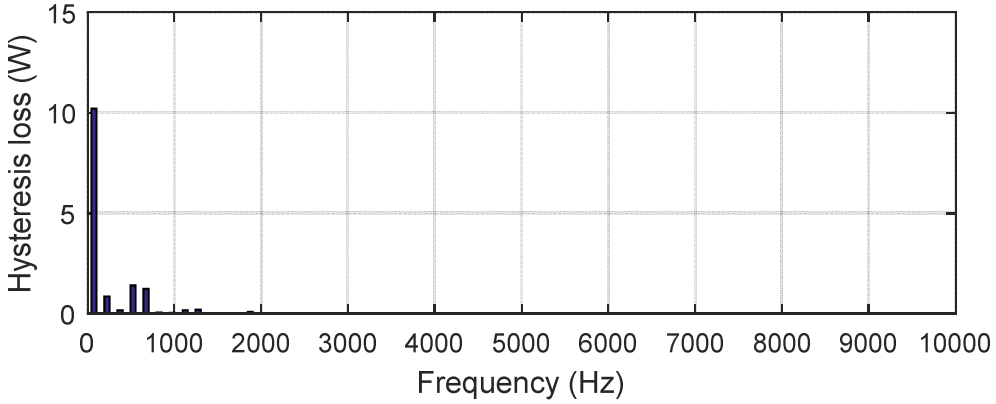

(c) Hysteresis loss in sinusoidal current drive

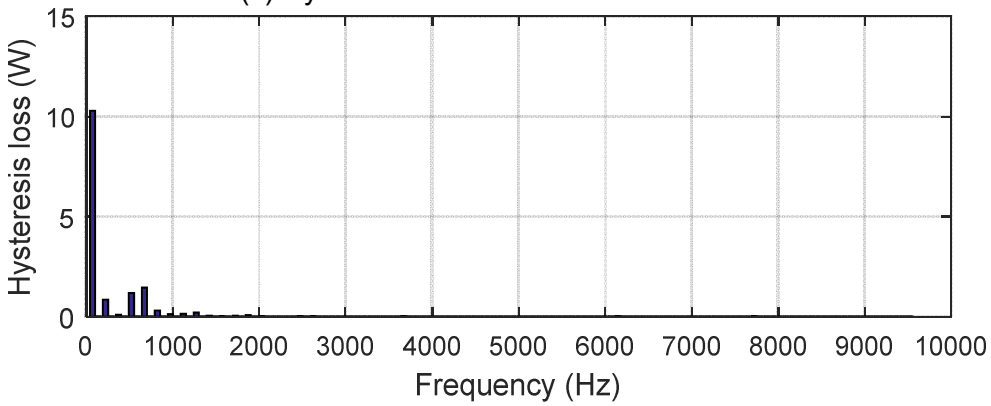

(d) Hysteresis loss in PWM inverter drive

Figure 5-21 Iron loss frequency components in the stator core

The significant components of eddy current loss and hysteresis loss in the stator core are the multiples of the fundamental frequency 75 Hz, such as 75 Hz (1^{st} order), 525 Hz (5^{th} order), and 675 Hz (7^{th} order), as shown in Figure 5-21. The IPM motors driven by both PWM inverter and sinusoidal current have almost same amount of eddy current loss in the stator in relatively low frequency, under 3000 Hz. But in the high-frequency region the PWM inverter driven motor exhibits more eddy current losses, especially around 8000 Hz, which are generally induced by PWM carrier waves. There is no much difference of the hysteresis loss in the stator core, and only some of the low-frequency components in PWM inverter driven motor have slightly larger losses.

In addition, more than three quarters of the iron losses are generated in the stator core whatever the current drive is used, because the fundamental current component, the largest one, does not cause any iron loss in the rotor core in a synchronous motor. More than two-thirds of the iron losses are from eddy current losses whatever the current drive is used. That's because the eddy current loss is proportional to the square of variation frequency, but hysteresis loss is linear with variation frequency, which are indicated in equations (5-12) and (5-13). Hence more eddy current losses are produced when motor speed increases, and the high-frequency harmonic components of input current will contribute more eddy current losses than hysteresis losses. This is obviously depicted in Figure 5-20 and Figure 5-21. In both rotor and stator cores, there are almost no or very less hysteresis losses in high frequency, but, in contrast, there are many perceivable eddy current losses in high-frequency area.

The difference of iron losses generated by PWM inverter driven motor and sinusoidal current driven motor can also be observed in the iron loss distributions in Figure 5-22 and Figure 5-23. In the rotor core, the majority of the iron losses occur around the circumference of the rotor, where the flux density is high. Since the eddy current loss is larger than the hysteresis loss in the IPM motor, there are more high loss density regions in Figure 5-22 (a) and (b) than that in Figure 5-22 (c) and (d). Comparing the eddy current loss density in Figure 5-22 (a) and (b), it is found that the motor driven by PWM inverter has

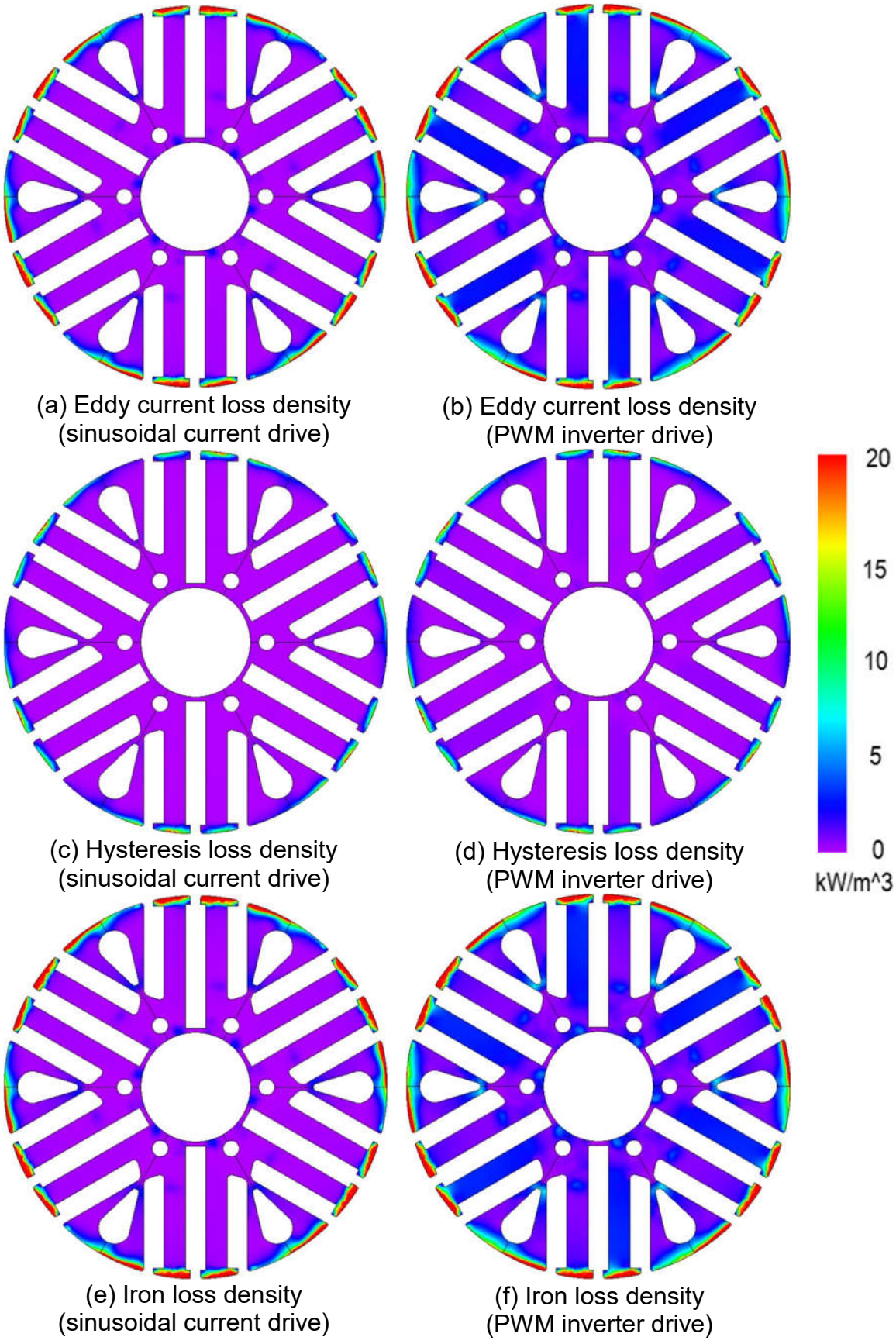

(a) Eddy current loss density (sinusoidal current drive)

(b) Eddy current loss density (PWM inverter drive)

(c) Hysteresis loss density (sinusoidal current drive)

(d) Hysteresis loss density (PWM inverter drive)

(e) Iron loss density (sinusoidal current drive)

(f) Iron loss density (PWM inverter drive)

Figure 5-22 Iron loss density distribution in the rotor core

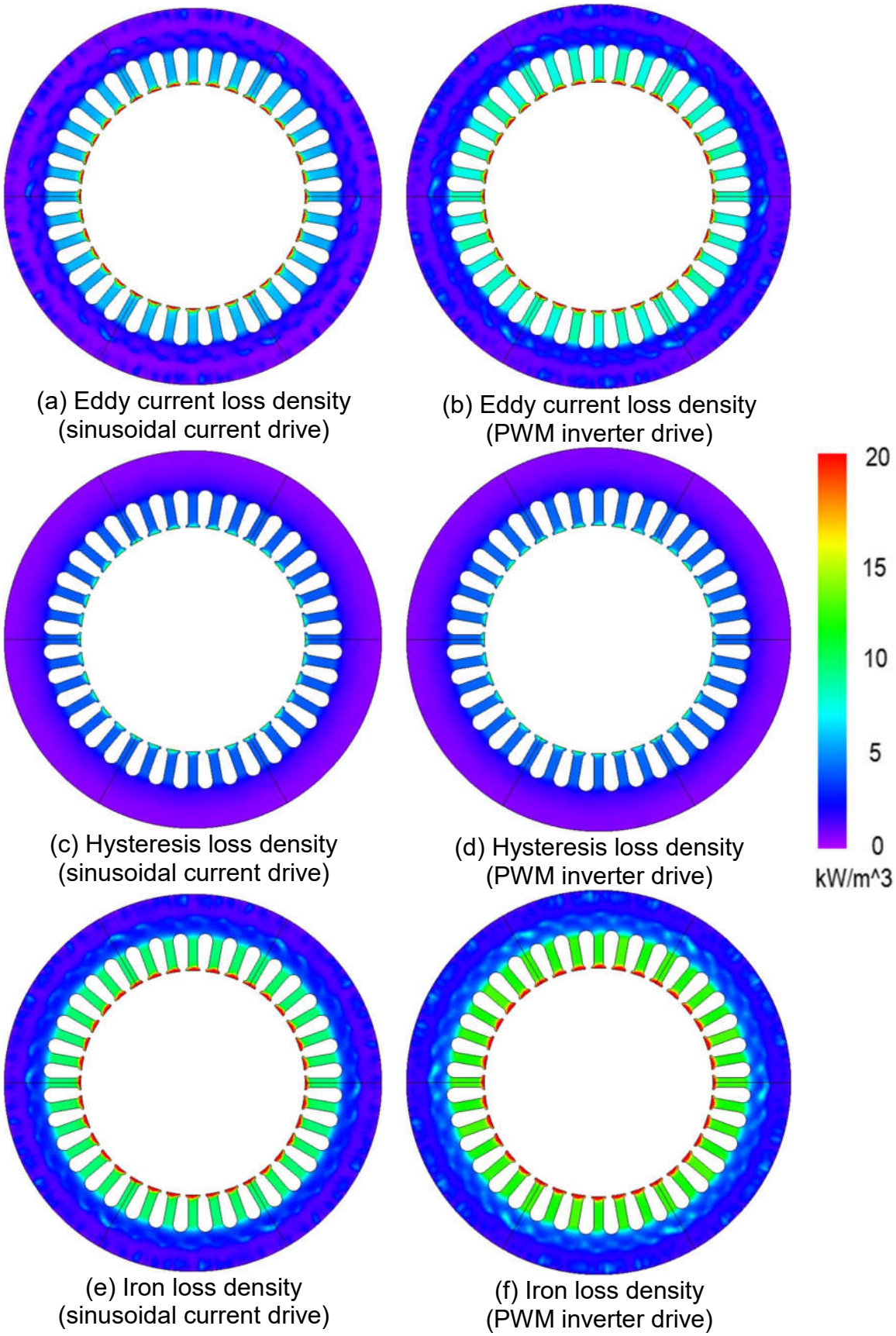

(a) Eddy current loss density (sinusoidal current drive)

(b) Eddy current loss density (PWM inverter drive)

(c) Hysteresis loss density (sinusoidal current drive)

(d) Hysteresis loss density (PWM inverter drive)

(e) Iron loss density (sinusoidal current drive)

(f) Iron loss density (PWM inverter drive)

Figure 5-23 Iron loss density distribution in the stator core

more eddy current loss at the inner part of the rotor core. There is no much difference between the hysteresis loss density in Figure 5-22 (c) and (d), while the PWM inverter driven motor has slightly higher loss in the inner side part of the rotor. Comparing with sinusoidal current drive, the PWM inverter driven motor has more iron loss distributed in the inner areas of the rotor core, and it has larger high loss density areas around rotor circumference, which are shown in Figure 5-22 (e) and (f).

Figure 5-23 shows the loss distributions of eddy current loss, hysteresis loss and iron loss in the stator. In all these six distribution graphs, the loss density decreases from inside to outside. The loss density at the tooth tips is the highest, flowed by the stator teeth, and at the stator yoke the loss density is the lowest. Comparing the eddy current loss density in Figure 5-23 (a) and (b), it is seen that the PWM driven motor has higher loss density in the teeth and a little more eddy current loss distributed in the stator yoke. There is no observable difference of the stator hysteresis loss distribution in Figure 5-23 (c) and (d), as they have almost the same amount of hysteresis losses. Combining eddy current loss and hysteresis loss, the stator iron loss density in PWM inverter driven motor is higher than that in sinusoidal current driven motor, as shown in Figure 5-23 (e) and (f). As both of its rotor and stator have higher loss density, the motor powered by PWM inverter drive generate more iron losses.In this section, the effects of PWM carrier harmonics on the iron loss of the ferrite IPM motor are analysed. The current waveform that is supplied by PWM inverter has PWM carrier waves superimposed on the basic current wave control. And with this PWM carrier harmonic current, high-frequency of the magnetic field is applied to the motor core and more iron loss occurs. The PWM affected iron loss is discussed in details, broken down into eddy current loss and hysteresis loss, the losses in rotor and in stator, and it is compared with the iron loss caused by conventional sinusoidal current drive. From the comparison of iron loss frequency components and iron loss distribution, it is concluded that the motor driven by a PWM inverter will generate more iron losses than that driven by the conventional sinusoidal current. Thus, the effect of PWM should be considered when actual prediction of iron loss is required. In order to improve

the efficiency of the PWM electric drive, the current harmonics should be further minimised. And increasing the frequency of PWM carrier wave will be helpful to mitigate the effects of PWM on iron loss.

5.3 FEA Results and Comparison with Induction Machine

Due to the nonlinear properties of magnetic materials, it is extremely difficult to obtain iron losses accurately by magnetic circuit method. Thus finite element method (FEM) is used to carry out a detailed analysis on motor losses and efficiency. The performance of IM is used as a benchmark to evaluate the proposed ferrite IPM machine.

5.3.1 Copper Loss Results and Comparison

As a basic condition for the performance comparisons between the ferrite IPM and IM, the stator copper losses are set to be equal at rated operational condition, so that the electrical loading and thermal condition of the stators are the same. Since torque can be approximately regarded as proportional to current below rated speed, copper loss of stator windings increases with torque and is independent on the speed for both the IPM and IM, as shown in Figure 5-25 and Figure 5-25. Although the two machines under comparison have the

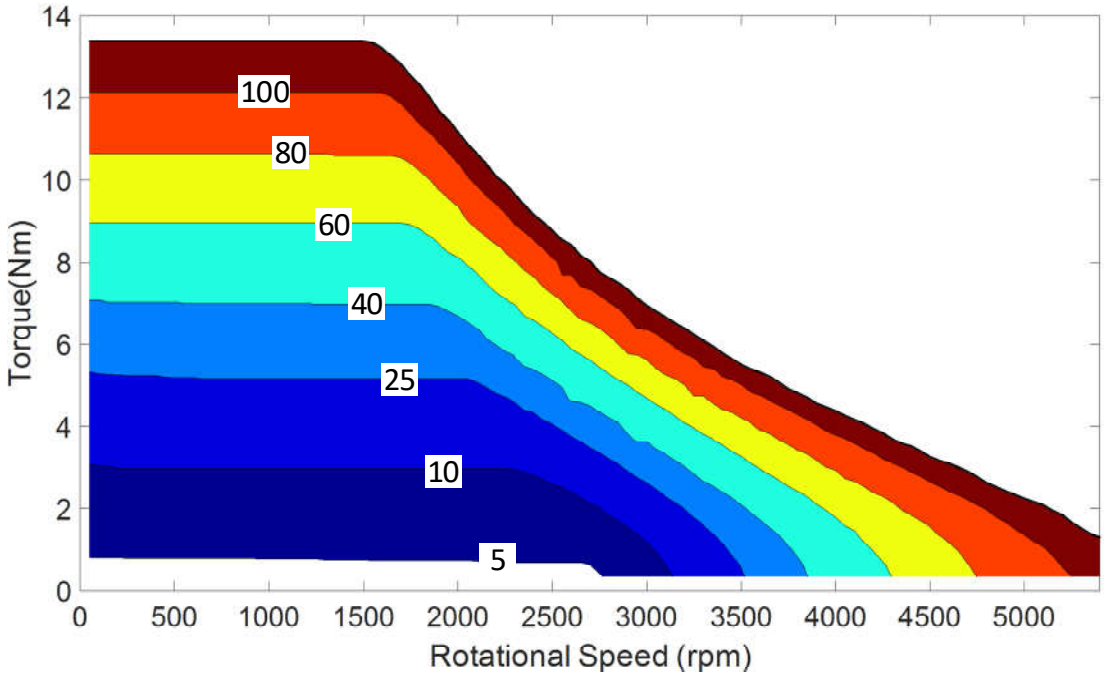

Figure 5-24 Stator copper loss map of the IPM (W)

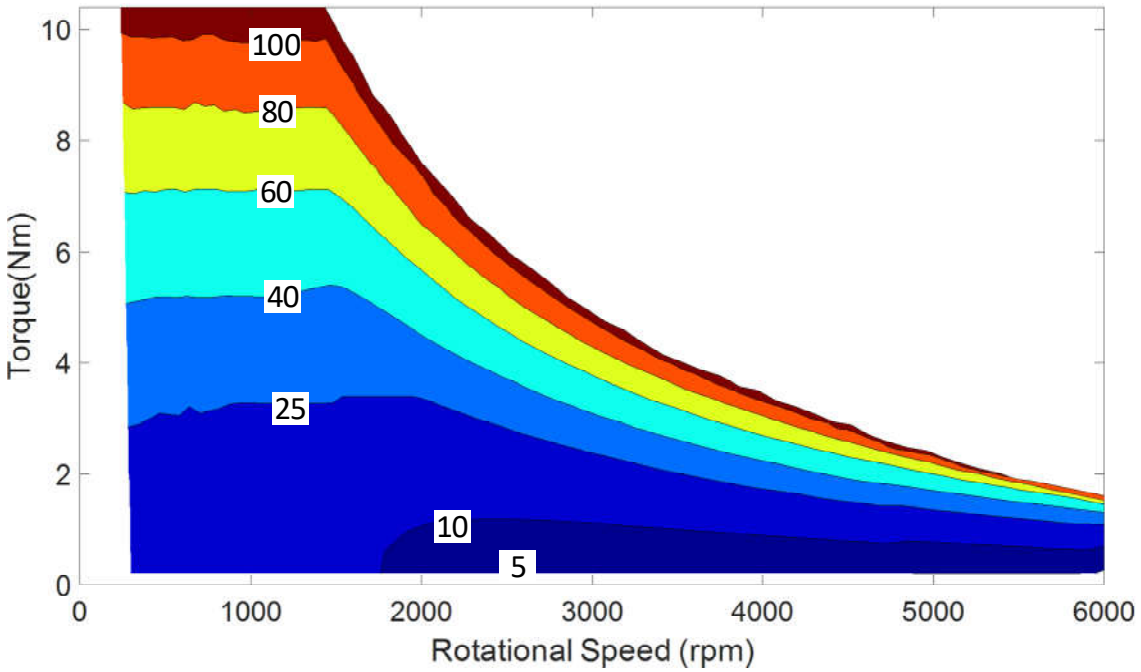

Figure 5-25 Stator copper loss map of the IM (W)

same maximum copper loss in the stator, their copper loss features are quite different under various operational conditions because of the different operating principles due to different machine types. When below the rated speed and torque, the ferrite IPM machine achieves lower copper loss level because of the advantage of IPM excitation, while higher copper loss is observed in the IM as excitation current is required to establish the flux field. The difference is more obvious at light or no-load conditions when copper loss is close to zero for the ferrite IPM but over 15 W for the IM. However, the result is completely different when it comes to high speed range. Decrease in copper loss for the IM is observed with speed under no-load condition since the excitation current is reduced during flux weakening control. But under loaded condition, torque generating current increases to maintain the same torque, and thus copper loss still increases with speed. On the other hand, much higher stator copper loss is observed for the IPM as larger d-axis current is necessary to achieve flux weakening operation. Accordingly, the copper loss increases dramatically with speed.

For the IM, there is considerable amount of copper loss in the rotor side due to the existence of squirrel cage. Since the current in the rotor cage is induced

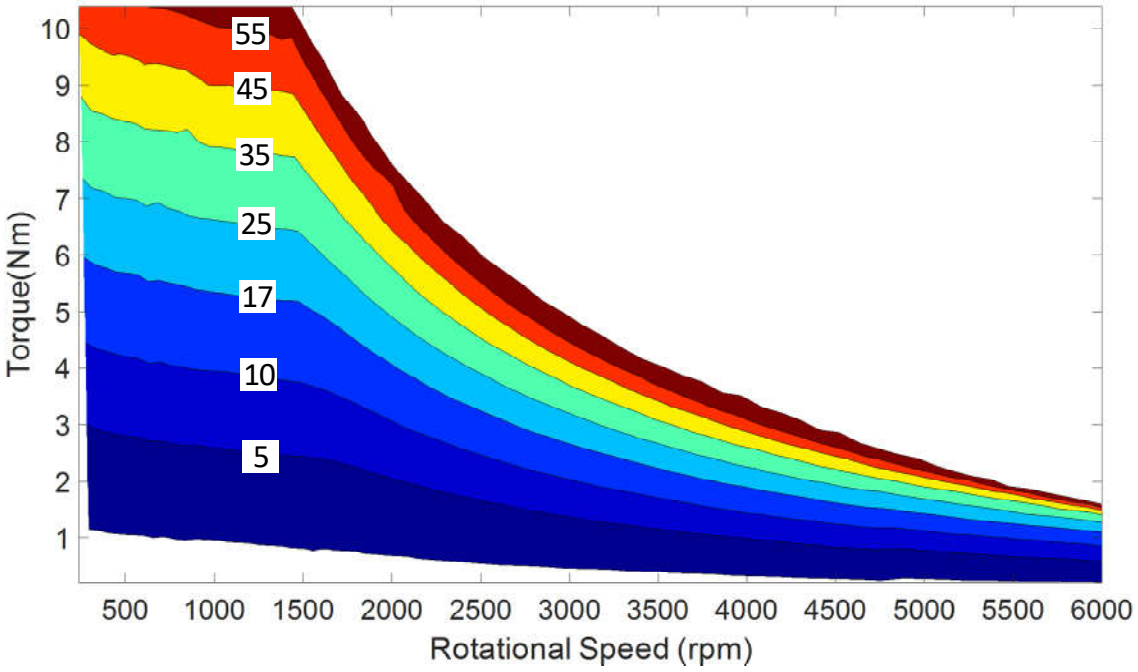

Figure 5-26 Rotor copper loss map of the IM (W)

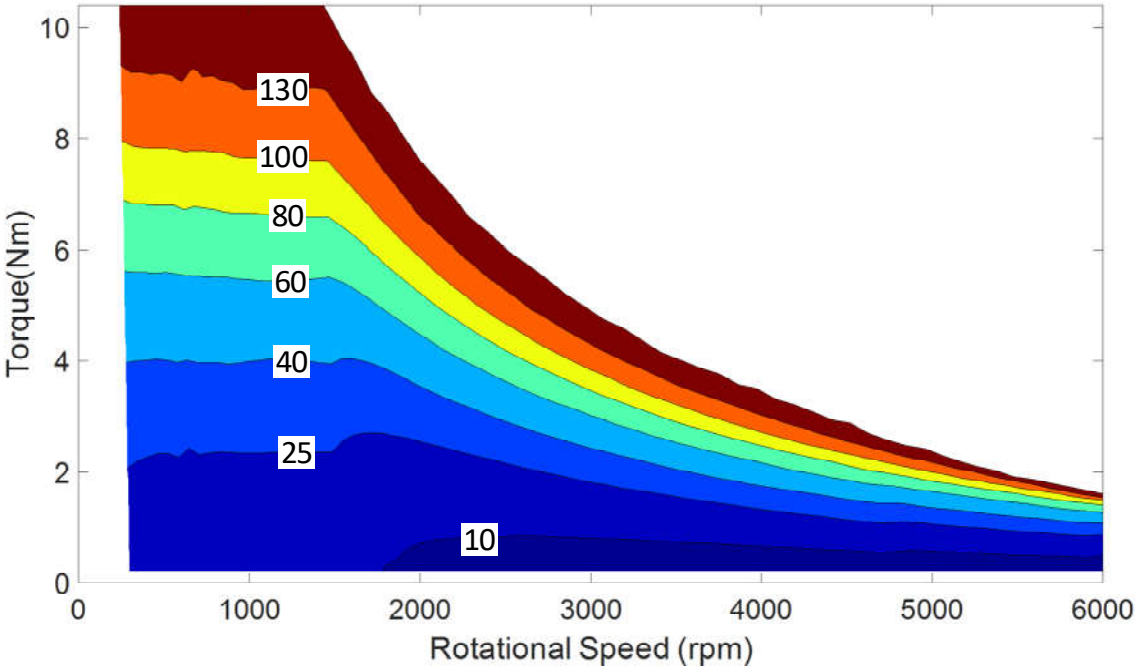

Figure 5-27 Total copper loss map of the IM (W)

from stator reactive field, the copper loss increases with stator current and rotating speed, as depicted in Figure 5-26. The rotor copper loss of the IM can reach up to half of stator copper loss at rated torque output, which means 50% higher overall copper loss for the IM compared with the ferrite IPM. Considering only the stator copper loss, those of the IM and IPM are comparable below

rated speed. But with the rotor copper loss taken into consideration, the overall copper loss of the IM is much higher than that of ferrite PM when the speed is lower than 3000rpm. Nevertheless, at very high speed, the copper loss of the ferrite PM machine is still higher because extremely large d-axis current is required for the deep flux weakening control, as demonstrated in Figure 5-27.

5.3.2 Core Loss Results and Comparison

From the discussion in subsection 5.1.3 it is known that core loss is affected by magnetic flux density and operating frequency, which is verified by the FEA results in Figure 5-28 and Figure 5-29 for ferrite IPM and IM. However, the distribution of core loss is quite different in the maps of the two machines.

For the ferrite IPM machine, the excitation field is largely decided by its PMs, so the core loss is mainly influenced by the rotational speed and less affected by armature current over the whole operational range. Due to the stronger armature reaction the core loss of IPM rises as the increase of loading. And for the IM, the flux field is almost constant under the rated speed, because excitation is controlled by armature current that is unchanged at a specific speed. Thus the core loss of IM can be approximately regarded as only

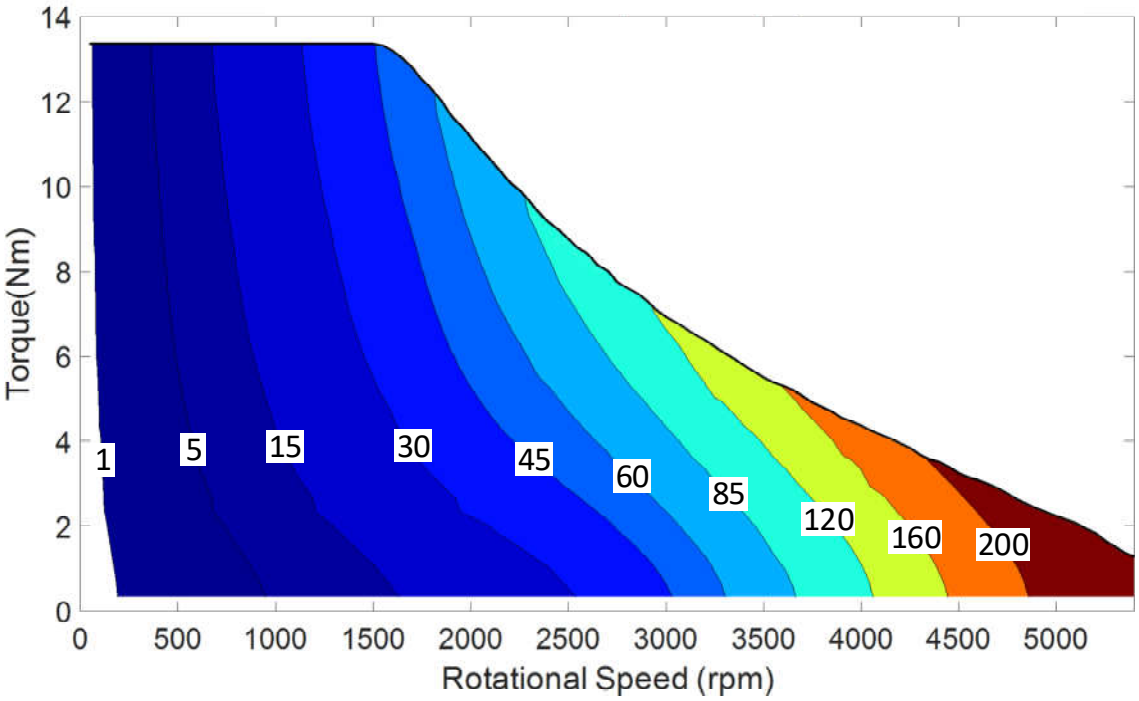

Figure 5-28 Core loss map of the IPM (W)

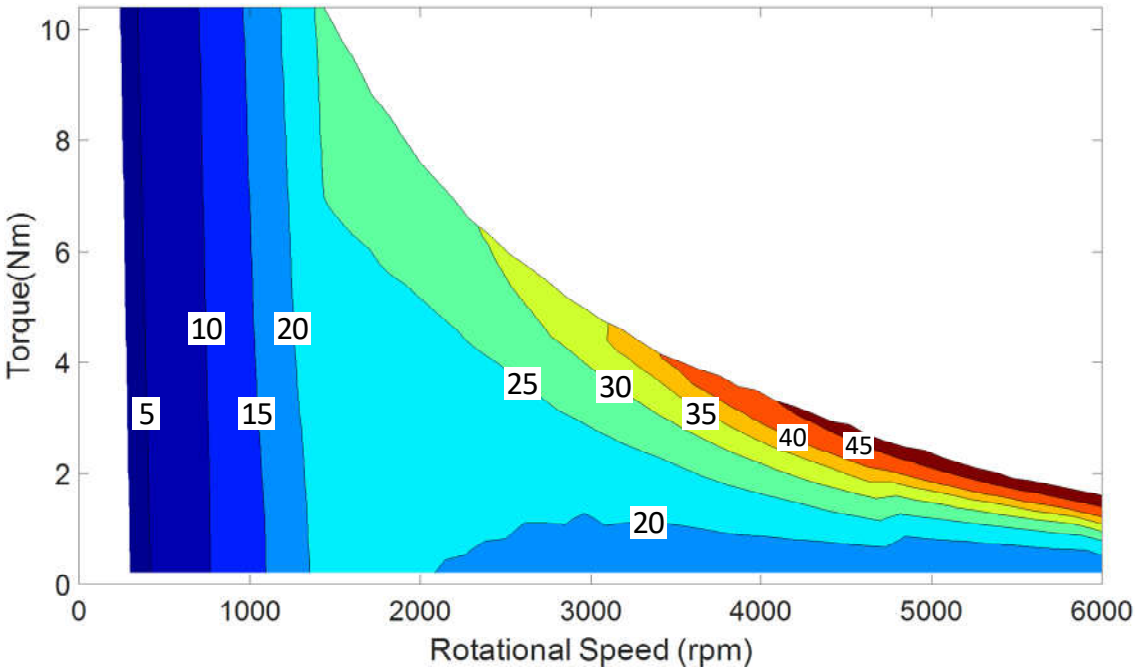

Figure 5-29 Core loss map of the IM (W)

dependent on rotational speed. But in the flux weakening region, the core loss distribution becomes more complex. The excitation current decreases as flux weakening, and lower core loss is observed under no-load condition. But when the output torque is increased, the core loss of IM grows significantly due to the influence of reactive field at high speed.

The core losses of both machines are quite small under rated speed. Compared with the IM, the core loss of the IPM machine is slightly higher because of higher flux density owing to the PM excitation and higher electrical frequency due to higher number of poles. The core loss of ferrite IPM becomes much higher than IM when the speed is over nominal value. As a result of better flux weakening ability for the IM, much lower flux density can be achieved as the speed grows, which results in much slower rise in core loss. On the other hand, the flux density of the ferrite PM stays at a relative high level owing to the fixed PM excitation and inferior flux weakening ability, which leads to exponential increase in core loss with speed. This is certainly one of the factors that deteriorate the performance of the IPM machine in high speed range.

5.3.3 Efficiency Results and Comparison

One of the demands for the low-cost IPM motors is to achieve high efficiency over a wide range of rotation speeds. The motors with high efficiency will reduce the overall cost over its life operating time, so the pursuit of high efficiency become more important to the design of low-cost motors.

The basic definition and calculation equations of motor efficiency are introduced firstly. The efficiency is defined as:

$$\text{Efficiency} = \frac{P_{mech}}{P_{mech} + P_{loss}} \tag{5-21}$$

$$P_{mech} = T \cdot \omega = T \cdot \frac{2\pi \cdot n}{60} = \pi/30 \cdot n \cdot T \tag{5-22}$$

$$P_{loss} = P_{crl} + P_{cpl} \tag{5-23}$$

where, P means power in watt and P_{mech} and P_{loss} are mechanical output powder and total losses of the motor respectively; T is the output torque in Nm, ω is the rotational speed in radian/s, n is the spinning speed of the motor in rpm, P_{crl} is the core loss, P_{cpl} is the copper loss. So the efficiency is summarised as

$$\text{Efficiency} = \frac{\pi/30 \cdot n \cdot T}{\pi/30 \cdot n \cdot T + P_{crl} + P_{cpl}} \tag{5-24}$$

T, P_{crl} and P_{cpl} of the motor can be obtained from FEA simulations.

The efficiency changes with rotation speed and load, so it is beneficial to create efficiency map when designing the motor and its controls.
By compiling the losses calculated in the previous sections, efficiency maps of the proposed ferrite PM and the commercial IM are derived, as shown in Figure 5-30 and Figure 5-31. Due to the different loss features under different torque and speed conditions, the whole speed-torque operation region is divided into four sub-regions for detailed comparisons and discussions.

- Sub-Region I: Low Speed and Low Torque

In this sub-region the load torque is less than 40% of rated and the rotating speed is lower than 1000rpm. As the speed is relatively low, the core loss for the two machines is similar. The difference in behaviour mainly lies in copper loss. The main flux field of the IPM is established by PMs and thus the armature

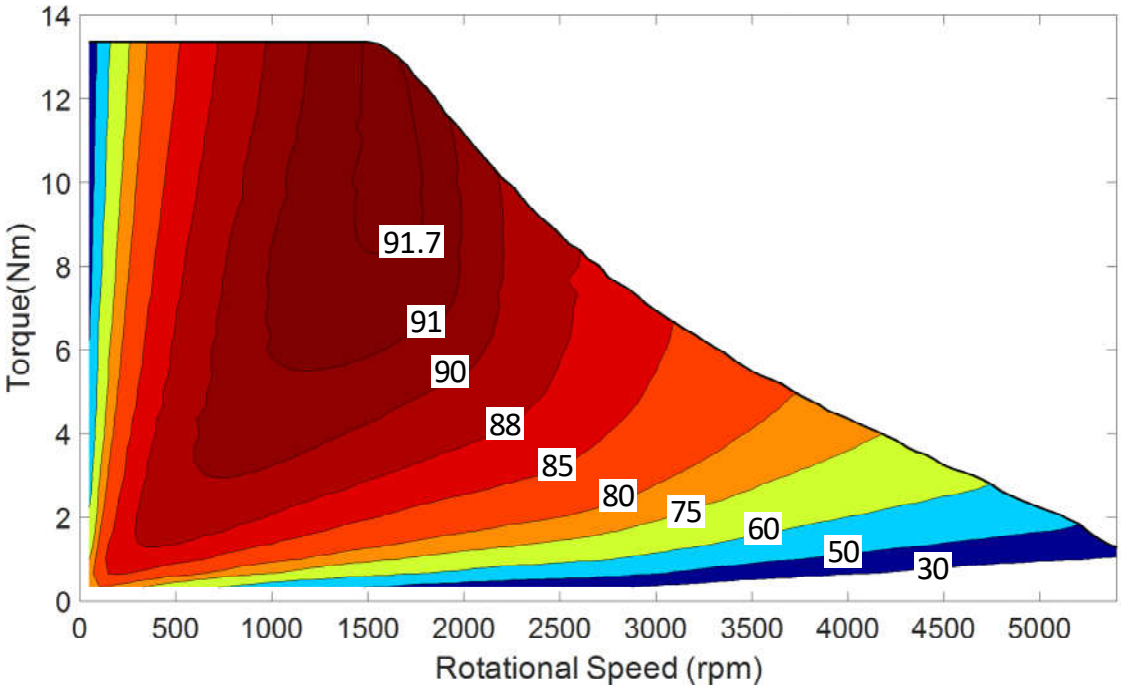

Figure 5-30 Efficiency map of the IPM (%)

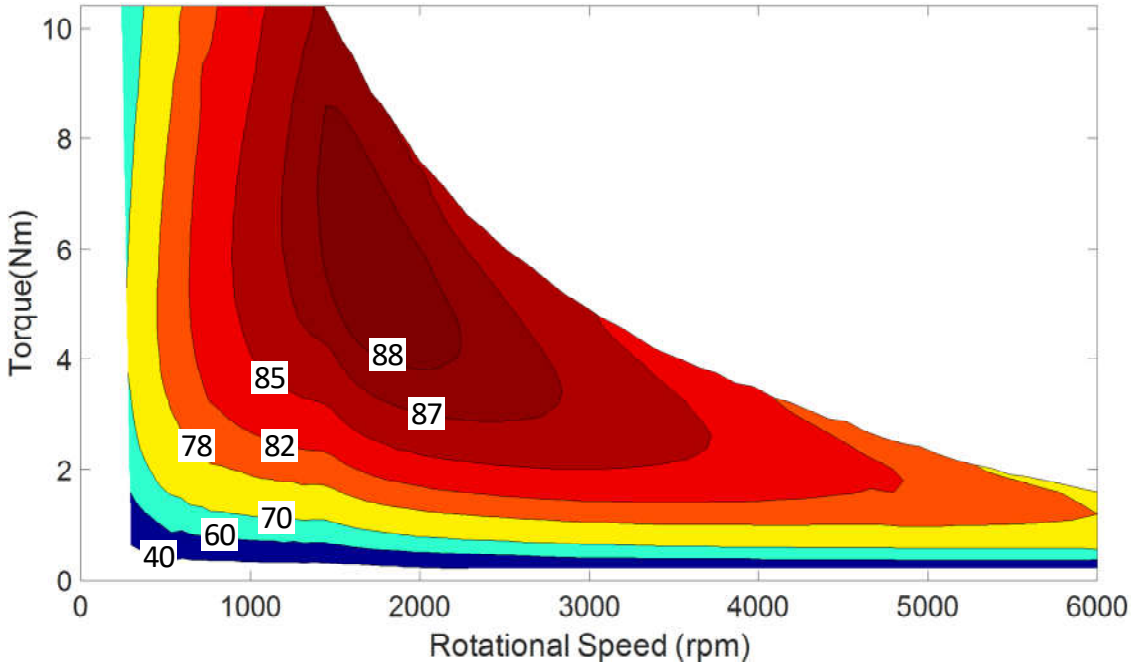

Figure 5-31 Efficiency map of the IM (%)

current is much lower, while a large part of the armature current is for the build-up of field excitation in IM. As a result, the efficiency of the IPM is much better than the IM for lower copper loss in the region.

- Sub-Region II: Low Speed and High Torque

Since the current is high under these circumstances, copper loss dominates the overall loss. Although the maximum stator electric loadings are kept the same for both the machines, extra copper loss in the rotor bar can add up to 25% of the total loss for the IM. What's more, higher torque per ampere can be achieved for the IPM, which means higher power output. Combining the two factors, much higher efficiency is expected for the IPM in this sub-region.

- Sub-Region III: Medium Speed and Medium to High Torque

Normally the most frequent operational ranges for a motor lie in this region, and both of the motors are designed to exhibit the highest efficiency under the torque-speed range of 1000 to 2000 rpm speed and half to full load torque. Apparently, the ferrite IPM shows better performance in efficiency against its IM counterpart. At rated working points, the proposed IPM machine operates with efficiency of over 91.7%, against that of 87.8% for the IM. Within this sub region, the IPM maintains the efficiency over 90% with the highest achieving 91.9%, while the IM obtains over 85% with the highest efficiency of 88.7%. About 2-4% higher efficiency can be attained compared with the IM, which makes big difference for the energy saving because the motors work in this region for most of the time in operation.

- Sub-Region IV: High Speed

The motors enter deep flux weakening operation in this sub-region. For the IPM, negative d-axis current is necessary to weaken the PM excited field so as to reduce the induced voltage during high speed operations. The increased demagnetizing current will not only increase the copper loss but also intensify the spatial harmonic of the armature MMF resulting in higher core loss. Thus, the efficiency of the IPM decreases significantly with speed. On the other hand, the excitation current of the IM can be reduced for weaker flux field, and both

copper loss and core loss are much lower than the IPM. Therefore, the efficiency of the IM exceeds that of IPM when the speed is over 3000 rpm, and becomes far more superior over 4000 rpm.

In summary, the IPM achieves higher efficiency in most of the operational region, and most importantly in the most frequently operating sub-region III. Although the IM obtains higher efficiency during high speed range, it is not the main working region for most of the small-scale industrial applications. On this basis, the IPM exhibits much higher overall efficiency.

5.4 Thermal Analysis and Temperature Distribution

As the power and torque density of an electric machine is decided by its thermal performance in operation, it is a critical issue to resolve the problem of rising temperature when trying to achieve an improvement in a motor's efficiency and output torque. In order to solve this problem, it is important to investigate a magnetic design that reduces the losses themselves because the losses are a source of heat; it is also important to study a thermal design that improves heat dissipation and reduce the temperature rise to an acceptable range. In electrical machines temperature has an effect on lifetime/degradation and performance. Current density, which is usually proportional to torque density, is thermally limited. Over-temperature will lead to premature failure, for example of stator winding insulation. The insulation lifetime of a machine varies inversely with working temperature. Thus, it is necessary to evaluate the thermal properties of the motor at the design stage.

The losses discussed in the above sections are the heat sources in the motor's thermal system. A magnetic field-thermal analysis model is created based on the motor's structure and operating environment, which is used to investigate the motor's thermal properties in steady state and transient state. The consecutive operating time in over load condition is evaluated as well, which is a critical characteristic of a motor's power capability.

5.4.1 Thermal Modelling of the Machine

In order to carry out an accurate thermal analysis, it is necessary to first correctly understand the amount and location of heat generation. It would be advantageous to calculate the losses in a magnetic field analysis simulation using the finite element method, and from there to carry out a thermal analysis using the resulting loss distribution.

Table 5-2 Loss in each part at rated load

Heat generation parts	Iron loss in the rotor core	Iron loss in the stator core	Copper loss in the coils
Losses (W)	9.49	38.28	117.8

Table 5-2 shows the loss in each part of the motor at rated load and speed. Copper loss in the coils and iron loss in the core are the dominant heat sources, so this analysis mainly evaluates the effects of this heat. The loss in the coil is relatively large, about 2/3–3/4 of the total loss, so it is expected to be the main source of heat. On the other hand the majority of iron loss comes from the stator core, because in synchronous machines the fundamental component of magnetic field does not generate iron loss in rotor, only harmonics causing losses. Even though the loss in rotor is only about 5% of total loss, the heat will be accumulated due to poor dissipating condition and cause rotor temperature to increase. The properties of ferrite magnet, such as residual flux density and coercivity, are sensitive to temperature. What's more, the heat resistance of ferrite magnet is low, so lots of attention is required to prevent it being irreversibly damaged.

According to the structure of the designed ferrite IPM machine, a thermal circuit model is built and shown in Figure 5-32. The square blocks in the circuit represent the motor's core parts that generate and transmit heat, and they are meshed in FEA simulation. The circle blocks represent the surroundings and ambiences, and they absorb the heat from inner motor. The resistance signs are illustrated as *thermal resistance* among the square and circles blocks, such as thermal resistance between coil and stator core, stator core and cover, cover and air, and so on. The capacitor sign attached to cover is *heat capacitor*, and

the cover's heat capacity is related to its volume, density and specific heat. All of the heat will eventually transfer into the ambient air. As is illustrated in the Figure 5-32, the rotor has three routes to transfer its generated heat. Some of the heat is brought out through rotor shaft to the housing cover; some goes through the internal air to the cover; and the others is transferred to the stator core by the air gap. For the heat occurs in copper coils, most of it is transmitted to stator core and the rest is dissipated to housing cover through internal air. Since stator core is seamless connected to housing cover and has large heat radiating surface, the majority of heat generated in the motor is finally dispelled away through stator core to the cover, and only a small fraction is transferred through internal air to the cover. Based on the thermal circuit model the temperature of the ferrite IPM machine can be calculated.

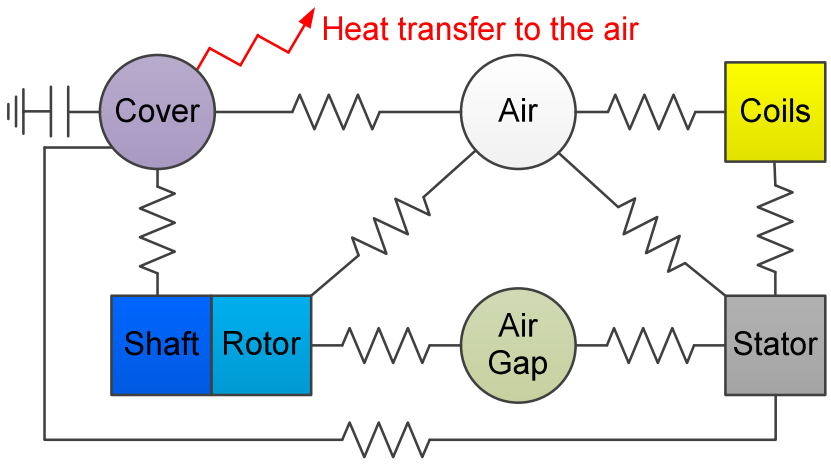

Figure 5-32 Thermal circuit model of the designed motor

5.4.2 Temperature Distribution at Steady State

The simulation of thermal circuit model is carried out with rated motor load. The motor operates continuously until a thermal balanced state is reached. The final balanced state is also called steady state, and the temperature distribution of it is shown in Figure 5-33. According to the temperature distribution, the motor are generally divided into three thermal regions: the copper coils, the rotor and the stator. The highest temperature region is the copper coils, as copper loss is the dominant source of heat. The highest temperature is about 104°C. Most of the heat from the coils is transferred to the cover through the stator core, and the

rest goes through the air inside of motor to the cover and finally dissipates to the ambience. The moderate temperature region is the rotor. Since ferrite PM is non-conductive, no loss is generated in magnets. The heat accumulated in the rotor is mainly from its iron loss. As the majority of the rotor's surface area is encompassed by air, which has high heat transfer resistance, it is hard for the rotor to dispel the generated heat. The accrued heat increases the temperature of the rotor and the magnets imbedded. It can be seen that the rotor has higher temperature than the stator core. Most of the heat generated in the rotor flows through the air around it and then to the stator and cover, and the rest is transferred to cover through the bearings and shaft.

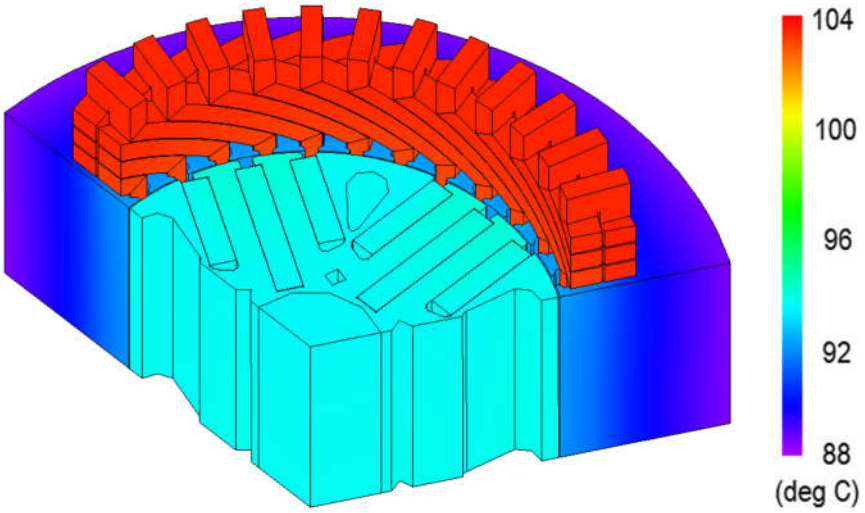

Figure 5-33 Temperature distribution at a steady state

The relatively low temperature region is the stator core, with the lowest temperature about 88°C at the contact surface to cover. The stator core is not only a heat source that generated from iron loss, but also a very important heat transfer channel/medium, through which most of the heat generated inside of the motor are transferred to the motor housing/cover and finally dissipated into ambient air. It is depicted in Figure 5-33 that from the outer to inner side of the stator core the temperature is increasing gradually. The outer side is cooler because it is connected to cooling source, the cover. The inner side is hotter as heat is concentrated, where the stator iron loss density is the highest and it also receives a lot of heat from copper windings and rotor core.

With the help of temperature distribution analysis, several thermal design approaches can be concluded for the ferrite IPM machine:

- Fill the gap between coils and stator core with high thermal conductivity material, so that heat from copper loss can be more easily transferred to stator core and dissipated to the ambience.
- Minimise the air gap between rotor core and stator core, in order to improve the heat transfer efficiency from rotor to stator core.
- Enhance the air circulation inside of the motor to speed up the heat transferring through the air, such as installing fans.
- Cool down the motor housing/cover, the larger the temperature difference between stator and cover, the faster the heat is transferred.

5.4.3 Temperature Variation Process

In order to further understand the process of temperature changing, the temperature of some typical points in the motor are measured and compared. The measuring points are indicated in Figure 5-34, which include points on rotor core, coil, magnet, and stator core. The initial temperature is 20°C. The temperature measurement lasts for four hours and it is recorded in Figure 5-35. The temperature of the four points increase fast in the first two hours and gradually become stable in the last two hours. In contrast with the temperature distribution at steady state, the increased temperature is quite close to the thermal balanced temperature after four hours of running.

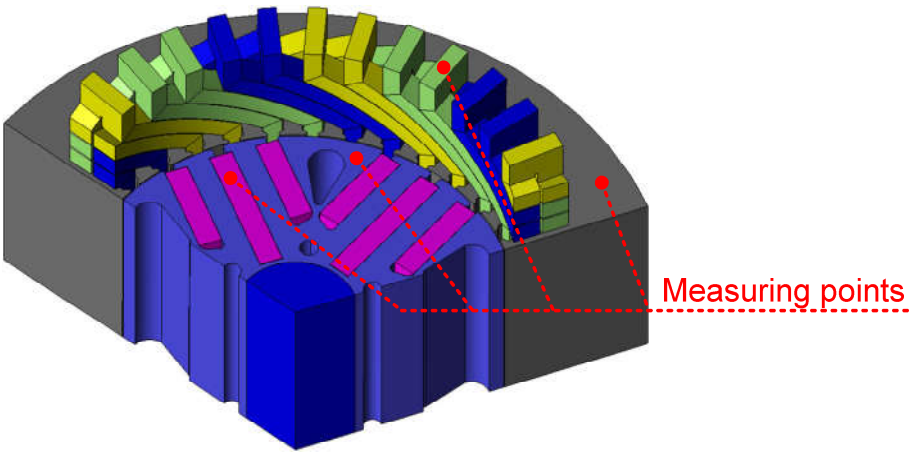

Figure 5-34 Points of measuring temperature for each part

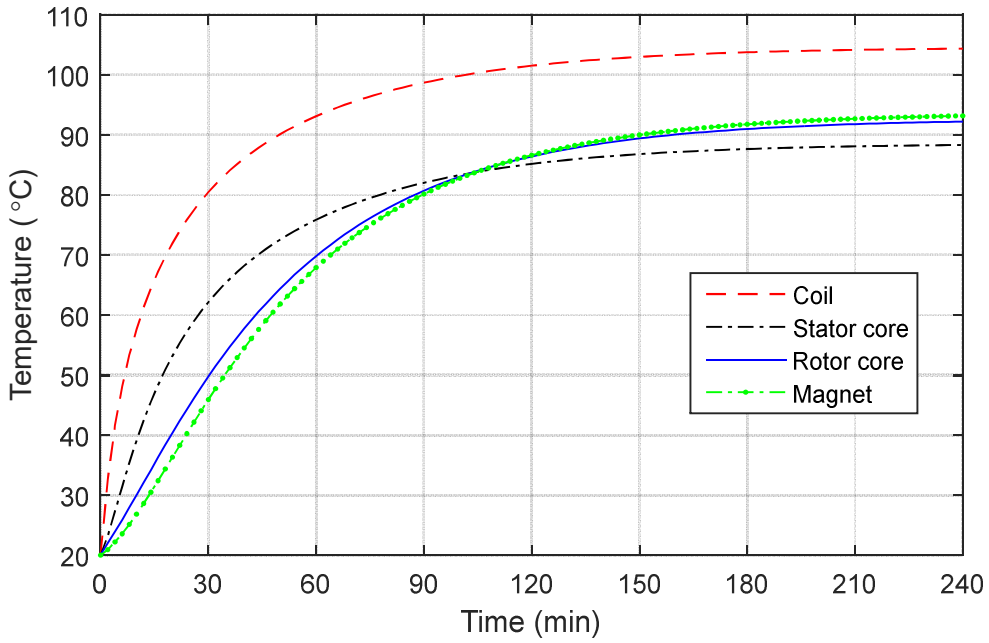

Figure 5-35 Temperature variation of the measured points

The highest temperature appears in the coil. As the main source of heat comes from copper loss, the winding temperature is growing faster at the beginning and more than 10°C higher than other measuring points at the end. In the first 100 minutes, the temperature of stator core is higher than rotor core and magnet, but it is exceeded later. The losses in the stator are much higher than rotor, and the stator temperature rises much faster than rotor at first. However, the rotor has worse heat dissipation conditions as it is largely surrounded by air and the heat generated in rotor is difficult to transfer to the outside; while the stator core is directly (interference) fitted to motor housing that transfer the heat from stator efficiently. The accumulated heat in rotor makes it hotter than stator in relatively long running time. The results are consistent with the temperature distribution of steady state in Figure 5-33.

The rotor core itself is also a heat source from its iron loss. The ferrite magnet does not generate heat but is heated by its adjacent rotor core. So there is a temperature difference at beginning between the two parts. But the difference is reduced with time and almost to zero in the thermal balanced state. In addition, the property of the ferrite PM is affected by increased temperature of the rotor. Thus special attention should be paid to the rising temperature during operation, and make sure the PMs are operating in acceptable temperature range.

5.4.4 Continuous Operating Time at Over-load Conditions

In some applications, motors are required to work in over load conditions for a short while. The over load capacity is an essential characteristic to evaluate a motor and also useful for motor selection. Larger output power requires larger input current. Although increasing the current produces a higher torque, it also boosts the heat generation in terms of copper losses and core losses. Owing to the large input current, the copper losses generated in the windings increase exponentially. Along with coil temperature surging up, the resistivity of the copper rises, which further deteriorates the copper losses. The iron losses in stator and rotor cores are also increased due to the large armature reaction of the designed IPM machine. Accordingly, the temperature of stator and rotor will increase dramatically with current, and the properties of the ferrite PMs will be worsen by high temperature.

Table 5-3 Current and average torque

Input Current	1 C	2 C	3 C
Average Torque (pu)	1	2.1	3.1

Therefore, it is vital to find the longest consecutive operating time under over load condition before causing any irreversible damage. In addition to the evaluation under rated load in subsection 5.4.3, simulations with two and three times the rated input current are carried out, and the temperatures of coil and magnet are analysed and discussed. The rated current is 6.2 A (RMS value), designated as 1 C, and the corresponding average torque is 13.32 Nm, designated as 1 pu. When the input current is increased from 1 C to 3 C, the output torque grows from 1pu to 3.1pu, which are summarised in Table 5-3.

The temperature measuring points are same as the ones in Figure 5-34, and temperature variations of the coil and magnet with various currents are recorded in Figure 5-36 and Figure 5-37 respectively. The enamelled copper wire used in the designed motor is in thermal Class H (180°C), and the temperature limit is indicated in green dash-dot line in Figure 5-36. The shape of the temperature variation lines with various currents is similar, but slop of them is different. The larger the input current, the steeper the temperature

changing line is. In rated load condition (input current is 1 C) the temperature of the coil is always under the temperature limit; in double load condition (input current is 2 C) it takes about 13 minutes to reach the temperature limit; and in triple load condition (input current is 3 C) the coil's temperature exceeds the temperature limit in about 3 minutes, which is much shorter than double load.

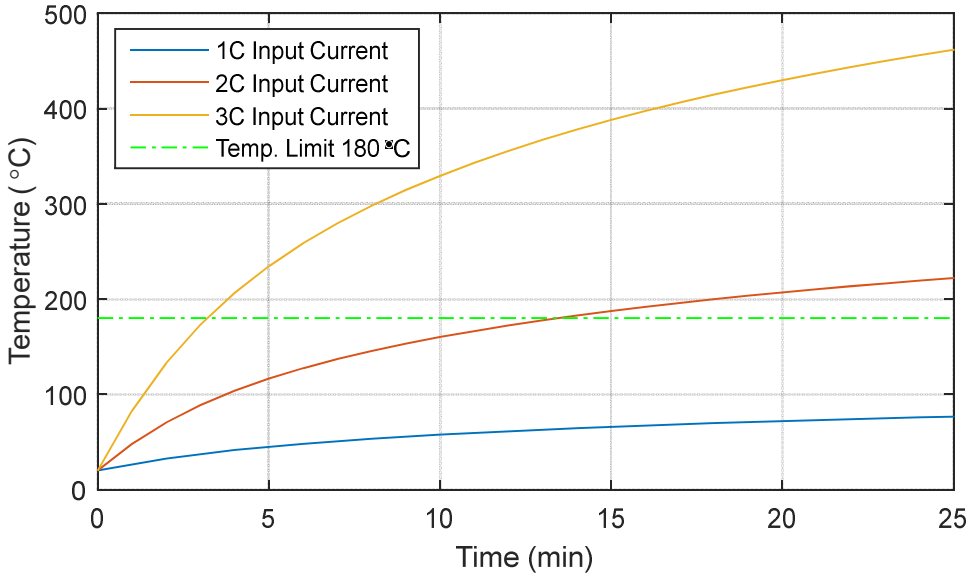

Figure 5-36 Temperature variation of the coil with various currents

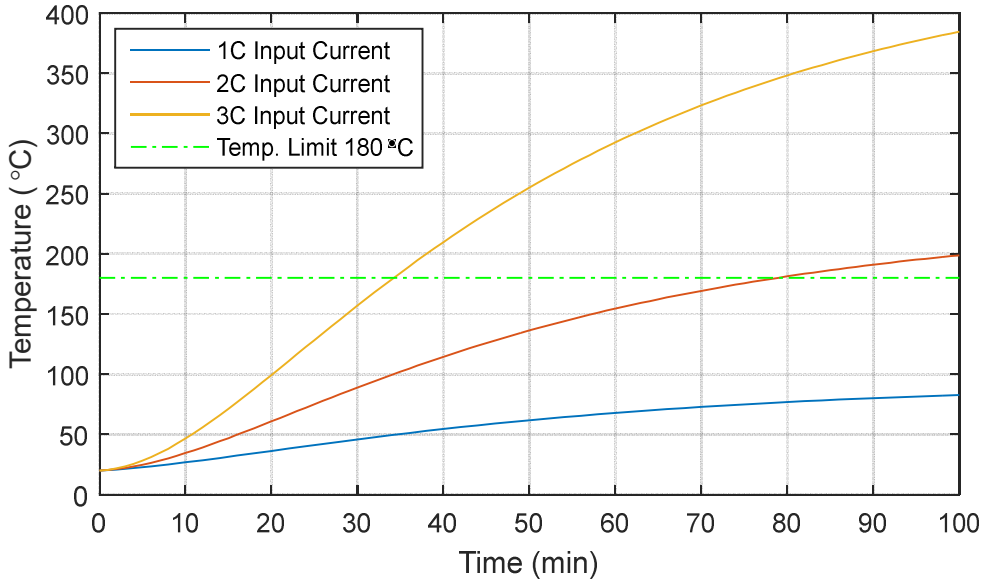

Figure 5-37 Temperature variation of the magnet with various currents

The magnet material used in the designed motor is ferrite *Y30*, the maximum working temperature of which is 180°C that is indicated in green dash-dot line in Figure 5-37**Error! Reference source not found.**. Similar to the temperature variation of the coil, the temperature trend of the magnet with various input

currents have similar shapes but different slops. In the rated load condition (input current is 1 C) the magnet's temperature stays under 70°C; in double load condition (input current is 2 C) it does not reach the temperature in the 78 minutes running time; and in triple load condition (input current is 3 C) the magnet's temperature exceeds the temperature limit in no more than 34 minutes. The consecutive operating time with various currents is determined by the weaker part, the one with shorter time to reach the temperature limit. Therefore, considering both of the coil and the magnet, it is concluded that the consecutive operating time is 29 minutes under double load and 5 minutes under triple load. The consecutive operating time should be paid serious attention when a motor is working in over load condition. Beyond the allowable time, it is possible for the motor to be permanently damaged.

5.5 Summary

The demand for high performance and low cost motors has grown from the need to accommodate devices that incorporate energy efficiency in their designs. In order to meet this demand, motors have to improve their output density and reduce their losses. The losses of ferrite IPM mainly consist of copper loss and iron loss, both of which are thoroughly analysed in the chapter. And the iron losses analysis also considers the effects of press fitting stress, shrink fitting, and PWM harmonics. In the premise of meeting installation requirement, it is better to minimise the interference in press fitting or the temperature difference in shrink fitting so that to reduce the extra iron loss. With the consideration of PWM harmonics effect, the iron loss estimation of the studied motor becomes more accurate. The losses and efficiency maps of the studied motor are plotted from the FEA results, and compared with that of IM. The proposed ferrite PM machine exhibits great superiority to the IM in terms of efficiency below the rated speed, with about 3-4% higher efficiency. All of the losses are converted into heat and increase temperature of a motor. The rising temperature will worsen properties of PMs and is possible to wreak irreversible damage to a motor. A detailed thermal analysis is implemented to the ferrite IPM, and the consecutive operating time with over load is estimated as well.

6. LOW COST SCHEME OF MOTOR CONTROLLER

6.1 Control System Design

In the most generic sense, an electric drive is a system transferring electrical energy into mechanical energy, and it mainly consists of electric machine, inverter and motor controller. The studied ferrite IPM machine drive system is shown in Figure 6-1. The ferrite IPM machine is powered by three-phase AC current that is converted from DC electric source by voltage source inverter (power module), and its output torque drives the load through a coupler. Motor controller as the crucial part of electric drive system controls speed, torque, direction, and the resulting horsepower of a system. The controller, by comparing the input command for speed with the actual values measured through sensors, provides appropriate control signals to the inverter consisting of power semiconductor switches.

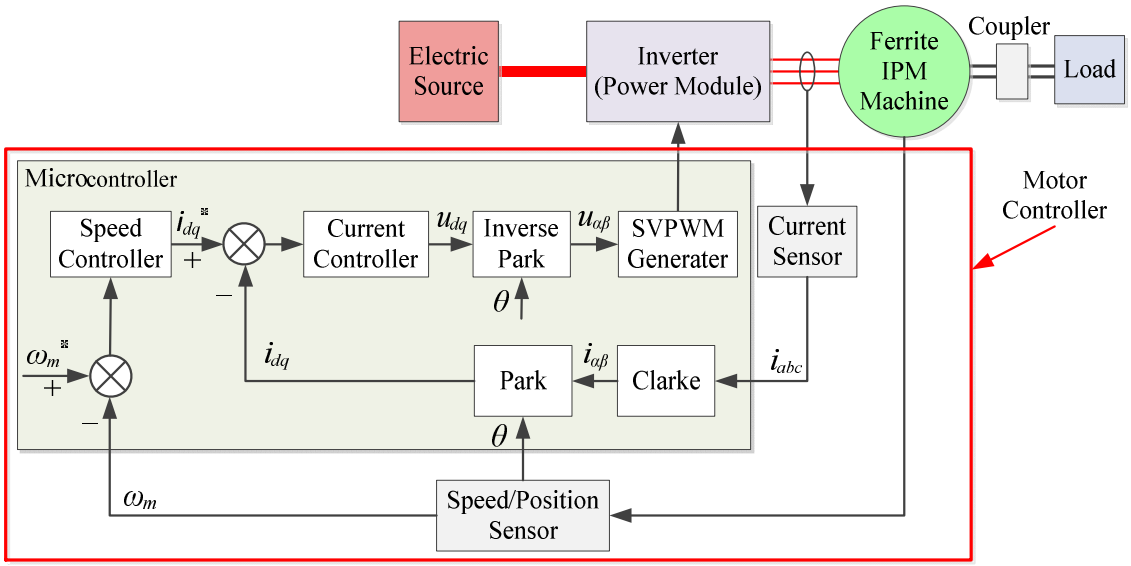

Figure 6-1 Ferrite IPM machine vector control system diagram

The vector control method, also known as field-oriented control (FOC), is adopted in the ferrite IPM machine control system. Because of the wide speed range, to generate the current references in the d-q frame, maximum torque per ampere (MTPA) algorithm is used at low speed, and flux-weakening strategy is used when the voltage limitation is reach at very high speed [225,226]. The electrical model of a sinusoidal, unsaturated PMSM motor in Park's d-q frame is:

$$\begin{cases} u_d = R_s i_d + L_d \dfrac{di_d}{dt} - \omega_e \varphi_q \\ u_q = R_s i_q + L_q \dfrac{di_q}{dt} - \omega_e \varphi_d \end{cases} \quad \textbf{(6-1)}$$

where the winding flux linkage can be derived as

$$\varphi_d = L_d i_d + \varphi_f \ , \quad \varphi_q = L_q i_q \ , \quad \textbf{(6-2)}$$

The electromagnetic torque can be represented as

$$T_{em} = \frac{3}{2} p\left(\varphi_d i_q - \varphi_q i_d\right) = \frac{3}{2} p\left(\varphi_f i_q + \left(L_d - L_q\right) i_d i_q\right) \quad \textbf{(6-3)}$$

Figure 6-1 presents the vector control scheme of the ferrite IPM motor, which is carried out in sequence of normal operation. The control system adopts speed-current double closed loop control structure, processing signals through microcontroller to complete the control of the inverter electronic switches. In the outer speed loop, the position θ and speed ω_m signals are measured and calculated by feedback sensors. The deviation between measured speed ω_m and target speed ω_m^* is regulated by speed PI controller to obtain current reference of i_d^* and i_q^*. Three-phase current i_a, i_b and i_c are measured by stator current sensor, and through *Clarke-Park* coordinate transformation converted into i_d and i_q components in d-q coordinate, which are taken as current loop feedback. And through current controller and *inverse-Park* coordinate transformation the deviations between i_{dq} and i_{dq}^* are calculated to judge V_α and V_β in sectors. Using PWM signal produced by space vector pulse width modulation (SVPWM) technology to control inverter, thus the double closed-loop vector control of permanent magnet synchronous motor is achieved.

It is noted that a PMSM machine cannot work without a controller that requires current sensor and speed/position sensor to provide necessary signals. However, its low-cost counterpart IM is able to work without controller, directly driven by AC current, in the cases with no need of speed adjusting. In order to further increase the competitive capability of the designed ferrite IPM electric drive system, apart from its high efficiency and high power density, the cost of

motor controller is minimised as well. The low-cost Hall-effect sensors are adopted in estimating velocity and position of the PMSM, and only one high-precision shunt resistor is used for the current sampling. This scheme of control system is with much lower hardware cost than that equipped with high-precision encoder and three shunt current sampling resistors.

In the motor control system study, both of encoder and Hall Effect sensors are discussed and tested for the speed/position feedback, and both of three-shunt and single-shunt current sensing are applied and compared in the thesis.

6.2 Speed and Position Feedback

Position and speed sensors are introduced in literature review Section 2.4.4.and Hall Effect sensors are used in the studied low-cost drive system due to their reliable and economical features. An incremental encoder is also used in the control system as a reference position and speed sensor to evaluate the accuracy of Hall Effect sensor.

6.2.1 Encoder Sensor and Experiment Test

Quadrature incremental encoders are widely used to obtain the rotor position of electric machines. As the name implies, the incremental encoders read the angular displacements with respect to its reference position. When the reference position is defined, the absolute angular displacements can be obtained by counting the incremental steps starting from the position. For this reason, a rotor prepositioning process is always necessary to define the reference angular position after the first start-up or any fault event or microcontroller reset.

The measured signals of the encoder used in the motor prototype at different speed are shown in Figure 6-2. Quadrature encoders have two output signals, clock signal A and B, with a phase difference of a quarter of period between them. Each clock has both a rising edge and a falling edge for each pulse, so by counting all edges of both the A and B clock phases, the counter (controller's encoder timer) obtains an incremental signal that is four times the resolution of any single output clock signal. The encoder used in the prototype has 2500 slits

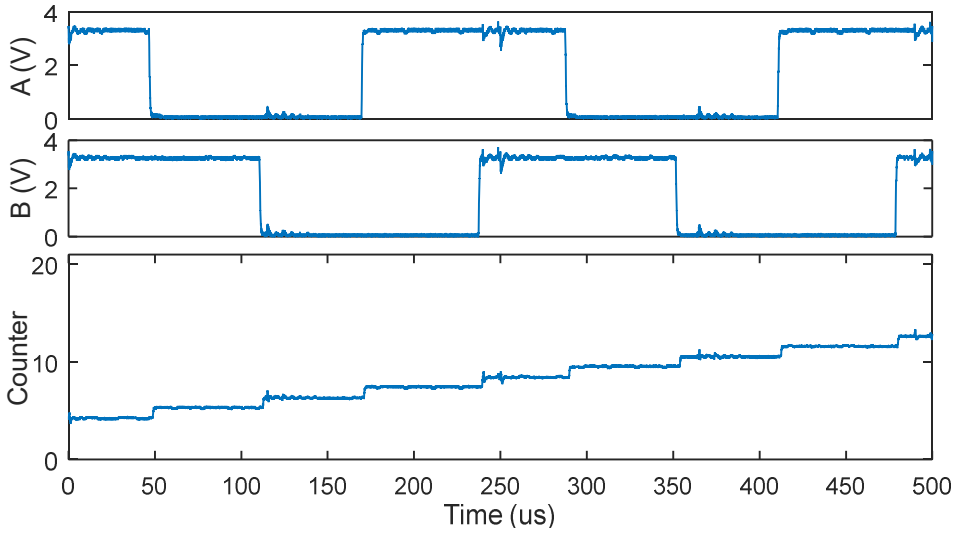

(a) Speed is 100 RPM

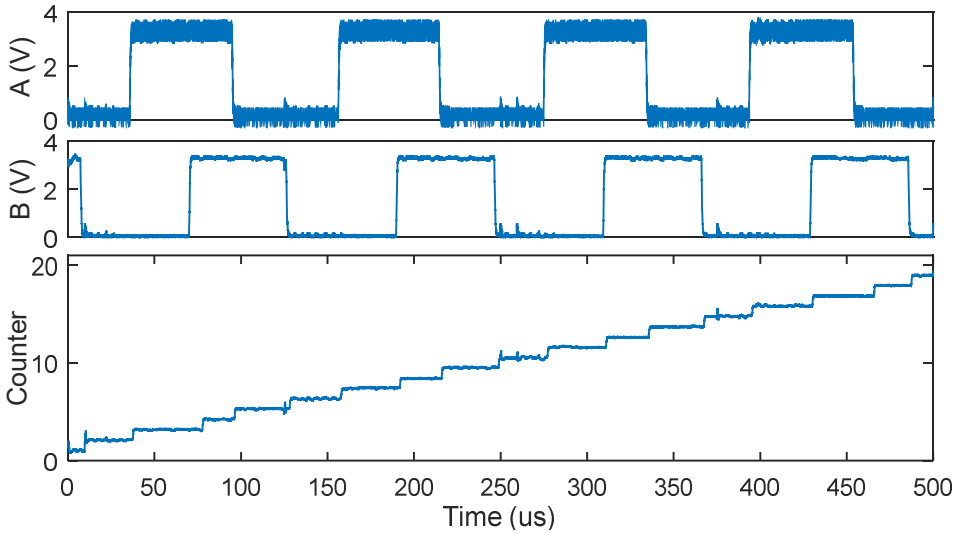

(b) Speed is 200 RPM

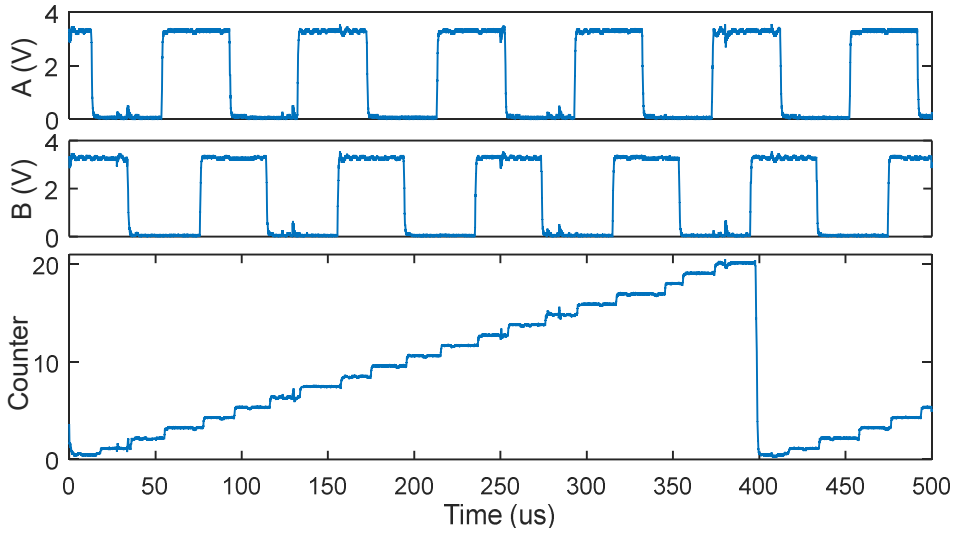

(c) Speed is 300 RPM

Figure 6-2 Encoder signals at different speed

per revolution, so there are 10000 edge signals when the rotor spins one round. Thus the minimum observable angle is 0.036° that is accurate enough for the motor control system. As shown in Figure 6-2, when motor speed is increased from 100 rpm to 300 rpm, more edge signals are observed in a fixed period of time. Hence the speed can be calculated by counting the number of incremental steps in a specific time, which is expressed in equation (6-4).

$$n_{encoder} = 60 \cdot \frac{N_{counter}}{4 \cdot N_{slit}} \cdot f_{sample} \quad \textbf{(6-4)}$$

N_{slit} is number of encoder slits, $N_{counter}$ is number of observed edge signals by counter, f_{sample} is frequency of sampling, and $n_{encoder}$ is the calculated speed of the encoder in rpm. The measuring frequency $f_{measure}$ is 2 kHz in the prototype controller, thus the minimum measurable speed of the encoder is 12 rpm. There are some unavoidable noises and vibrations in the observed encoder signals, so the eventual measured speed is the result after filtering. Simple first-order filter or mean filter is widely used in speed processing. The motor's rolling direction can be simply obtained from counter timer by comparing the rising edges and falling edges of the two output signals.

Absolute position information is required for performing field-oriented control, but the quadrature encoder is a relative position sensor. So it is necessary to establish a 0° position to get information about actual rotor angle. This task is performed by means of an alignment phase and shall be carried out at the first motor start-up and optionally after any fault event. It consists of imposing a stator flux with a linearly increasing magnitude and a constant orientation. If properly configured, at the end of this phase, the rotor is locked in a well-known position and the encoder timer counter is initialised accordingly.

Commonly, the rotor with PM Field will spin and orient along with stator flux that is established by conducting I_d with alignment current. And the locked position is defined as the reference 0° position. However, during motor test it is found that the prototype motor cannot be always locked at the expected position and the flux of rotor is always aligned with the teeth of stator. The main reason of that is because the IPM machine has large cogging torque that overtakes the

alignment torque. When rotor polarity intends to stop somewhere near a stator tooth, the strong cogging torque will attract the rotor and make it align with stator tooth. The phenomenon is depicted by schematic diagram Figure 6-3. The red arrow indicates the torque direction of cogging torque.

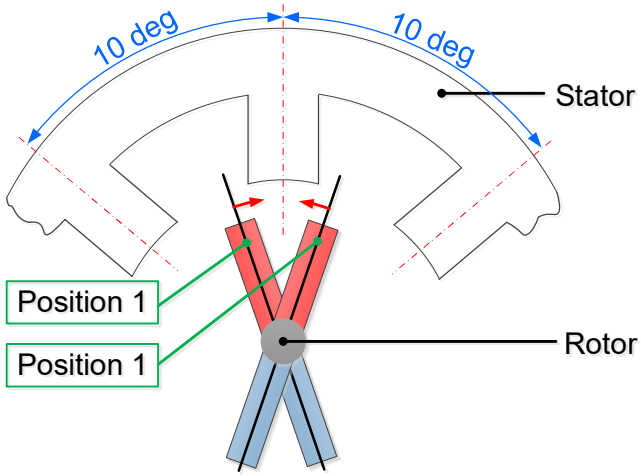

Figure 6-3 Alignment to stator tooth by cogging torque

The phenomenon is further validated by FEA simulation. The position where rotor polarity is in alignment with stator tooth (red dash-dot line shown in Figure 6-3) is set as reference point. On the premise that same input current (2.2 A) and same voltage phase angle (voltage vector along with magnetic field vector) are employed in the stator windings, different starting torques are applied on

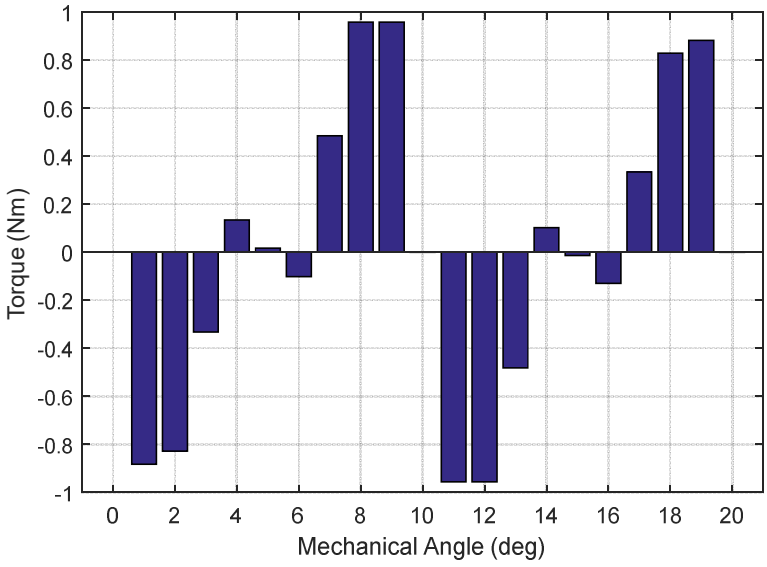

Figure 6-4 Output torque at start point in every 20 mechanical degrees

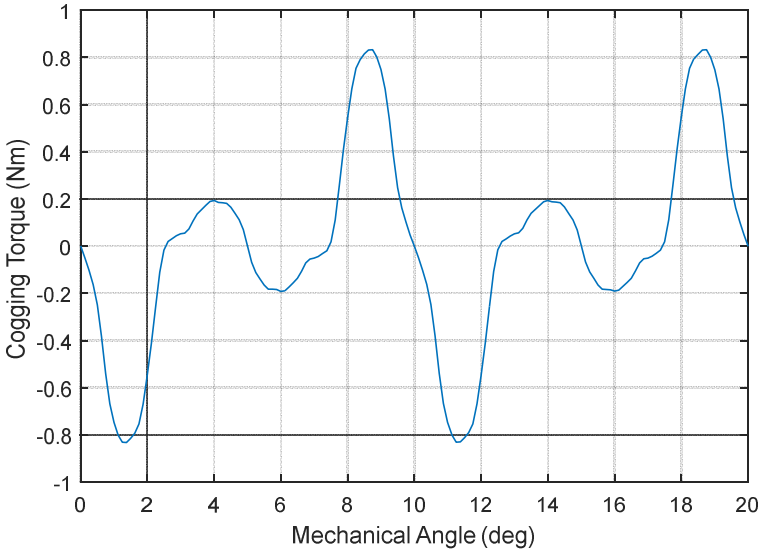

Figure 6-5 Cogging torque in every 20 mechanical degrees

rotor when its position is changed from 0 to 19 mechanical degrees， which is shown in Figure 6-4. The same reacting torques are repeated every 20 mechanical degrees, because every phase section occupies two slots and each slot corresponds to 10 mechanical degrees.

This figure is clearly shown that only when the rotor is at 0°, 10°, 20° position (stable position), where magnetic field direction is along with the central line of the stator tooth, there is no torque acted on the rotor, but at other positions the rotor undertakes some torques. Although the input the current is positive, the applied torque on rotor might be positive or negative. That is because the torques at initial point is mainly determined by cogging torque that is shown in Figure 6-5. The profile of the bar chart in Figure 6-4 is quite similar to the shape of the waveform in Figure 6-5. Either negative torque after stable position or positive torque before stable position will attract rotor back to stable position.

Figure 6-6 shows the process of rotor movement. There are ten different intended positions (in 23 deg–38 deg range), but finally the rotor only stops at three positions (20 deg, 30 deg, and 40 deg) that are the central lines of teeth. Further, if the rotating angle is too small, such as less than 20 deg, the rotor generally does not move as alignment torque is less than cogging torque. From the analysis it is concluded that the rotor can only be locked at the central lines of stator teeth and during the alignment process the intended rotating angle

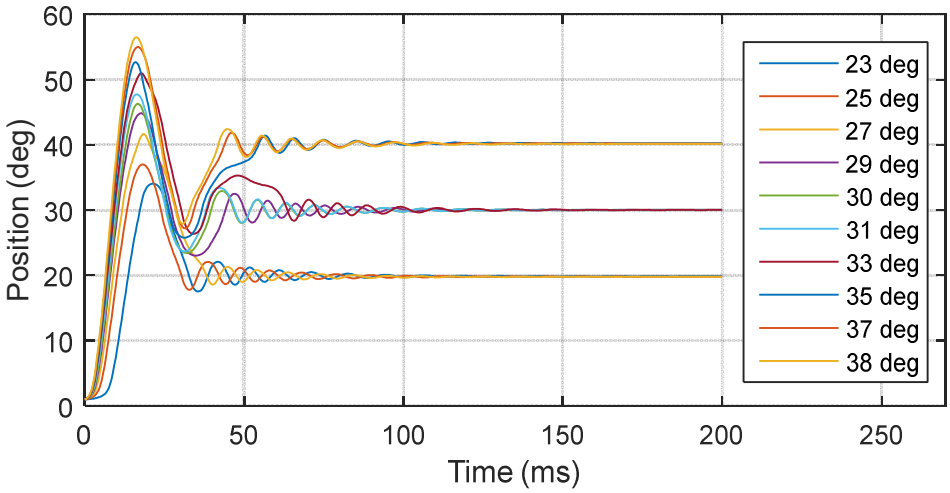

Figure 6-6 Process of rotor movement

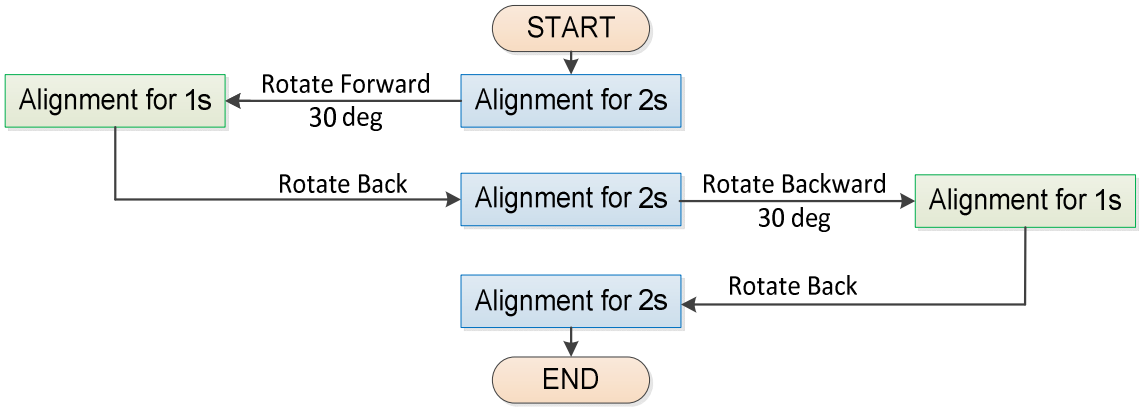

Figure 6-7 Flow chart of enhanced alignment procedure

cannot be too small otherwise the rotor is not able to be locked at expected position. In order to make the starting alignment successful and provide right reference position of rotation angle, an enhanced alignment procedure is proposed, which is illustrated in the flow chart in Figure 6-7. Although the alignment procedure is simple without complicated algorithm only spinning rotor forward and backward, it has effective results successfully aligning D-axis of rotor with A-axis of stator. The same alignment procedure is also in Hall Effect sensor system.

A feedback edge signal from encoder represents a fixed fractional angle, so that when the starting position is defined the angle position can be easily obtained by equation (6-5).

$$\theta_{encoder} = 360° \cdot \frac{N_{counter}}{4N_{slit}} \quad \textbf{(6-5)}$$

Figure 6-17 shows the position signals measured from experiments from speed 100 rpm to 400 rpm. The details are discussed in 6.2.3.

6.2.2 Hall Effect Sensor and Experiment Test

Hall Effect sensors are applied in the low-cost drive system due to their economical price and reliable performance. The application of Hall Effect sensors on ferrite motor is described in details in this section and measured results of speed and position are shown in 6.2.3.

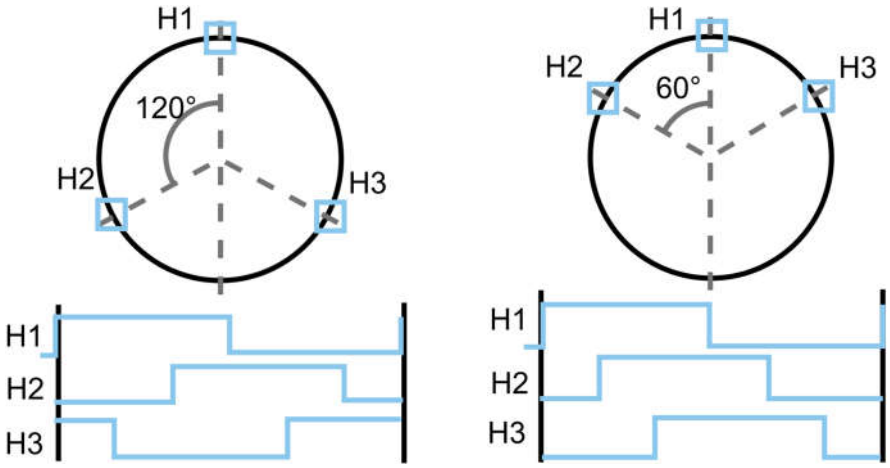

(a) 3 sensors in 120° (b) 3 sensors in 60°

Figure 6-8 Hall sensors location and output-state correspondence

There are generally two ways of locating Hall Effect sensors in the motor, which is illustrated in Figure 6-8. The schematic diagrams only exhibit one electrical period and the values of angles are in electrical degrees. Considering H3-H2-H1 as a three-digit binary number (H3 is the most significant bit), it is possible to associate a rotor position with a numbered state that is a combination of the three Hall Effect sensor output. As shown in Figure 6-8, in 3 sensors 120° topology, the numbered states are: *State 5 -> State 1 -> State 3 -> State 2 -> State 6 -> State 4*; in in 3 sensors 60° topology, the numbered states are: *State 1 -> State 3 -> State 7 -> State 6 -> State 4 -> State 0*. Consequently, it is possible to reconstruct the rolling direction of the rotor by comparing the present

state with the previous one. In the study, 3 sensors 120° topology is used, and the actual location of the Hall Effect sensors are shown in Figure 6-9.

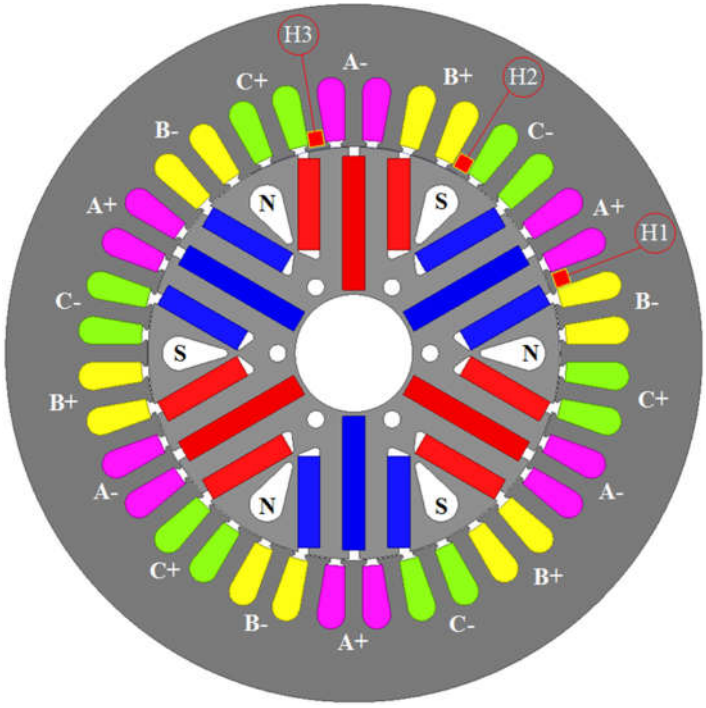

Figure 6-9 The location of Hall Effect sensors

When a Hall Effect sensor faces a *North Pole* of the rotor, it will generate a high-voltage signal regarded as "*1*", and it faces a South Pole, a low-voltage signal will be obtained as "*0*". The signals of Hall Effect sensors in our designed motor are measured and showed in Figure 6-10. As the motor speed is increased from 100 rpm to 300 rpm, more pulse signals are obtained by Hall Effect sensor. The frequency of the obtained waveform is proportional to the motor speed, so the rotational speed can be calculated from the measured Hall signals. As the frequency of Hall Effect sensor is much lower than that of encoder, only six signals in an electrical period. So the speed calculation of Hall Effect sensor is carried out by another way that is expressed in equation (6-6).

$$n_{Hall} = 60 \cdot \frac{1}{6p} \cdot \frac{1}{t_{interval}} \quad \textbf{(6-6)}$$

where p is number of pole-pairs, $t_{interval}$ is time interval between two edge signals (either rising or falling edge) in second, and n_{Hall} is the calculated mechanical speed in rpm.

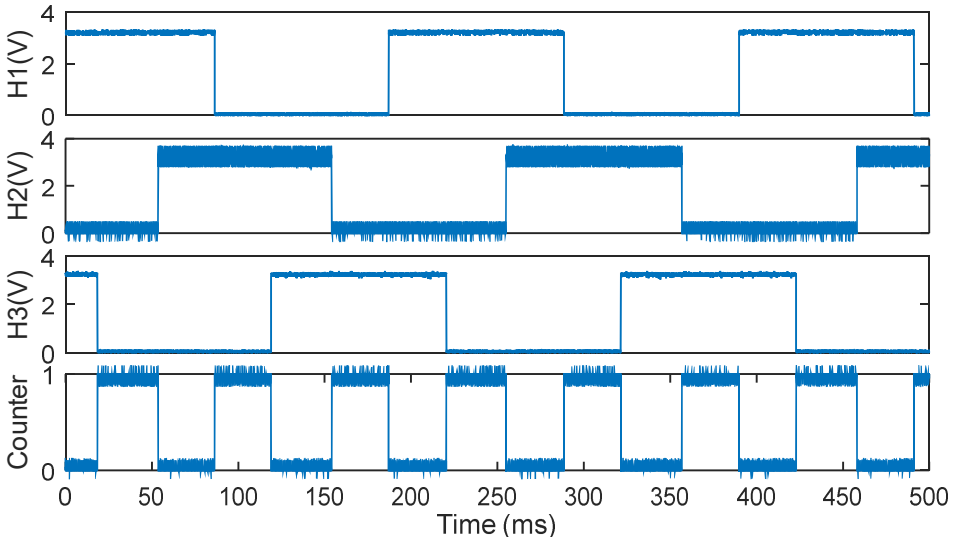

(a) Speed is 100 RPM

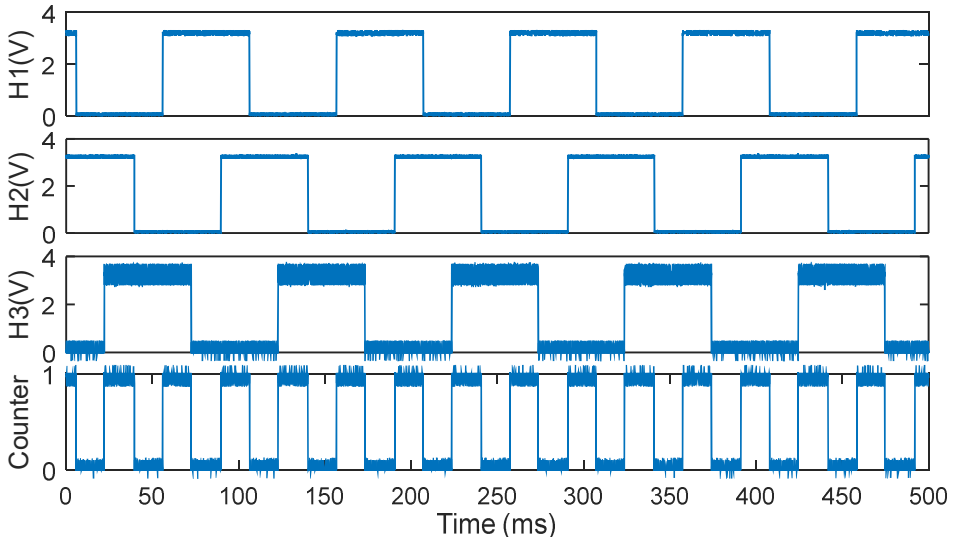

(b) Speed is 200 RPM

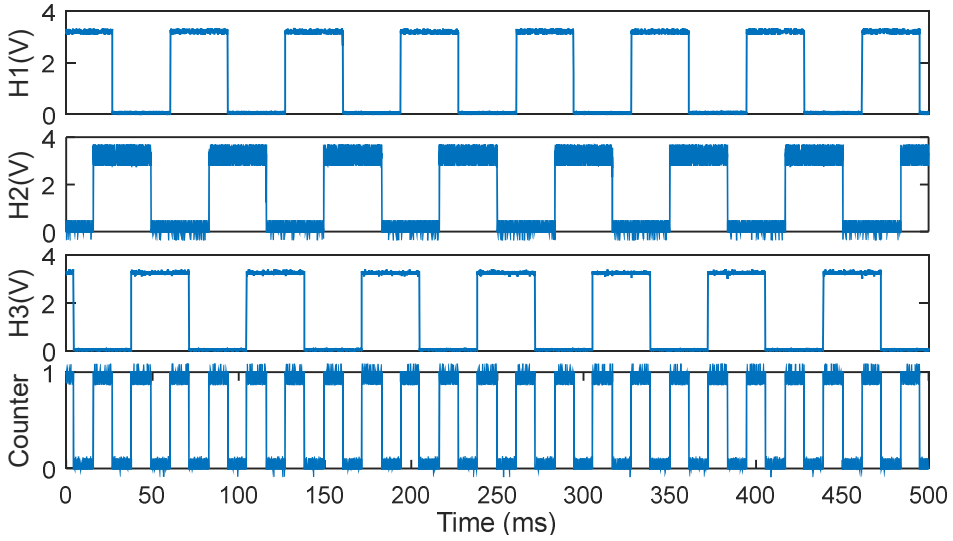

(c) Speed is 300 RPM

Figure 6-10 Signals of Hall Effect sensors at different speed

The limited edge signals of Hall Effect sensor are not directly used to present angle interval like encoder but used as trigger signals to obtain time interval between edge signals. Because the angle difference Hall sensors is known, 120 electrical degrees, when the time passing by the fixed distance is obtained by Hall timer, the rotating speed can be calculated. Some speed test results are shown in Figure 6-16 and discussed in 6.2.3.

The position estimation of Hall Effect sensor is more complex than that of encoder sensor due to its less feedback signals from sensor in a revolution. In order to improve the accuracy of position estimation, an elaborate method is proposed and validated in the thesis. Generally, the angle difference between two adjacent Hall sensors is set as 120 electrical degrees, but the specific location of sensors is not indicated. Theoretically, the Hall sensors can be installed at any place on the inner circumference of stator core. After alignment procedure, the same one used in encoder sensor, the position where D-axis of rotor coordinating with A-axis of stator is set at reference angle position. The Hall state of the reference angle can be easily obtained from Hall sensor feedback, but the accurate relative position in the angle interval that covers 60 electrical degrees is still unknown. Therefore a further process is necessary to deduce the accurate relative position of reference angle in the Hall feedback waveform.

The only position directly measured by Hall Effect sensor is the place triggering an edge signal, which is the boundary between Hall states, such as the starting point in Figure 6-8(a) the boundary between State 4 and State 5. And the method of locating reference position is to find a nearby state transition point and calculate the angle difference between them.

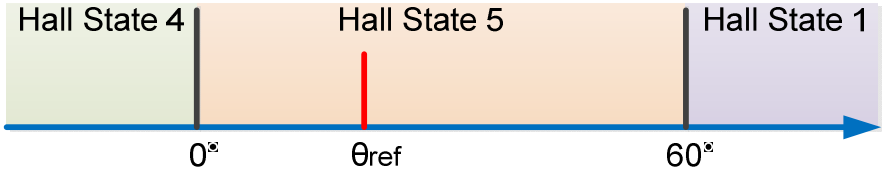

Figure 6-11 Relative position of reference angle

There are six Hall states (State 5, 1, 3, 2, 6, and 4), each state covers 60 electrical degree of angle interval. The Hall state of reference position can be easily obtained by Hall timer, for example in Figure 6-11 the reference position is in State 5. And Figure 6-12 shows the procedure to calculate the relative angle θ_{ref} of reference position so that the actual positions of sensors can be deduced.

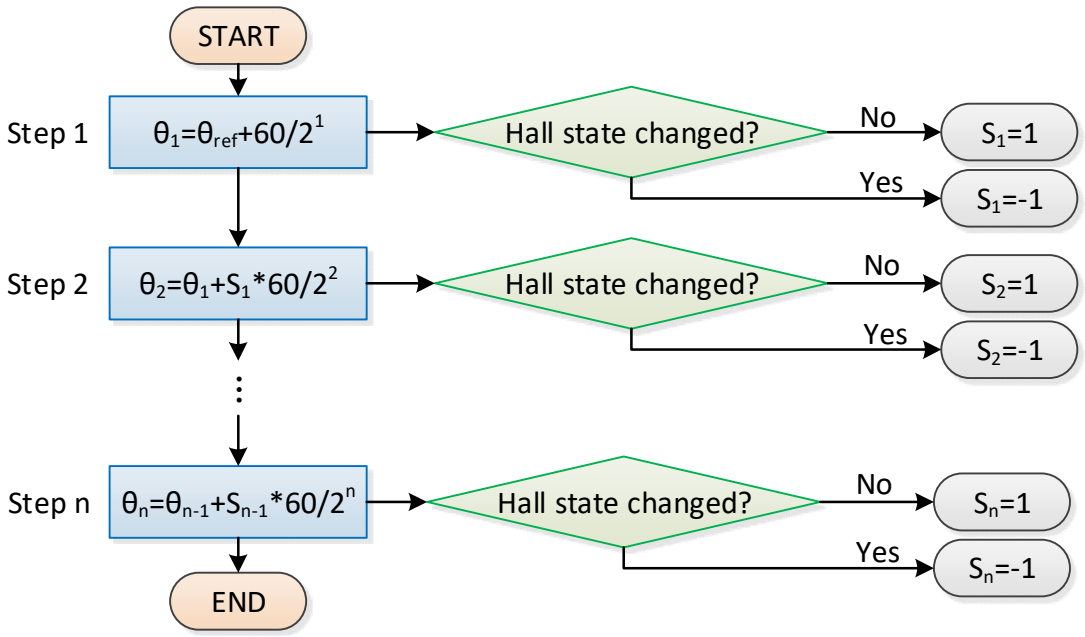

Figure 6-12 Flow chart of locating reference position

After alignment procedure, the rotor is locked at θ_{ref}, and changing Id and Iq the rotor will be rotated forward to new position, such as. $\theta_1 = \theta_{ref} + 60/2^1$ in step 1. If the Hall state of the new position, obtained by Hall timer, is different from the previous one, that means the trying angle is too large and will be reduced in next step; if the hall state does not change, that means the trying angle is small and can be added in next step. The trying angle θ_n is expressed in equation (6-7) where *n* is the times of trying. After several steps, θ_n is gradually closing to 60°. For example, at the 10th step the difference between θ_n and 60° is less than 0.1° that is accurate enough for most applications. Assuming $\theta_n = 60°$, the relative position θ_{ref} is obtained by equation (6-8) and consequently the positions of Hall sensors are deduced. Figure 6-13 shows the positions of Hall sensors in an electrical period if $\theta_{ref} = 23°$.

$$\theta_n = \theta_{ref} + \frac{60}{2^1} + S_1\frac{60}{2^2}\cdots + S_{n-2}\frac{60}{2^{(n-1)}} + S_{n-1}\frac{60}{2^n} \quad \textbf{(6-7)}$$

$$\theta_{ref} = 60 - \left(\frac{60}{2^1} + S_1\frac{60}{2^2}\cdots + S_{n-2}\frac{60}{2^{(n-1)}} + S_{n-1}\frac{60}{2^n}\right) \quad \textbf{(6-8)}$$

This general method of locating Hall sensors is tested in the designed ferrite motor, but it does not work. Because this type motor has strong cogging torque, which is discussed in 6.2.1, the rotor cannot be locked any required position only orienting along stator teeth so that the approximating approach described in Figure 6-12 is not applicable to the motor prototype.

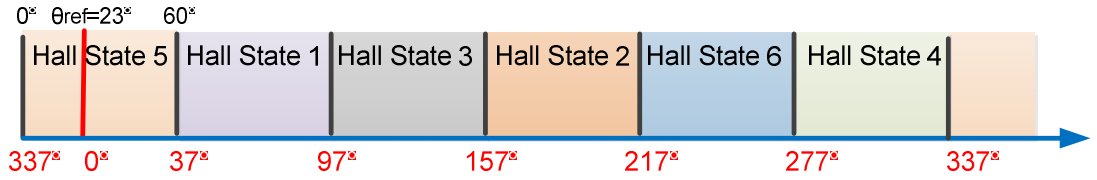

Figure 6-13 Positions of Hall sensors in an electrical period when $\theta_{ref} = 23°$

The special features of the machine make it impossible to use regular method to locate Hall sensor position, but they can be properly utilised by directly arranging the physical locations of sensors around stator teeth. As shown in Figure 6-9, the Hall sensors are stuck just right at the central line of stator teeth. And from the location of sensors the reference angle after alignment procedure can be easily identified, which is depicted in Figure 6-14. The reference angle is just right at the centre of State 5.

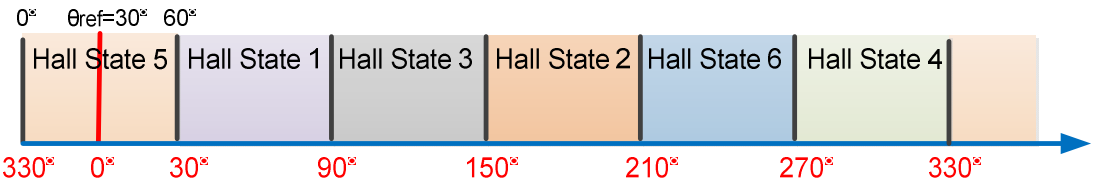

Figure 6-14 Hall sensor positions of prototype motor

Position signals are in need of vector control of the designed motor, but there are only six measured positions in an electrical period and all other positions are estimated by the available measured position. An improved position estimation approach of Hall sensor is used for the prototype, the assumption of

which is that in a short time the speed is changed linearly, i.e. acceleration is constant is a short period. Figure 6-15 illustrates all the relative variables that will be used in position estimation.

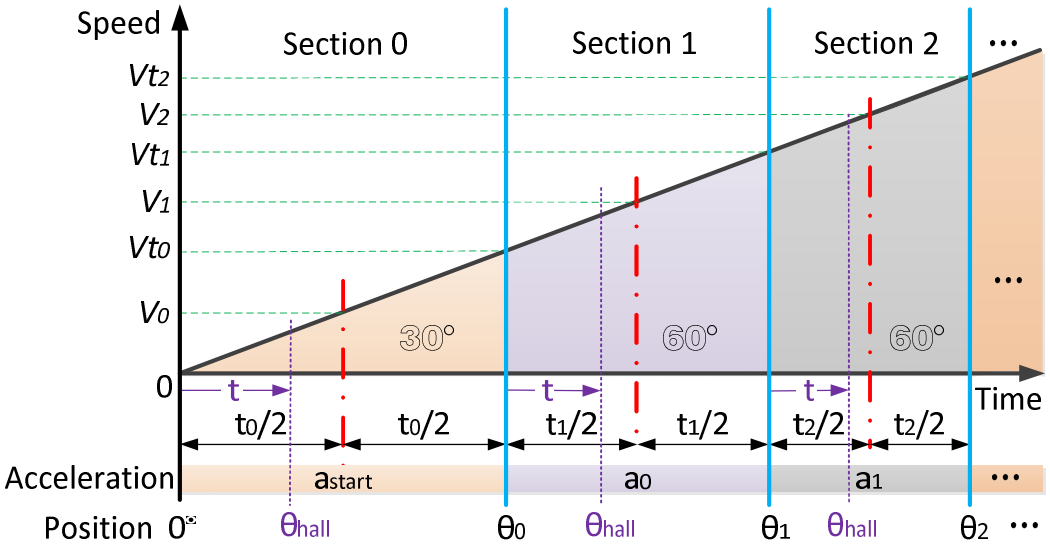

Figure 6-15 Angle position estimation of Hall Effect sensor

When the rotor is start to spin, Hall timer will be triggered by any edge signal and the experienced time between two consecutive triggers is recorded, such as t_0, t_1, and t_2 in Figure 6-15. The average speed of each state section can be calculated by equation (6-6). As motor speed is assumed changing linearly, the average speed is equal to the median speed in each section, which is V_0, V_1, and V_2 in Figure 6-15.Refering to Figure 6-14, it is noted that the first state section only has 30°, and all the other sections cover 60°. With the measured time and calculated speed, the acceleration between two speeds can be calculated by equation (6-9) and (6-10).

$$a_0 = \frac{V_0}{\frac{t_0}{2}} \tag{6-9}$$

$$a_n = \frac{V_n - V_{n-1}}{\frac{t_n}{2} + \frac{t_{n-1}}{2}} \ , (n = 1, 2, \cdots) \tag{6-10}$$

The acceleration calculated by available data will be used in the next section to estimate angle position, depicted in Figure 6-15. At the start section (Section 0),

acceleration a_{start} is directly assigned by control system as no previous data available.

$$V_{t_0} = 2V_0 \quad \textbf{(6-11)}$$

$$V_{t_n} = V_n + a_n \frac{t_n}{2} \text{ , } (n = 1, 2, \cdots) \quad \textbf{(6-12)}$$

$$\theta_{hall} = \frac{1}{2} a_{start} t^2 \text{ , } (only\ used\ in\ Section\ 0) \quad \textbf{(6-13)}$$

$$\theta_{hall} = \theta_{n-1} + V_{t_{n-1}} t + \frac{1}{2} a_{n-1} t^2 \text{ , } (used\ in\ Section\ n, n = 1, 2, \cdots) \quad \textbf{(6-14)}$$

Motor speed at triggering moment is estimated by equation (6-11) and (6-12). And finally the angle position θ_{hall} at any instant time t is able to be predicted by equation (6-13) and (6-14). The estimated instant position is applied in vector control of the ferrite motor and the angle position measured from experiments is shown in Figure 6-17 and compared with encoder position feedback. More details will be discussed in 6.2.3.

6.2.3 Comparison and Analysis

The motor speed and position measuring methods of encoder and Hall Effect sensors have been discussed in Section 6.2.1 and 6.2.2, and they are tested in the prototype drive system. The test results are compared and analysed in this section.

Figure 6-16 shows speed test results of encoder and Hall sensor. In the speed-up test, as shown in Figure 6-16 (a), the motor starts from constant speed of 100 rpm and then speeds up to 400 rpm. After the ramp-up, the motor runs constantly at 400 rpm till the end. In the constant speed region, the results of both of the two sensors are stable. And in the speed-up region, both of the speeds grow gradually and linearly. And in the speed-down test, the motor starts from constant speed of 400 rpm and then speeds down to 100 rpm. After the ramp-down, the motor runs constantly at 100 rpm till the end. Similar to speed-up test, both of the two sensors have stable speed at the constant region, and their speeds change smoothly and linearly in the ramp-down region.

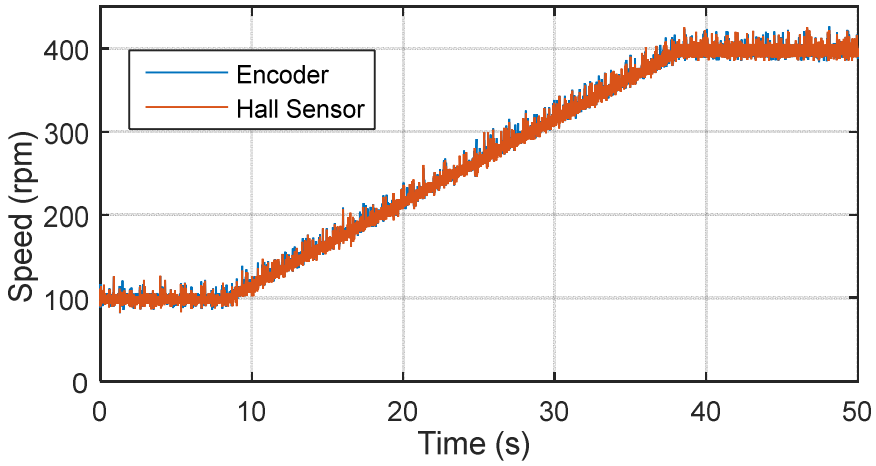

(a) Test 1: Speed up

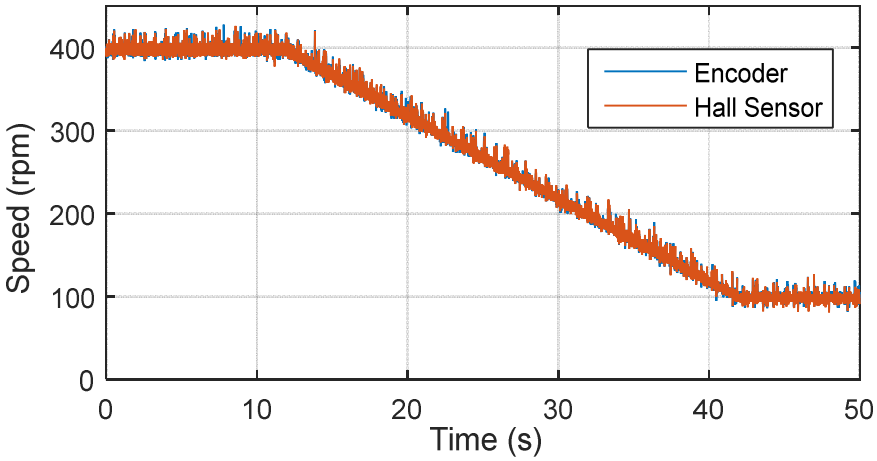

(b) Test 2: Speed down

Figure 6-16 Speed feedback comparison from experiment

Generally, encoder has higher accuracy of speed measurement, and it is used as benchmark in the test to validate the speed measurement by Hall Effect sensors. From the comparison shown in Figure 6-16, it is seen that the speed measurements of Hall Effect sensors have close agreement with that of encoder in both speed-up and speed-down conditions. Therefore, it is validated that the Hall Effect sensors are able to provide comparable speed feedback like encoder for the motor controller.

Figure 6-17 shows the angular position tests of both encoder and Hall Effect sensors. The measurements are taken at different constant speeds, which are 100 rpm, 200 rpm, 300 rpm and 400 rpm. As the motor is rotating forwards, the angular position (electrical angle) grow gradually from 0° to 360°, and then jumps back to 0°. The cycle is repeated as the motor is moving forwards. When

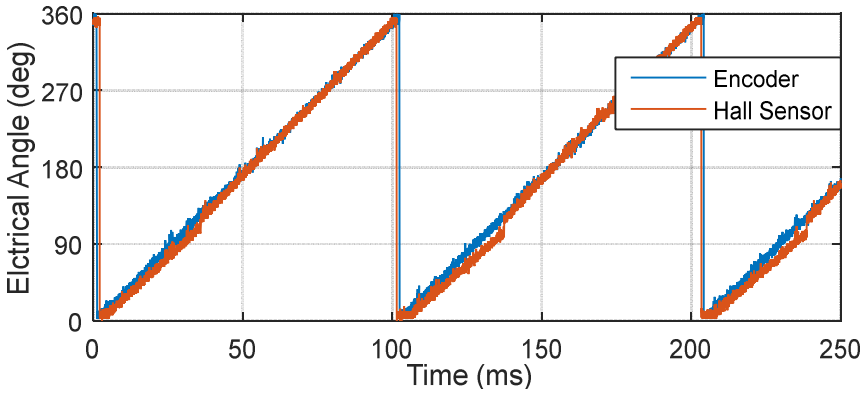

(a) Speed at 100 rpm

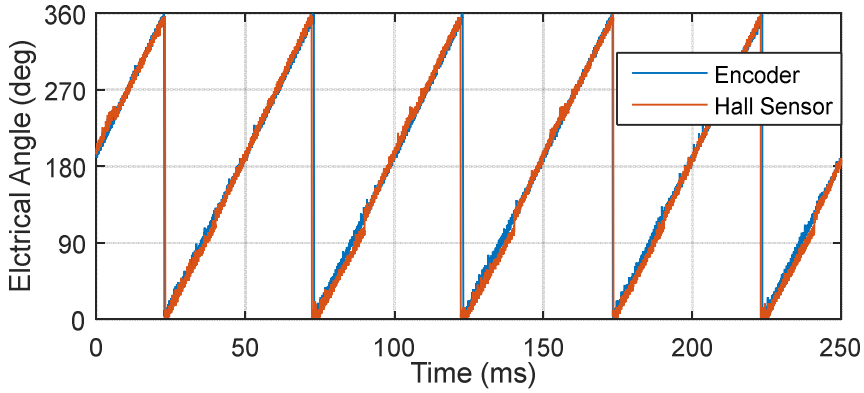

(b) Speed at 200 rpm

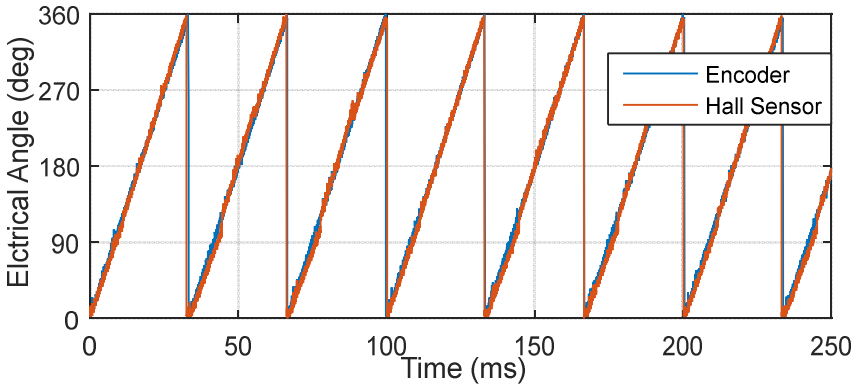

(c) Speed at 300 rpm

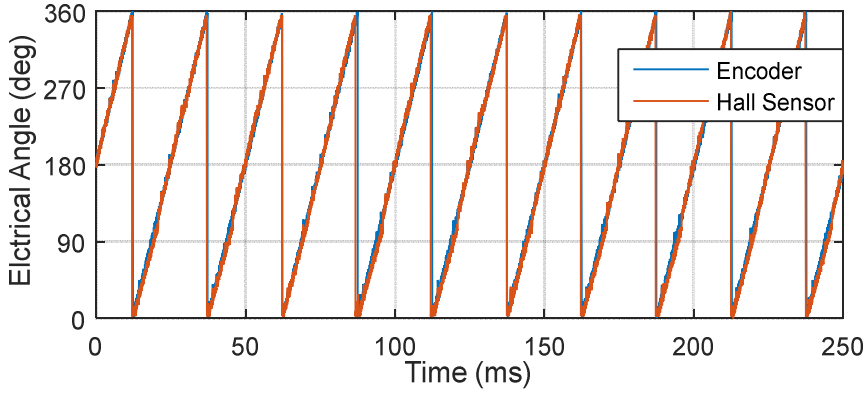

(d) Speed at 400 rpm

Figure 6-17 Position feedback comparison from experiment at different speed

the motor speed increases, more cycles are repeated in a specific time period. As shown in Figure 6-17, the encoder provides good quality of angular position feedback, and the measured angle is changing smoothly. The encoder is used as benchmark to validate the position measurement of Hall Effect sensors. From the comparisons of the test results of the two sensors, it is found that the measurement of Hall Effect sensor has some deviations from that of encoder around 70° –110°, but the deviations are with the acceptable range. And when the motor speed is increased, the deviations become unnoticeable. In other angular regions, Hall Effect results have good agreement with encoder results. Therefore it is validated that the Hall Effect sensors are able to provide comparable position feedback like encoder for the motor controller.

6.3 Current Sampling

Current sampling plays a crucial role in PMSM field-oriented control and the feedback currents are used in motor torque control. With different hardware facilities, such as three-shunt or single-shunt current sampling resistors, the approaches of current measurement are different. As the cost of single-shunt current sampling is lower, it is preferably used in the low-cost drive system. In the section, both of the three-shunt and single-shunt current sampling are discussed and compared. The three-shunt topology is used as benchmark to validate the single-shunt topology. More details are followed in the section.

6.3.1 Three-shunt Current Sampling

The three currents I_A, I_B, and I_C flowing through a three-phase system follow the mathematical relation:

$$I_A + I_B + I_C = 0 \tag{6-15}$$

For this reason, to reconstruct the currents flowing through a generic three-phase load, it is sufficient to sample only two out of the three currents while the third one can be computed by using the above relation.

Current shunt resistors are low resistance precision resistors used to measure AC or DC electrical currents by the voltage drop those currents create across

the resistance. Sometimes called an ammeter shunt, it is a type of current sensor. The current shunt resistor is much more expensive than normal resistors. So if less shunt resistors are used, the overall cost of the electric drive system will be reduced. Therefore in the low-cost electric drive research single-shunt current sampling is applied and the effectiveness is validated by experiments and compared with three-shunt sampling topology.

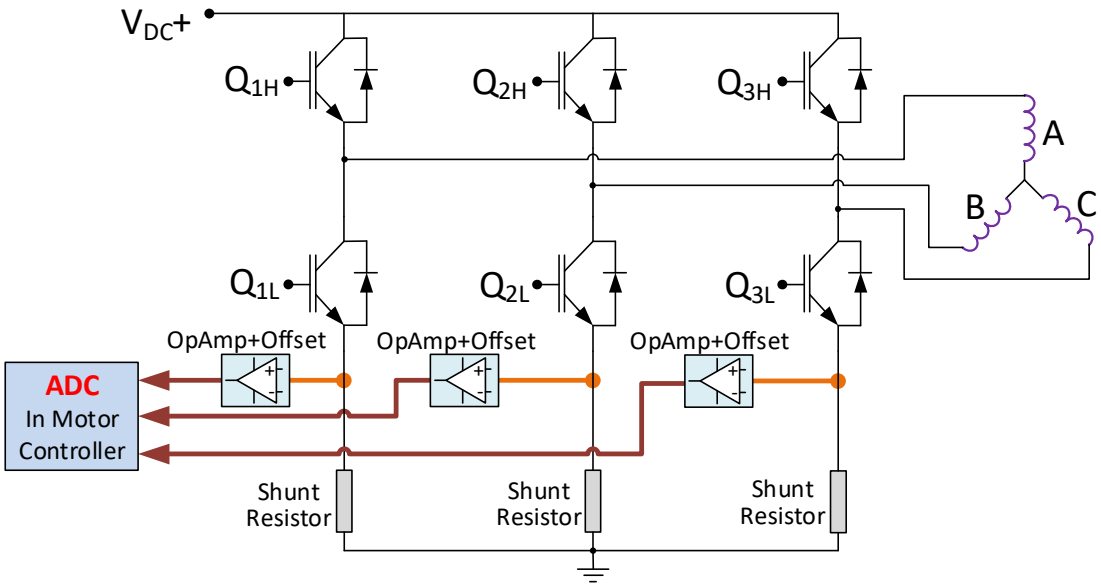

Figure 6-18 Three-shunt topology hardware architecture

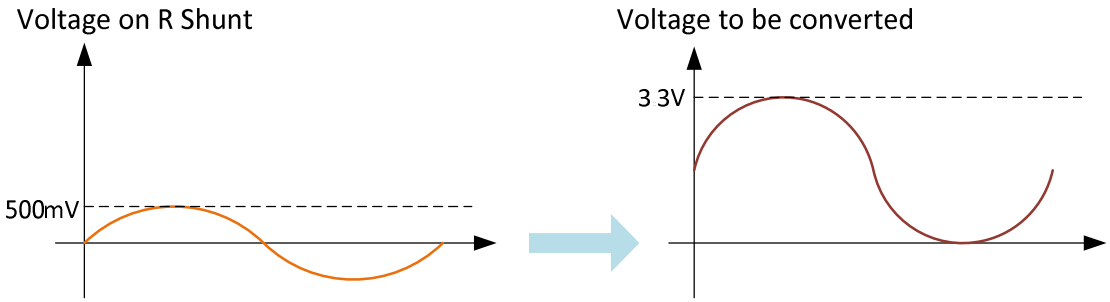

Figure 6-19 Measured signal is amplified and offset by a current sensing circuit

Figure 6-18 shows the three-shunt current sampling topology, where three current sampling resistors located separately in each inverter leg. When current is going through a sampling resistor, its value is measured by the voltage drop across the resistor. As shown in Figure 6-18, an end of current sampling resistor is connect to ground, and the voltage on the other end represents the

voltage drop across shunt resistor. Because the measured voltage signals have small amplitudes and have both positive and negative values, they are amplified and offset by an op-amp circuit, depicted in Figure 6-19, and then the processed voltage is sent to ADC module of motor controller.

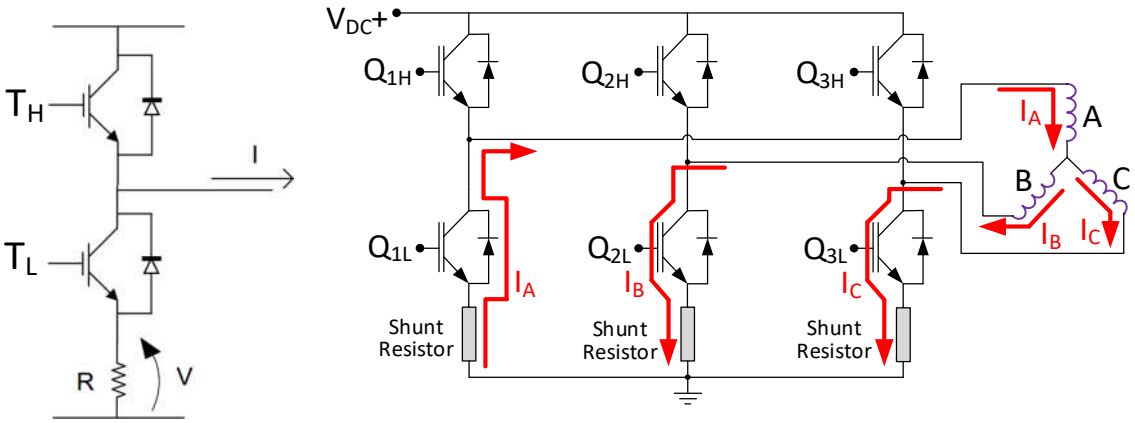

(a) A inverter leg (b) Current route when I_A>0, I_B<0,I_C<0

Figure 6-20 Demonstration of current sampling by shunt resister

The current can be sampled only when it passes through shunt resistor. As shown in Figure 6-20(a), in each inverter leg, if transistor S_L is switched on and S_H is switched off, whatever the direction of current I, it always flows through the shunt resistor R. Thus in a three-shunt topology the best current sampling time is the moment when all the lower transistors are off. For example, if currents I_A>0, I_B<0, and I_C<0, when all the upper transistors are switched off and all the lower transistors are switched on, the current route is shown in Figure 6-20(b). The current I_B and I_C flow through transistors and current I_A with different direction goes through the bypass diode. If the direction of current is defined as positive, it is worthy to note that the measured voltage has opposite sign with the current. And the obtained signal will be corrected by controller processor.

In order to properly reconstruct the current flowing through one of the inverter legs, it is necessary to properly synchronise the conversion start with the generated PWM signals. The current sampling moment is discussed in the following three cases according to different modulation index.

Case 1: ΔDuty > DT+T_N

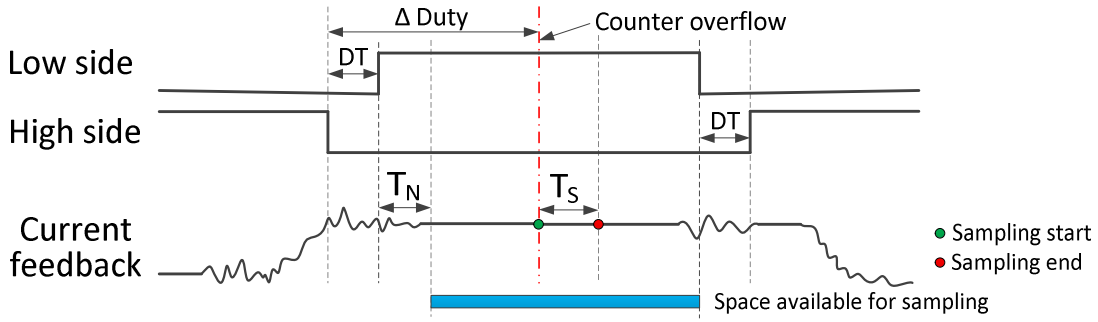

Figure 6-21 Case 1: ΔDuty > DT+T_N

Because currents are measured when all the low side IGBTs are off in three-shunt topology, it is only necessary to consider the inverter leg with lowest duty cycle. The time parameters used in the discussion are defined below.

- DT is dead time.
- T_N is the duration of the noise induced on the shunt resistor voltage of a phase by the commutation of a switch belonging to another phase.
- T_S is the sampling time of the A/D converter (presuming T_S < DT + T_N).

Case 1 typically occurs when SVPWM with low modulation index is generated, the duty cycle ΔDuty > DT+T_N as shown in Figure 6-21, there is a relatively large space available for sampling. In this case, the current sampling time usually starts from counter overflow point, so that the current has more time to stabilise. The currents of Phase A and Phase B are sampled simultaneously by two A/D converters that are triggered by the fourth channel of PWM timer (PWM4) or by the overflow signal.

Case 2: (DT+T_N+T_S)/2 < ΔDuty < DT+T_N

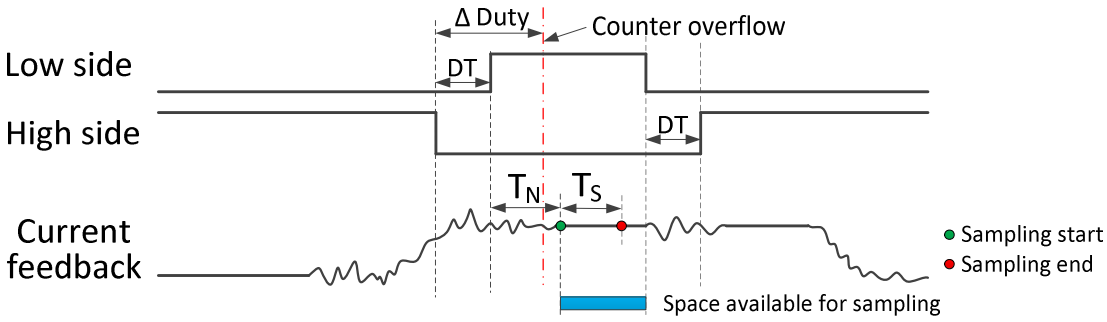

Figure 6-22 Case 2: (DT+T_N+T_S)/2 < ΔDuty < DT+T_N

With the increase in modulation index, ΔDuty may have values smaller than DT + T_N but still larger than (DT+T_N+T_S)/2. In this case, the start point of current sampling will be after counter overflow line, so that the counter overflow signal cannot be used as trigger to synchronise ADC sampling. The A/D converters are triggered by PWM4 output and sample the currents of Phase A and Phase B. Figure 6-22 shows that the space available for sampling is much smaller than that of Case 1.

Case 3: ΔDuty < (DT+T_N+T_S)/2

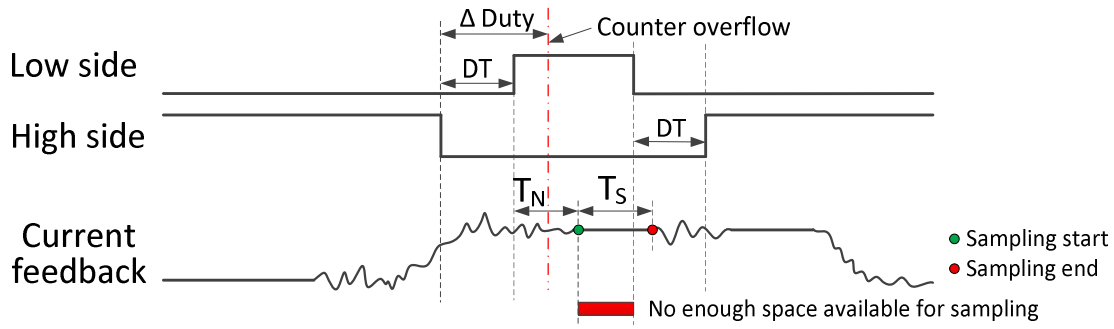

Figure 6-23 Case 3: ΔDuty < (DT+T_N+T_S)/2

If the modulation index is too large, the duty cycle ΔDuty may be even less than (DT+T_N+T_S)/2. In this case, the current reading cannot be performed as there is not enough time for sampling, which is illustrated in Figure 6-23. In order to successfully sample current in the three-shunt current sampling topology, the modulation index cannot be too large and generally limited up to 95%.

6.3.2 Single-shunt Current Sampling

Figure 6 24 shows the hardware architecture of single-shunt current sampling topology. Comparing with three-shunt topology, the single-shunt topology saves two shunt resistors and two op-amp circuits, so that the overall hardware cost of the electric drive system is reduced. Like that in three-shunt topology, the measured voltage signals are amplified and offset by an op-amp circuit, depicted in Figure 6 19, and then the processed voltage is sent to ADC module of motor controller.

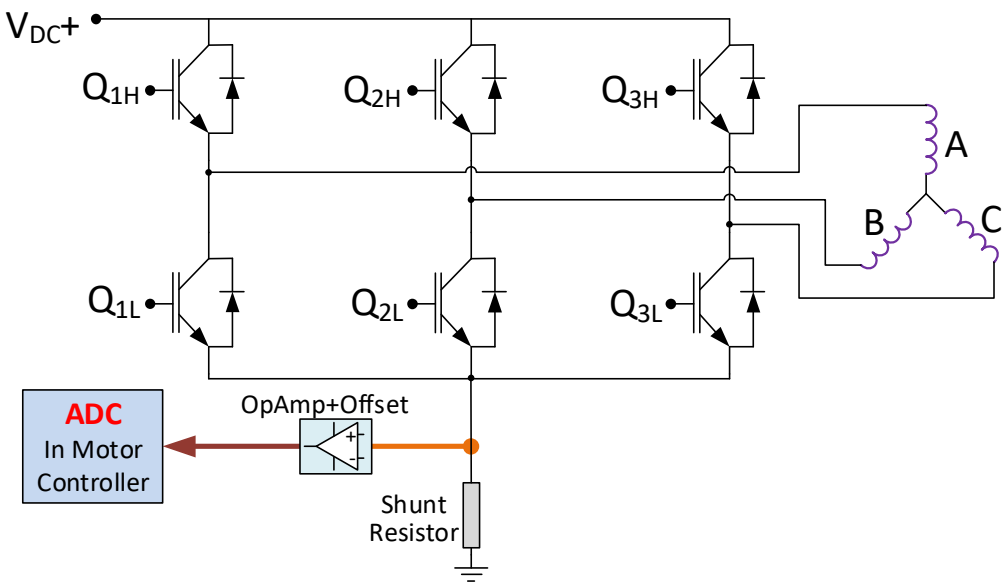

Figure 6-24 Single-shunt topology hardware architecture

The current sensing procedure of single-shunt topology is quite different from that of three-shunt topology as only one current sensor can be utilised. The currents cannot be sampled simultaneously, so that sensing current when all the low-side IGBTs are switch on in three-shunt topology is not applicable to single-shunt topology.

Table 6-1 Current through the shunt resistor

Q_{1L}	Q_{2L}	Q_{3L}	I_{Shunt}
0	0	0	0
0	1	1	i_A
1	0	1	i_B
0	0	1	$-i_C$
1	1	0	i_C
0	1	0	$-i_B$
1	0	0	$-i_A$
1	1	1	0

It is possible to demonstrate that, for each configuration of the high-side switches, the current through the shunt resistor is given in Table 6-1. In this table, value “1” means that the switch is closed whereas value “0” means that the switch is open. Q_{1H}, Q_{2H} and Q_{3H} assume the complementary values of Q_{1L}, Q_{2L} and Q_{3L}, respectively.

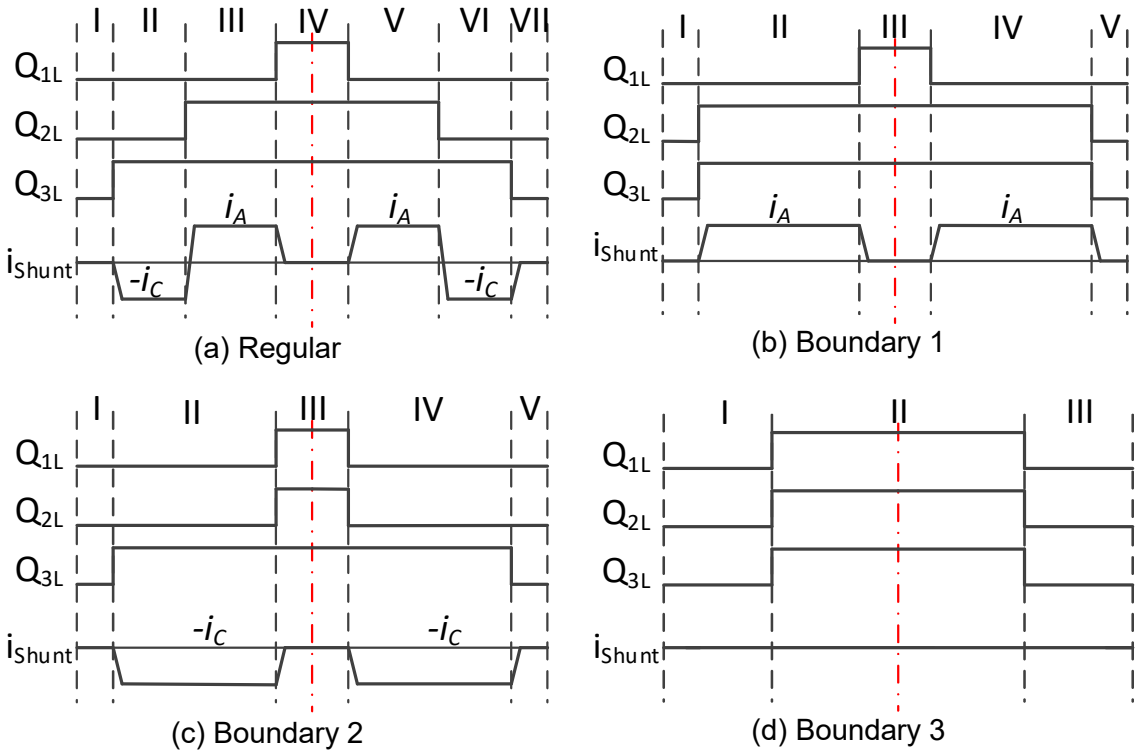

Figure 6-25 Single-shunt current reading at different conditions

In order to reconstruct the current flowing through the motor, at least two phase currents are in need to be sampled by shunt resistor. Figure 6-25(a) shows an example to demonstrate how to sense current in single-shunt topology. Using the centred-aligned pattern, each PWM period is subdivided into seven sub-periods. During three sub-periods (I, IV, VII), the current through the shunt resistor is zero. During the other sub-periods, the current through the shunt resistor is symmetrical with respect to the centre of the PWM.

- In sub-periods II and VI, i_{Shunt} is equal to $-i_C$.
- In sub-periods III and V, i_{Shunt} is equal to i_A.

Under these conditions, it is possible to reconstruct the three-phase current through the motor from the sampled values:

- i_A is i_{Shunt} measured during sub-period III or V.
- i_C is $-i_{Shunt}$ measured during sub-period II or VI.
- $i_B = -i_A - i_C$.

If the stator-voltage demand vector lies in the boundary space between two space vector sectors, which is indicated in Figure 6-26 the purple region, two out of the three duty cycles will assume approximately the same value. In this case, the seven sub-periods are reduced to five sub-periods, as is shown in Figure 6-25 (b) and (c). Under these conditions, only one current can be sampled, the other two cannot be reconstructed. This means that it is not possible to sense both currents during the same PWM period.

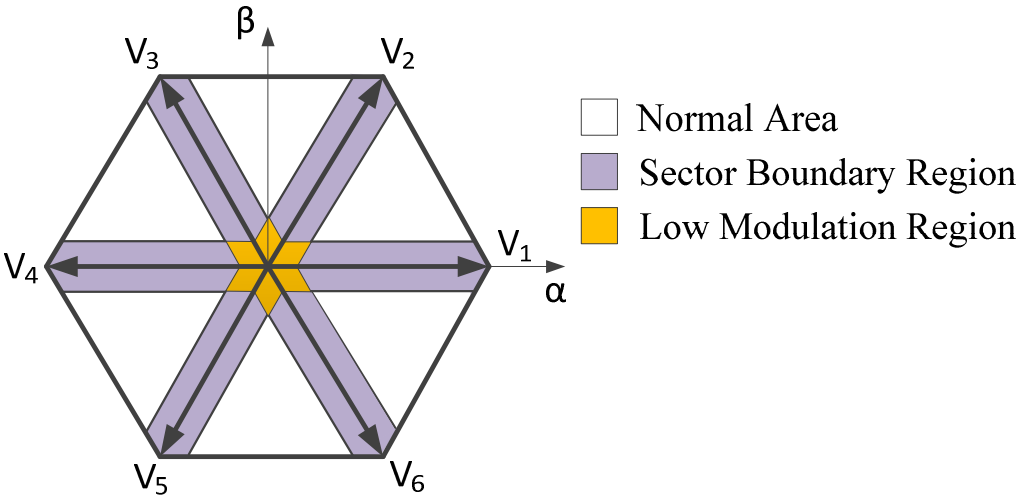

Figure 6-26 Voltage space vector plane divided by different regions

Similarly, for a low modulation index, the three duty cycles assume approximately the same value. In this case, the seven sub-periods are reduced to three sub-periods, which is shown in Figure 6-25 (d). During all three sub-periods, the current through the shunt resistor is zero. This means that it is not possible to sense any current when the imposed voltage vector falls in the orange region of the space vector diagram represented in Figure 6-26.

In order to successfully sample current in any regions of space vector plane by single-shunt resistor, the algorithm is well designed. Different approaches are carried out according to different conditions. Before detailed discussion some useful parameters are defined in advance. DT, T_N and T_S are dead time, noise time and sampling time respectively and defined as that in 6.3.1. T_{MIN} is the minimum time required to perform the sampling, and $T_{MIN} = DT + T_N + T_S$.

The original duty cycles of each phase are generated from SVPWM module, and they sequenced from small to large. To be convenient, here discusses only one combination of phase duty cycles that $Duty_{T1} < Duty_{T2} < Duty_{T3}$. And other combinations will follow the same approach after being sequenced.

Case 1: Regular region

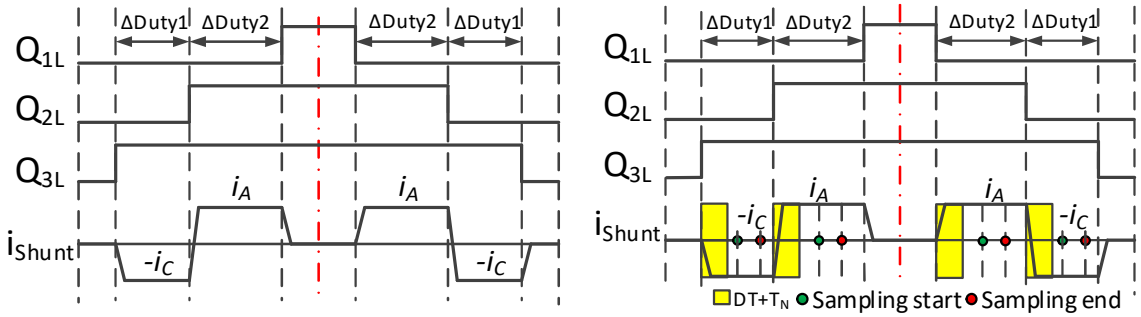

(a) Original from SVPWM (b) Sampling points

Figure 6-27 Current sampling in regular region

In regular region, shown in Figure 6-27, both of *ΔDuty1* and *ΔDuty2* are larger than T_{MIN}, so they have enough time for current sampling, no need for further adjustment. The space available for sampling is the scope in each *ΔDuty* after dead time and stabilising time ($DT+T_N$). If the available space is larger than two times sampling time T_S, current sampling usually starts from the middle point of *ΔDuty*, which is more stable and representative; otherwise, current sampling will start just after stabilising time T_N. Since there is no adjustment of any duty cycle in the regular region, PWM patterns are symmetrical by counter overflow line, so that it is possible to sense current either before or after counter overflow point, but usually it is preferred to sample in the front section that is consistent with other conditions.

Case 2 and Case 3 will discuss boundary region, the purple area in Figure 6-26. Because there are two possible causes of boundary condition and their corresponding solutions are slightly different, this region will be discussed in Case 2 and Case 3 respectively.

Case 2: Boundary 1 region

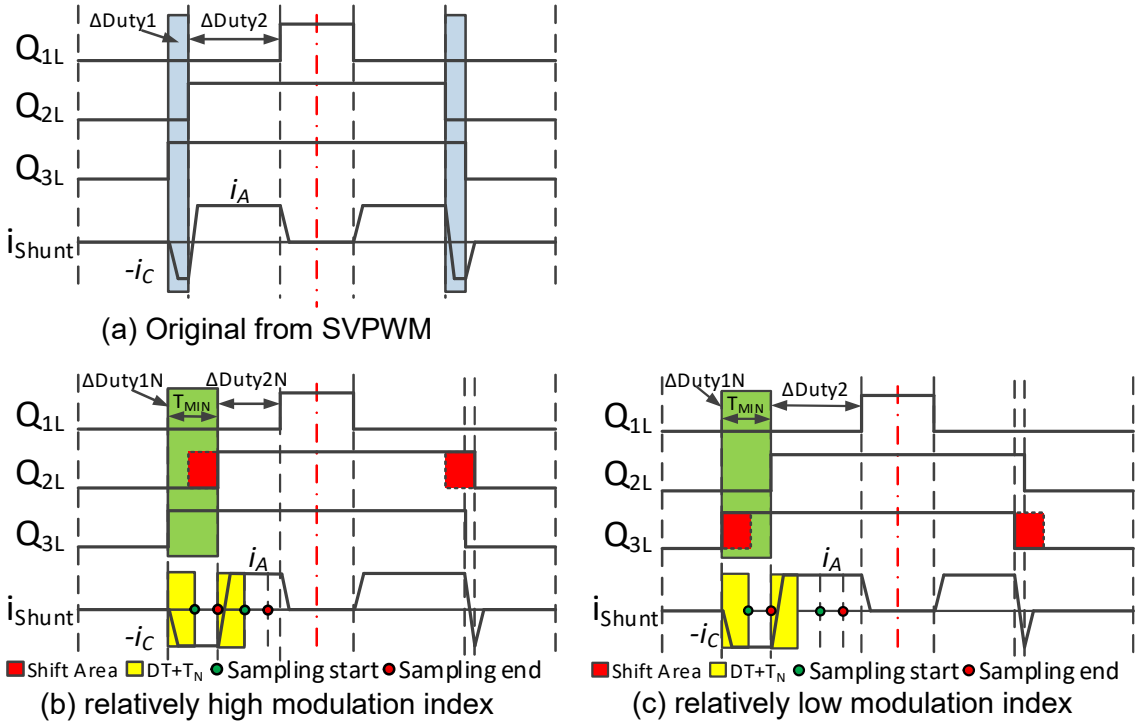

Figure 6-28 Current sampling in boundary 1 region

As shown in Figure 6-28(a), Boundary 1 region is defined as *ΔDuty2* > T_{MIN} but *ΔDuty1* < T_{MIN}, so that there is not enough time for an A/D converter to sample current i_C. In order to solve the problem, one of ΔDuty1's adjacent duty cycles (either Q2 or Q3) is necessary to shift a bit to give the unmeasurable current the minimum required sampling T_{MIN}. The counter overflow line divides the centred-aligned PWM pattern into two sections: left section and right section. To avoid any change in final effect, the amount of duty cycle of any phase adjusted (either increased or reduced) in one section will be compensated in another section.

If modulation index is relatively high, i.e. (*ΔDuty1 + ΔDuty2)* > 2*T_{MIN}, duty cycle of T2 will be shifted from left to right, which is illustrated in Figure 6-28(b). Then *ΔDuty1* is increased to minimum required sampling T_{MIN}, and *ΔDuty2* gets smaller but is still larger than T_{MIN}. The new *ΔDuty1 and ΔDuty2* are assigned as *ΔDuty1N and ΔDuty2N that is shown in* Figure 6-28. In this condition, the available space to sample current i_A is (*ΔDuty2N - DT-*T_N). If the available space is larger than two times sampling time T_S, current sampling usually starts from the middle point of *ΔDuty2N*, which is more stable and representative;

otherwise, current sampling will start just after dead time and stabilising time ($DT+T_N$). Because $\Delta Duty1N = T_{MIN}$, the sampling start point of current i_C is just after ($DT+T_N$).

If modulation index is relatively low, i.e. ($\Delta Duty1 + \Delta Duty2$) < $2*T_{MIN}$, duty cycle of T3 will be shifted from right to left, which is illustrated in Figure 6-28(c). There is no change in $\Delta Duty2$, but $\Delta Duty1$ is increased to minimum required sampling T_{MIN} and renamed as $\Delta Duty1N$. In this condition, the available space to sample current i_A is ($\Delta Duty2$ - DT-T_N). If the available space is larger than two times sampling time T_S, current sampling usually starts from the middle point of $\Delta Duty2$, otherwise, current sampling will start just after ($DT+T_N$). And the sampling start point of current i_C is just after ($DT+T_N$).

Case 3: Boundary 2 region

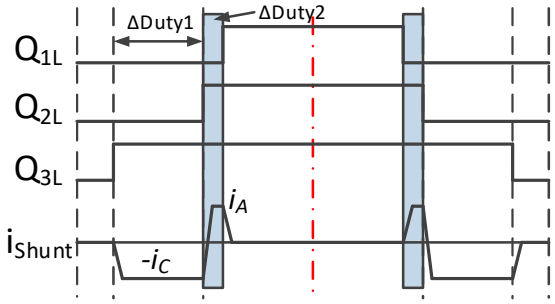

(a) Original from SVPWM

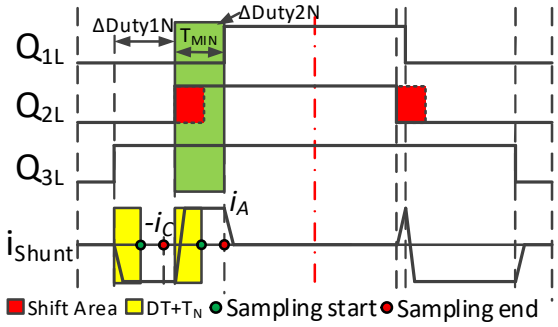

(b) relatively high modulation index

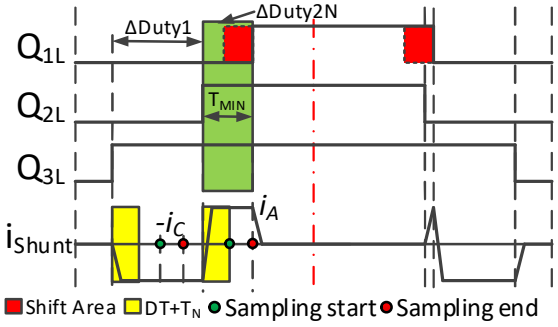

(b) relatively low modulation index

Figure 6-29 Current sampling in boundary 2 region

As shown in Figure 6-29(a), Boundary 2 region is defined as $\Delta Duty1 > T_{MIN}$ but $\Delta Duty2 < T_{MIN}$, so that there is not enough time for an A/D converter to sample current i_A. The approach to solve the problem in Boundary 2 region is similar to

that in Boundary 1 region. Here is emphasised only the difference between the two conditions.

Since *ΔDuty2* < T_{MIN}, the adjusted duty cycle is one of ΔDuty1's neighbours (either T1 or T2). If modulation index is relatively high, duty cycle of T2 will be shifted from right to left, which is illustrated in Figure 6-29(b). Then *ΔDuty2* is increased to minimum required sampling T_{MIN}, and *ΔDuty1* gets smaller but is still larger than T_{MIN}. If modulation index is relatively low, duty cycle of T1 will be shifted from left to right, which is illustrated in Figure 6-29(c). There is no change in *ΔDuty1*, but *ΔDuty2* is increased to minimum required sampling T_{MIN}.

If *ΔDuty*= T_{MIN}, the corresponding current sampling will start just after dead time and stabilising time ($DT+T_N$). And if the available space is larger than two times sampling time T_S, current sampling usually starts from the middle point of ΔDuty, otherwise, current sampling will start just after (DT+TN).

Case 4: Boundary 3 region

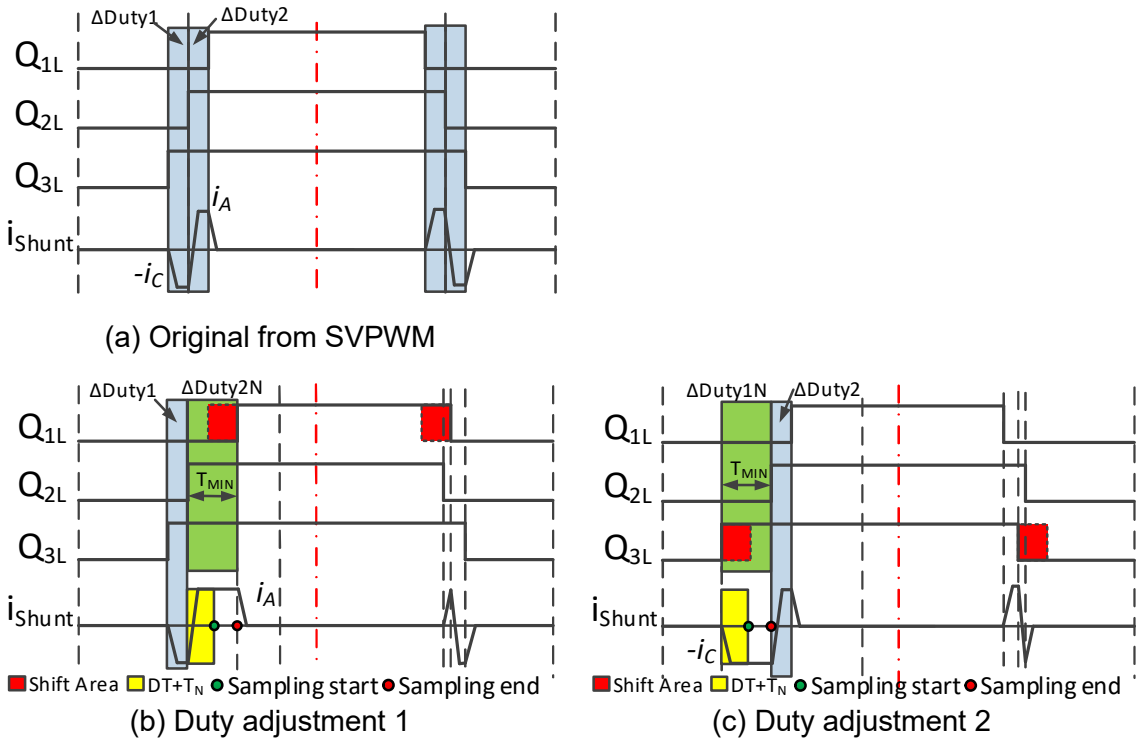

(a) Original from SVPWM

(b) Duty adjustment 1

(c) Duty adjustment 2

Figure 6-30 Current sampling in boundary 3 region

As shown in Figure 6-30(a), in Boundary 3 region both of *ΔDuty1* and *ΔDuty2* are less than T_{MIN}, which is low modulation region in Figure 6-26. In this

condition, there is not enough time for an A/D converter to sample any current. Even if one of the duty cycles is shifted, such as T1 shifted from left (Figure 6-30(b)) to right or T3 shifted from right to left (Figure 6-30(c)), it is still impossible to sample two currents in one period. If both of the two PWM patterns are adjusted in the left section and then compensated in the right section, it is possible to sense two current values, but the variation of duty cycle adjustment is too large in the low modulation region and it will cause lots of unnecessary vibrations making feedback current inaccurate.

As this region is of low modulation, the change of any phase current is not much in a PWM period, thus the approach used in Case 4 is that current i_A and i_C are sampled alternatively in each PWM period and the unmeasured current will be assigned by previous value. Fox example, in a period, duty cycle of T1 is shifted from left to right and current i_A is measured, and the unmeasured current i_C is assigned by its measured value from last period; in the next period, duty cycle of T3 is shifted from right to left and current i_C is measured, and the unmeasured current i_A is assigned by its measured value from last period. By this method, both of the currents are able to update their values, and it will not cause much vibration on them.

After PWM duty cycle adjustment, the new $\Delta Duty = T_{MIN}$, so the corresponding current sampling will start just after dead time and stabilising time ($DT+T_N$).

6.3.3 Single-shunt and Three-shunt Current Sampling Comparison

Three-shunt current sampling is commonly used in most motor controllers due to its stable, accurate feedback and simple control algorithm. But in the study of low-cost drive system single-shunt current sampling is preferred thanks to its lower hardware cost and satisfactory feedback performance. In this section, comparison of experiment results and controller resources used are carried out between the two types of current sampling topologies.

Figure 6-31 shows measured currents of Phase C and Phase A, and there is 120°-shift between the two phases. The blue curve is the current results directly measured on the motor power supply wire by a high-accuracy clamp-on type

current meter, so the result is the most accurate and used as reference to validate the results of three-shunt and single-shunt current sampling. The current curve of red line is measured by three shunt resistors. It is seen that the three-shunt feedback current has close agreement with the meter-measured current, and there is no obvious difference between the two measurements. Thus it is validated that the three-shunt topology are able to provide good quality of current feedback for motor controller.

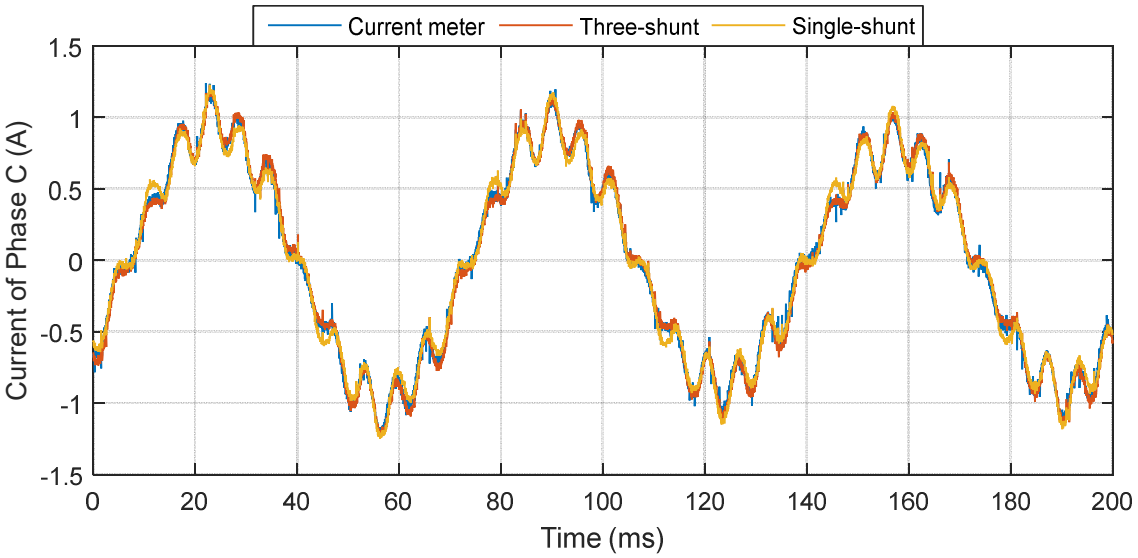

(a) Measured current of Phase C

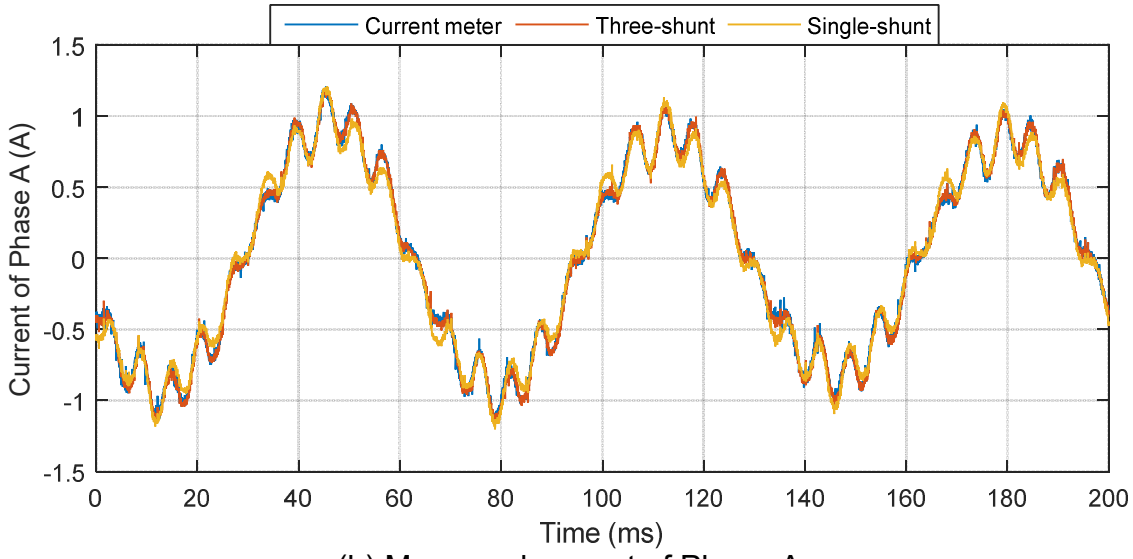

(b) Measured current of Phase A

Figure 6-31 Comparison of measured current feedback

The orange curve represents single-shunt current feedback. There are some errors between single-shunt current and meter-measured current, but they are

within the acceptable range and their general shape and amplitude are same as the meter-measured current. Therefore, the single-shunt current feedback is accurate enough for engineering application and is used in motor control of the prototype ferrite machine. Compared with three-shunt current sampling, the single-shunt one saves some hardware resources, such as shunt resisters and op-amp circuits. However, due to its complex control algorithm that is discussed in 6.3.2, it consumes more resources of microcontroller, such as timers, DMA channels and interrupts. As all of these processor modules are in the same microcontroller chip, it won't increase the cost of hardware. Therefore, the single-shunt current sampling scheme is effective and cost-efficient for the PMSM control system.

6.4 Summary

The control system of the ferrite IPM electric drive is discussed in the chapter. In order to increase the competitive capability of the designed ferrite IPM electric drive system, apart from its high efficiency and high power density, the cost of motor controller is minimised as well. The low-cost Hall-effect sensors are used in the controller to measure the speed and position of the motor, and the single-shunt current sampling is used for current feedback. For the speed and position feedback, both of the encoder and Hall Effect sensors are discussed in details and tested in the prototype drive system. The test results show that Hall Effect sensors are able to provide comparable speed and position feedback for the controller like the encoder. The single-shunt and three-shunt current sampling are compared in the study. The well-designed control method makes it possible for the single-shunt current sensor to sample current at boundary and low-modulation condition. And the experimental results show that the single-shunt current sensor is able to provide good quality current signals to the control system.

7. EXPERIMENTAL VALIDATION OF THE PROPOSED MACHINE

A prototype ferrite IPM machine is manufactured according to the motor design in Chapter 3 and the optimal mechanical tolerances in Chapter 4. In order to obtain the characteristics of the prototype machine, a serial of tests are performed under various working conditions. The proposed methods and ideas are validated by the comprehensive comparisons of the performances between FEA and experimental results. The detailed discussion and analysis are shown in the following sections.

7.1 Validation of the Motor Design

7.1.1 Manufacture of Prototype Motor

Some major steps of the prototype motor manufacture are demonstrated in Figure 7-1. Due to the brittle physical nature of ferrite materials, there is a risk of chipping and breaking the magnets when stress is exerted on them. For the convenience of magnet manufacture and rotor assembly, each of the PM poles is divided into two parts in axial direction and then inserted inside the rotor from different end of the rotor lamination. The required cuboid ferrite magnets are shaped and magnetised first, the primary and secondary magnet pieces shown in Figure 7-1(a). After being fixed on rotor shaft and inserted with the magnet pieces, the rotor lamination is clipped and machined to the final outer circumference, shown in Figure 7-1(b). Finally, two pieces of aluminium end-plates are used at each end of the rotor lamination to increase the robustness of the rotor, and two bearings are installed at each end of the rotor shaft. The completed rotor is shown in Figure 7-1(c). The housing and stator lamination is directly adopted from a commercial IM. In order to adapt the design of ferrite IPM motor the stator coils are re-winded with four strands of 0.6mm diameter copper wires. Because thinner copper wires and chain coil configuration with shorter end-winding are employed for the IPM, there are eight more conductors per stator slot than the original IM. The new stator windings are shown in Figure 7-1(d). Three Hall Effect sensors are delicately glued on the stator core, and

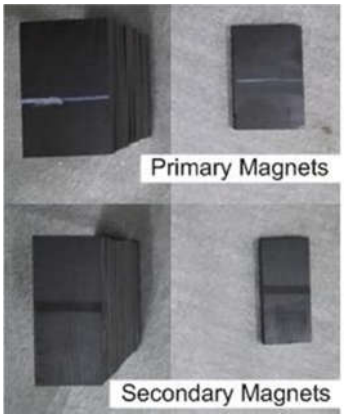

(a) Ferrite magnets

(b) Assembled rotor

(c) Completed rotor

(d) Stator windings

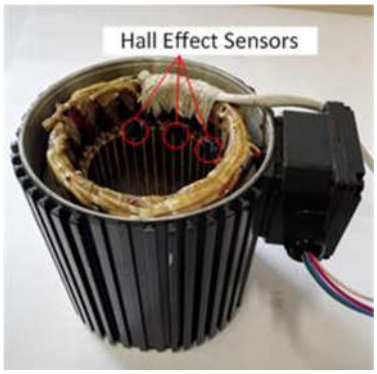

(e) Completed stator

(f) Completed Motor

Figure 7-1 Manufacture of prototype motor

their signal wires are extended through stator cover, as shown in Figure 7-1(e). At last, all the prototype components are carefully assembled together to make the final motor, shown in Figure 7-1(f). In the following several sections, a series of experiment tests will be carried out on the prototype motor to validate the design of the machine.

7.1.2 Open-Circuit Test

Open Circuit Test is performed on the prototype machine to obtain the back EMF of the proposed ferrite IPM machine. The machine is driven at a constant speed and the open terminal voltage is measured by voltage acquisition device. The rig for back EMF test is illustrated in Figure 7-2. An IM that is controlled by a variable frequency converter works as a primary motor and drives the prototype motor through a coupling. Since the IM is primarily used for low speed applications, only 300 rpm can be achieved for the back EMF testing. Motor

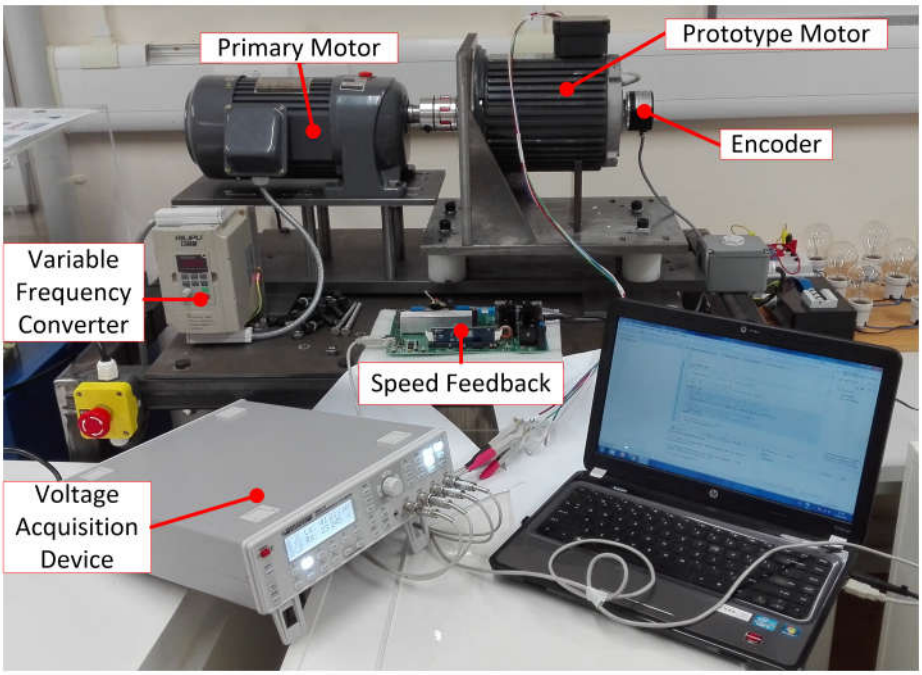

Figure 7-2 Back EMF test rig

speed is measured by an incremental encoder and fed back to monitoring computer by a speed feedback controller. The back EMF of the prototype motor is obtained by an oscilloscope or voltage acquisition device, and their waveforms and spectra are depicted in Figure 7-3. The fundamental component of the back EMF is about 20 V, and it also consists of some noticeable harmonics, such as the 3rd and 11th order. That's mainly caused by the special structure of the IPM motor that has strong cogging torque, and it is also affected by demagnetisation.

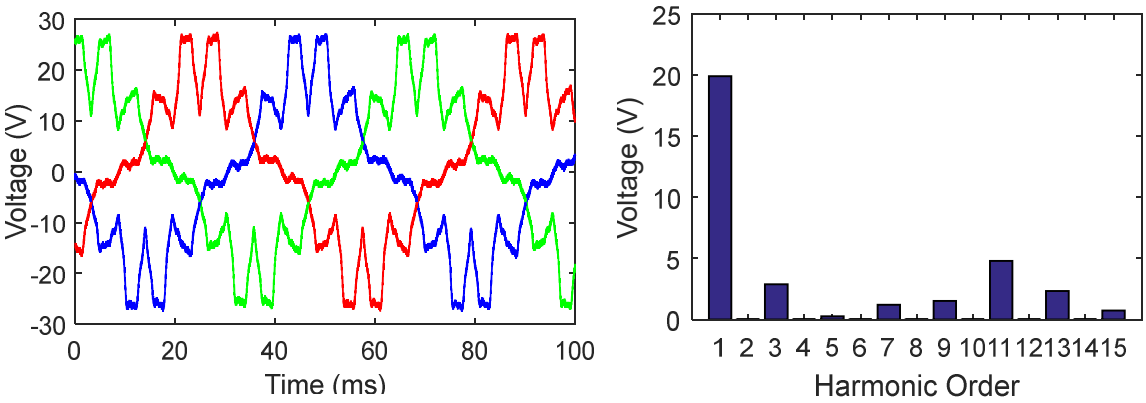

(a) Three phase back EMF waveforms

(b) Spectra

Figure 7-3 Waveforms and spectra of the prototype machine's back EMF

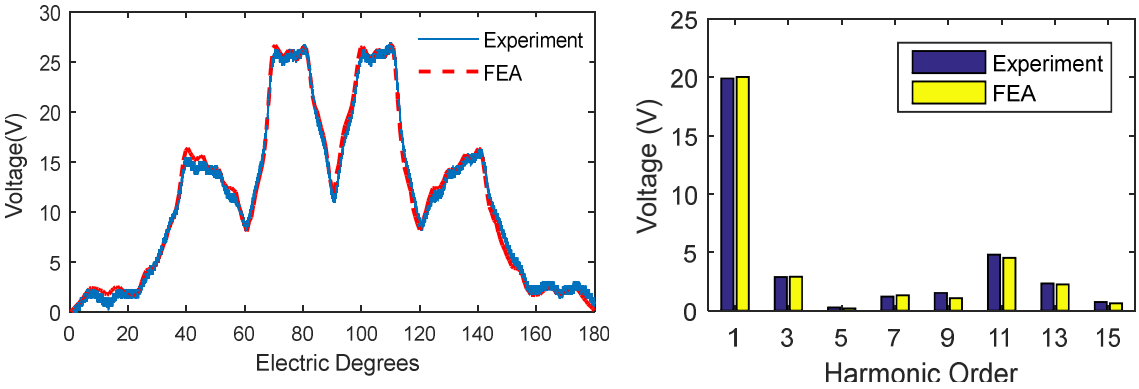

(a) Back EMF waveform comparison (b) Spectra

Figure 7-4 Back EMF comparisons between FEA and experiment

In order to validate the FEA simulation results in Chapter 3, the back EMF of which is compared with that of experiments. Figure 7-4 shows the comparison of back EMF waveforms and their spectra between FEA and experiment results. It is seen that FEA results have good agreement with tested results, and the slight difference may come from manufacture errors and material inconsistency.

In conclusion, the open-circuit test validates the FEA simulation results and they have good agreement. And the noticeable harmonics should be aware when carrying out control algorithm design or motor test.

7.1.3 No-Load Test

After the open-circuit test, the prototype motor is transported to motor performance test rig, which is shown in Figure 7-5.

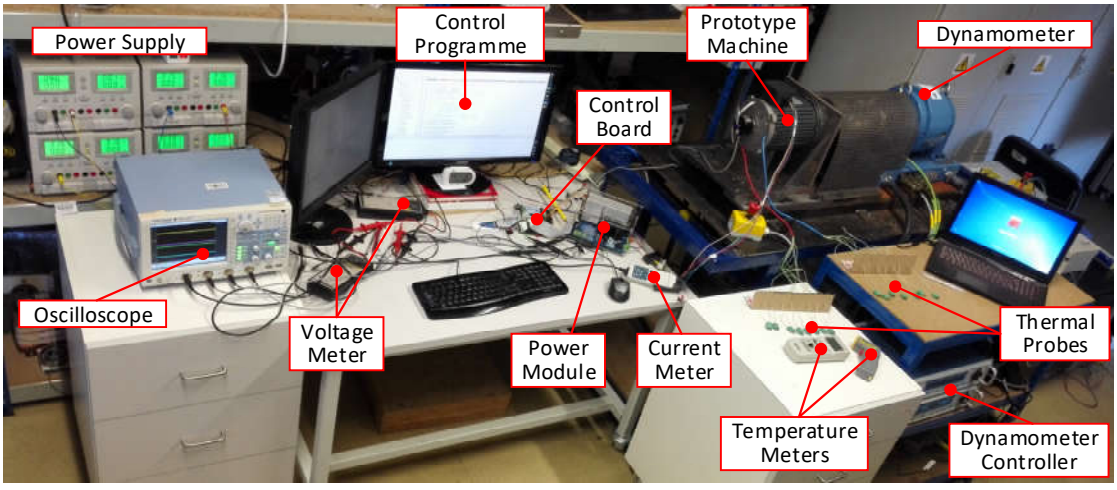

Figure 7-5 Setup of motor test rig

In this test rig, the prototype motor is powered by STEVAL-IHM028V2 power module that is connected to DC power supply and controlled by STM3210E-EVAL evaluation board. The power module and control board are introduced in Appendix D. The output shaft of the prototype motor is coupled with torque sensor that is connected to dynamometer, so the actual speed and output torque are measured by them and fed back to dynamometer controller. The output power of test motor is absorbed by dynamometer and transferred into heat, and the dynamometer is cooled down by flowing water that circulates from a water tank. An instruction of the programmable dynamometer system is attached in Appendix E. During motor test, the online current and voltage are measured by current meter and voltage meter and displayed on oscilloscope.

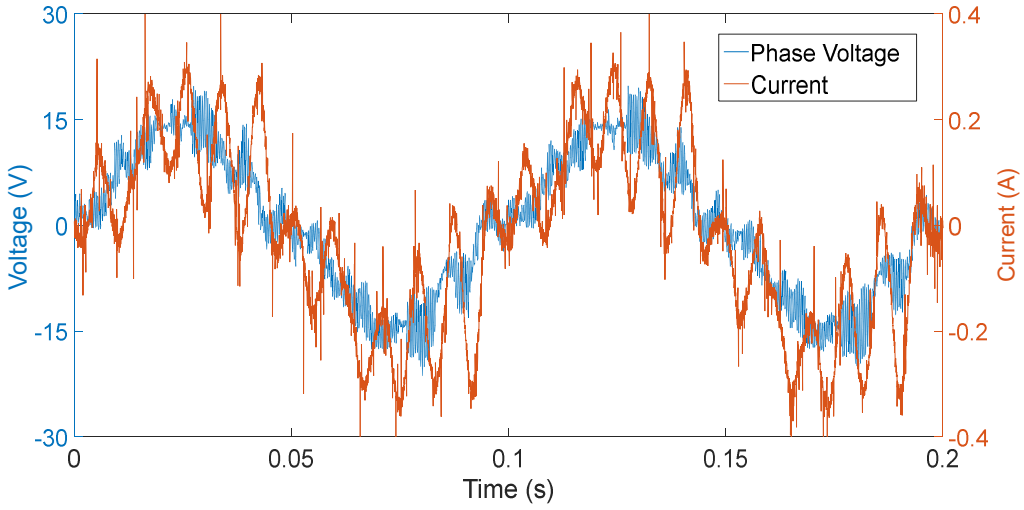

Figure 7-6 No-load phase voltage and current waveforms at 200rpm

In the no-load current measurement, the prototype machine is tested without exerting any load to the output rotor shaft, and the measured phase voltage and current are depicted in Figure 7-6. The fundamental amplitude of no-load current is only 0.206 A, and the no-load loss is 4.6 W running at 200 rpm. As the fundamental current is very small, the magnitude of spatial harmonics appears to have the similar level with the fundamental, especially 11th and 13th tooth harmonics. In the no-load test, there is no phase difference between the current and voltage.

7.1.4 Loaded Test

The loaded experiments are carried out by the same test rig that is used for no-load test, depicted in Figure 7-5. But the rotor shaft is exerted different loads by the programmable dynamometer to explore torque capacity and efficiency of the motor prototype. More detailed data and discussion are described in the following sections.

7.1.4.1 Torque Characteristics

The performance of an electric motor is mainly revealed by its torque characteristics. The generated torque in an IPM motor depends on both the magnitude and phase of the current. Since the prototype machine is designed with large saliency ratio and flux focusing structure, similar portions of reluctance and PM torque will be achieved to for torque enhancement. Thus, relatively large advanced current angle should be expected under loaded operations for harnessing considerable reluctance torque component. To validate the torque curve, the prototype machine is tested with different d-axis current under various loading torque. Lower speed is preferred for the torque tests so as to minimise the influence of core loss and mechanical loss, as they all increase significantly with speed and difficult to measure directly. On the other hand, the stability of the system reduces at very low speed. As a balance from both sides, rotational speed of 200 rpm is chosen for the torque tests, and

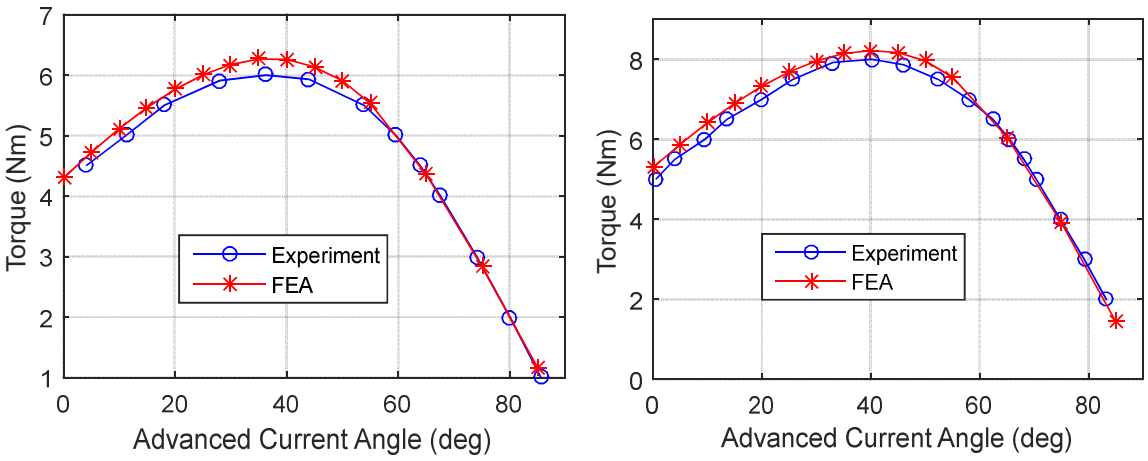

(a) Armature current amplitude of 5A (b) Armature current amplitude of 6.2A

Figure 7-7 Torque curve against current angle

the impact of mechanical loss and core loss will later be considered based on the no-load test under this speed. By giving different d-axis current commands to the controller while keeping the amplitude of armature current constant, torque curves against advanced current angle are measured, and the attained results are compared with FEA models. As illustrated in Figure 7-7 (a) and (b), the amplitudes of the armature current are 5 A and 6.2 A respectively. The maximum deviations between FEA and experimental results are 4.25% and 2.64% when the amplitude of the armature current is 5 A and 6.2A. With the consideration of the imperfection in manufacturing and on-load current, the deviations (less than 5%) are acceptable, thus the FEA models exhibit good agreement with experiments. It can also be noticed that the tested torque is slightly smaller than FEA under lower current angle, and coincides with FEA when negative d-axis current is very high. That may be caused by slightly lower coercivity of the magnet material or slightly lower knee point in the B-H curve of the lamination.

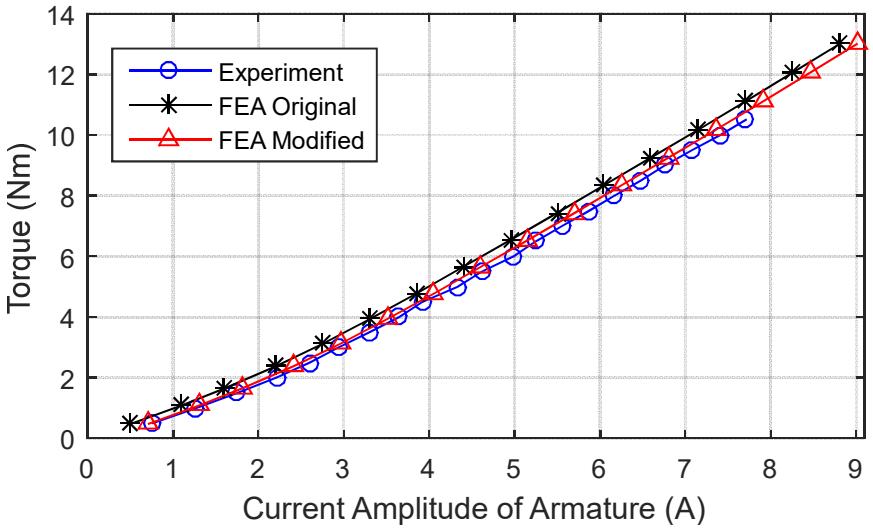

Figure 7-8 Torque output versus current amplitude

Efficiency is also a key indicator for machine performance. It is of special meaning for the prototype machine in the aim of replacing the widely used IMs in industry. Several control principles have been developed for the motor operations to reduce the loss and improve the performance. Among them the maximum torque-per-ampere current control is one of the most widely used

control strategies as the copper loss can be minimised with minimum current. The MTPA algorithm is adopted based on the loss analysis result that copper loss contributes the largest part to the total loss from medium to full loading operation range, will be more effective for efficiency improvement.

The torque-current curve is obtained under MTPA control strategy, and the results from experiment and FEA models are compared in Figure 7-8. Since the ideal FEA model is set up in ideal mechanical condition without any frictional torque, the output torque predicted is slightly higher than experiment, and the difference stays approximately constant despite of the increase of the current. If the frictional torque is compensated by the current under no-load in FEA model, the modified FEA results will be in great agreement with the torque tested. Therefore, the experimental results validate the torque capability of the designed low-cost ferrite IPM motor.

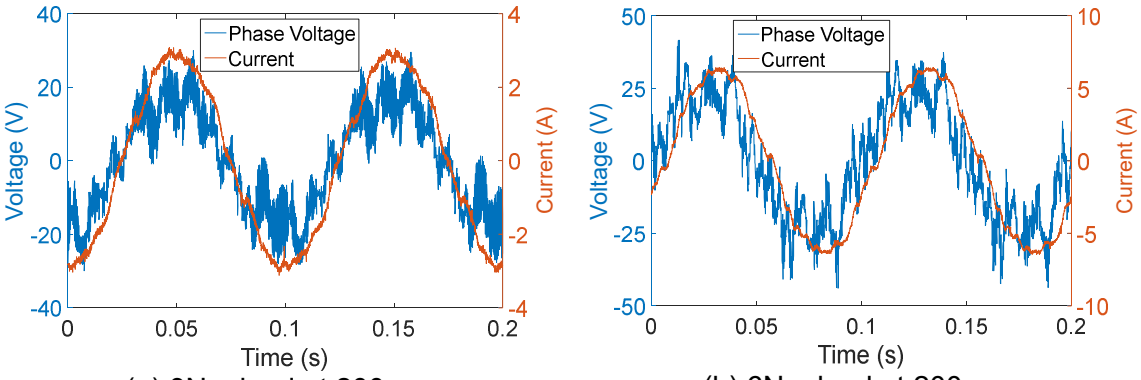

(a) 3Nm load at 200rpm (b) 6Nm load at 200 rpm

Figure 7-9 Phase voltage and current under loaded conditions

Figure 7-9 depicts the phase voltage and current under 3 and 6 Nm at 200 rpm with MTPA method. As the fundamental current component increases with the load, the current waveforms are much more sinusoidal than no-load, which indicates low harmonic current content. Because the motor is fed by PWM controller inverter, 8 kHz filter is applied to the phase voltage for a clear view. As shown in Figure 7-9(a), the phase angles of voltage and current are almost aligned, indicating high power factor under low load condition. With the increase of output, slightly larger phase shift between voltage and current can be

observed in Figure 7-9(b), owing to higher armature reaction and larger reluctance torque component.

7.1.4.2 Efficiency

Due to the power limitation of the controller available, the prototype machine is tested from 1–8 Nm with maximum speed of 1500 rpm for power and efficiency validation. The efficiency of the prototype machine is obtained and compared with FEA model, and good agreement is achieved as illustrated in Figure 7-10 and Figure 7-11.

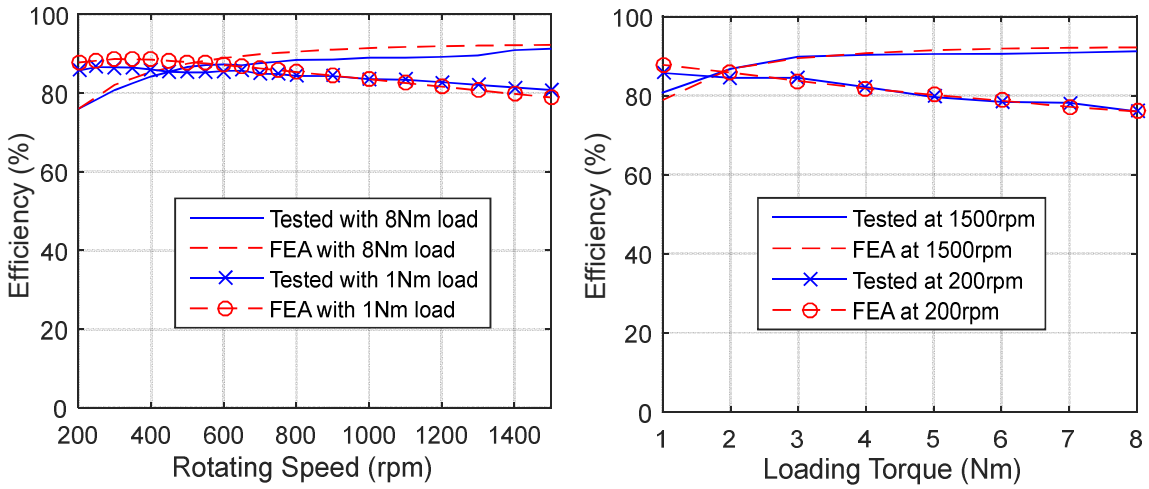

(a) Against rotational speed

(b) Against torque output

Figure 7-10 Efficiency comparisons between the tested and FEA results

Figure 7-10(a) depicts the efficiency of experimental and FEA results against rotational speed. Efficiency increases with speed at higher torque loading while decreases during light load. Because copper loss contributes more to the overall losses at high load and can be regarded as constant under such constant torque conditions, the efficiency increases at higher speed when power is increased. On the other hand, core loss dominates at light load and is aggrandized more significantly with speed, resulting decrease of efficiency.

Figure 7-10(b) shows that under constant speed conditions, core loss is far less sensitive to armature current comparing to copper loss, and the mechanical loss is constant. On the other hand, copper loss is proportional to current square and increase exponentially with load. Thus, at low speed when copper loss takes up

contributes to most the overall losses, the motor efficiency decrease with load due to the higher loss increment. However, the efficiency increases with load at rated speed when core loss and mechanical loss take up considerable portion of the total loss whose increment is less significant.

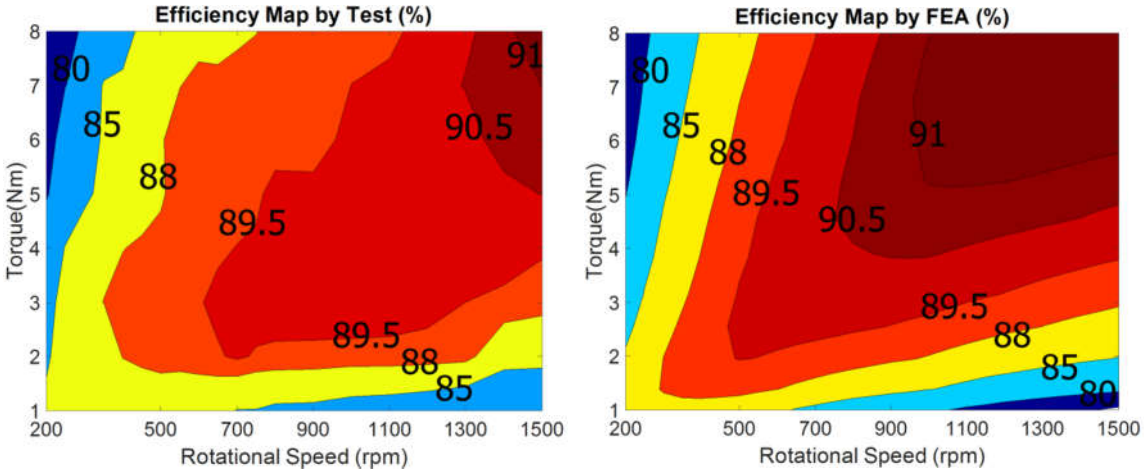

(a) Efficiency map of experimental results (b) Efficiency map of FEA results

Figure 7-11 Efficiency maps of experimental and FEA results

As demonstrated in Figure 7-11, the efficiency of the prototype machine is 0.5–1.5% lower than FEA at relatively high speed and torque operating conditions, and slightly high efficiency is obtained for experiment when the loading torque is small. There are two possible reasons that would contribute to the difference. To simplify the FEA simulation, the armature resistance is calculated at 80°C and set as a constant. But under light load conditions, the temperature rise is very low. Thus, the resistance for simulation is actually higher than actual value, resulting higher copper loss and lower efficiency for the FEA. What's more, since it is too time-consuming to consider PWM signal in FEA simulation, pure sinusoidal current is injected to the windings instead. As a result, the core loss in practical should be higher and the efficiency is lower since the harmonics caused by PWM control is ignored in simulation. Under high speed high torque operation when core loss is serious, larger differences is seen in efficiency.

The fact that the efficiency by test and FEA agrees with each other better under low speed high torque conditions can also be explained based on the theory. Because the core loss is very low and the armature temperature in simulation is

closer to that in actual situation within this operational range, the working conditions are quite close to the actual testing environment, and good accuracy is achieved.

7.2 Validation of the Thermal Analysis

The motor losses are exclusively analysed in Chapter 5, but the amount of each type of loss is very difficult to validate directly from experiments because they are coupled with each other with mechanical frication losses. Thus they are indirectly validated by motor efficiency and temperature change. The overall loss is the supplied input power deducted by output power, which is validated by efficiency results in 1. All the losses will transfer into heat and increase the temperature of the motor, so the resultant temperature can also indirectly validate the amount of losses. The temperature in a steady and transient state has been simulated by FEA simulation in Section 5.4, and in this section it will be validated by experiment results.

7.2.1 Thermal Experiment Setup

Wired thermal meter (shown in Figure 7-12) and infrared thermal meter (shown in Figure 7-13) are used to measure the temperature of different parts of the prototype motor. The infrared thermal meter measures the temperature of the motor housing surface, and is movable and convenient to measure at any point of the surface. Inside of the housing frame, the temperature of the copper windings and stator core are measured by wired thermal meter.

(Courtesy: RS company)

Figure 7-12 Wired thermal meter

(Courtesy: CENTER Technology Corp.)

Figure 7-13 Infrared thermal meter

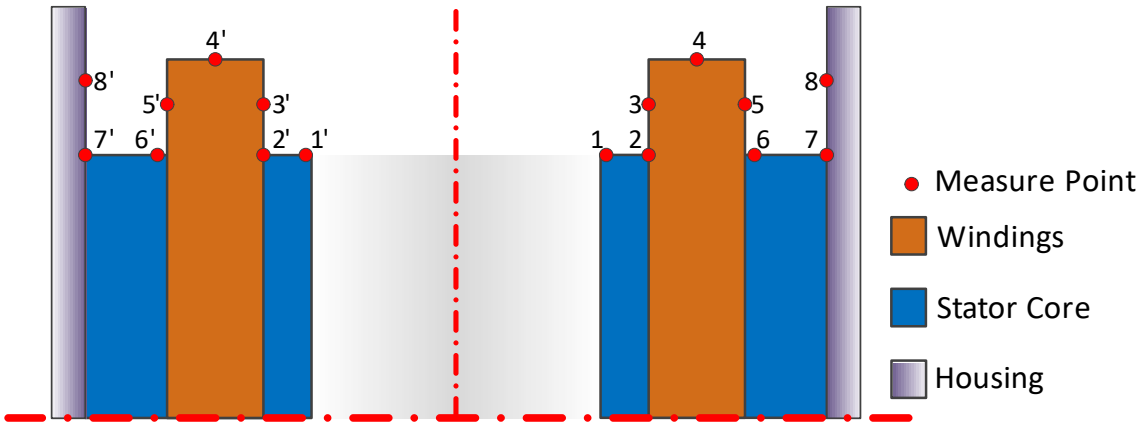

Figure 7-14 Cross-section of stator end and thermal measuring points

As shown in Figure 7-14, 16 thermal probes are divided in two groups, and each group has 8 probes and are numbered from 1 to 8. Measure point 2, 3, 4, and 5 are fixed on the surface of copper windings, where point 2 is around the corner between the winding and stator teeth. Measure point 1, 6, and 7 are fixed on the top surface of stator core, where point 6 is at the corner between winding and stator core. And measure point 8 is mounted on the inner surface of the housing frame.

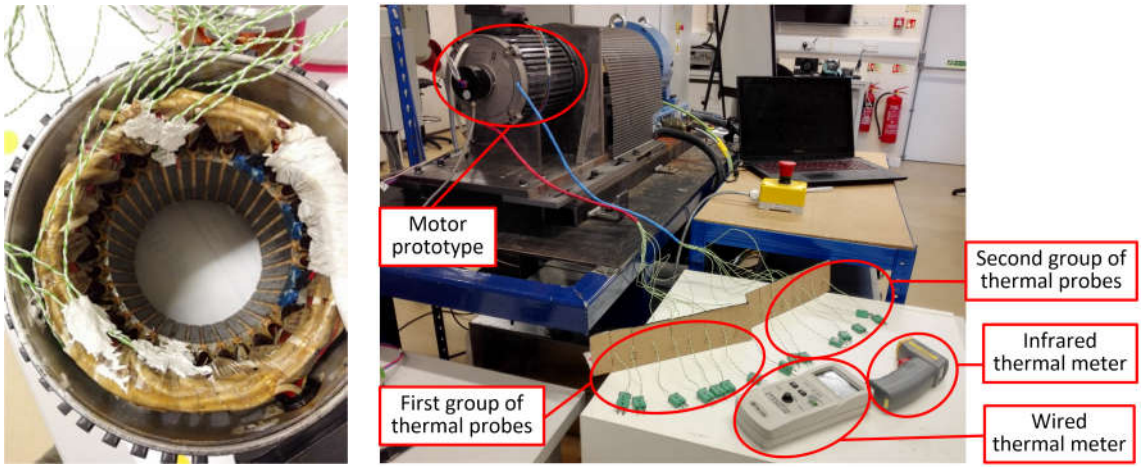

(a) Probes installation (b) Thermal experiment setup

Figure 7-15 Thermal probes installation and experiment measurement

When all the thermal probes have been properly fixed inside of the motor housing, shown in Figure 7-15(a), the prototype motor is reassembled and installed on the testing rig. As shown in Figure 7-15(b), the setup of the thermal testing consists of two groups of thermal probes, a wired thermal meter and a

infrared thermal meter. The wires of the first and second group of thermal probes are bundled in red and blue heat-shrink tubes respectively. The temperature of each measuring point inside of the motor can be measured by the external end of each thermal probe. During the thermal test, the internal temperature of the prototype motor is read by the wired thermal meter, and the temperature of the motor housing exterior surface is measured by the infrared contactless thermal meter.

7.2.2 Temperature measurement and discussion

The thermal test of the designed ferrite IPM motor takes 240 minutes and the measuring results are displayed in Figure 7-16. Since the relative measuring positions of the two groups of thermal probes are the same, the temperature results shown in Figure 7-16 are the average of the two groups. Before starting the motor, the temperatures of all the parts of the machine are the same, which is the ambient temperature 27.2°C. In order to compare with the simulation results conveniently, the beginning temperature is adjusted to 20°C while the temperature increases are kept unchanged.

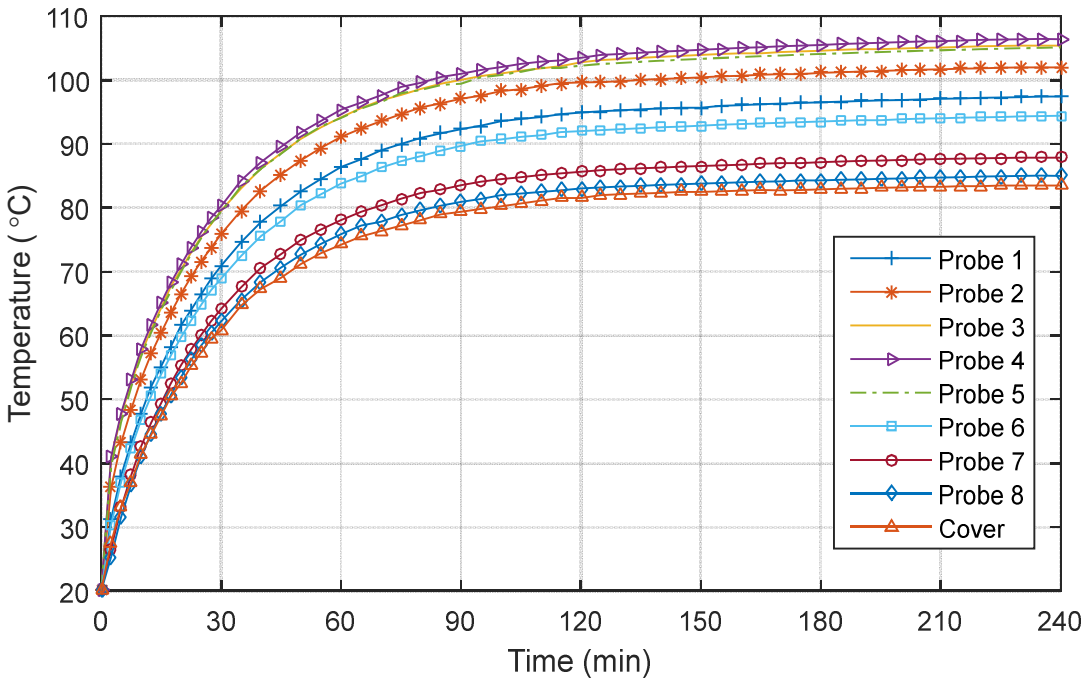

Figure 7-16 Measured temperature of the ferrite IPM motor

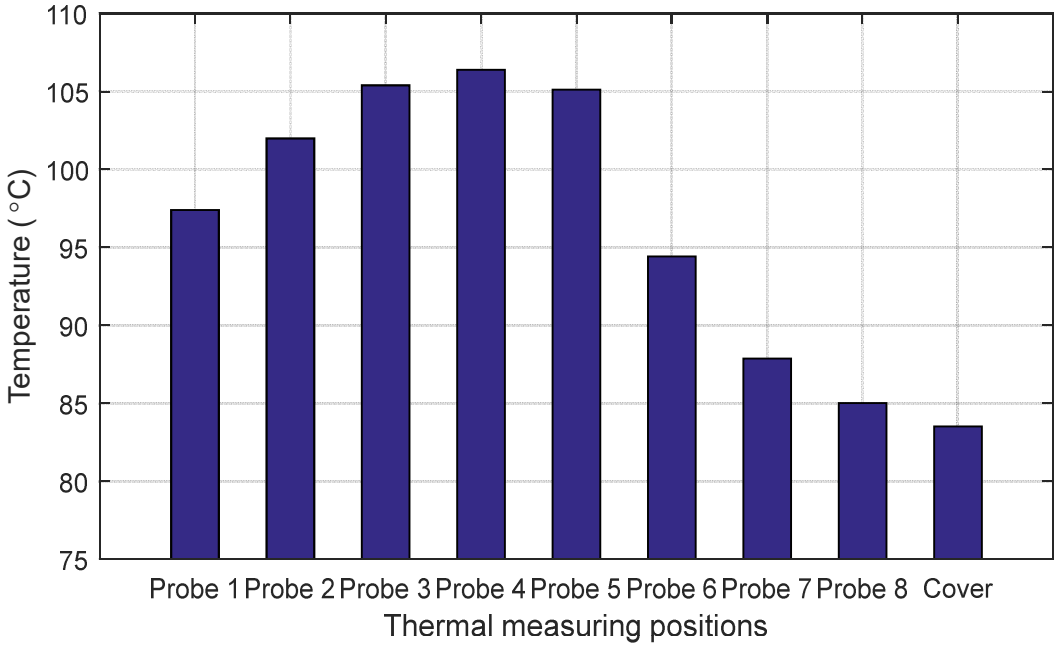

Figure 7-17 Temperature distribution of the motor at steady sate

As shown in Figure 7-16, the temperatures of the motor increase in the first hour and gradually slow down in the second hour. After two hours of running, the motor is getting into a thermal balanced state, and there is little variation of temperature in the last two hours. Although the temperature growing rates are different for these various measuring positions, there is no cross lines in the temperature changing curves. That means all the measuring points maintain the same thermal gradients all the time, and the temperature distribution of the motor at a steady state is depicted in Figure 7-17. The temperature sequence of the measurement is: *Probe 4 > Probe 3 > Probe 5 > Probe 2 > Probe 1 > Probe 6 > Probe 7 > Probe 8 > Cover*. Since the copper loss is the primary heat source, the temperature of the winding increases rapidly and is always higher than any other part of the motor. As illustrated in Figure 7-14, the probe 3, 4 and 5 measure the copper winding temperature. The measuring point 4 is at the top of the coil, and it is much harder for it to dissipate heat to the stator core, so its temperature is a little higher than the other two points'. Since all the generated heat is transferred from the inside to the outside and the area near the housing is cooler, the temperature of point 5 is slightly lower than that of point 3. The point 2, at the corner of copper coil and stator tooth, is heated by the winding but is easier than point 3, 4 and 5 to dissipate its heat as it is adhered to stator

core. Measuring points 1, 6 and 7 are all glued on the stator core, from the tooth tip to stator yoke. From the analysis in Figure 5-25, it is known that the iron loss density at the tooth tip area is the highest, followed by stator tooth and then stator yoke. In addition, the rotor is also a heat source caused by the iron loss of rotor core, and most of its heat is transferred through the air gap to the stator core. Hence the inner part of the stator core is hotter than the outer part, and the temperature of measuring point 1 is higher than point 6 that is higher than point 7. The point 8 is fixed on the interior side of the motor housing but not on the stator core, so its temperature is between point 7 and exterior cover. The temperature of the exterior cover is the lowest, which is the thermal interface between the motor and the ambient air. Due to the temperature difference, the generated heat can be continuously brought away from the inside of the motor to the ambience. In addition, in the current design the motor does not consist of a cooling fan to help dissipate heat. Since it is solely dependent on natural cooling, it takes a relatively long time for the motor to get into thermal steady state and the steady temperature is relatively high. A cooling fan can be involved in the next generation of motor design, so that the overall temperature will be lower and it will take a shorter time to become thermal steady.

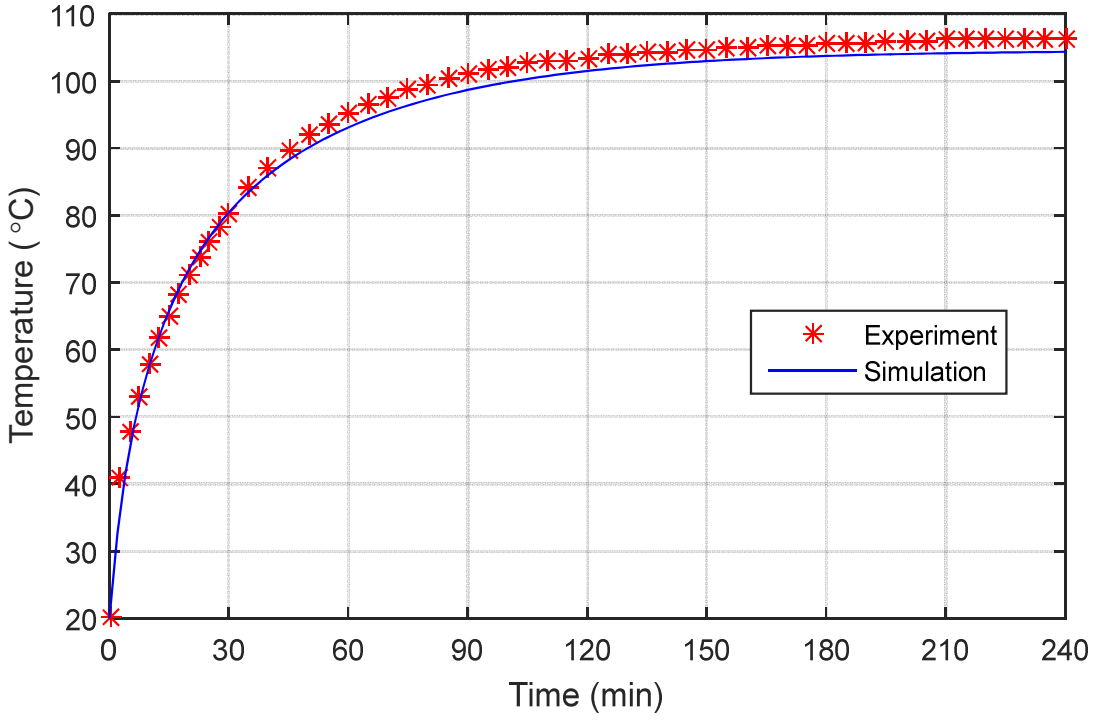

Figure 7-18 Temperature comparison of copper coil

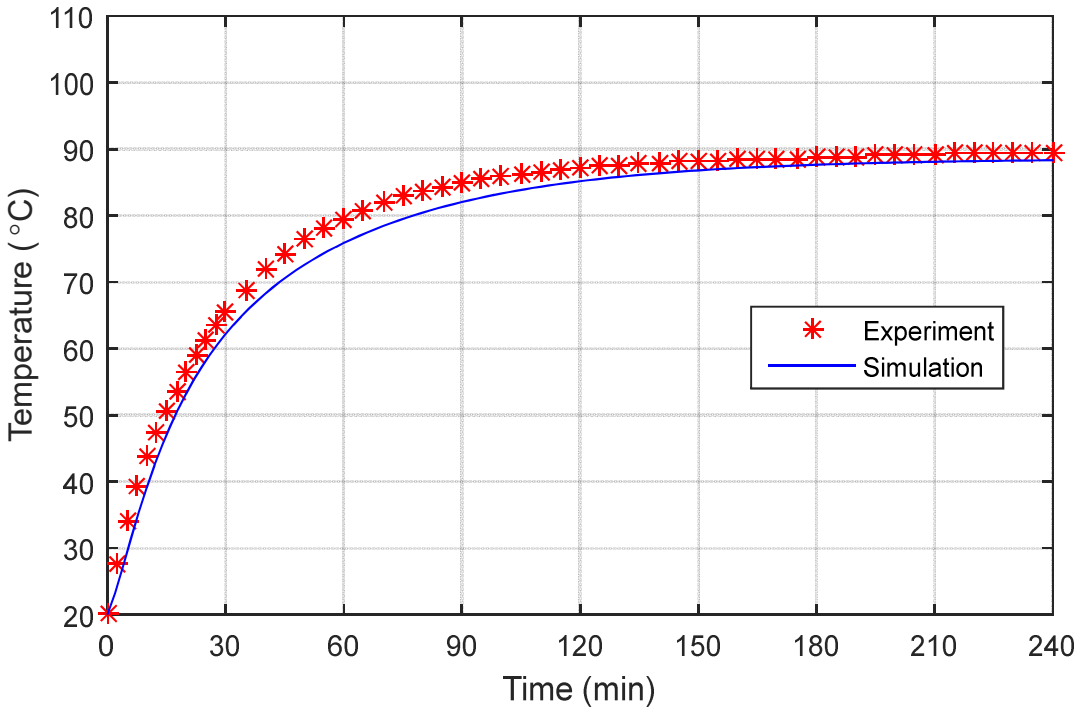

Figure 7-19 Temperature comparison of stator core

The thermal testing results of the designed ferrite IPM motor are compared with its simulation results that are obtained in 5.4.3. The comparison of copper coil temperature and stator core temperature are depicted in Figure 7-18 and Figure 7-19 respectively. As shown in Figure 7-18, the temperature results of the experiment have close agreement with that of simulation in the first half hour, but after that the experimental temperature is about 2°C higher than the simulated temperature. This might be because the actual thermal testing is conducted in a closed room and the ambient temperature is increasing during the experiment, which is caused by the heat that is generated from the running motor. But the ambient temperature in the simulation is set to be constant, with virtually no increase during the operating process.

According to the sampling position in Figure 5-34, the stator core temperature at the corresponding position is estimated from the temperatures of its nearby measuring point 6 and 7, and compared with simulated results in Figure 7-19. The actual testing stator core temperature grows a little faster than the simulated temperature, and all get into equilibrium state after around 150 minutes. The testing temperature is higher, and the largest difference is about

4°C happening around the 60th minute. And in the steady state the temperature is about 1.5°C. The difference of the stator core temperature may be caused by the inconsistency of lamination material. The actual loss coefficient of steel sheets might be higher than the one used in simulation. The increasing room temperature also affects the experimental results. Despite the discrepancies between the experiment and simulation results, the general tendencies are the same. Therefore, the thermal analysis of the ferrite IPM motor is validated by the experiment testing.

7.3 Summary

A prototype ferrite IPM machine is manufactured and tested to validate the proposed motor design methods and ideas. A serial of tests are performed under various working conditions to obtain the characteristics of the prototype machine, which include open-circuit test, no-load test, loaded test and thermal test. From the comprehensive comparison between the FEA and experimental results, it is seen that the FEA analyses have close agreement with the actual prototype tests in terms of back EMF, torque capacity and motor efficiency. The four-hour continuous thermal test shows the temperature distribution and change of the stator. The simulation results of the temperature changes of copper coil and stator core exhibit good agreement with the experimental results. Therefore, the proposed methods and ideas are well validated by the experiments.

8. CONCLUSION AND FUTURE WORK

In the thesis a two-layer spoke type ferrite IPM machine is designed by PSO method, and its quality is guaranteed by DOE assisted Six Sigma DMADV quality control method in mass production. Loss analysis and thermal analysis of the machine are carried out, followed by an investigation of the motor controller with single-shunt current sensor and Hall Effect speed feedback. A prototype electric drive system with the designed machine and controller is built, and experimental tests are employed to validate the proposed the methods and idea. The corresponding conclusions and possible further works are presented hereafter.

8.1 Conclusions

The nonlinearities in materials and the complex relationships between geometrical parameters truly make the optimal machine design a difficult and challenging task. PSO is an effective method for the design of electric machine with multi-dimensional parameters and it is superior in terms of simplicity and effectiveness. With the help of VBScript programming language, FEA simulation, data processing and PSO algorithm can be integrated into an automatic electric machine design tool. Once the solution space, objective function, and iterative parameters are well set in the programme, the optimisation of electric machine design will be carried out automatically. This time-efficient and convenient approach saves designers' operating time, so that the overall cost of motor designing could be reduced.

Different PSO setup parameters have been adopted on the design of two-layer spoke type ferrite IPM motor in the thesis. Some useful conclusions have been made from the research results. The invisible walls boundary condition is better than absorbing walls boundary condition in the electric machine case, as it explores more thoroughly and is not easy to be trapped in an edge positon. *Vmax* is an important setting parameter in PSO method. It is recommended to set *Vmax* to 10–20% of the dynamic range, so that the particles are able to explore the solution space sufficiently without flying past the optimal design

points, especially for the PSO algorithm using *Clerc-Carlisle* parameters. Both of the *Clerc-Kenney* and *Clerc-Carlisle* parameters are suitable for PSO method in electric machine design application. And the difference between them is that when *Vmax* is equal to the full dynamic range the PSO with *Clerc-Kenney* parameters performs a little better, and when *Vmax* is equal to 15% dynamic range the PSO using *Clerc-Carlisle* parameters exhibits slightly better performance.

The electric machine manufacturing is a complicated process from various assorted raw materials to a well-functioned machine. The quality control method Six Sigma DMADV is able to improve the quality of the electric machine. In the thesis, the machine quality is improved by increasing its performance consistency, which is implemented by realistic adjustment of their mechanical tolerances. Due to the complexity of electric machine, the conventional OFAT method is suitable to deal the coupled and dependent system. The statistical DOE is an effective approach to explore multi-factorial space, only a fraction of samples exhibiting the essential characteristics of electric machine, which makes the Six Sigma quality control of the studied machine possible. With the help of DOE assisted Six Sigma DMADV approach, the output torque variation of studied motor is reduced from the initial 9.7674% to the final1.9865%, thus the performance consistency is much improved. The applications of DOE optimality designs on the machine quality control also endorse that D-optimality criterion is good at identifying the significances of the factors and I-optimality criterion has merits of good prediction across the entire design region.

The characteristics of the stator core material are worsened when being pressed upon with pressure. Thus the iron loss of stator core is affected by press fitting or shrink fitting of the motor housing. The iron loss is increased when the interference is enlarged in press fitting, or when the temperature difference is increased in shrink fitting. High-frequency PWM carrier waves are superimposed on the basic current forms when it is supplied by PWM inverter. And the induced high-frequency magnetic field will increase core losses of the electric machine. The iron loss analysis considering the effects of press fitting

stress, shrink fitting, and PWM harmonics makes the loss estimation more accurate and provides useful advices for motor housing installation and motor PWM control. The losses and efficiency maps of the studied motor are plotted, and compared with that of induction machine. The proposed ferrite IPM machine exhibits great superiority to its counterpart IM in terms of efficiency below the rated speed.

From the FEA simulation and experiment test, it is seen that the high temperature region is the winding, as copper loss is the dominant source of heat. The moderate temperature region is the rotor, where the heat is accumulated from rotor iron loss but difficult to dissipate. The temperature of stator core is relatively low, because the heat generated from stator core loss is easy to run away into the ambience. The thermal analysis of the studied motor provides a deeper understanding of motor losses and helps to determine consecutive operating time in overload conditions.

Due to the special structure of the proposed machine, the flux of rotor is prone to align with the teeth of stator but does not lock at the expected position, which makes it difficult to provide the correct initial reference angle for the position feedback. A simple but effective approach is proposed in the study. The rotor is spun forward and backward in 30° around the initial location when each time the motor is started. So that the rotor is able to align with magnet flux and correct initial position is provided for the control system.

In order to reduce the cost of motor controller, Hall Effect speed feedback and single-shunt current sampling are used in the control system. Since there are only six available signals from Hall Effect sensors in an electrical period, this increases the difficulty of predicting speed and position. A position estimation approach considering motor starting location is proposed, and accurate speed and position are obtained from the Hall Effect sensors. At least two phase-currents are required to reconstruct the current pattern, and this makes it challenging for shingle-shunt current sampling system especially when voltage space vectors are in boundary region and low modulation region. The proposed single-shunt current sampling method thoroughly considers different situations

and provides effective solutions for each case. With the well-designed control algorithms the low-cost controller is able to collect motor speed and electric current data for the control system, and this is validated by the prototype drive system.

8.2 Future Work

The studied ferrite IPM machine could also be optimised by other computational intelligence based methods, such as genetic algorithm (GA). The comparison of different design algorithms will be helpful to understand their features and select the most suitable method for different electric machine design applications. Additionally more geometrical parameters could be involved in the PSO motor design, such as slot opening, air gap, and rotor diameter. The mechanical constricts could also be considered in the FEA motor models, so that the resultant optimal design from POS method is easier to meet mechanical requirements without much more post-correction.

In the process of motor manufacturing, there are many factors affecting the ultimate performance of the motor. In the thesis, only the machining accuracy is considered and other factors are assumed ideal and constant. In the future works, the factors such as material consistency and assembling accuracy should be included in the electric machine quality control. The proposed DOE assisted Six Sigma DMADV method could also be used for other types of electric machines. It is better to have more results to validate the effectiveness of the method. Due to the limitation of budget, only one prototype machine is manufactured in the study, which cannot fully validate the effectiveness of the proposed method. Thus the DOE assisted Six Sigma DMADV approach is necessary to be further validated in electric machine company with many motor samples.

The iron loss of stator core is affected by press fitting or shrink fitting when it is fixed in the housing shell. The analysis is only validated by FEA results, hence in the future more prototype machines with different geometrical interferences are needed to validate the effects of press fitting or shrink fitting to the iron loss of stator core. The maximum consecutive operating time in the over-load

condition is estimated by FEA approach, which requires further validation from experimental results. It should be noted that the maximum consecutive operating time test would make irreversible damage to the motor.

Control strategies of the electric drive system. The i_d=0 vector control and MTPA control have been implemented in the electric drive. Some other control strategies could also be used to further improve the capability of the drive system, such as unity powder factor control, flux weakening control, direct torque control, maximum efficiency per ampere control, and so on. Since the low-cost electric drive using Hall Effect speed feedback and single-shunt current sensing, this would induce some new issues when the motor is controlled by above strategies. Hence some new control algorithms are required to solve the problems.

The use of Hall Effect sensors can provide accurate speed feedback when the speed is higher than about 120 rpm. However, when the speed is too slow, the feedback is unstable. Hence some new algorithms are needed to improve the low speed feedback quality. There are still some small errors in the position prediction by Hall Effect sensors, therefore the position feedback can be further polished by an advanced algorithm. Due to the unstable speed feedback in the low speed condition, the position prediction method does not work well the motor speed is too low, which requires more research in the future.

REFERENCES

[1] Statista Inc., “Production of washing machines in China” Available: https://www.statista.com/statistics/307684/china-washing-machine-production/, [Accessed: 1st Dec. 2017].

[2] P. Waide and C.U. Brunner, “Energy-Efficiency Policy Opportunities for Electric Motor-Driven Systems,” *International Energy Agency Working Paper*, 2011.

[3] A.T. de Almeida, F.J.T.E. Ferreira, and G. Baoming, “Beyond Induction Motors—Technology Trends to Move Up Efficiency,” *IEEE Transactions on Industry Applications*, vol. 50, 2014, pp. 2103–2114.

[4] A. Boglietti, A. Cavagnino, and S. Vaschetto, “Induction motor EU standards for efficiency evaluation: The scenario after IEC 60034-2-1,” *IECON 2011 - 37th Annual Conference on IEEE Industrial Electronics Society*, 2011, pp. 2786–2791.

[5] Y. Guan, Z.Q. Zhu, I.A.A. Afinowi, J.C. Mipo, and P. Farah, “Comparison between induction machine and interior permanent magnet machine for electric vehicle application,” *17th International Conference on Electrical Machines and Systems (ICEMS)*, 2014, pp. 144–150.

[6] E.B. Agamloh and A. Cavagnino, “High efficiency design of induction machines for industrial applications,” *Workshop on Electrical Machines Design, Control and Diagnosis (WEMDCD)*, IEEE, 2013, pp. 33–46.

[7] D.G. Dorrell, “The Challenges of Meeting IE4 Efficiency Standards for Induction and Other Machines,” *International Conference on Industrial Technology (ICIT)*, IEEE, 2014, pp. 213–218.

[8] G. Bramerdorfer, S. Silber, G. Weidenholzer, and W. Amrhein, “Comprehensive cost optimization study of high-efficiency brushless synchronous machines,” *IEEE International Electric Machines & Drives Conference (IEMDC)*, 2013, pp. 1126–1131.

[9] E. Richter, T.J.E. Miller, T.W. Neumann, and T.L. Hudson, “The Ferrite Permanent Magnet AC Motor--A Technical and Economical Assessment,” *IEEE Transactions on Industry Applications*, vol. IA-21, 1985, pp. 644–650.

[10] K. Chau, C. Chan, and C. Liu, “Overview of permanent-magnet brushless drives for electric and hybrid electric vehicles,” *IEEE Transactions on Industrial Electronics*, vol. 55, 2008, pp. 2246–2257.

[11] S. Javadi and M. Mirsalim, “Design and Analysis of 42-V Coreless Axial-Flux Permanent-Magnet Generators for Automotive Applications,” *IEEE Transactions on Magnetics*, vol. 46, 2010, pp. 1015–1023.

[12] E. Sulaiman, T. Kosaka, and N. Matsui, “High Power Density Design of 6-Slot-8-Pole Hybrid Excitation Flux Switching Machine for Hybrid Electric Vehicles,” *IEEE Transactions on Magnetics*, vol. 47, 2011, pp. 4453–4456.

[13] Z.Q. Zhu and D. Howe, “Electrical Machines and Drives for Electric, Hybrid, and Fuel Cell Vehicles,” *Proceedings of the IEEE*, vol. 95, Apr. 2007, pp. 746–765.

[14] N. Hashemnia and B. Asaei, “Comparative study of using different electric motors in the electric vehicles,” *18th International Conference on Electrical Machines*, 2008, pp. 1–5.

[15] Roskill Information Service, *Rare Earths: Global Industry, Markets & Outlook*, 2015.

[16] I. Boldea, L.N. Tutelea, L. Parsa, and D. Dorrell, “Automotive electric propulsion systems with reduced or no permanent magnets: An overview,” *IEEE Transactions on Industrial Electronics*, vol. 61, 2014, pp. 5696–5711.

[17] D. Dorrell, L. Parsa, and I. Boldea, “Automotive Electric Motors, Generators, and Actuator Drive Systems With Reduced or No Permanent Magnets and Innovative Design Concepts,” *IEEE Transactions on Industrial Electronics*, vol. 61, 2014, pp. 5693–5695.

[18] S. Morimoto, Y. Asano, T. Kosaka, and Y. Enomoto, “Recent technical trends in PMSM,” *International Power Electronics Conference (IPEC-Hiroshima 2014 - ECCE-ASIA)*, 2014, pp. 1997–2003.

[19] M.M. Rahman, K.T. Kim, and J. Hur, “Design and optimization of neodymium-free SPOKE-type motor with segmented wing-shaped PM,” *IEEE Transactions on Magnetics*, vol. 50, 2014, pp. 10–13.

[20] B. Xia, W. Fei, and P. Luk, “Analysis and design of V-spoke ferrite interior permanent magnet machine for traction applications,” *6th International Conference on Power Electronics Systems and Applications (PESA)*, IEEE, 2015.

[21] B. Xia, W. Fei, P.C.K. Luk, and D. Wu, “Design of a multi-layer interior ferrite permanent magnet synchronous machine for traction applications,” *7th IET International Conference on Power Electronics, Machines and Drives (PEMD 2014)*, 2014, pp. 1–6.

[22] T.J.E. Miller, *Brushless Permanent-Magnet and Reluctance Motor Drives (Electrical & Electronic Engineering Monographs)*, Oxford University Press, 1989.

[23] S.-J. Lee, S.-I. Kim, J.-P. Hong, B.-Y. Song, and J.-W. Park, “Characteristic analysis of the water pump motor considering polar anisotropie ferrite bonded magnet,” *International Conference on Electrical Machines and Systems (ICEMS)*, 2010, pp. 1242–1245.

[24] D. Polka, *Motors and drives : a practical technology guide*, The Instrumentation, Systems, and Automation Society, 2002.

[25] G. Mirzaeva, R.E. Betz, and T.J. Summers, “Evaluation of current density in DC motor brushes for mining machines based on Air-gap field measurement,” *IEEE Transactions on Industry Applications*, vol. 46, 2010, pp. 1255–1263.

[26] A.H.Z. Farnaz, H.S. Sajith, P.J. Binduhewa, M.P.B. Ekanayake, and B.G.L.T. Samaranayake, “Low cost torque estimator for DC servo motors,” *IEEE 10th International Conference on Industrial and Information Systems*, 2015, pp. 187–192.

[27] G. Mirzaeva, R.E.E. Betz, and T.J.J. Summers, “Performance evaluation of DC motors for electric rope shovels based on air gap flux measurement,” *Australasian Universities Power Engineering Conference (AUPEC)*, 2009, pp. 1–6.

[28] A. Kiyoumarsi, “Analysis and Comparison of a Permanent-Magnet DC Motor with a Field-Winding DC Motor,” *Journal of Electrical Engineering & Technology*, vol. 4, 2009, pp. 370–376.

[29] A. Trzynadlowski, *Control of Induction Motors*, San Diego,US: Elsevier Science Publishing Co Inc, 2001.

[30] J. Gieras, *Permanent Magnet Motor Technology Design and Applications*, CRC Press, 2010.

[31] P. Vas, *Sensorless Vector and Direct Torque Control*, Oxford University Pysics Pub., 1998.

[32] M. Bash, S. Pekarek, S. Sudhoff, J. Whitmore, and M. Frantzen, “A Comparison of Permanent Magnet and Wound Rotor Synchronous Machines for Portable Power Generation,” *Power and Energy Conference at Illinois (PECI)*, 2010, pp. 1–6.

[33] P. Roshanfekr, “Design and Assessment of HVDC Off-shore Wind Turbine Generator,” Chalmers University of Technology, 2015.

[34] S. Sjökvist, “Demagnetization Studies on Permanent Magnets - Comparing FEM Simulations with Experiments,” Uppsala University, 2014.

[35] J.R. Hendershot and T.J.E. Miller, *Design of Brushless Permanent Magnet Motors*, Magna Physics Pub., 1994.

[36] C. Xia, *Permanent Magnet Brushless DC Motor Drives and Controls*, John Wiley & Sons Inc, 2012.

[37] D.C. Hanselman, *Brushless permanent magnet motor design*, Magna Physics Publishing, 2003.

[38] A.M. El-Refaie, Z.Q. Zhu, T.M. Jahns, and D. Howe, “Winding Inductances of Fractional Slot Surface-Mounted Permanent Magnet Brushless Machines,” *IEEE Industry Applications Society Annual Meeting*, Ieee, 2008, pp. 1–8.

[39] F. Magnussen and C. Sadarangani, “Winding Factors and Joule Losses of Permanent Magnet Machines with Concentrated Windings,” 2003.

[40] J.F. Gieras, R.J. Wang, and M.J. Kamper, *Axial Flux Permanent Magnet Brushless Machines*, Springer Netherlands, 2008.

[41] A.J. Rix, M.J. Kamper, and S. Member, “Radial-Flux Permanent-Magnet Hub Drives : A Comparison Based on Stator and Rotor Topologies,” vol. 59, 2012, pp. 2475–2483.

[42] J. Eastham and F. Profumo, “Novel axial flux machine for aircraft drive: Design and modeling,” *IEEE Transactions on Magnetics*, vol. 38, 2002, pp. 3003–3005.

[43] D. Lu and N. Kar, “A review of flux-weakening control in permanent magnet synchronous machines,” *Vehicle Power and and Propulsion Conference (VPPC)*, IEEE, 2010.

[44] J.F. Gieras, Z.J. Piech, and B. Tomczuk, *Linear Synchronous Motors: Transportation and Automation Systems (Electric Power Engineering Series)*, CRC Press, 1999.

[45] F. Libert and J. Soulard, “Design study of different direct-driven permanent-magnet motors for a low speed application,” *Proceedings of the Nordic Workshop on Power and Industrial Electronics (NORpie)*, Trondheim, Norway: 2004, pp. 1–6.

[46] A. El-Refaie, “Fractional-slot concentrated-windings synchronous permanent magnet machines: Opportunities and challenges,” *IEEE Transactions on Industrial Electronics*, vol. 57, 2010, pp. 107–121.

[47] F. Magnussen, P. Thelin, and C. Sadarangani, “Performance evaluation of permanent magnet synchronous machines with concentrated and distributed windings including the effect of field-weakening,” *International Conference on Power Electronics, Machines and Drives (PEMD 2004).*, IET, 2004.

[48] M.T. Abolhassani, “A New Concentrated Windings Surface Mounted Permanent Magnet Synchronous Machine for Wind Energy Application,” *IEEE International Conference on Electric Machines and Drives*, 2005, pp. 931–936.

[49] S.-C. Yang, Y.-P. Yang, and J.-J. Liu, “Design and Control Optimization of Surface-Mounted Permanent-Magnet Machines with High Torque and Low Ripples,” *IECON 2007 - 33rd Annual Conference of the IEEE Industrial Electronics Society*, 2007, pp. 198–203.

[50] A. Faggion, “Ringed-Pole Permanent-Magnet Synchronous Motor for Position Sensorless Drives,” *IEEE Transactions on Industry ApplicationsIndustry Applications*, vol. 47, 2011, pp. 1759–1766.

[51] N. Bianchi, S. Bolognani, and A. Faggion, “Rotor design arrangement of SPM motors for the sensorless control at low speed and standstill,” *Proceedings of 14th International Power Electronics and Motion Control Conference EPE-PEMC 2010*, Sep. 2010, pp. 23–28.

[52] K. Rasmussen, “Analytical prediction of magnetic field from surface mounted permanent magnet motor,” *International Conference Electric Machines and Drives (IEMD)*, IEEE, 1999, pp. 34–36.

[53] K. Rasmussen and J. Davies, “Analytical and numerical computation of air-gap magnetic fields in brushless motors with surface permanent magnets,” *IEEE Transanctions on Industry Applications*, vol. 36, 2000, pp. 1547–1554.

[54] K.T. Chau, “Analytical Calculation of Magnetic Field in Surface-Inset

Permanent Magnet Motors," *IEEE Transactions on Magnetics*, vol. 45, Oct. 2009, pp. 4688–4691.

[55] A. Rahideh and T. Korakianitis, "Analytical Magnetic Field Calculation of Slotted Brushless Permanent-Magnet Machines With Surface Inset Magnets," *IEEE Transactions on Magnetics*, vol. 48, Oct. 2012, pp. 2633–2649.

[56] A. Rahideh and T. Korakianitis, "Analytical Armature Reaction Field Distribution of Slotless Brushless Machines With Inset Permanent Magnets," *IEEE Transactions on Magnetics*, vol. 48, Jul. 2012, pp. 2178–2191.

[57] T.M. Jahns, "Flux-weakening regime operation of an interior permanent-magnet synchronous motor drive," *IEEE Transactions on Industry Applications*, vol. IA-23, 1987, pp. 681–689.

[58] M. Barcaro, N. Bianchi, and F. Magnussen, "Permanent-magnet optimization in permanent-magnet-assisted synchronous reluctance motor for a wide constant-power speed range," *IEEE Transactions on Industrial Electronics*, vol. 59, 2012, pp. 2495–2502.

[59] P.B. Reddy, A. El-Refaie, K.K. Huh, J.K. Tangudu, and T.M. Jahns, "Comparison of interior and surface PM machines equipped with fractional-slot concentrated windings for hybrid traction applications," *IEEE Energy Conversion Congress and Exposition: Energy Conversion Innovation for a Clean Energy Future*, 2011, pp. 2252–2259.

[60] D.M. Ionel, J.F. Eastham, T.J.E. Miller, and E. Demeter, "Design considerations for permanent magnet synchronous motors for flux weakening applications," *IEE Proceedings - Electric Power Applications*, vol. 145, 1998, p. 435.

[61] G. Pellegrino, A. Vagati, P. Guglielmi, and B. Boazzo, "Performance comparison between surface-mounted and interior PM motor drives for electric vehicle application," *IEEE Transactions on Industrial Electronics*, vol. 59, 2012, pp. 803–811.

[62] S. Wu, L. Tian, and S. Cui, "A comparative study of the interior permanent magnet electrical machine's rotor configurations for a single shaft hybrid electric bus," *2008 IEEE Vehicle Power and Propulsion Conference*, Sep. 2008, pp. 1–4.

[63] S. Hahlbeck and D. Gerling, "Design considerations for rotors with embedded v-shape Permanent Magnets," *Proceedings of the 2008 International Conference on Electrical Machines, ICEM'08*, 2008, pp. 1–4.

[64] W. Soong, D. Staton, and T. Miller, "Design of a new axially-laminated interior permanent magnet motor," *IEEE Transactions on Industry Applications*, vol. 31, 1995, pp. 358–367.

[65] Eclipse Magnetics Ltd, *Ferrite Magnets / Ceramic Magnets Datasheet*, Sheffield, England: 2007.

[66] C.B. Carter and M.G. Norton, *Ceramic Materials Science and Engineering*, Springer, 2007.

[67] J.E. Gould, “Permanent magnets,” *Proceedings of the Institution of Electrical Engineers*, vol. 125, 1978, pp. 1137–1151.

[68] U.S. Deshpande, “Recent advances in materials for use in permanent magnet machines-a review,” *IEEE International Electric Machines and Drives Conference*, vol. 1, 2003, pp. 509–515.

[69] S. Zhang, J. Xu, J. Junak, D. Fiederling, G. Sawczuk, M. Koch, A. Schalja, M. Podack, and J. Baumgartner, “Permanent magnet technology for electric motors in automotive applications,” *International Electric Drives Production Conference (EDPC)*, 2012, pp. 1–11.

[70] E. Grant and L.M. Roszyk, “Design Consideration for Permanent Magnet Motors in Appliance Applications,” *EEE Transactions on Industry and General Applications*, vol. IGA-4, 1968, pp. 535–544.

[71] T.W. Nehl, F.A. Fouad, and N.A. Demerdash, “Digital simulation of power conditioner-machine interaction for electronically commutated DC permanent magnet machines,” *IEEE Transactions on Magnetics*, vol. 17, 1981, pp. 3284–3286.

[72] F.A. Fouad, T.W. Nehl, and N.A. Demerdash, “Permanent magnet modeling for use in vector potential finite element field analysis in electrical machinery,” *IEEE Transactions on Magnetics*, vol. 17, 1981, pp. 3002–3004.

[73] H.R. Bolton, Y.D. Liu, and N.M. Mallinson, “Investigation into a class of brushless DC motor with quasisquare voltages and currents,” *IEE Proceedings B-Electric Power Applications*, vol. 133, 1986, pp. 103–111.

[74] E. Richter and T. Neumann, “Line start permanent magnet motors with different materials,” *IEEE Transactions on Magnetics*, vol. 20, 1984, pp. 1762–1764.

[75] A. Fasolo, L. Alberti, and N. Bianchi, “Performance Comparison Between Switching-Flux and IPM Machines With Rare-Earth and Ferrite PMs,” *IEEE Transactions on Industry Applications*, vol. 50, 2014, pp. 3708–3716.

[76] E.E. Montalvo-Ortiz, S.N. Foster, J.G. Cintron-Rivera, and E.G. Strangas, “Comparison between a spoke-type PMSM and a PMASynRM using ferrite magnets,” *IEEE International Electric Machines & Drives Conference (IEMDC)*, 2013, pp. 1080–1087.

[77] E. Carraro, M. Degano, M. Morandin, and N. Bianchi, “PM synchronous machine comparison for light electric vehicles,” *IEEE International Electric Vehicle Conference (IEVC)*, 2014, pp. 1–8.

[78] S.B. Bhat, S.P. Nikam, and B.G. Fernandes, “Design and analysis of ferrite based permanent magnet motor for electric assist bicycle,” *International Conference on Electrical Machines (ICEM)*, 2014, pp. 106–111.

[79] R.K. Gupta and N. Mohan, “A Three-Phase Permanent Magnet Brushless DC Motor for Low-Power Low-Speed Fan Applications - Optimizing Cost and Efficiency,” *Conference Record of the 2007 IEEE*

Industry Applications Conference Annual Meeting, 2007, pp. 846–852.

[80] S.K. Pal, “Comparative study of the design and manufacturing processes of electrical motors with low and high energy permanent magnets,” *Sixth International Conference on Electrical Machines and Drives (Conf. Publ. No. 376)*, 1993, pp. 339–346.

[81] P. Sekerak, V. Hrabovcova, J. Pyrhonen, S. Kalamen, P. Rafajdus, and M. Onufer, “Comparison of Synchronous Motors With Different Permanent Magnet and Winding Types,” *IEEE Transactions on Magnetics*, vol. 49, 2013, pp. 1256–1263.

[82] A.M. Mihai, S. Benelghali, L. Livadaru, A. Simion, and R. Outbib, “FEM analysis upon significance of different permanent magnet types used in a five-phase PM generator for gearless small-scale wind,” *20th International Conference on Electrical Machines (ICEM)*, 2012, pp. 267–273.

[83] S. Laurit, A. Kallaste, T. Vaimann, and A. Belahcen, “Cost efficiency analysis of slow-speed slotless permanent magnet synchronous generator using different magnetic materials,” *Electric Power Quality and Supply Reliability Conference*, 2014, pp. 221–224.

[84] G.-C. Lee and T.-U. Jung, “Design comparisons of BLDC motors for electric water pump,” *IEEE Vehicle Power and Propulsion Conference (VPPC)*, 2012, pp. 48–50.

[85] J.A. Krizan and S.D. Sudhoff, “Theoretical performance boundaries for permanent magnet machines as a function of magnet type,” *IEEE Power and Energy Society General Meeting*, 2012, pp. 1–6.

[86] K.H. Kim, H.I. Park, S.M. Jang, D.J. You, and J.Y. Choi, “Comparative Study of Electromagnetic Performance of High-Speed Synchronous Motors with Rare-Earth and Ferrite Permanent Magnets,” *IEEE Transactions on Magnetics*, vol. PP, 2016, p. 1.

[87] S.-M. Jang, H.-J. Seo, Y.-S. Park, H.-I. Park, and J.-Y. Choi, “Design and Electromagnetic Field Characteristic Analysis of 1.5 kW Small Scale Wind Power Generator for Substitution of Nd-Fe-B to Ferrite Permanent Magnet,” *IEEE Transactions on Magnetics*, vol. 48, 2012, pp. 2933–2936.

[88] P. Sekerak, V. Hrabovcova, M. Onufer, L. Kaiamen, and P. Rafajdus, “Synchronous motors with different PM materials,” *Proceedings 9th International conference-ELEKTRO*, 2012, pp. 241–246.

[89] D.-K. Woo, D.-K. Lim, H.-K. Yeo, J.-S. Ro, and H.-K. Jung, “A 2-D Finite-Element Analysis for a Permanent Magnet Synchronous Motor Taking an Overhang Effect Into Consideration,” *IEEE Transactions on Magnetics*, vol. 49, 2013, pp. 4894–4899.

[90] H.-C. Kim and T.-U. Jung, “Analysis of rotor overhang effect considering load torque variance in automobile BLDC fan motor,” *IEEE Vehicle Power and Propulsion Conference (VPPC)*, 2012, pp. 68–71.

[91] R. Vartanian, H.A. Toliyat, B. Akin, and R. Poley, “Power factor improvement of synchronous reluctance motors (SynRM) using permanent magnets for drive size reduction,” *IEEE Applied Power*

Electronics Conference and Exposition (APEC), 2012, pp. 628–633.

[92] J.X. Shen, S. Cai, H. Shao, and H. Hao, “Evaluation of low-cost high-performance synchronous motors for ventilation application,” *International Conference on Sustainable Mobility Applications, Renewables and Technology (SMART)*, 2015, pp. 1–6.

[93] Y. Wang, D.M. Ionel, M. Jiang, and S.J. Stretz, “Establishing the Relative Merits of Synchronous Reluctance and PM Assisted Technology Through Systematic Design Optimization,” *IEEE Transactions on Industry Applications*, vol. PP, 2016, p. 1.

[94] E. Armando, P. Guglielmi, M. Pastorelli, G. Pellegrino, and A. Vagati, “Performance of IPM-PMASR Motors with Ferrite Injection for Home Appliance Washing Machine,” *IEEE Industry Applications Society Annual Meeting*, 2008, pp. 1–6.

[95] M. Barcaro and N. Bianchi, “Interior PM Machines using Ferrite to Replace Rare-Earth Surface PM Machines,” *IEEE Transactions on Industry Applications*, vol. 50, 2014, pp. 979–985.

[96] R. Vartanian, Y. Deshpande, and H.A. Toliyat, “Performance analysis of a ferrite based fractional horsepower permanent magnet assisted SynRM for fan and pump applications,” *IEEE International Electric Machines & Drives Conference (IEMDC)*, 2013, pp. 1405–1410.

[97] R. Vartanian, Y. Deshpande, and H.A. Toliyat, “Performance analysis of a rare earth magnet based NEMA frame Permanent Magnet assisted Synchronous Reluctance Machine with different magnet type and quantity,” *IEEE International Electric Machines & Drives Conference (IEMDC)*, 2013, pp. 476–483.

[98] D. Prieto, B. Daguse, P. Dessante, and J.-C. Vannier, “Performance comparison of the permanent magnet assisted synchronous reluctance motor and the double magnet synchronous motor,” *15th European Conference on Power Electronics and Applications (EPE)*, 2013, pp. 1–7.

[99] S. Musuroi, C. Sorandaru, M. Greconici, V.N. Olarescu, and M. Weinman, “Low-cost ferrite permanent magnet assisted synchronous reluctance rotor an alternative solution for rare earth permanent magnet synchronous motors,” *IECON Proceedings (Industrial Electronics Conference)*, 2013, pp. 2966–2970.

[100] K. Hayakawa, M. Sanada, S. Morimoto, and Y. Inoue, “Evaluation of IPMSMs with concentrated windings using powder magnets for high torque,” *IEEE 10th International Conference on Power Electronics and Drive Systems (PEDS)*, 2013, pp. 735–740.

[101] Y. Matsumoto, I. Miki, and K. Morinaga, “Study on IPMSM with ferrite magnets driven at high speeds,” *International Conference on Electrical Machines and Systems (ICEMS)*, 2013, pp. 1064–1067.

[102] M. Obata, S. Morimoto, M. Sanada, and Y. Inoue, “Performance of PMASynRM With Ferrite Magnets for EV/HEV Applications Considering Productivity,” *IEEE Transactions on Industry Applications*, vol. 50, 2014,

pp. 2427–2435.

[103] M. Sanada, S. Morimoto, and Y. Inoue, “Development of high-power PMASynRM using ferrite magnets for reducing rare-earth material use,” *International Power Electronics Conference (IPEC-Hiroshima 2014 - ECCE-ASIA)*, 2014, pp. 3519–3524.

[104] M. Paradkar and J. Boecker, “Design of a high performance ferrite magnet-assisted synchronous reluctance motor for an electric vehicle,” *38th Annual Conference on IEEE Industrial Electronics Society*, 2012, pp. 4099–4103.

[105] Y.-H. Jeong, K. Kim, Y.-J. Kim, B.-S. Park, and S.-Y. Jung, “Design characteristics of PMa-SynRM and performance comparison with IPMSM based on numerical analysis,” *XXth International Conference on Electrical Machines (ICEM)*, 2012, pp. 164–170.

[106] H. Cai, B. Guan, and L. Xu, “Low-cost ferrite PM-assisted synchronous reluctance machine for electric vehicles,” *IEEE Transactions on Industrial Electronics*, vol. 61, 2014, pp. 5741–5748.

[107] S.J. Galioto, P.B. Reddy, A.M. El-Refaie, and J.P. Alexander, “Effect of Magnet Types on Performance of High-Speed Spoke Interior-Permanent-Magnet Machines Designed for Traction Applications,” *IEEE Transactions on Industry Applications*, vol. 51, 2015, pp. 2148–2160.

[108] A.-S. Isfanuti, M. Baba, L. Tutelea, A. Moldovan, and I. Boldea, “Surface NdFeB versus Ferrite IPM motor drive for low power (100W to 2000W) applications: FEM embedded optimal design with full step torque response validation in sensorless vector control,” *39th Annual Conference of the IEEE Industrial Electronics Society*, 2013, pp. 3177–3182.

[109] S. Eriksson and H. Bernhoff, “Rotor design for PM generators reflecting the unstable neodymium price,” *XXth International Conference on Electrical Machines (ICEM)*, 2012, pp. 1419–1423.

[110] E. Spooner, A.C. Williamson, and G. Catto, “Modular design of permanent-magnet generators for wind turbines,” *IEE Proceedings - Electric Power Applications*, vol. 143, 1996, pp. 388–395.

[111] D.G. Dorrell, M.-F. Hsieh, and A.M. Knight, “Alternative Rotor Designs for High Performance Brushless Permanent Magnet Machines for Hybrid Electric Vehicles,” *IEEE Transactions on Magnetics*, vol. 48, 2012, pp. 835–838.

[112] Q. Chen, G. Liu, W. Zhao, M. Shao, and Z. Liu, “Design and Analysis of the New High-Reliability Motors With Hybrid Permanent Magnet Material,” *IEEE Transactions on Magnetics*, vol. 50, 2014, pp. 1–10.

[113] F. Demmelmayr, B. Weiss, M. Troyer, and M. Schroedl, “Comparison of PM-machines with ferrite and NdFeB magnets in terms of machine performance and sensorless start-up control,” *IEEE International Conference on Industrial Technology (ICIT)*, 2013, pp. 272–277.

[114] K.-C. Kim and J. Lee, “The dynamic analysis of a spoke-type permanent magnet generator with large overhang,” *IEEE Transactions on Magnetics*,

vol. 41, 2005, pp. 3805–3807.

[115] I.C. Chabu, V.C. Silva, S.I. Nabeta, M.A.M. Afonso, and J.R. Cardoso, “Axial flux concentration technique applied to the design of permanent magnet motors: theoretical aspects and their numerical and experimental validation,” *IEEE International Conference on Electric Machines and Drives*, 2005, pp. 1988–1994.

[116] W. Kakihara, M. Takemoto, and S. Ogasawara, “Rotor Structure in 50 kW Spoke-Type Interior Permanent Magnet Synchronous Motor with Ferrite Permanent Magnets for Automotive Applications,” *IEEE Energy Conversion Congress and Exposition (ECCE)*, 2013, pp. 606–613.

[117] K. Chiba, M. Takemoto, S. Ogasawara, and W.G. Yim, “Ferrite-magnet spoke-type IPMSM with W-shaped magnet placement,” *39th Annual Conference of the IEEE Industrial Electronics Society (IECON)*, 2013, pp. 2869–2874.

[118] G.-H. Kang, J. Hur, H.-G. Sung, and J.-P. Hong, “Optimal design of spoke type BLDC motor considering irreversible demagnetization of permanent magnet,” *Sixth International Conference on Electrical Machines and Systems (ICEMS)*, vol. 1, 2003, pp. 234–237.

[119] D. Matsuhashi, K. Matsuo, T. Okitsu, T. Ashikaga, and T. Mizuno, “Comparison study of various motors for EVs and the potentiality of a ferrite magnet motor,” *International Power Electronics Conference (IPEC-Hiroshima 2014 - ECCE-ASIA)*, 2014, pp. 1886–1891.

[120] B. Lee, G.-H. Kang, J. Hur, and D.-W. You, “Design of spoke type BLDC motors with high power density for traction applications,” *39th Industry Applications Conference Annual Meeting*, vol. 2, 2004, pp. 1068–1074.

[121] S.-I. Kim, J. Cho, S. Park, T. Park, and S. Lim, “Characteristics Comparison of a Conventional and Modified Spoke-Type Ferrite Magnet Motor for Traction Drives of Low-Speed Electric Vehicles,” *IEEE Transactions on Industry Applications*, vol. 49, 2013, pp. 2516–2523.

[122] K. Kondo, S. Kusase, T. Maekawa, and K. Hanada, “A New PM-Assisted Synchronous Reluctance Motor With Three-Dimensional Trench Air Gap,” *IEEE Transactions on Industry Applications*, vol. 50, 2014, pp. 2485–2492.

[123] M. Kimiabeigi, J.D. Widmer, R. Long, Y. Gao, J. Goss, R. Martin, T. Lisle, J.M. Soler Vizan, A. Michaelides, and B. Mecrow, “High-performance low-cost electric motor for electric vehicles using ferrite magnets,” *IEEE Transactions on Industrial Electronics*, vol. 63, 2016, pp. 113–122.

[124] K.-Y. Hwang, S.-B. Rhee, J.-S. Lee, and B.-I. Kwon, “Shape optimization of rotor pole in spoke type permanent magnet motor for reducing partial demagnetization effect and cogging torque,” *International Conference on Electrical Machines and Systems (ICEMS)*, 2007, pp. 955–960.

[125] K.-Y. Hwang, S.-B. Rhee, B.-Y. Yang, and B.-I. Kwon, “Rotor Pole Design in Spoke-Type Brushless DC Motor by Response Surface Method,” *IEEE Transactions on Magnetics*, vol. 43, 2007, pp. 1833–1836.

[126] P. Zhang, G.Y. Sizov, D.M. Ionel, and N.A.O. Demerdash, “Establishing the Relative Merits of Interior and Spoke-Type Permanent-Magnet Machines With Ferrite or NdFeB Through Systematic Design Optimization,” *IEEE Transactions on Industry Applications*, vol. 51, 2015, pp. 2940–2948.

[127] D.M. Ionel, D.C. Jackson, G. Starr, and A.P. Turner, “Permanent magnet brushless motors for industrial variable speed drives,” *International Conference on Power Electronics, Machines and Drives (Conf. Publ. No. 487)*, 2002, pp. 650–654.

[128] S. Hlioui, L. Vido, Y. Amara, M. Gabsi, A. Miraoui, and M. Lecrivain, “Design of a synchronous machine with concentric stator windings and permanent magnets in focusing configuration,” *International Aegean Conference on Electrical Machines and Power Electronics (ACEMP)*, 2007, pp. 507–512.

[129] K. Boughrara, R. Ibtiouen, and N. Takorabet, “Analytic calculation of magnetic field and electromagnetic performances of spoke type IPM topologies with auxiliary magnets,” *International Conference on Electrical Machines (ICEM)*, 2014, pp. 51–57.

[130] M.R. Mohammad, K.-T. Kim, and J. Hur, “Design and Analysis of a Spoke Type Motor With Segmented Pushing Permanent Magnet for Concentrating Air-Gap Flux Density,” *IEEE Transactions on Magnetics*, vol. 49, 2013, pp. 2397–2400.

[131] M.M. Rahman, K.-T. Kim, and J. Hur, “Design and Optimization of Neodymium-Free SPOKE-Type Motor With Segmented Wing-Shaped PM,” *IEEE Transactions on Magnetics*, vol. 50, 2014, pp. 865–868.

[132] M.M. Rahman, K.-T. Kim, and J. Hur, “Design and analysis of neodymium free SPOKE-type motor with segmented wing shape permanent-magnet for concentrating flux density,” *IEEE Energy Conversion Congress and Exposition (ECCE)*, 2013, pp. 4991–4997.

[133] X. Jannot, J.C. Vannier, J. Saint-Michel, M. Gabsi, C. Marchand, and D. Sadarnac, “An analytical model for interior permanent-magnet synchronous machine with circumferential magnetization design,” *8th International Symposium on Advanced Electromechanical Motion Systems and Electric Drives Joint Symposium*, 2009, pp. 1–3.

[134] X. Jannot, J.-C. Vannier, C. Marchand, M. Gabsi, J. Saint-Michel, and D. Sadarnac, “Multiphysic Modeling of a High-Speed Interior Permanent-Magnet Synchronous Machine for a Multiobjective Optimal Design,” *IEEE Transactions on Energy Conversion*, vol. 26, 2011, pp. 457–467.

[135] R. Krishnan, *Permanent Magnet Synchronous and Brushless DC Motor Drives*, CRC Press, 2009.

[136] S.N. Vukosavic, *Digital Control of Electrical Drives*, Springer US, 2007.

[137] S.E. Ryvkin and E.P. Lever, *Sliding Mode Control for Synchronous Electric Drives*, CRC Press, 2011.

[138] M. Cirstea, A. Dinu, M. McCormick, and J.G. Khor, *eural and Fuzzy Logic*

Control of Drives and Power Systems, Elsevier Science, 2002.

[139] A. Emadi, A. Khaligh, Z. Nie, and Y.J. Lee, *Integrated Power Electronic Converters and Digital Control*, CRC Press, 2009.

[140] B. Wu, *High-power Converters and AC Drives*, Wiley-Interscience, 2006.

[141] A. Emadi, *Handbook of Automotive Power Electronics and Motor Drives*, CRC Taylor & Francis, 2005.

[142] C. Mitchell, J.A. Dierker, and G. Keyarts, "Current Sensing," *Telephone Energy conference*, 1978, pp. 322–327.

[143] F. Blaabjerg and J.K. Pedersen, "Modulation and Current Sensing Technique - An Integrated Part for Low-cost Motor-Drive," *Proceedings of IEEE International Symposium on Industrial Electronics*, 1996, pp. 476–481.

[144] M. Gucma, "Current transformers under transient conditions : subject review," *IEE Journal on Electric Power Applications*, vol. 2, 1979, pp. 87–98.

[145] W.T. Mclyman, "Reviewing Current Transformers and Current Transducers," *Electrical Insulation Conference and Electrical Manufacturing Expo*, IEEE, 2007, pp. 360–365.

[146] T. Astatic, L.D.C. Currents, M. System, W.S. Fig, and S. The, "A transductor-based astatic measuring system for measuring large DC currents," *Precision Electromagnetic Measurements*, IEEE, 1990, pp. 147–148.

[147] K. Xu and B. Jie, "A false-balance-avoidance transductor for measuring large DC currents," *IEEE Transactions on Instrumentation and Measurement*, vol. 46, 1997, pp. 1081–1083.

[148] A.D. Saha and V. John, "Power Consumption Reduction in High Current Closed Loop Hall Effect Current Sensors Using Class D Amplifier," *Power Electronics, Drives and Energy Systems (PEDES)*, IEEE, 2016, pp. 1–6.

[149] N. George and S. Gopalakrishna, "An Improved Anti-differential Configuration Based Hall-Effect Current Sensor," *India Conference (INDICON)*, IEEE, 2016, pp. 2–6.

[150] S. Ziegler, R.C. Woodward, H.H. Iu, S. Member, and L.J. Borle, "Current Sensing Techniques : A Review," *IEEE Sensors Journal*, vol. 9, 2009, pp. 354–376.

[151] Data Device Corporation, *Synchro/Resolver Conversion Handbook*, 1994.

[152] Advanced Micro Controls Inc., "What is a Resolver?" Available: https://www.amci.com/industrial-automation-resources/plc-automation-tutorials/what-resolver/, [Accessed 1st Dec. 2017].

[153] G.K. McMillan and D.M. Considine, *Process Instruments and Controls Handbook*, McGraw Hill, 1999.

[154] B. Joshi, R. Shrestha, and R. Chaudhary, "Modeling , Simulation and

Implementation of Brushed DC Motor Speed Control Using Optical Incremental Encoder Feedback," *Proceedings of IOE Graduate Conference*, 2014, pp. 497–505.

[155] E. Eitel, "Basics of rotary encoders: Overview and new technologies," *Machine Design Magazine, May 2017*.

[156] E. Ramsden, *Hall-effect sensors: theory and applications*, Elsevier, 2006.

[157] Honeywell Inc., "Hall Effect Sensing and Application," *MICRO SWITCH Sensing and Control*, 2011, pp. 1–126.

[158] R. Eberhart and J. Kennedy, "A new optimizer using particle swarm theory," *MHS'95. Proceedings of the Sixth International Symposium on Micro Machine and Human Science*, 1995, pp. 39–43.

[159] J. Kennedy and R. Eberhart, "Particle swarm optimization," *Proceedings of ICNN'95 - International Conference on Neural Networks*, vol. 4, 1995, pp. 1942–1948.

[160] J. Robinson and Y. Rahmat-Samii, "Particle Swarm Optimization in Electromagnetics," *IEEE Transactions on Antennas and Propagation*, vol. 52, Feb. 2004, pp. 397–407.

[161] M. Song and G. Gu, "Research on particle swarm optimization: a review," *Proceedings of International Conference on Machine Learning and Cybernetics (IEEE Cat. No.04EX826)*, vol. 4, 2004, pp. 2236–2241.

[162] R. Yu and Z. Limeng, "PMSM Control Research Based on Particle Swarm Optimization BP Neural Network," *2008 International Conference on Cyberworlds*, Sep. 2008, pp. 832–836.

[163] Y. del Valle, G.K. Venayagamoorthy, S. Mohagheghi, J.-C. Hernandez, and R.G. Harley, "Particle Swarm Optimization: Basic Concepts, Variants and Applications in Power Systems," *IEEE Transactions on Evolutionary Computation*, vol. 12, 2008, pp. 171–195.

[164] Y. Eberhart, Russell C.; Shi, "Particle swarm optimization: developments, applications and resources," *Proceedings of the 2001 Congress on Evolutionary Computation (IEEE Cat. No.01TH8546)*, 2001, pp. 81–86.

[165] Y. Duan and D.M. Ionel, "A review of recent developments in electrical machine design optimization methods with a permanent magnet synchronous motor benchmark study," *IEEE Energy Conversion Congress and Exposition*, Sep. 2011, pp. 3694–3701.

[166] Y. Duan, R.G. Harley, and T.G. Habetler, "Comparison of Particle Swarm Optimization and Genetic Algorithm in the design of permanent magnet motors," *IEEE 6th International Power Electronics and Motion Control Conference*, vol. 3, May. 2009, pp. 822–825.

[167] R.G. Harley and T.G. Habetler, "Multi-objective design optimization of Surface Mount Permanent Magnet machine with particle swarm intelligence," *IEEE Swarm Intelligence Symposium*, Sep. 2008, pp. 1–5.

[168] R. Wrobel and P.H. Mellor, "Particle Swarm Optimisation for the Design

of Brushless Permanent Magnet Machines," *IEEE 41st IAS Annual Meeting Industry Applications Conference*, 2006, pp. 1891–1897.

[169] C. Dongyang, S. Changzhi, and A. Yuejun, "The Application of Magnet Optimization of Permanent Magnet Synchronous Motor by Modified PSO," *6th World Congress on Intelligent Control and Automation*, vol. 1, 2006, pp. 1879–1882.

[170] A.A. Arkadan, M.N. Elbsat, and M.A. Mneimneh, "Particle swarm design optimization of ALA rotor Synrm for traction applications," *IEEE Transactions on Magnetics*, vol. 45, 2009, pp. 956–959.

[171] H.M. Emara, M.E. Ammar, A. Bahgat, and H.T. Dorrah, "Stator fault estimation in induction motors using particle swarm optimization," *IEEE International Electric Machines and Drives Conference (IEMDC03)*, 2003, pp. 1469–1475.

[172] Y. Duan and R.G. Harley, "A novel method for multiobjective design and optimization of three phase induction machines," *IEEE Transactions on Industry Applications*, vol. 47, 2011, pp. 1707–1715.

[173] M. Ashabani and Y.A.R.I. Mohamed, "Multiobjective shape optimization of segmented pole permanent-magnet synchronous machines with improved torque characteristics," *IEEE Transactions on Magnetics*, vol. 47, 2011, pp. 795–804.

[174] D. Wu, W. Fei, P.C.K. Luk, and B. Xia, "Design Considerations of Outer-Rotor Permanent Magnet Synchronous Machines for In-Wheel Electric Drivetrain Using Particle Swarm Optimization," *Power Electronics, Machines and Drives (PEMD 2014)*, 2014, pp. 1–6.

[175] A. Zare Bazghaleh, M.R. Naghashan, and M.R. Meshkatoddini, "Optimum design of single-sided linear induction motors for improved motor performance," *IEEE Transactions on Magnetics*, vol. 46, 2010, pp. 3939–3947.

[176] G.Q. Bao, D. Zhang, J.H. Shi, and J.Z. Jiang, "Optimal design for cogging torque reduction of transverse flux permanent motor using particle swarm optimization algorithm," *The 4th International Power Electronics and Motion Control Conference (IPEMC)*, 2004, pp. 260–263.

[177] J.H. Seo, C.H. Im, S.Y. Kwak, C.G. Lee, and H.K. Jung, "An improved particle swarm optimization algorithm mimicking territorial dispute between groups for multimodal function optimization problems," *IEEE Transactions on Magnetics*, vol. 44, 2008, pp. 1046–1049.

[178] J.H. Seo, S.M. Kim, and H.K. Jung, "Rotor-design strategy of IPMSM for 42 v integrated starter generator," *IEEE Transactions on Magnetics*, vol. 46, 2010, pp. 2458–2461.

[179] Y. Duan, R.G. Harley, and T.G. Habetler, "Method for multi-objective optimized designs of Surface Mount Permanent Magnet motors with concentrated or distributed stator windings," *IEEE International Electric Machines and Drives Conference*, May. 2009, pp. 323–328.

[180] H.S. Urade, "Study and Analysis of Particle Swarm Optimization : A

Review," *2nd National Conference on Information and Communication Technology (NCICT)*, 2011, pp. 1–5.

[181] A. Carlisle and G. Dozier, "An Off-The-Shelf PSO," *Proceeding of Workshop on Particle Swarm Optimization*, 2001, pp. 1–6.

[182] Y. Shi and R. Eberhart, "A modified particle swarm optimizer," *IEEE World Congress on Computational Intelligence*, 1998, pp. 69–73.

[183] Y. Shi and R. Eberhart, "Parameter selection in particle swarm optimization," *7th International Conference on Evolutionary Programming*, New York: Springer-Verlag, 1998, pp. 591–600.

[184] M. Clerc and J. Kennedy, "The particle swarm - explosion, stability, and convergence in a multidimensional complex space," *IEEE Transactions on Evolutionary Computation*, vol. 6, 2002, pp. 58–73.

[185] M. Clerc, "The swarm and the queen: towards a deterministic and adaptive particle swarm optimization," *Proceedings of the 1999 Congress on Evolutionary Computation-CEC99 (Cat. No. 99TH8406)*, 1999, pp. 1951–1957.

[186] J. Kennedy, "The particle swarm: social adaptation of knowledge," *Proceedings of 1997 IEEE International Conference on Evolutionary Computation (ICEC '97)*, 1997, pp. 303–308.

[187] P.R.N. Childs, *Mechanical Design Engineering Handbook*, Butterworth-Heinemann, 2003.

[188] R. Eberhart and Y. Shi, "Tracking and optimizing dynamic systems with particle swarms," *Proceedings of the 2001 Congress on Evolutionary Computation*, 2001, pp. 94–100.

[189] P. Lomax, *Learning VBScript*, O'Reilly & Associations, 1997.

[190] S. Key, *VBScript: Programming Success in a Day*, SAMKEY, 2015.

[191] M. Childs, P. Lomax, and R. Petrusha, *VBScript in a Nutshell: A Desktop Quick Reference*, O'REILLY, 2003.

[192] I.A.A. Afinowi, Z.Q. Zhu, Y. Guan, J.C. Mipo, and P. Farah, "Performance analysis of switched-flux machines with hybrid NdFeB and ferrite magnets," *17th International Conference on Electrical Machines and Systems (ICEMS)*, 2014, pp. 3110–3116.

[193] A. Houston and S.L. Dockstader, *Total Quality Leadership: A Primer*, Washington, D.C.:Dept. of the Navy, Total Quality Leadership Office: 1997.

[194] D.J. Rumsey, *Statistics For Dummies*, John Wiley & Sons, 2016.

[195] F.P. Brooks, "No Silver Bullet Essence and Accidents of Software Engineering," *Computer*, vol. 20, 1987, pp. 10–19.

[196] W.A. Shewhart, *Statistical Method from the Viewpoint of Quality Control*, Dover Publications, 2012.

[197] A.R. Martínez-Lorente, F. Dewhurst, and B.G. Dale, *Total Quality Management: Origins and Evolution of the Term*, Bingley, United

Kingdom: MCB University Publishers Ltd, 1998.

[198] B. Warzecha, *The Problem with Quality Management: Process orientation, controllability and zero-defect processes as modern myths*, Verlag für Planung und Organisation, 2017.

[199] M. Holweg, “The genealogy of lean production,” *Journal of Operations Management*, vol. 25, 2007, pp. 420–437.

[200] W.J. Hopp and M.L. Spearman, *Factory Physics: Foundations of Manufacturing Management*, Irwin/McGraw-Hill, 2001.

[201] Graphic Products Editorial Staff, “Six Sigma Principles” Available: https://www.graphicproducts.com/articles/six-sigma-principles/, [Accessed: 1st Dec. 2017].

[202] D.S. Moore, G.P. McCabe, and B.A. Craig, *Introduction to the Practice of Statistics*, New York: 2009.

[203] G. Tennant, *Six Sigma: SPC and TQM in Manufacturing and Services*, Gower Publishing, Ltd, 2001.

[204] “Lean Maunufacturing and Six Sigma Definitions” Available: http://leansixsigmadefinition.com/glossary/six-sigma/, [Accessed: 1st Dec. 2017].

[205] S. Lee, K. Kim, S. Cho, J. Jang, T. Lee, and J. Hong, “Optimal design of interior permanent magnet synchronous motor considering the manufacturing tolerances using Taguchi robust design,” *IET Electric Power Applications*, vol. 8, 2013, pp. 23–28.

[206] K. Kim, S. Lee, S. Cho, J. Jang, T. Lee, J. Hong, S. Member, and S. Kim, “Multi-Response Taguchi Robust Design of Back Electromotive Force and Cogging Torque Considering the Manufacturing Tolerance for Electric Machine,” *13th International Conference on Optimization of Electrical and Electronic Equipment (OPTIM)*, 2012, pp. 379–387.

[207] S. Deda and J.A. De Kock, “Induction Motor Efficiency Test Methods : A Comparison of Standards,” *Industrial and Commercial Use of Energy (ICUE)*, IEEE, 2017.

[208] Y. Ma, K. Huang, C. Xiang, W. Wang, and H. Liu, “A control strategy to reduce torque variation for dual- mode power-split hybrid electric vechile during mode shift,” *Modelling, Identification and Control (ICMIC)*, IEEE, 2015.

[209] L. Eriksson, E. Johansson, N. Kettaneh-Wold, C. Wikström, and S. Wold, *Design of Experiments - Principles and Application*, Umetrics AB, 2008.

[210] M. Uy and J.K. Telford, “Optimization by Design of Experiment techniques,” *IEEE Aerospace conference*, 2009, pp. 1–10.

[211] S.A. Weissman and N.G. Anderson, “Design of Experiments (DoE) and Process Optimization. A Review of Recent Publications,” *Organic Process Research & Development*, vol. 19, 2014, pp. 1605–1633.

[212] K. Deb, *Multi-Objective Optimization using Evolutionary Algorithms*, Wiley, 2008.

[213] T.P. Ryan, *Modern Experimental Design*, Acworth, GA: Wiley-Interscience, 2007.

[214] M. Proust, *JMP 11 Design of Experiments Guide*, SAS Institute Inc., 2014.

[215] D.R. Cox and D. V. Hinkley, *Theoretical Statistics*, Chapman & Hall/CRC, 1974.

[216] J. Rice, *Mathematical Statistics and Data Analysis*, Duxbury Press, 2006.

[217] JMP SAS Institute Inc, *Predictive and Specialized Modeling*, SAS Institute Inc., 2017.

[218] S.A. Glantz and B.K. Slinker, *Primer of Applied Regression and Analysis of Variance*, McGraw-Hill, 1990.

[219] R.G.D. Steel and J.H. Torrie, *Principles and Procedures of Statistics with Special Reference to the Biological Sciences*, McGraw-Hill, 1960.

[220] P.C. Sen, *Principles of Electric Machines and Power Electronics*, John Wiley & Sons, 1997.

[221] D.A. Gonzalez and D.M. Saban, “Study of the Copper Losses in a High-Speed Permanent-Magnet Machine With Form-Wound Windings,” *IEEE Transactions on Industrial Electronics*, vol. 61, 2013, pp. 3038–3045.

[222] X. Nan and C.R. Sullivan, “An Improved Calculation of Proximity-Effect Loss in High-Frequency Windings of Round Conductors,” *Power Electronics Specialist Conference*, 2003, pp. 853–860.

[223] H. Ebrahimi, “Coupled Magneto-Mechanical Analysis of Inverter-Driven Electrical Machines Taking Account of Magnetostriction,” pp. 83–90.

[224] A.O. Lebeck, *Principles and design of mechanical face seals*, Wiley-Interscience, 1991.

[225] S. Ekanayake, R. Dutta, M.F. Rahman, and D. Xiao, “Deep flux weakening control of a segmented interior permanent magnet synchronous motor with maximum torque per voltage control,” *41st Annual Conference of the IEEE Industrial Electronics Society (IECON)*, 2015, pp. 4802–4807.

[226] J. Kim and S. Sul, “Speed control of interior permanent magnet synchronous motor drive for the flux weakening operation,” *IEEE Transactions on Industry Applications*, vol. 33, 1997, pp. 43–48.

APPENDICES

Appendix A Programme of Machine Design by PSO Method in VBScript

The following is the VBScript programme used in the proposed automatic electric machine optimisation tool by PSO method.

```
' ----------------------------------------------------------
' The VBScript is coded for ANSYS Maxwell auto-run Simulation
' The electric machine is optimised by PSO method with 6 variables
' Edited by Demin Wu, Cranfield University, 22 June, 2016
' ----------------------------------------------------------

'File Address
'-----------------------Temporary CSV Files-----------------------------------
TorqueCSV = "D:/Ansoft/LowCostPSO1/DATA/Torque1.csv"
'-----------------------Result Excel Files------------------------------------
ParameterResultXLSX = "D:/Ansoft/LowCostPSO1/DATA/ParameterResult1.xlsx"
ParameterBestXLSX = "D:/Ansoft/LowCostPSO1/DATA/ParameterBest1.xlsx"
VelocityXLSX = "D:/Ansoft/LowCostPSO1/DATA/Velocity1.xlsx"
CounterXLSX = "D:/Ansoft/LowCostPSO1/DATA/Counter1.xlsx"
ErrorXLSX = "D:/Ansoft/LowCostPSO1/DATA/Error1.xlsx"

' Operation Functions of Maxwell
Dim oAnsoftApp
Dim oDesktop
Dim oProject
Dim oDesign
Dim oEditor
Dim oModule

' Often Changing Parameters
Dim Nm  : Nm = 30   'The number of motors simulated in every Generation
Dim Ng  : Ng = 30   'How many generations to simulate in the PSO
Dim Gen             'Which Generation the Simulation is in.

' Variables for REPAIRING
Dim Gin     : Gin = 1    'Which Generation the simulation is going on
Dim Ndone   : Ndone = 0 'How many motor have been done in Gin generation

' Definitions of Variables
Dim Theta, Theta1, Theta2, Theta3, Theta4, Theta5, ThtBest 'Current Angle
Dim Torque, Torque1, Torque2, Torque3, Torque4, Torque5, TrqBest'Mean Torque
Dim Counter 'To record the count of simulation times
Dim Add 'Count the times that flying out of solution space

' Definitions of Parameters
Dim Wt(29)      '(mm) the width of teeth of the stator
Dim Hs(29)      '(mm) the depth(height) of the slot in the stator
Dim W1(29)      '(mm) the width of Prime Magnet
Dim W2(29)      '(mm) the width of Secondary Magnet
Dim D1(29)      '(mm) the Upper distance between Secondary magnet and central line
Dim D2(29)      '(mm) the Lower distance between Secondary magnet and central line
Dim Vwt(29),Vhs(29),Vw1(29),Vw2(29),Vd1(29),Vd2(29)     'Velocity of Parameters
Dim WtN(29),HsN(29),W1N(29),W2N(29),D1N(29),D2N(29)
Dim VwtN(29),VhsN(29),Vw1N(29),Vw2N(29),Vd1N(29),Vd2N(29)
Dim WtE(29),HsE(29),W1E(29),W2E(29),D1E(29),D2E(29)
Dim Wtpb(29),Hspb(29),W1pb(29),W2pb(29),D1pb(29),D2pb(29)   'Personal best
Dim Wtgb,Hsgb,W1gb,W2gb,D1gb,D2gb   'Globle best
Dim Tpb(29), Tgb    '(Nm) Personal Best Torque and Globle Best Torque
Dim Thtpb(29), Thtgb    ' the corresponding current angle

' The basic setting of Maxwell, and Project and Design names
Set oAnsoftApp = CreateObject("AnsoftMaxwell.MaxwellScriptInterface")
Set oDesktop = oAnsoftApp.GetAppDesktop()
oDesktop.RestoreWindow
```

```
Set oProject = oDesktop.SetActiveProject("LowCostPSO1")
Set oDesign = oProject.SetActiveDesign("PSO1")

'------Start-----------Initialisation-----------------------------------------------
Gen = 1      'The First Generation, i.e. the initial values
For i= 0 To Nm-1     'For each motor
    'Initialise the parameters
    Wt(i) = 1 + 5*Rnd    '[1  6]
    Hs(i) = 6 + 26*Rnd   '[6  32]
    W1(i) = 1 + 9*Rnd    '[1  10]
    W2(i) = 1 + 9*Rnd    '[1  10]

    D1(i) = 2 + 19*Rnd       '[2  21]
    While D1(i) < (W1(i)/2+W2(i)+0.5)
        D1(i) = 2 + 19*Rnd       '[2  21]
    Wend

    D2(i) = 8 + 12.5*Rnd         '[8  20.5]
    While D2(i) < (W1(i)/2+W2(i)+0.5) Or (D1(i)-D2(i)) >6
        D2(i) = 8 + 12.5*Rnd
    Wend

    'Initial Personal Best Torque
    Tpb(i)=0
    'Initial Velocity of each parameter
    Vwt(i)=(6-1)*0.15*(1-2*Rnd)    '<<refer 15% of the parameter range
    Vhs(i)=(32-6)*0.15*(1-2*Rnd)   '<<The end part "*(1-2*Rnd)" is to
    Vw1(i)=(10-1)*0.15*(1-2*Rnd)   '<<make the initial velocity randomly
    Vw2(i)=(10-1)*0.15*(1-2*Rnd)   '<<refer 15% of the parameter range
    Vd1(i)=(21-2)*0.15*(1-2*Rnd)     '<<The end part "*(1-2*Rnd)" is to
    Vd2(i)=(20.5-8)*0.15*(1-2*Rnd)   '<<make the initial velocity randomly
Next
'Initial Globle Best Torque
Tgb=0

'Save the Parameters to <<Parameter>> file
Set objExcel = CreateObject("Excel.Application")
    Set objWorkbook = objExcel.Workbooks.Open(ParameterResultXLSX)
    For i= 0 To Nm-1
        objExcel.Cells(i+3,8*Gen-6).Value = Wt(i)
        objExcel.Cells(i+3,8*Gen-5).Value = Hs(i)
        objExcel.Cells(i+3,8*Gen-4).Value = W1(i)
        objExcel.Cells(i+3,8*Gen-3).Value = W2(i)
        objExcel.Cells(i+3,8*Gen-2).Value = D1(i)
        objExcel.Cells(i+3,8*Gen-1).Value = D2(i)
    Next
    objWorkbook.Save
objExcel.Quit

'Save the Velocities to <<Velocity>> file
Set objExcel = CreateObject("Excel.Application")
    Set objWorkbook = objExcel.Workbooks.Open(VelocityXLSX)
    For i= 0 To Nm-1
        objExcel.Cells(i+3,6*Gen-4).Value = Vwt(i)
        objExcel.Cells(i+3,6*Gen-3).Value = Vhs(i)
        objExcel.Cells(i+3,6*Gen-2).Value = Vw1(i)
        objExcel.Cells(i+3,6*Gen-1).Value = Vw2(i)
        objExcel.Cells(i+3,6*Gen+0).Value = Vd1(i)
        objExcel.Cells(i+3,6*Gen+1).Value = Vd2(i)
    Next
    objWorkbook.Save
objExcel.Quit
'------End-----------Initialisation-------------------------------------------------

For Gen = 1 To Ng 'Repeating Simulation in each generation
    'Save the Begining time of simulation for each Generation
    Set objExcel = CreateObject("Excel.Application")
        Set objWorkbook = objExcel.Workbooks.Open(CounterXLSX)
        objExcel.Cells(2,3*Gen).Value = Date & " "& Time
        objWorkbook.Save
    objExcel.Quit

    'For each motor in a generation
    For i =0 To Nm-1
        Counter = 0      'Reset Counter to zero

```

```
136         'Setting of the Parameters in Maxwell software
137         oDesign.ChangeProperty Array("NAME:AllTabs", Array("NAME:LocalVariableTab",
            Array("NAME:PropServers",
138           "LocalVariables"), Array("NAME:ChangedProps", Array("NAME:Wt", "Value:=",
              Wt(i) & "mm"))))
139         oDesign.ChangeProperty Array("NAME:AllTabs", Array("NAME:LocalVariableTab",
            Array("NAME:PropServers",
140           "LocalVariables"), Array("NAME:ChangedProps", Array("NAME:Hs", "Value:=",
              Hs(i) & "mm"))))
141         oDesign.ChangeProperty Array("NAME:AllTabs", Array("NAME:LocalVariableTab",
            Array("NAME:PropServers",
142           "LocalVariables"), Array("NAME:ChangedProps", Array("NAME:Mag1_W1",
              "Value:=", W1(i) & "mm"))))
143         oDesign.ChangeProperty Array("NAME:AllTabs", Array("NAME:LocalVariableTab",
            Array("NAME:PropServers",
144           "LocalVariables"), Array("NAME:ChangedProps", Array("NAME:Mag2_W1",
              "Value:=", W2(i) & "mm"))))
145         oDesign.ChangeProperty Array("NAME:AllTabs", Array("NAME:LocalVariableTab",
            Array("NAME:PropServers",
146           "LocalVariables"), Array("NAME:ChangedProps", Array("NAME:Dm1", "Value:="
              D1(i) & "mm"))))
147         oDesign.ChangeProperty Array("NAME:AllTabs", Array("NAME:LocalVariableTab",
            Array("NAME:PropServers",
148           "LocalVariables"), Array("NAME:ChangedProps", Array("NAME:Dm2", "Value:="
              D2(i) & "mm"))))
149
150         '------Begin------------<< Save ALL the BEST Results >> Module---
151         Set objExcel = CreateObject("Excel.Application")
152             Set objWorkbook = objExcel.Workbooks.Open(ParameterResultXLSX)
153                 objExcel.Cells(i+3,8*Gen+0).Value = ThtBest
154                 objExcel.Cells(i+3,8*Gen+1).Value = TrqBest
155         objWorkbook.Save
156         objExcel.Quit
157         '-----End------------<< Save ALL the BEST Results >> Module------
158
159         'Objective Function comparison: Personal Best
160         If TrqBest > Tpb(i) Then
161             Tpb(i) = TrqBest
162             Wtpb(i) = Wt(i)
163             Hspb(i) = Hs(i)
164             W1pb(i) = W1(i)
165             W2pb(i) = W2(i)
166             D1pb(i) = D1(i)
167             D2pb(i) = D2(i)
168             Thtpb(i)=ThtBest
169             Else
170         End If
171         'Objective Function comparison: Globle Best
172         If TrqBest > Tgb Then
173             Tgb = TrqBest
174             Wtgb = Wt(i)
175             Hsgb = Hs(i)
176             W1gb = W1(i)
177             W2gb = W2(i)
178             D1gb = D1(i)
179             D2gb = D2(i)
180             Thtgb = ThtBest
181             Else
182         End If
183         'Save all the pbest and gbest parameters to excel file
184         Set objExcel = CreateObject("Excel.Application")
185             Set objWorkbook = objExcel.Workbooks.Open(ParameterBestXLSX)
186                 'Personal best parameters
187                 objExcel.Cells(i+3,8*Gen-6).Value = Wtpb(i)
188                 objExcel.Cells(i+3,8*Gen-5).Value = Hspb(i)
189                 objExcel.Cells(i+3,8*Gen-4).Value = W1pb(i)
190                 objExcel.Cells(i+3,8*Gen-3).Value = W2pb(i)
191                 objExcel.Cells(i+3,8*Gen-2).Value = D1pb(i)
192                 objExcel.Cells(i+3,8*Gen-1).Value = D2pb(i)
193                 objExcel.Cells(i+3,8*Gen+0).Value = Thtpb(i)
194                 objExcel.Cells(i+3,8*Gen+1).Value = Tpb(i)
195                 'Globle best parameters
196                 objExcel.Cells(33,8*Gen-6).Value = Wtgb
197                 objExcel.Cells(33,8*Gen-5).Value = Hsgb
198                 objExcel.Cells(33,8*Gen-4).Value = W1gb
```

```
                objExcel.Cells(33,8*Gen-3).Value = W2gb
                objExcel.Cells(33,8*Gen-2).Value = D1gb
                objExcel.Cells(33,8*Gen-1).Value = D2gb
                objExcel.Cells(33,8*Gen+0).Value = Thtgb
                objExcel.Cells(33,8*Gen+1).Value = Tgb
            objWorkbook.Save
        objExcel.Quit
        'Output Counter and  date&time to the excel file
        Set objExcel = CreateObject("Excel.Application")
            Set objWorkbook = objExcel.Workbooks.Open(CounterXLSX)
                objExcel.Cells(i+3,3*Gen-1).Value = Counter
                objExcel.Cells(i+3,3*Gen).Value = Date & " "& Time
            objWorkbook.Save
        objExcel.Quit
    Next

    'Use PSO algorithm to generate NEW parameters for next generation
    Wv = 0.9-(Gen-1)*(0.9-0.4)/Ng ' Wv varies linearly from 0.9 to 0.4
    c1 = 1.494  : c2 = 1.494

    'Generate PSO related parameters
    For i = 0 To Nm-1
        VwtN(i)=Wv*Vwt(i)+c1*Rnd*(Wtpb(i)-Wt(i))+c2*Rnd*(Wtgb-Wt(i))
        VhsN(i)=Wv*Vhs(i)+c1*Rnd*(Hspb(i)-Hs(i))+c2*Rnd*(Hsgb-Hs(i))
        Vw1N(i)=Wv*Vw1(i)+c1*Rnd*(W1pb(i)-W1(i))+c2*Rnd*(W1gb-W1(i))
        Vw2N(i)=Wv*Vw2(i)+c1*Rnd*(W2pb(i)-W2(i))+c2*Rnd*(W2gb-W2(i))
        Vd1N(i)=Wv*Vd1(i)+c1*Rnd*(D1pb(i)-D1(i))+c2*Rnd*(D1gb-D1(i))
        Vd2N(i)=Wv*Vd2(i)+c1*Rnd*(D2pb(i)-D1(i))+c2*Rnd*(D1gb-D1(i))
        'Calculate the new parameters.
        WtE(i)=0: HsE(i)=0: W1E(i)=0: W2E(i)=0: D1E(i)=0: D2E(i)=0
        'Generate New Wt(i)
        WtN(i)=Wt(i)+VwtN(i)  'Wt range [1 6]
        Add=0   'Clear to Zero
        Do While  WtN(i) < 1 Or WtN(i) > 6
            VwtN(i)=Wv*Vwt(i)+c1*Rnd*(Wtpb(i)-Wt(i))+c2*Rnd*(Wtgb-Wt(i))
            WtN(i)=Wt(i)+VwtN(i)  'Wt range [1 6]
            Add = Add + 1
            If Add > 1000 Then
                WtE(i)=1
                Do While WtN(i) < 1 Or WtN(i) > 6
                    WtN(i) = 1 + 5*Rnd  '[1  6]
                Loop
                VwtN(i) = Vwt(i)
                Exit Do
            End If
        Loop
        Wt(i) = WtN(i): Vwt(i) = VwtN(i)

        'Generate New Hs(i)
        HsN(i)=Hs(i)+VhsN(i)    'Hs range [6  32]
        Add=0   'Clear to Zero
        Do While HsN(i) < 6 Or HsN(i) > 32
            VhsN(i)=Wv*Vhs(i)+c1*Rnd*(Hspb(i)-Hs(i))+c2*Rnd*(Hsgb-Hs(i))
            HsN(i)=Hs(i)+VhsN(i)    'Hs range [6  32]
            Add = Add + 1
            If Add > 1000 Then
                HsE(i)=1
                Do While HsN(i) < 6 Or HsN(i) > 32
                    HsN(i) = 6 + 26*Rnd '[6  32]
                Loop
                VhsN(i) = Vhs(i)
                Exit Do
            End If
        Loop
        Hs(i) = HsN(i): Vhs(i) = VhsN(i)

        'Generate New W1(i)
        W1N(i)=W1(i)+Vw1N(i)   'W1 range [1 10]
        Add=0   'Clear to Zero
        Do While W1N(i) < 1 Or W1N(i) > 10
            Vw1N(i)=Wv*Vw1(i)+c1*Rnd*(W1pb(i)-W1(i))+c2*Rnd*(W1gb-W1(i))
            W1N(i)=W1(i)+Vw1N(i)   'W1 range [1 10]
            Add = Add + 1
            If Add > 1000 Then
                W1E(i)=1
                Do While W1N(i) < 1 Or W1N(i) > 10
```

```
                    W1N(i) = 1 + 9*Rnd  '[1  10]
                Loop
                Vw1N(i) = Vw2(i)
                Exit Do
            End If
        Loop
        W1(i) = W1N(i): Vw1(i) = Vw1N(i)

        'Generate New W2(i)
        W2N(i)=W2(i)+Vw2N(i)     'W2 range [1 10]
        Add=0   'Clear to Zero
        Do While W2N(i) < 1 Or W2N(i) > 10
            Vw2N(i)=Wv*Vw2(i)+c1*Rnd*(W2pb(i)-W2(i))+c2*Rnd*(W2gb-W2(i))
            W2N(i)=W2(i)+Vw2N(i)     'W2 range [1 10]
            Add = Add + 1
            If Add > 1000 Then
                W2E(i)=1
                Do While W2N(i) < 1 Or W2N(i) > 10
                    W2N(i) = 1 + 9*Rnd  '[1  10]
                Loop
                Vw2N(i) = Vw2(i)
                Exit Do
            End If
        Loop
        W2(i) = W2N(i): Vw2(i) = Vw2N(i)

        'Generate New D1(i)
        D1N(i)=D1(i)+Vd1N(i)  'D1 range [2 21]
        Add=0   'Clear to Zero
        Do While D1N(i) < 2 Or D1N(i) > 21 Or D1N(i) < (W1(i)/2+W2(i)+0.5)
            Vd1N(i)=Wv*Vd1(i)+c1*Rnd*(D1pb(i)-D1(i))+c2*Rnd*(D1gb-D1(i))
            D1N(i)=D1(i)+Vd1N(i)  'D1 range [2 21]
            Add = Add + 1
            If Add > 1000 Then
                D1E(i)=1
                Do While D1N(i) < 2 Or D1N(i) > 21 Or D1N(i) < (W1(i)/2+W2(i)+0.5)
                    D1N(i) = 2 + 19*Rnd     '[2  21]
                Loop
                Vd1N(i) = Vd1(i)
                Exit Do
            End If
        Loop
        D1(i) = D1N(i): Vd1(i) = Vd1N(i)

        'Generate New D2(i)
        D2N(i)=D2(i)+Vd2N(i)  'D2 range [8 20.5]
        Add=0   'Clear to Zero
        Do While D2N(i) < 8 Or D2N(i) > 20.5 Or D2N(i) < (W1(i)/2+W2(i)+0.5) Or
        (D1(i)-D2N(i)) >6
            Vd2N(i)=Wv*Vd2(i)+c1*Rnd*(D2pb(i)-D1(i))+c2*Rnd*(D1gb-D1(i))
            D2N(i)=D2(i)+Vd2N(i)  'D2 range [8 20.5]
            Add = Add + 1
            If Add > 1000 Then
                D2E(i)=1
                Do While D2N(i) < 8 Or D2N(i) > 20.5 Or D2N(i) < (W1(i)/2+W2(i)+0.5
                Or (D1(i)-D2N(i)) >6
                    D2N(i) = 8 + 12.5*Rnd       '[8  20.5]
                Loop
                Vd2N(i) = Vd2(i)
                Exit Do
            End If
        Loop
        D2(i) = D2N(i): Vd2(i) = Vd2N(i)
    Next

    'Save the NEW Parameters to <<Parameter>> file
    Set objExcel = CreateObject("Excel.Application")
        Set objWorkbook = objExcel.Workbooks.Open(ParameterResultXLSX)
        For i= 0 To Nm-1
            objExcel.Cells(i+3,8*(Gen+1)-6).Value = Wt(i)
            objExcel.Cells(i+3,8*(Gen+1)-5).Value = Hs(i)
            objExcel.Cells(i+3,8*(Gen+1)-4).Value = W1(i)
            objExcel.Cells(i+3,8*(Gen+1)-3).Value = W2(i)
            objExcel.Cells(i+3,8*(Gen+1)-2).Value = D1(i)
            objExcel.Cells(i+3,8*(Gen+1)-1).Value = D2(i)
        Next
```

```
349             objWorkbook.Save
350         objExcel.Quit
351         'Save the NEW Velocities to <<Velocity>> file
352         Set objExcel = CreateObject("Excel.Application")
353             Set objWorkbook = objExcel.Workbooks.Open(VelocityXLSX)
354             For i= 0 To Nm-1
355                 objExcel.Cells(i+3,6*(Gen+1)-4).Value = Vwt(i)
356                 objExcel.Cells(i+3,6*(Gen+1)-3).Value = Vhs(i)
357                 objExcel.Cells(i+3,6*(Gen+1)-2).Value = Vw1(i)
358                 objExcel.Cells(i+3,6*(Gen+1)-1).Value = Vw2(i)
359                 objExcel.Cells(i+3,6*(Gen+1)+0).Value = Vd1(i)
360                 objExcel.Cells(i+3,6*(Gen+1)+1).Value = Vd2(i)
361             Next
362             objWorkbook.Save
363         objExcel.Quit
364         'Save the Error Marks to <<Error>> file
365         Set objExcel = CreateObject("Excel.Application")
366             Set objWorkbook = objExcel.Workbooks.Open(ErrorXLSX)
367             For i= 0 To Nm-1
368                 objExcel.Cells(i+3,6*(Gen+1)-4).Value = WtE(i)
369                 objExcel.Cells(i+3,6*(Gen+1)-3).Value = HsE(i)
370                 objExcel.Cells(i+3,6*(Gen+1)-2).Value = W1E(i)
371                 objExcel.Cells(i+3,6*(Gen+1)-1).Value = W2E(i)
372                 objExcel.Cells(i+3,6*(Gen+1)+0).Value = D1E(i)
373                 objExcel.Cells(i+3,6*(Gen+1)+1).Value = D2E(i)
374             Next
375             objWorkbook.Save
376         objExcel.Quit
377     Next
378     MsgBox("ALL The PSO Simulation is FINISHED!")
```

Appendix B Mechanical Drawing for the Machine and the Testing Rig

B.1 The Prototype Machine

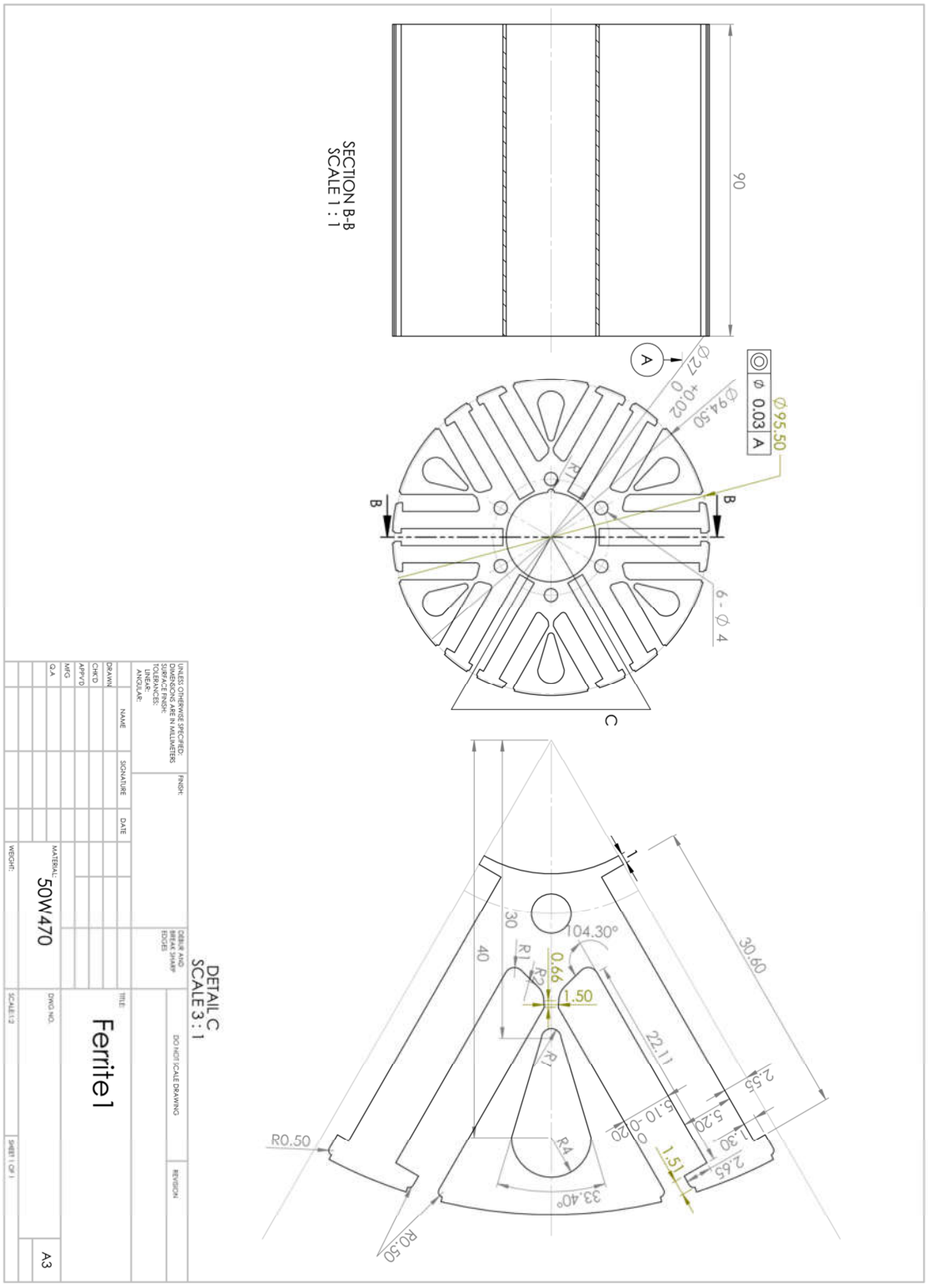

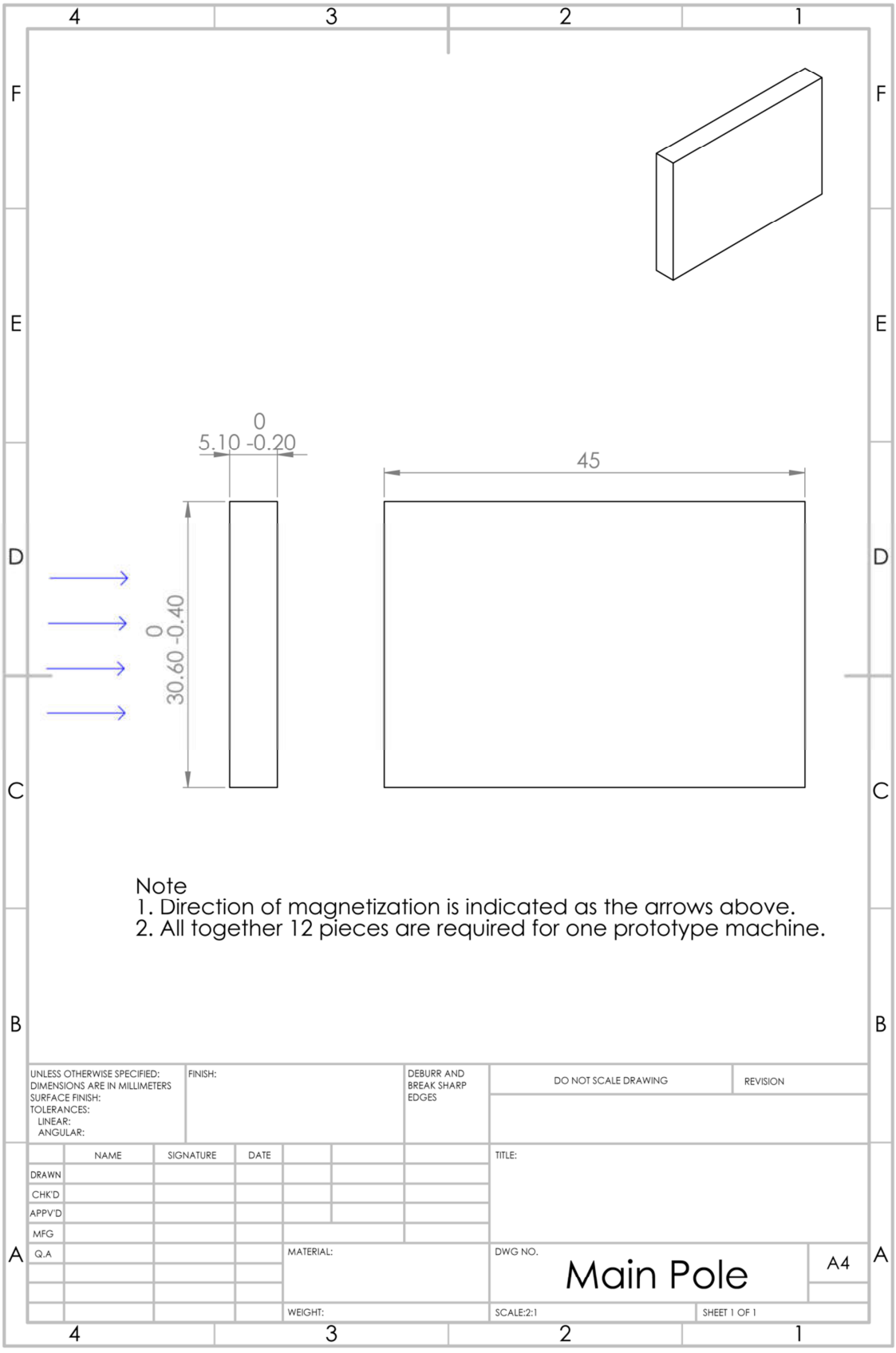
4
3
2
1
F
E
D
C
B
A
0
5.10 -0.20
45
0
30.60 -0.40
Note
1. Direction of magnetization is indicated as the arrows above.
2. All together 12 pieces are required for one prototype machine.
UNLESS OTHERWISE SPECIFIED:
DIMENSIONS ARE IN MILLIMETERS
SURFACE FINISH:
TOLERANCES:
LINEAR:
ANGULAR:
FINISH:
DEBURR AND BREAK SHARP EDGES
DO NOT SCALE DRAWING
REVISION
NAME
SIGNATURE
DATE
DRAWN
CHK'D
APPV'D
MFG
Q.A
TITLE:
MATERIAL:
DWG NO.
Main Pole
A4
WEIGHT:
SCALE:2:1
SHEET 1 OF 1

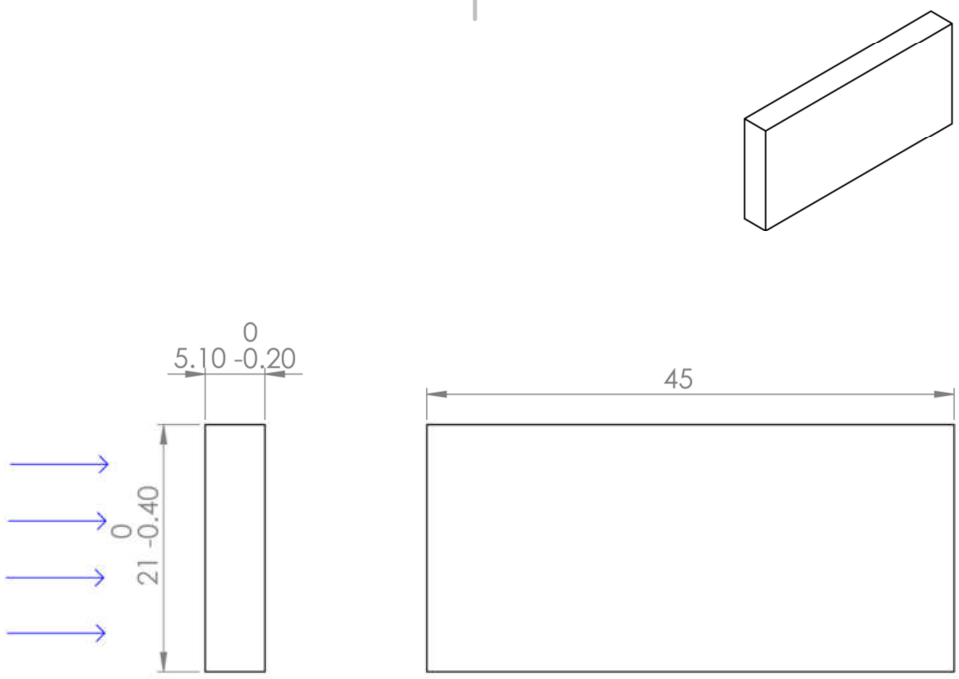

Note
1. Direction of magnetization is indicated as the arrows above.
2. All together 24 pieces are required for one prototype machine.

UNLESS OTHERWISE SPECIFIED: DIMENSIONS ARE IN MILLIMETERS SURFACE FINISH: TOLERANCES: LINEAR: ANGULAR:	FINISH:	DEBURR AND BREAK SHARP EDGES	DO NOT SCALE DRAWING	REVISION	
	NAME	SIGNATURE	DATE	TITLE:	Secondary Pole
DRAWN					
CHK'D					
APPV'D					
MFG					
Q.A				MATERIAL: Y30H	DWG NO. A4
				WEIGHT:	SCALE:2:1 SHEET 1 OF 1

B.2 The Testing Rig

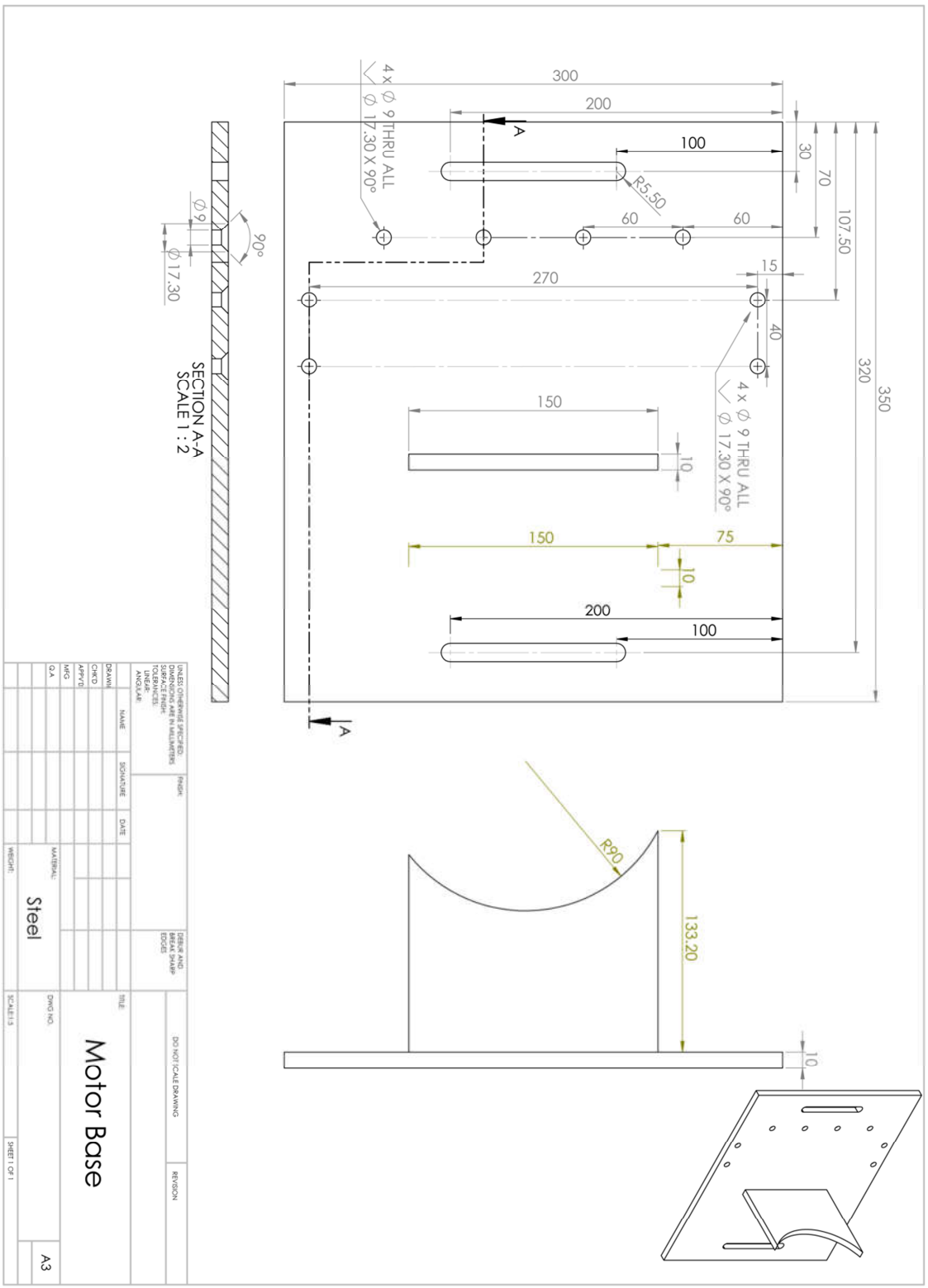

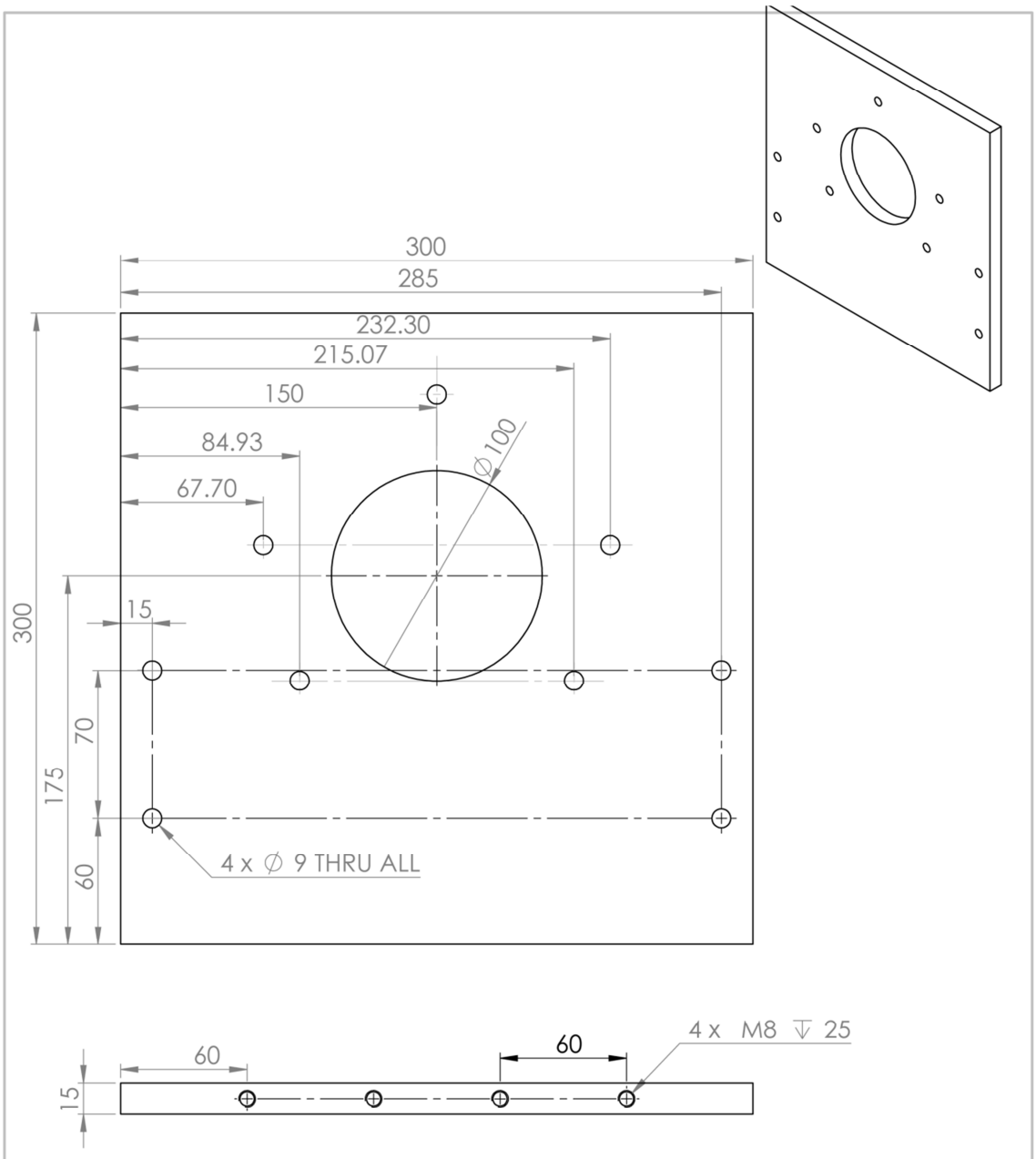

UNLESS OTHERWISE SPECIFIED: DIMENSIONS ARE IN MILLIMETERS SURFACE FINISH: TOLERANCES: LINEAR: ANGULAR:	FINISH:		DEBUR AND BREAK SHARP EDGES			DO NOT SCALE DRAWING	REVISION
	NAME	SIGNATURE	DATE			TITLE:	
DRAWN						Motor Fixture Plate	
CHK'D							
APPV'D							
MFG							
Q.A				MATERIAL:		DWG NO.	A4
				Steel			
				WEIGHT:		SCALE:1:5	SHEET 1 OF 1

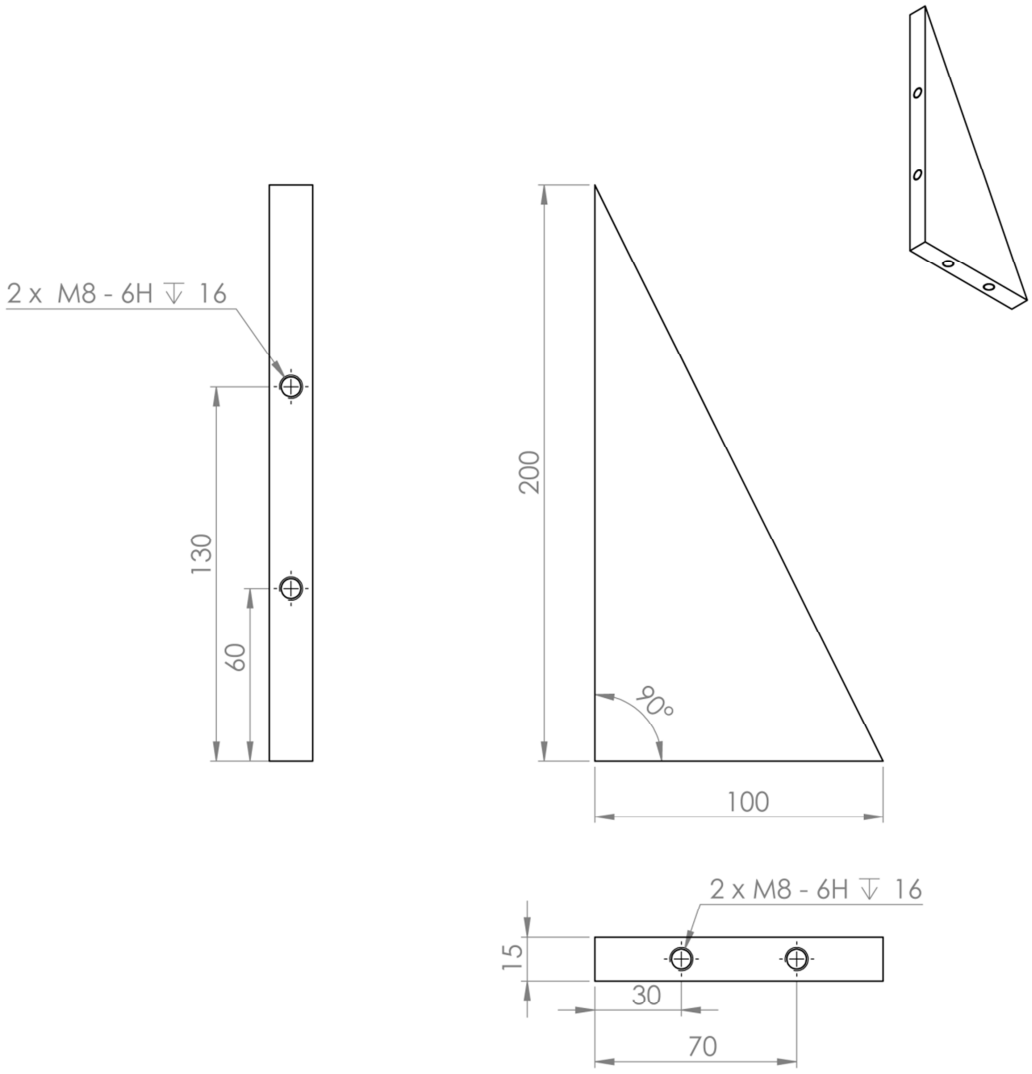

UNLESS OTHERWISE SPECIFIED: DIMENSIONS ARE IN MILLIMETERS SURFACE FINISH: TOLERANCES: LINEAR: ANGULAR:	FINISH:		DEBUR AND BREAK SHARP EDGES		DO NOT SCALE DRAWING	REVISION
	NAME	SIGNATURE	DATE		TITLE:	
DRAWN					Triangle Support	
CHK'D						
APPV'D						
MFG						
Q.A				MATERIAL: Steel	DWG NO.	A4
				WEIGHT:	SCALE:1:2	SHEET 1 OF 1

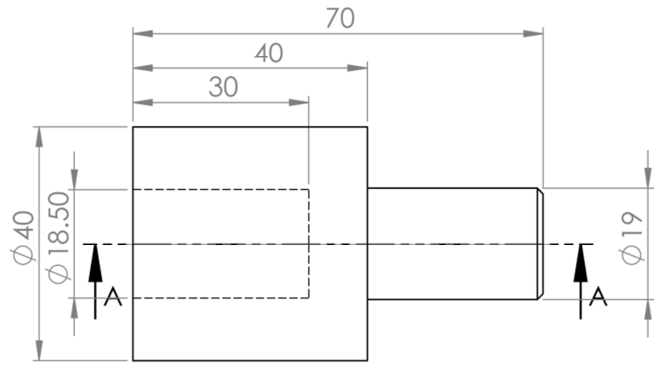

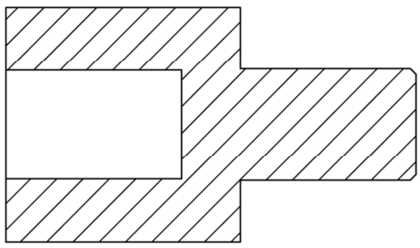

SECTION A-A

UNLESS OTHERWISE SPECIFIED: DIMENSIONS ARE IN MILLIMETERS SURFACE FINISH: TOLERANCES: LINEAR: ANGULAR:		FINISH:		DEBURR AND BREAK SHARP EDGES		DO NOT SCALE DRAWING	REVISION
	NAME	SIGNATURE	DATE			TITLE:	
DRAWN						Coupler for Dyno	
CHK'D							
APPV'D							
MFG							
Q.A				MATERIAL:		DWG NO.	A4
				Aluminum			
				WEIGHT:		SCALE:1:1	SHEET 1 OF 1

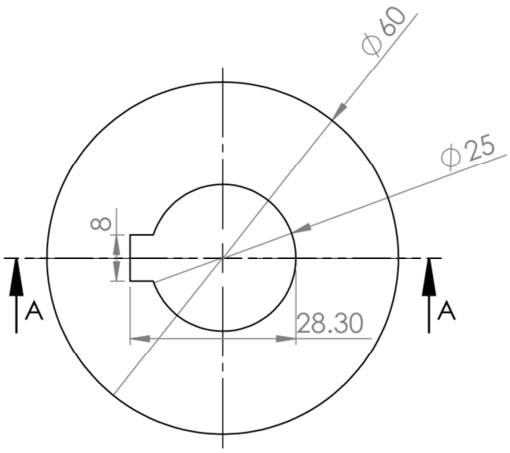

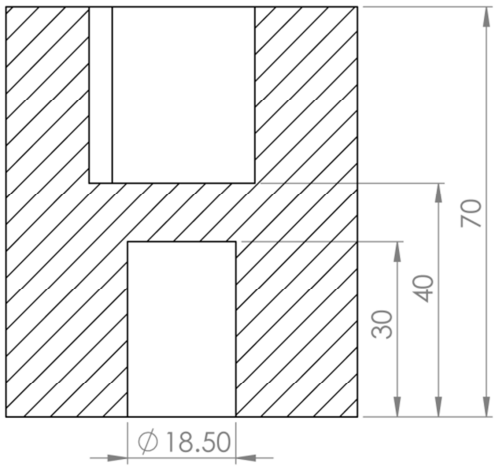

SECTION A-A
SCALE 1 : 1

UNLESS OTHERWISE SPECIFIED: DIMENSIONS ARE IN MILLIMETERS SURFACE FINISH: TOLERANCES: LINEAR: ANGULAR:	FINISH:	DEBURR AND BREAK SHARP EDGES	DO NOT SCALE DRAWING / REVISION

	NAME	SIGNATURE	DATE
DRAWN			
CHK'D			
APPV'D			
MFG			
Q.A			

TITLE: Coupler for the IM

MATERIAL: Aluminum

DWG NO. A4

WEIGHT:

SCALE:1:2

SHEET 1 OF 1

Appendix C Tables Used in Motor Quality Control

C.1 D-optimality Table of Initial Factors and Its Response

Runs	T1	T2	T3	T4	T5	T6	T7	T8	T9	T10	T11	T12	Torque (Nm)	Efficiency (%)
1	0.1	0.2	0	0	0	0.1	0	0.01	0	0.1	0	0.2	12.6873	92.8365
2	0	0	0	0.4	0.1	0.1	0.1	0	0.1	0	0.2	0.1	12.0118	92.6612
3	0	0.4	0	0	0.1	0.1	0.1	0.02	0	0	0	0	13.4314	92.8021
4	0.1	0.4	0	0.4	0.05	0.05	0	0	0.2	0.1	0	0.1	13.0129	92.8318
5	0.2	0	0	0	0	0.1	0	0.02	0.2	0	0	0	13.5643	92.8807
6	0	0	0	0	0	0	0	0.02	0.2	0.2	0	0.2	12.8389	92.9313
7	0.2	0	0.2	0	0.1	0	0.1	0.02	0.2	0	0.2	0	12.4159	92.7107
8	0.2	0.4	0	0.4	0.1	0.1	0.1	0.02	0	0.2	0.2	0.2	11.5437	92.5357
9	0.2	0.4	0	0	0.1	0	0	0.02	0.2	0.1	0.1	0	13.0802	92.8443
10	0	0.4	0	0.4	0	0	0.1	0.02	0.2	0	0.2	0	12.6693	92.8434
11	0	0.4	0.1	0	0	0.1	0.1	0	0	0.2	0.2	0	12.5194	92.7683
12	0	0.4	0.2	0.4	0	0.1	0.1	0	0.2	0	0	0	13.2617	92.7705
13	0	0.4	0.2	0.4	0	0	0	0.02	0	0.2	0	0.2	12.5608	92.7957
14	0	0	0	0.4	0	0	0.1	0	0	0.2	0	0.2	12.7274	92.8617
15	0.2	0.2	0.2	0	0	0	0	0.01	0.2	0.2	0.2	0	12.5351	92.7843
16	0.2	0	0	0.4	0.1	0	0	0	0.2	0	0.2	0	12.5120	92.7545
17	0.2	0	0.2	0.4	0.05	0.05	0	0.01	0.1	0	0.1	0.2	11.9320	92.6243
18	0	0.4	0	0	0.1	0.1	0	0.02	0.2	0	0.2	0.2	11.6667	92.6142
19	0.1	0	0.2	0	0.1	0	0	0.02	0	0.2	0	0	13.4420	92.8287
20	0	0	0.2	0	0	0.1	0	0	0	0.2	0	0	13.4563	92.8565
21	0	0	0	0.4	0.1	0	0.1	0.02	0.2	0.2	0.2	0.2	11.7761	92.6734
22	0	0.4	0.2	0.2	0.1	0	0.1	0.02	0.1	0.2	0.1	0.1	12.4326	92.7292
23	0.2	0	0.2	0.2	0.1	0.1	0.1	0.02	0.2	0.2	0.2	0.2	11.4495	92.5074
24	0	0.4	0	0	0	0	0	0	0.2	0.2	0	0	13.7365	92.9799
25	0.2	0.4	0.2	0.4	0	0	0.1	0	0	0.1	0.2	0	12.4216	92.7045
26	0.2	0.4	0	0.4	0	0.1	0	0.02	0	0.2	0	0	13.4648	92.8318
27	0	0.4	0	0.4	0.1	0	0	0.02	0.1	0	0	0.2	12.6209	92.8080
28	0	0	0	0.4	0.1	0.1	0	0.02	0	0.2	0	0.2	12.5192	92.7643
29	0.2	0.4	0	0	0.05	0	0	0.02	0	0	0.2	0.1	12.1804	92.7186
30	0.2	0	0	0	0.05	0.1	0	0	0.2	0.2	0.2	0.2	11.6893	92.6236
31	0	0.4	0.2	0	0.1	0.1	0	0	0	0.2	0.2	0.2	11.5095	92.5355
32	0.2	0	0.2	0.4	0.1	0	0.1	0.02	0	0.2	0	0.2	12.3861	92.6851
33	0	0.2	0.2	0	0.1	0.1	0	0	0.2	0	0	0	13.2811	92.7699
34	0	0.4	0.2	0	0	0.1	0	0.02	0.2	0.1	0.1	0	12.9043	92.8083
35	0.2	0	0	0	0	0	0.1	0.02	0	0.2	0.2	0	12.7117	92.8378
36	0.2	0.4	0.2	0.4	0.1	0	0.1	0	0.2	0	0	0.2	12.3163	92.6574
37	0	0	0.2	0	0	0	0.1	0.01	0	0.2	0.2	0.2	11.7746	92.6705
38	0.2	0.2	0.2	0	0.1	0.1	0.1	0	0	0	0.2	0.2	11.4516	92.4929
39	0.2	0.4	0	0.4	0.1	0	0.1	0.01	0.2	0.2	0	0	13.4260	92.8130
40	0	0	0	0.4	0	0.05	0	0	0	0.2	0.2	0.1	12.2174	92.7665
41	0	0.2	0.1	0.2	0.1	0	0	0	0.2	0.1	0.1	0.2	12.1327	92.7321
42	0	0	0	0	0.1	0.1	0	0.01	0	0	0.2	0	12.5153	92.7526
43	0.2	0.4	0.2	0.4	0	0	0	0.02	0.2	0	0	0	13.3915	92.8151
44	0.2	0	0.2	0.4	0.1	0.1	0	0	0	0.2	0.2	0.1	11.7810	92.5411
45	0.1	0	0.2	0.4	0	0.1	0	0	0.2	0	0.2	0	12.3320	92.6939
46	0	0	0.1	0.4	0.1	0.1	0	0.01	0.2	0.2	0.2	0	12.3733	92.7193
47	0	0	0	0.4	0	0.1	0	0	0.2	0	0	0.2	12.6187	92.8332

Runs	T1	T2	T3	T4	T5	T6	T7	T8	T9	T10	T11	T12	Torque (Nm)	Efficiency (%)
48	0	0.4	0.2	0.4	0.1	0.05	0	0	0	0	0.2	0	12.3152	92.6639
49	0.2	0	0	0	0.1	0.1	0	0.02	0	0	0	0.2	12.5618	92.7614
50	0.2	0	0.2	0	0.1	0.1	0.1	0.01	0	0.2	0	0	13.2456	92.7264
51	0	0	0	0.2	0	0.1	0.1	0.02	0.2	0.2	0	0	13.5426	92.9053
52	0.1	0.4	0.2	0	0	0	0.1	0.02	0	0	0	0	13.4899	92.8438
53	0.2	0.4	0	0	0	0.05	0.1	0	0	0	0	0	13.5648	92.8590
54	0.2	0	0	0.4	0.1	0.05	0.1	0.02	0	0	0.2	0	12.4728	92.7186
55	0	0.2	0	0.4	0.1	0.1	0.1	0	0	0.2	0	0	13.3690	92.7904
56	0	0.4	0.2	0	0	0	0	0	0.1	0	0.2	0.2	11.7140	92.6394
57	0	0	0.2	0.4	0	0.1	0.1	0.02	0	0.2	0.2	0	12.4115	92.7308
58	0	0	0.2	0.4	0.1	0	0	0	0.2	0.2	0	0.1	12.8845	92.7914
59	0.2	0.4	0.1	0.4	0.1	0.1	0.05	0.01	0.2	0	0.2	0.1	11.8423	92.5749
60	0.1	0.4	0.2	0.2	0.1	0.1	0.05	0.01	0	0	0	0	13.1975	92.7033
61	0.1	0.4	0.2	0	0.1	0	0.1	0	0.2	0.2	0.2	0	12.4292	92.7274
62	0	0.4	0	0	0.1	0	0.1	0	0	0	0.2	0.2	11.7895	92.6581
63	0.2	0	0	0.4	0	0.1	0	0.02	0.2	0.1	0.2	0.2	11.6764	92.6203
64	0	0	0.2	0.4	0.1	0	0	0.02	0	0	0.2	0.2	11.5574	92.5565
65	0.2	0	0.1	0.4	0.1	0	0	0	0	0	0	0	13.4239	92.8078
66	0	0.4	0.2	0.4	0	0.1	0.1	0.02	0	0	0.2	0.2	11.5489	92.5546
67	0.2	0.4	0	0	0.1	0	0	0	0	0.2	0	0.2	12.6685	92.8072
68	0.2	0	0.2	0.4	0	0.1	0.1	0.02	0	0	0	0.1	12.8183	92.7263
69	0	0.2	0.1	0.4	0.05	0.1	0	0.02	0.1	0	0.2	0	12.4150	92.7259
70	0	0	0	0	0	0	0.1	0	0.2	0.1	0.2	0	12.7486	92.8830
71	0.2	0	0.1	0.4	0	0.05	0.1	0	0.2	0	0.2	0.2	11.6250	92.5895
72	0.2	0	0	0.4	0	0.1	0.1	0	0.2	0.2	0.1	0	12.9750	93.3090
73	0	0	0.2	0	0.1	0.05	0.1	0	0	0	0	0.2	12.4504	93.0466
74	0.1	0.2	0	0	0.1	0.1	0.05	0.02	0.2	0.2	0.2	0	12.4613	93.0523
75	0.2	0	0.2	0	0	0	0	0	0	0	0.1	0.2	12.1048	92.8623
76	0.2	0.4	0	0	0	0	0.1	0	0.2	0.2	0.2	0.2	11.8465	92.7180
77	0.2	0.4	0.2	0	0	0.1	0	0.02	0	0.2	0.2	0.2	11.5481	92.5438
78	0	0	0	0.4	0	0	0	0.02	0	0	0	0	13.6862	93.6345
79	0	0	0.2	0.4	0.1	0.1	0.1	0.02	0.2	0	0	0.2	12.2787	92.9562
80	0	0.2	0.2	0.4	0	0.1	0.05	0	0.2	0.2	0.2	0.2	11.5525	92.5464
81	0.2	0.4	0	0.4	0	0.1	0	0	0	0	0.2	0.2	11.6200	92.5865
82	0.2	0.4	0	0.2	0.1	0.1	0	0	0.1	0.2	0.2	0	12.4206	93.0311
83	0	0	0.2	0.2	0.05	0	0.1	0	0	0	0.2	0	12.5011	93.0728
84	0	0	0	0	0	0.1	0.1	0.02	0	0	0.1	0.2	12.2446	92.9380
85	0.1	0	0.2	0.4	0	0	0.1	0.02	0.2	0.2	0.1	0.1	12.5144	93.0797
86	0.2	0.4	0	0.4	0	0.1	0.1	0.02	0.2	0	0	0.2	12.4996	93.0721
87	0.2	0	0.2	0.4	0.1	0.1	0.05	0	0.2	0.1	0	0	13.1510	93.3926
88	0.1	0	0.1	0	0.1	0	0.05	0	0.1	0.2	0.2	0.2	11.7027	92.6351
89	0.2	0	0	0	0.1	0	0.1	0.01	0.2	0	0	0.2	12.6336	93.1406
90	0	0.4	0.2	0	0.05	0	0.05	0.02	0.2	0.1	0	0.2	12.5293	93.0874
91	0.2	0.4	0.2	0.4	0	0.1	0.1	0	0	0.2	0	0.2	12.3127	92.9743
92	0.1	0.4	0.2	0.4	0.1	0	0	0.02	0.2	0.2	0.2	0.2	11.5219	92.5282
93	0.2	0	0.2	0	0	0.1	0.1	0	0.2	0	0	0.2	12.4289	93.0354
94	0.2	0	0	0.4	0	0	0	0	0.1	0.2	0	0.2	12.7280	93.1880
95	0.2	0.4	0.2	0.4	0.05	0.1	0.1	0.02	0.2	0.2	0.2	0	12.2580	92.9452
96	0	0.4	0	0	0.1	0.1	0.1	0	0.2	0.2	0	0.2	12.5282	93.0868
97	0.2	0.4	0.2	0	0.1	0.1	0	0.02	0.2	0.2	0	0.2	12.3172	92.9767

*The units of T1~T12 is mm.

C.2 I-optimality Table of Initial Factors and Its Response

Runs	T1	T2	T3	T4	T5	T6	T7	T8	T9	T10	T11	T12	Torque (Nm)	Efficiency (%)
1	0.2	0.4	0	0	0	0.1	0	0.02	0	0.2	0.2	0	12.5618	92.7691
2	0.1	0	0.2	0.2	0.1	0	0.1	0.02	0	0.2	0.1	0	12.8913	92.7714
3	0.1	0	0.1	0	0	0.1	0	0.01	0.2	0	0	0	13.4947	92.8653
4	0	0.4	0.2	0	0.1	0.05	0.05	0.02	0	0.2	0	0.1	12.8734	92.7614
5	0.2	0	0	0.2	0.05	0.05	0.1	0.02	0.1	0	0	0	13.4841	92.8291
6	0.2	0	0	0	0	0	0.1	0	0.2	0	0.1	0	13.1812	92.8989
7	0.1	0.4	0.1	0	0	0.05	0.1	0.02	0	0	0.2	0	12.5521	92.7677
8	0.2	0.4	0.2	0.4	0.05	0.1	0	0.01	0	0.1	0	0.2	12.2946	92.6467
9	0.2	0.4	0.1	0.2	0	0	0	0.02	0.2	0	0.1	0	13.0066	92.8254
10	0.2	0.4	0	0.4	0.1	0	0	0.02	0	0.1	0.2	0.2	11.6480	92.5857
11	0.1	0.4	0.2	0	0	0.05	0	0.02	0.1	0.1	0.1	0.2	12.0748	92.6999
12	0	0	0	0.2	0.1	0.1	0.05	0.02	0.1	0.1	0	0.1	12.9626	92.8080
13	0.1	0	0.2	0	0	0.05	0.1	0	0.2	0	0.2	0.2	11.6650	92.6159
14	0	0	0	0	0.1	0	0.05	0	0	0	0.2	0.2	11.7848	92.6587
15	0.2	0	0.2	0	0.05	0.05	0.1	0	0	0.2	0.2	0.1	11.9937	92.6448
16	0.1	0.4	0.2	0.4	0.1	0.05	0.05	0.02	0.2	0	0.2	0.2	11.4444	92.5029
17	0	0	0	0.2	0	0.1	0.1	0.02	0	0.2	0.2	0	12.6106	92.8128
18	0	0	0	0.4	0	0	0	0.02	0.2	0	0	0.2	12.7524	92.8917
19	0.1	0.4	0.2	0.2	0.1	0.1	0.1	0.01	0.1	0	0	0	13.1689	92.6939
20	0	0.4	0.1	0.4	0.1	0	0.1	0.02	0.2	0	0	0	13.3772	92.8043
21	0.2	0.2	0	0	0	0.1	0.05	0.02	0	0	0	0.2	12.6035	92.7826
22	0.2	0	0.2	0	0	0	0	0	0.2	0.2	0	0.2	12.5834	92.8066
23	0.2	0.4	0.1	0	0.05	0	0	0	0.1	0.2	0	0	13.5354	92.8615
24	0	0.2	0.2	0.2	0.1	0	0	0.02	0	0	0.1	0.1	12.4640	92.7367
25	0	0.2	0	0	0	0.05	0.05	0.02	0.2	0.2	0	0	13.6307	92.9367
26	0	0.4	0	0	0.05	0.1	0.1	0.01	0	0.1	0	0	13.4885	92.8397
27	0.2	0.4	0	0	0.1	0.1	0.1	0	0.1	0	0.2	0.2	11.6064	92.5671
28	0.2	0	0.2	0.4	0.1	0	0	0	0	0	0	0	13.3510	92.7807
29	0	0	0.2	0	0.05	0.1	0	0	0	0.2	0	0	13.3844	92.8174
30	0	0.4	0.2	0.2	0	0	0.1	0	0.2	0.2	0.2	0	12.5227	92.7904
31	0.2	0.2	0.1	0.4	0	0	0.1	0.02	0	0	0.2	0.2	11.6754	92.6028
32	0.1	0.2	0	0	0.1	0.05	0	0.01	0.1	0.2	0.1	0.1	12.5938	92.7914
33	0.2	0	0.1	0.4	0.05	0	0.1	0	0.1	0.1	0.1	0.2	12.1039	92.7013
34	0.1	0.4	0	0.2	0	0.05	0.05	0	0	0.2	0.1	0.2	12.2049	92.7458
35	0	0	0	0.4	0.05	0	0	0	0.1	0	0.2	0	12.6350	92.8232
36	0.1	0.4	0	0	0.1	0.1	0.1	0.02	0.2	0.2	0.2	0	12.4628	92.7375
37	0.2	0	0.2	0	0	0	0.05	0.02	0	0	0	0	13.4939	92.8432
38	0.1	0.2	0.2	0.4	0.05	0	0.05	0	0.2	0.1	0	0.1	12.8826	92.7774
39	0.2	0	0.2	0.2	0	0.05	0	0	0.2	0.1	0.2	0	12.4255	92.7331
40	0.2	0.2	0.2	0.2	0	0.1	0.1	0.02	0.2	0.2	0.1	0.1	12.3666	92.7023
41	0	0.2	0	0	0.05	0	0.1	0.02	0.1	0.2	0.2	0.2	11.8542	92.7025
42	0	0.4	0	0.4	0	0	0.1	0.02	0.2	0.1	0.2	0.1	12.2507	92.7853
43	0	0.2	0.1	0.2	0.1	0.1	0.05	0.01	0.1	0.1	0.1	0.2	11.9812	92.6508
44	0.2	0.4	0.2	0	0.1	0	0.1	0.02	0.2	0.1	0.1	0.2	11.9807	92.6412
45	0.2	0.4	0.2	0	0.05	0.1	0	0.01	0.2	0	0.2	0.1	11.8763	92.5978
46	0	0.2	0.2	0	0.1	0	0.05	0.01	0.1	0.1	0.2	0	12.4463	92.7343
47	0.1	0.2	0	0	0.1	0	0	0.02	0	0	0	0	13.6308	92.8911

Runs	T1	T2	T3	T4	T5	T6	T7	T8	T9	T10	T11	T12	Torque (Nm)	Efficiency (%)
48	0	0	0	0.4	0	0.1	0.1	0	0.2	0.2	0	0.2	12.5982	92.8236
49	0.2	0	0.2	0	0.1	0.05	0	0.02	0.2	0.2	0	0	13.3252	92.7831
50	0	0	0.2	0.4	0	0.1	0.05	0	0.2	0	0	0.2	12.4046	92.7375
51	0.2	0.4	0	0.4	0.05	0	0.1	0	0	0.1	0.1	0	13.0508	92.8245
52	0	0.2	0	0	0	0.1	0.05	0	0.1	0.1	0.2	0	12.6342	92.8267
53	0	0.2	0.1	0.2	0.05	0.05	0.1	0	0.2	0	0.1	0	12.9504	92.8092
54	0.2	0.4	0.1	0	0	0.05	0.1	0	0.2	0	0	0.2	12.5758	92.7870
55	0	0.4	0.1	0.4	0.1	0	0.1	0	0	0.2	0	0.2	12.5005	92.7469
56	0.1	0	0.1	0.4	0.05	0.05	0.05	0.01	0.1	0.2	0	0	13.4031	92.8211
57	0.2	0	0	0	0.1	0.1	0.1	0.01	0	0.2	0	0.2	12.5206	92.7411
58	0.2	0.2	0	0.2	0.1	0.1	0.05	0	0.2	0	0	0.1	12.8898	92.7563
59	0.1	0	0.1	0	0.05	0.1	0	0	0.1	0	0	0.2	12.5402	92.7774
60	0	0	0.1	0.4	0.1	0.1	0	0	0.2	0.1	0.2	0.1	11.9558	92.6510
61	0.2	0.2	0	0.4	0.1	0	0.1	0.01	0.2	0	0.2	0	12.5115	92.7475
62	0.1	0	0	0.4	0.1	0.1	0.1	0.01	0	0	0.1	0.2	12.0121	92.6484
63	0	0.4	0.2	0	0.05	0.1	0.1	0.01	0	0	0.2	0.2	11.5611	92.5577
64	0	0	0.1	0.4	0	0	0.05	0	0	0.2	0.2	0.1	12.1733	92.7456
65	0.2	0.4	0.1	0.4	0	0	0	0	0.2	0.2	0.2	0.2	11.6858	92.6245
66	0.2	0	0.1	0	0.1	0.1	0.05	0.02	0	0	0.1	0	12.7933	92.7044
67	0.2	0	0	0.2	0	0	0	0.01	0	0.1	0.1	0.1	12.7081	92.8374
68	0.2	0.4	0.1	0.4	0.1	0.05	0.1	0.01	0.1	0.2	0.1	0.1	12.3917	92.6923
69	0	0.2	0.2	0.4	0	0.05	0	0.02	0.2	0.2	0.2	0	12.4313	92.7551
70	0	0.4	0	0.4	0.1	0.1	0	0	0.2	0.1	0	0	13.3776	92.8035
71	0.2	0.2	0	0.2	0.05	0.05	0.05	0.01	0.2	0.1	0.2	0.2	11.6922	92.6192
72	0	0.4	0	0	0.1	0	0	0	0.2	0	0	0.2	12.7036	92.8493
73	0.1	0	0.1	0	0.05	0	0.05	0.02	0.2	0.2	0.2	0.1	12.1700	92.7475
74	0.2	0	0.2	0.2	0.1	0.1	0	0.02	0	0.2	0.2	0.2	11.4424	92.4962
75	0	0	0.2	0	0	0	0.1	0.01	0	0.1	0	0.2	12.6253	92.8184
76	0.1	0.2	0.1	0.4	0	0.1	0	0.01	0	0	0.2	0.1	12.0238	92.6683
77	0.1	0.2	0.1	0.4	0.05	0.1	0.1	0.02	0	0.1	0	0.1	12.8461	92.7403
78	0.2	0	0	0.4	0.05	0.1	0	0.02	0.2	0.2	0.1	0.1	12.4686	92.7449
79	0.1	0.4	0.2	0.4	0.05	0	0	0.02	0	0.2	0.1	0	12.8987	92.7797
80	0.1	0.4	0.1	0.2	0.1	0.05	0.05	0	0	0.1	0.2	0	12.4276	92.7058
81	0	0	0.2	0.4	0.1	0.1	0.1	0.02	0	0	0.2	0	12.2775	92.6492
82	0.2	0	0.2	0.4	0	0.1	0.1	0	0	0.2	0	0	13.2647	92.7492
83	0	0.4	0.1	0.2	0.05	0	0	0.02	0.2	0.2	0	0.2	12.6185	92.8286
84	0.2	0	0	0.4	0.1	0.1	0	0	0	0.2	0.2	0	12.4062	92.6969
85	0.1	0.4	0	0.2	0.05	0	0.05	0.01	0.1	0	0.1	0.2	12.1930	92.7395
86	0.1	0	0.2	0	0.1	0.1	0.1	0.02	0.2	0	0	0.2	12.3442	92.6870
87	0	0	0.2	0.4	0.05	0.05	0.05	0.02	0	0.2	0.1	0.2	11.9815	92.6551
88	0	0.4	0	0.4	0	0.05	0	0	0	0	0	0	13.5823	92.8928
89	0.1	0.2	0.1	0.2	0.05	0.05	0.05	0.01	0.1	0.1	0.1	0.1	12.4937	92.7497
90	0.2	0.4	0.1	0.4	0	0.1	0.1	0.01	0.2	0	0.2	0	12.3905	92.7034
91	0	0.4	0.2	0.4	0	0.1	0.05	0	0.1	0.2	0.1	0.1	12.3726	92.7127
92	0.1	0.4	0.2	0	0.1	0.1	0.05	0	0.2	0.2	0.1	0.2	11.8875	92.6099
93	0	0	0	0.2	0.1	0	0.05	0	0.2	0.2	0.1	0	13.0753	92.8712
94	0	0.4	0	0	0	0	0	0.02	0	0.2	0.2	0.2	11.8959	92.7211
95	0	0.4	0	0	0.05	0.1	0	0.02	0.2	0	0.2	0.2	11.7224	92.6430
96	0.2	0.4	0.2	0	0	0	0	0	0	0	0.2	0.2	11.6603	92.6006
97	0.2	0.4	0	0.4	0	0	0.1	0.02	0.2	0.2	0	0.2	12.6345	92.8137

*The units of T1~T12 is mm.

C.3 Coefficients of Torque Prediction Expression with Initial Set of Tolerances

Coef	T1(0,0.2)	T2(0,0.4)	T3(0,0.2)	T4(0,0.4)	T5(0,0.1)	T6(0,0.1)	T7(0,0.1)	T8(0,0.02)	T9(0,0.2)	T10(0,0.2)	T11(0,0.2)	T12(0,0.2)	Torque
T1(0,0.2)	-0.006283	0.000831	-1.52E-05	0.0008292	0.0012937	-0.002751	0.0029713	-0.002414	0.0003237	0.0034099	-0.003291	-0.000306	-0.028775
T2(0,0.4)		0.0023896	-5.70E-06	-0.00062	0.0010825	0.0016375	-0.00063	-0.002423	-0.000655	0.0002968	0.0041226	-0.000694	-0.013879
T3(0,0.2)			-0.00309	0.0016504	0.0022784	0.0023459	-0.001235	0.0017028	-0.003612	-0.000102	0.0055065	0.0009484	-0.090857
T4(0,0.4)				-0.001249	0.0050852	1.208E-05	0.0042875	-0.002103	0.0005558	0.0008081	0.0072323	-0.000735	-0.03743
T5(0,0.1)					0.0026633	-0.004154	-0.000807	0.0007699	-0.000209	0.0037095	-0.002302	0.0017508	-0.054559
T6(0,0.1)						0.002298	0.000508	-0.001852	-0.000502	0.0013257	0.0061463	0.0050236	-0.065876
T7(0,0.1)							0.0140154	-0.001741	0.0017692	-6.92E-05	0.0102546	0.0034319	-0.006646
T8(0,0.02)								-0.000759	0.0017036	0.0030918	-0.001527	0.0016143	-0.005367
T9(0,0.2)									0.000989	0.0011676	0.0028141	0.0047336	-0.004832
T10(0,0.2)										-0.003708	0.0044081	-1.73E-05	0.0065317
T11(0,0.2)											0.0145203	0.0184613	-0.456288
T12(0,0.2)												0.0056428	-0.433282

* The intercept term is 12.4952859, which is the value of torque response when factors are equal to median value.

C.4 Coefficients of Efficiency Prediction Expression with Initial Set of Tolerances

Coef	T1(0,0.2)	T2(0,0.4)	T3(0,0.2)	T4(0,0.4)	T5(0,0.1)	T6(0,0.1)	T7(0,0.1)	T8(0,0.02)	T9(0,0.2)	T10(0,0.2)	T11(0,0.2)	T12(0,0.2)	Efficiency
T1(0,0.2)	-0.001941	0.0004446	3.60E-04	0.0010992	0.0009841	-0.001486	0.0011769	-0.001329	5.566E-05	0.000753	-0.00027	0.0005766	-0.020991
T2(0,0.4)		0.0011789	1.05E-04	-0.000149	-0.000222	0.0004497	0.0001015	-0.000776	-0.000748	0.0001993	0.0026882	1.514E-05	-0.009064
T3(0,0.2)			-0.002264	0.0006693	0.000698	0.0010723	-0.000705	0.0012346	-0.001878	-9.99E-05	0.0012048	-0.001	-0.038222
T4(0,0.4)				-0.000617	0.0021205	-0.000355	0.0016045	-0.000602	0.0001595	-0.000132	0.002678	-0.001426	-0.016076
T5(0,0.1)					0.0014073	-0.002103	-5.68E-05	0.0008042	-0.0002	0.0019097	-0.000797	0.0009783	-0.029941
T6(0,0.1)						0.0017178	0.000491	-0.000925	3.856E-05	0.0006054	0.002909	0.0025564	-0.030165
T7(0,0.1)							0.0067169	-0.001266	0.0006146	0.0004054	0.0046995	0.0012171	-0.004723
T8(0,0.02)								0.0006825	0.0005594	0.0019558	-0.000606	0.0007716	-0.002412
T9(0,0.2)									1.96E-05	0.0012888	0.0005416	0.002106	0.0049825
T10(0,0.2)										-0.001342	0.0020306	-1.23E-03	0.0058847
T11(0,0.2)											-0.008879	-0.021702	-0.060794
T12(0,0.2)												-0.011665	-0.050769

* The intercept term is 92.75055, which is the value of efficiency response when factors are equal to median value.

C.5 Numerical Values Table of Standard Tolerance

Basic Dimension (mm)		Standard Tolerance Grade																	
		IT1	IT2	IT3	IT4	IT5	IT6	IT7	IT8	IT9	IT10	IT11	IT12	IT13	IT14	IT15	IT16	IT17	IT18
OVER	TO	μm											mm						
—	3	0.8	1.2	2	3	4	6	10	14	25	40	60	0.1	0.14	0.25	0.4	0.6	1	1.4
3	6	1	1.5	2.5	4	5	8	12	18	30	48	75	0.12	0.18	0.3	0.48	0.75	1.2	1.8
6	10	1	1.5	2.5	4	6	9	15	22	36	58	90	0.15	0.22	0.36	0.58	0.9	1.5	2.2
10	18	1.2	2	3	5	8	11	18	27	43	70	110	0.18	0.27	0.43	0.7	1.1	1.8	2.7
18	30	1.5	2.5	4	6	9	13	21	33	52	84	130	0.21	0.33	0.52	0.84	1.3	2.1	3.3
30	50	1.5	2.5	4	7	11	16	25	39	62	100	160	0.25	0.39	0.62	1	1.6	2.5	3.9
50	80	2	3	5	8	13	19	30	46	74	120	190	0.3	0.46	0.74	1.2	1.9	3	4.6
80	120	2.5	4	6	10	15	22	35	54	87	140	220	0.35	0.54	0.87	1.4	2.2	3.5	5.4
120	180	3.5	5	8	12	18	25	40	63	100	160	250	0.4	0.63	1	1.6	2.5	4	6.3
180	250	4.5	7	10	14	20	29	46	72	115	185	290	0.46	0.72	1.15	1.85	2.9	4.6	7.2
250	315	6	8	12	16	23	32	52	81	130	210	320	0.52	0.81	1.3	2.1	3.2	5.2	8.1
315	400	7	9	13	18	25	36	57	89	140	230	360	0.57	0.89	1.4	2.3	3.6	5.7	8.9
400	500	8	10	15	20	27	40	63	97	155	250	400	0.63	0.97	1.55	2.5	4	6.3	9.7
500	630	9	11	16	22	32	44	70	110	175	280	440	0.7	1.1	1.75	2.8	4.4	7	11
630	800	10	13	18	25	36	50	80	125	200	320	500	0.8	1.25	2	3.2	5	8	12.5
800	1 000	11	15	21	28	40	56	90	140	230	360	560	0.9	1.4	2.3	3.6	5.6	9	14
1 000	1 250	13	18	24	33	47	66	105	165	260	420	660	1.05	1.65	2.6	4.2	6.6	10.5	16.5
1 250	1 600	15	21	29	39	55	78	125	195	310	500	780	1.25	1.95	3.1	5	7.8	12.5	19.5
1 600	2 000	18	25	35	46	65	92	150	230	370	600	920	1.5	2.3	3.7	6	9.2	15	23
2 000	2 500	22	30	41	55	78	110	175	280	440	700	1100	1.75	2.8	4.4	7	11	17.5	28
2 500	3 150	26	36	50	68	96	135	210	330	540	860	1350	2.1	3.3	5.4	8.6	13.5	21	33

(Courtesy: GB/T 1800.3 – 1998)

Appendix D Motor Control Hardware and Test Rig

D.1 Motor Control Power Module STEVAL-IHM028V2

2 kW 3-phase motor control evaluation board featuring the STGIPS20C60 IGBT intelligent power module

Description

The goal of the STEVAL-IHM028V2 product evaluation board is to present a universal, fully tested and populated design consisting of a 3- phase inverter bridge based on the 600V, 17A intelligent power module STGIPS20C60. The IPM itself consists of short-circuit rugged IGBTs with negative temperature co-efficiency. It also contains a wide range of auxiliary functions like under voltage lockout and smart shutdown.

Thanks to these advanced characteristics, the system has been specifically designed to achieve accurate and fast conditioning of the current feedback, matching the typical requirements for field oriented control (FOC).

This board can be used to evaluate a wide range of applications such as HVAC (air conditioners), power white goods and high-end single-phase power tools.

Features

- Complete solution for a 2 kW power inverter
- HV supply mode: voltage 90 VAC to 285 VAC or direct DC line 125 V DC to 400 V DC
- Input voltage range extended to +400 V, for PFC compliance
- Input inrush limiter with bypassing relay
- Brake feature with overvoltage comparator
- Single- or three-shunt resistor current sensing method
- Hall sensor or encoder input
- Tachometer input
- Over temperature and overcurrent hardware protection
- Active fan with automatic over temperature switching
- Compact and safe design
- Universal conception for further evaluation with bread board and testing pins
- RoHS compliant

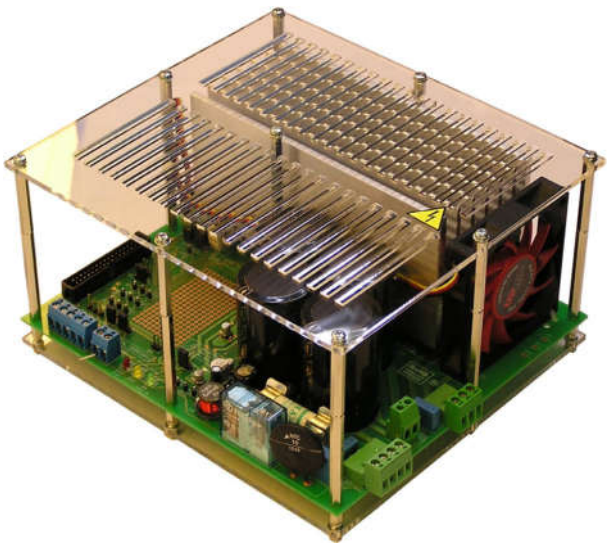

D.2 Motor Controller STM3210E-EVAL Evaluation Board

STM3210E-EVAL evaluation board

Description

The STM3210E-EVAL evaluation board is a complete development platform for STMicroelectronic's ARM Cortex-M3 core-based STM32F103ZET6 or STM32F103ZGT6 microcontroller. The range of hardware features on the board help you to evaluate all peripherals (LCD, SPI Flash, USART, IrDA, USB, audio, CAN bus, smartcard, MicroSD Card, NOR Flash, NAND Flash, SRAM, temperature sensor, audio DAC and motor control) and develop your own applications.

Extension headers make it easy to connect a daughterboard or wrapping board for your specific application.

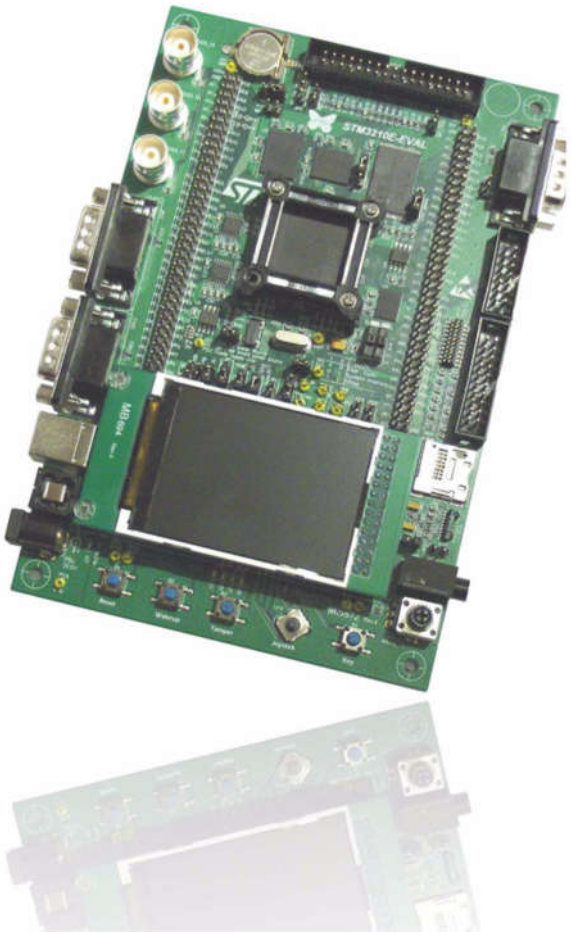

Features

- Three 5 V power supply options:
  - power jack
  - USB connector
  - daughterboard
- Boot from user Flash, system memory or SRAM
- I2S audio DAC, stereo audio jack
- 128 Mbyte MicroSD Card™ or bigger
- Both A and B type smartcard support
- 64 or 128 Mbit serial Flash, 512 Kx16 SRAM, 512 Mbit or 1 Gbit NAND Flash and 128 Mbit NOR Flash
- I2C/SMBus compatible serial interface temperature sensor
- Two RS-232 channels with RTS/CTS handshake support on one channel
- IrDA transceiver
- USB 2.0 full speed connection
- CAN 2.0A/B compliant connection
- Inductor motor control connector
- JTAG and trace debug support
- 240x320 TFT colour LCD
- Joystick with 4-direction control and selector
- Reset, wakeup, tamper and user buttons
- 4 colour LEDs
- RTC with backup battery

Appendix E The Programmable Dynamometer System

To validate the performances of the prototype machine under various working conditions, the programmable dynamometer system is necessary to provide required torque loadings under different rotational speeds. The whole testing system in the lab consists of the powder brake dynamometer, the controller, brake supply, torque transducer and cooling sub-system.

E.1 The Powder Brake Dynamometer

The Magtrol powder brake dynamometer (PB Series) contains magnetic powders inside. When electrical current is passing through the coils, magnetic field is generated, and the property of the powders changes. Accordingly, smooth braking torque is produced because of the friction between the powders and spinning rotor. Since the braking torque is generated by friction, relatively large torque can be achieved under low speed range, and the powder brake dynamometer is ideal for applications operating in the low to middle speed range or when operating in the middle to high torque range. The powder brake provides full torque at zero speed and requires water-cooling. The PB dynamometer has accuracy ratings of ± 0.3% to 0.5% full scale with integrated optical speed sensor, and is quite suitable for performance tests of electric motors.

E.2 The Programmable Dynamometer Controller

Magtrol programmable dynamometer controller employs state-of-the-art digital signal processing technology to provide superior motor testing capabilities. In the laboratory, the controller's high sample rate provides superior resolution for data acquisition and curve plotting. This allows for capturing more usable motor test data during switching, breakdown and other transitional areas of the motor test curve, with complete PC control via IEEE-488 or RS-232 interface. On the other hand, the controller can display torque, speed and power at all times, which can also be used as a manual standalone unit or part of a PC controlling system.

E.3 The Dynamometer Power Supply

The dynamometer power supplies (DES 311) are suited to the entire range of Magtrol's powder brake dynamometers. The unit supplies the required current to the coils of the brake within the dynamometer to generate torque loadings, and the current can be controlled by analogue and digital set-points coming from an electronic peripheral, in this case, from the Magtrol's programmable dynamometer controller. To avoid any disruption of the surrounding electronic modules, the power supply is fitted in an industrial housing made of extruded cast aluminium.

E.4 The Controller In-Line Torque Transducers

The Magtrol's in-line torque transducer is a standalone measuring chain. The transducer provides extremely accurate torque and speed measurement over a very broad range. The torque transducer is very reliable, providing high overload protection, excellent long term stability and high noise immunity. Non-contact differential transformer torque measuring technology is employed for the transducer, and no electronic components rotate during operation. The transducer consists of a hardened stainless steel shaft with smooth shaft ends, an anodized aluminium housing containing the guide bearings and an electronic measurement conditioner. The integrated electronic circuit, supplied by single DC voltage, provides torque and speed signals without any additional amplifier.

E.5 The Overall Diagram of the Testing System

The overall diagram of the testing system is demonstrated in Figure_Apx 1. The connections among the equipment can be divided into three categories, mechanical, electrical and water cooling. The prototype machine is connected to the dynamometer through the torque transducer for mechanical power output testing. The controlling and measuring units are connected to provide the drive for the prototype machine and collect experimental data. To dissipate the heat generated in the power brake, water cooling pipes are necessary for continuous loading tests.

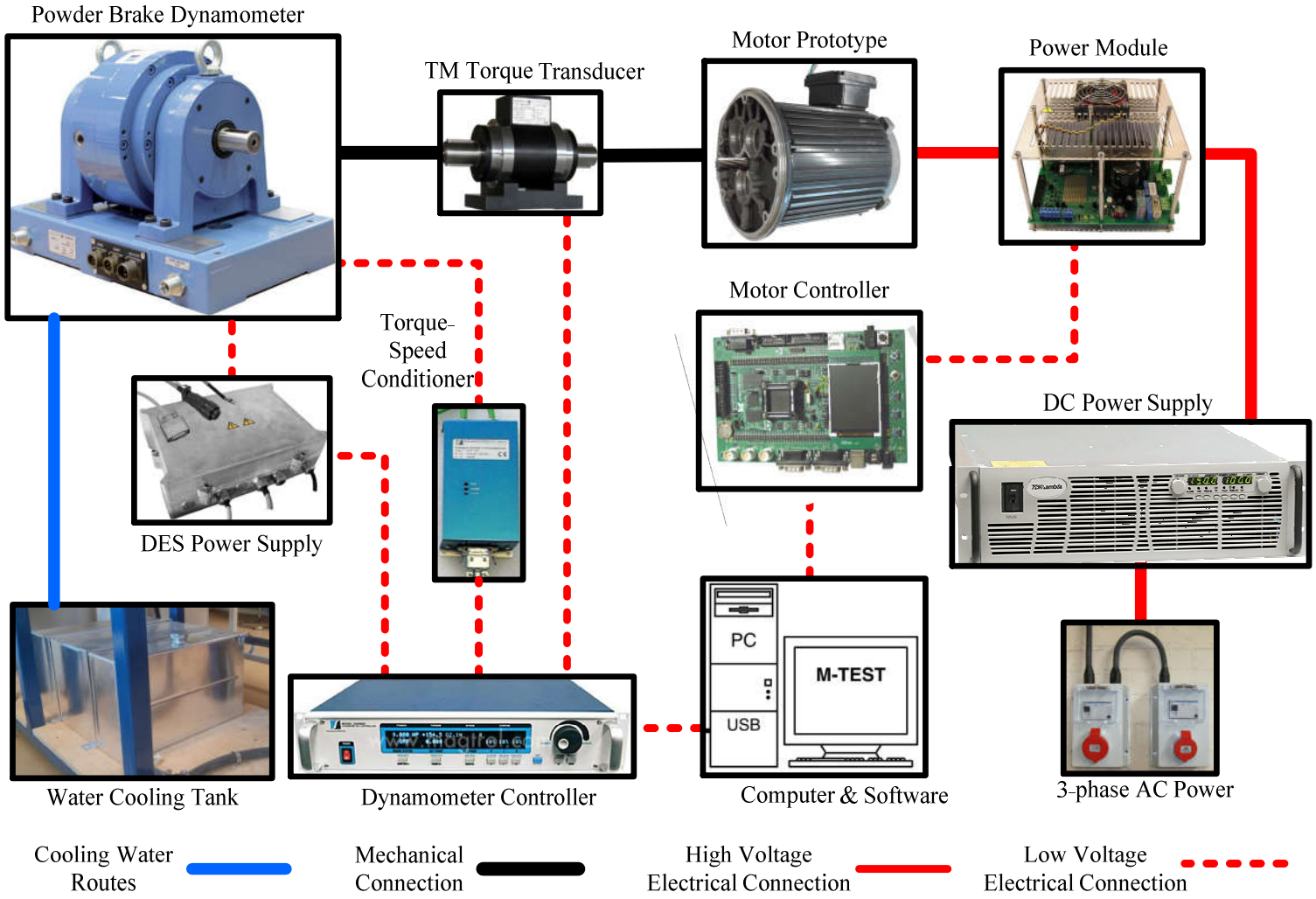

Figure_Apx 1 Motor test rig hardware connection diagram